UNIVERSITE BRETAGNE LOIRE

ESTACA ÉCOLE D'INGÉNIEURS Groupe ISAE

UNIVERSITÉ DE NANTES

Thèse de Doctorat

Thibaut VOGEL

Mémoire présenté en vue de l'obtention du
grade de Docteur de l'Université de Nantes
sous le sceau de l'Université Bretagne Loire

École doctorale : Sciences Pour l'Ingénieur (SPI)

Discipline : Mécanique des solides, des matériaux, des structures et des surfaces
Spécialité : Génie Mécanique
Unité de recherche : Institut de recherche en Génie Civil et Mécanique (GeM-EMM, UMR CNRS 6183)

Soutenue le 19/12/2017

Multiphysics analyses and modelling for the development of composite structures embedding electrical wires

JURY

Président du jury :	**Jean-Claude GRANDIDIER**	Professeur, ISAE-ENSMA, UPR CNRS 3346
Rapporteurs :	**Jean-François FERRERO** **Franck LAURO**	Professeur, Université Paul Sabatier, UMR CNRS 5312 Professeur, Université de Valenciennes, UMR CNRS 8201
Examinateurs :	**Caroline PETIOT** **Jean-Christophe WALRICK**	Docteur-ingénieure de recherche, AIRBUS SAS Central R&T Maître de Conférences, ESTACA Laval
Invité(s) :	**Jesus ASPAS-PUERTOLAS**	Ingénieur de recherche, ARIANE Group
Directeur de Thèse :	**Pascal CASARI**	Professeur, Université de Nantes, UMR CNRS 6183

UNIVERSITE BRETAGNE LOIRE

ESTACA ÉCOLE D'INGÉNIEURS Groupe ISAE

UNIVERSITÉ DE NANTES

Thèse de Doctorat

Thibaut VOGEL

Multiphysics analyses and modelling for the development of composite structures embedding electrical wires

Analyses et modélisations multi-physiques pour le développement de structures composites intégrant des conducteurs électriques

Résumé

A partir de l'étude d'une structure composite multifonctionnelle prédéfinie, cette thèse a pour objectif l'analyse du comportement thermomécanique et des modes d'endommagement d'une structure composite intégrant des conducteurs électriques. Des éprouvettes représentatives sont fabriquées et testées sous différentes conditions mécaniques, thermiques et électriques. L'influence des chargements mécaniques hors-plan, et plus particulièrement d'un impact basse énergie, sur la fonctionnalité électromécanique de la structure est ensuite étudiée. Des mesures de résistance électrique et te tension de claquage sont réalisées afin de déterminer les performances électriques post-impact de la structure. L'échauffement résistif interne des conducteurs, conjugué à l'environnement thermique d'une structure aéronautique nous invite finalement à étudier le comportement thermomécanique de tels assemblages multicouches et multi-matériaux. Nous présentons donc une méthodologie de caractérisation du comportement thermomécanique d'un assemblage sandwich multicouche via l'analyse de ses composants pris séparément et caractérisés par des analyses mécaniques dynamiques (DMA). La contribution majeure de ce travail réside dans la détermination de critères de dégradation électrique, et de dimensionnement, pour le développement de structures composites intégrant des conducteurs électriques.

Mots clés
Structure multifonctionnelle, endommagement, impact basse énergie, structure sandwich, couplages multi-physiques

Abstract

From the study of a particular multifunctional composite structure, this thesis aims at analyzing the thermo-mechanical behavior and failure modes of a composite structure embedding electrical wires. Representative test specimens embedding flat electrical cables are manufactured and tested under various conditions. The influence of out-of-plane loadings, and especially of low energy impacts on the electro-mechanical functionality of the structure is then investigated with both experimental and numerical considerations. Post impact electrical tests such as resistance measurements and dielectric strength tests are carried out to investigate on the post-impact electrical performances of the structure. Then, resistive heating of the embedded electrical components combined to the thermal environment of an aerospace structure lead us to further investigate on the thermo-mechanical behaviour of such multi-layered multi-materials structures. Hence, a methodology using Dynamic Mechanical Analysis (DMA) testings is developed to characterize both the temperature-dependent stiffness of the constituents, and the resulting thermo-mechanical behaviour of the assembly. The main contribution of this work consists in determining electrical degradation and sizing criteria for the development of robust composite structures embedding electrical wires.

Key Words
Multifunctional structure, damage, low energy impact, sandwich structure, multi-physic couplings

Remerciements

Ce travail est le fruit d'une étroite collaboration entre AIRBUS GROUP, l'institut de recherche en Génie Civil et Mécanique (GeM) de l'IUT de St Nazaire, et l'ESTACA de Laval. A travers ces entités, ce sont autant d'acteurs et de contributeurs qui m'ont accompagné pendant ces 3 années, et que je me fais désormais un plaisir de remercier.

Je commencerai par remercier tout particulièrement **Michel Bermudez** pour m'avoir fait confiance et accueilli au sein du bureau d'études à Suresnes ; **Audric Saillard** pour m'avoir lancé sur la voie du doctorat, **Bruno Thomas** auprès de qui j'ai appris les dessous de la cuisson des composites et pour son relationnel ; **Didier Mesnage**, **Jocelin Morio** et **Albert Abisror** qui ont tous contribué de près ou de loin à une ambiance de travail plus qu'agréable et nécessaire au bon déroulement de mes travaux. Je tiens également à adresser un remerciement particulier à **Caroline Petiot** pour son investissement au cours des dernières semaines de ma thèse, et sans qui la qualité de ma soutenance aurait sans doute été bien moindre. Enfin, j'adresse une pensée affective et reconnaissante à tous mes autres collègues de Suresnes, particulièrement **Christophe Dondina**, **Richard Perraud** et **Olivier Urea** ; Toulouse et Nantes, que je ne peux tous nommer sans risquer d'en oublier, et qui ont contribué à mon épanouissement au sein d'AGI et à la qualité des connaissances que j'ai acquises pendant 3 ans.

Cette thèse n'aurait sans doute jamais existé sans **Jesus Aspas-Puertolas**, père de la technologie ESC, à qui je dois énormément et que je tiens à remercier pour m'avoir accompagné tout au long de mes travaux. Toujours disponible et enclin à m'expliquer des notions d'électromagnétismes, il a su orienter mes travaux avec un regard critique, me conseiller et me booster quand j'en avais besoin. La qualité aussi bien de son expertise que de son relationnel font de lui une pièce maîtresse de ces travaux. Je n'oublie pas non plus **François Nguyen** et son équipe qui m'ont toujours accueilli aux Mureaux à bras ouverts.

Un grand merci à toutes les personnes de l'ESTACA de Laval : **Philippe Cuvelier** pour m'avoir accueilli au sein de son pôle, **Michael Chauvin** aussi bien pour les échanges techniques que pour la rigolade, et **Sandrine Pioger** pour sa gentillesse. Sans oublier les doctorants Romain, Federico et Jean pour les moments de détente au bureau ou au bar… J'ai gardé le meilleur pour la fin et voudrais maintenant remercier très sincèrement **Jean-Christophe Walrick** pour son encadrement, sa disponibilité et tout ce qu'il m'a appris sur l'endommagement des stratifiés. Mais tout cela ne serait rien sans son savoir-être et sa générosité qui ont grandement contribué à la réussite de ces travaux.

Je voudrais enfin remercier le laboratoire GeM de l'IUT de Saint-Nazaire et toutes les personnes qui y travaillent pour m'avoir toujours accueilli chaleureusement et s'être rendu disponible pour échanger sur mes travaux. **Marion Girard** et **Maël Perron** pour l'initiation aux essais DMA, **Sabrina Samson** pour sa gentillesse et son travail de l'ombre, **Frédéric Jacquemin** pour m'avoir accueillir au laboratoire. J'ai encore gardé le meilleur pour la fin puisque je terminerai par remercier chaleureusement **Pascal Casari** pour son accompagnement, ses conseils avisés et son regard critique sur mes travaux. Merci également à lui d'avoir donné une dimension humaine à ce travail, de m'avoir accueilli chez lui et soutenu pendant ces 3 années.

Table of Contents

General Introduction 3

Chapter 1 : Literature Review 9

1. Composite Materials 11
2. Multifunctional Composite Structures 16
3. Aerospace Wiring Practices (Specifications & Requirements) 28
4. Definition of the scientific and technological challenges 35

Chapter 2 : Presentation of the materials and characterizations of the constituents of the multifunctional structure 41

1. Presentation of the multifunctional structure 43
2. Manufacturing of the multifunctional structure 45
3. Mechanical characterization of the host composite structure 49
4. Mechanical characterization of the flat electrical cable 51
5. Critical defaults to the electrical performances of the electrical cable 56
6. Concluding remarks 62

Chapter 3: Influence of the embodiment of flat electrical cables on the mechanical behaviour and damage modes of a composite laminate 65

1. Tensile tests 68
2. Quasi-static short 3 point bend tests 71
3. Dynamic bending tests 80
4. Impact tests 88
5. Post-impact electrical performances 94
6. Concluding remarks 97

Chapter 4: Numerical simulation of the mechanical behaviour and damage modes of a composite structure embedding flat electrical cables 99

1. Damage modelling of woven fabric composite laminates 102
2. Damage of the multifunctional structure under quasi-static short 3 point bend tests 108
3. Failure of the multifunctional structure under impact tests 119
4. Concluding remarks 125

Chapter 5: Temperature-dependent bending stiffness and shear effects of a sandwich composite 129

1. Literature background 132
2. Internal heating of the core due to resistive heating of the embedded wires 134
3. Temperature-dependent stiffness of the constituents 143
4. Sandwich composite beam theory 147
5. Finite element modelling 153
6. Concluding remarks 157

General Conclusion and Prospects 161

General Introduction

Driven by the need to save weight, many industries (avionic, space, automotive, buildings, infrastructure, etc.) have been implementing composite materials in their product for the past thirty years. Yet, the advantages of composite materials (weight-saving, can be tailored to any specific application, etc.) are counter-balanced by some drawbacks such as their poor electrical and thermal conductivities, and the need to develop manufacturing processes guaranteeing their optimal performances.
In addition, airworthiness, cost-savings, and safety requirements have led these same industries to shift their mind so as to develop “more electrical” products and to install an increasing number of electrically conductive paths among their systems (miniaturization, increasing number of devices and sensors, health monitoring). Currently, cables lengths go up to 400km in an aircraft such as the A380, up to 4km in a modern car, and up to 5000km in a nuclear power plant. The cumulative length of these wires makes the wired network’s installation a time-consuming task. Besides, their increasing number as well as the secondary systems needed to ensure their proper installation and segregation is weight and volume-consuming.

To account for these drawbacks, researches have focused on the design of multifunctional structures and materials by developing structures that combine both structural (load bearing capacity, stiffness, strength) and non-structural (electrically conductive, self-healing, thermal insulation, etc.) functions. Such structures would allow dealing with the drawbacks involved by composite materials while saving considerable time, volume and mass as regards to the installation and design of wired networks.
Yet, the development of such structures is challenging as they undergo multi-physics couplings, present manufacturing issues due to the combination of different materials, and specific damage modes which may hinder their strength.

These above mentioned issues are addressed in this thesis through the study of a particular multifunctional composite structure developed within the frame of the industrial partnership with AIRBUS GROUP and ARIANE GROUP. It is divided in five chapters, as follows:

- **First Chapter**

The first chapter consists in presenting a literature survey on the subject. The first part presents an overview on composite materials (mechanics, failure modes, manufacturing, etc.). Then, a focus is made on existing multifunctional composite structures and the challenges associated with their development. Finally, some aerospace wiring practices (requirements, specifications, operating environment, wire design, etc.) are presented. This helps defining the objectives of the present thesis and unveiling critical issues to be addressed in the frame of this study.

- **Second Chapter**

The second chapter presents the multifunctional structure that is investigated in this work and its constitution. It details the mechanical, thermal and electrical tests that have been performed to characterize the multifunctional structure and its constituents. Such tests allowed to identify and characterize the modes of failure of the electrical conductors.

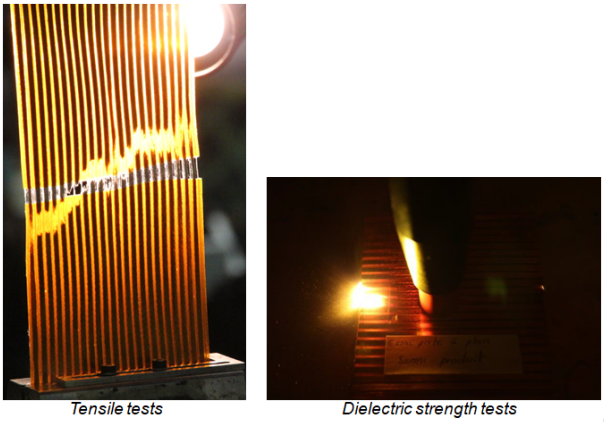

Identification of the modes of failure of the electrical conductors

- **Third Chapter**

The third chapter investigates on the influence of the embodiment of flat electrical cables on the structural performances of the structure under tensile and bending loads. In particular, the study aims at characterising the impact response of the multifunctional structure in terms of induced damage and post-impact electrical performances.
Due to the complexity of the structure, quasi-static short 3 point bend tests are first performed, followed by dynamic bending tests and finally impact tests. Experimental tools such as Digital Image Correlation (DIC) combined with a dynamic bending test bench are used.

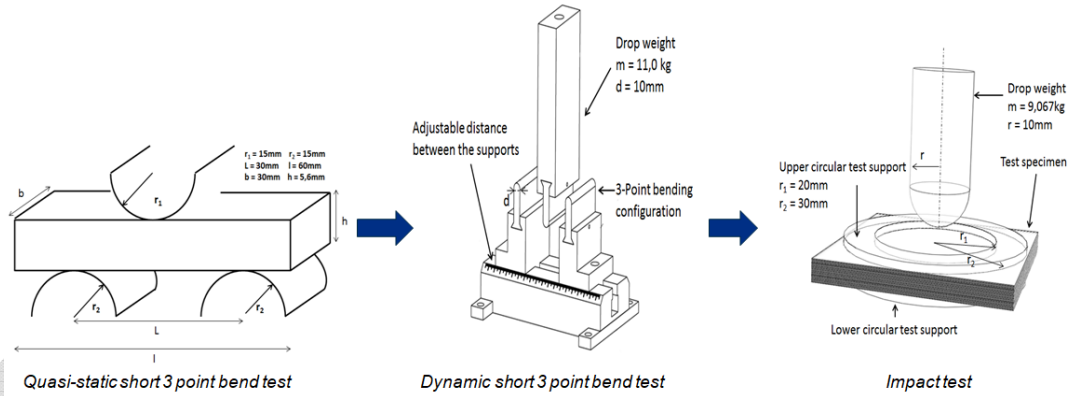

The impact response of the structure is analysed through quasi-static short 3 point bend tests, dynamic bending tests and finally impact tests

The post impact electrical performances of the structure are characterised with electrical resistance and dielectric breakdown measurements.

- **Fourth Chapter**

The fourth chapter of this thesis deals with the numerical simulation of the damage modes identified and presented in chapter 3. The numerical simulations are performed with ABAQUS CAE and include a progressive damage model (coded in a VUMAT subroutine) and the use of cohesive elements.

➢ Fifth Chapter

The fifth chapter consists in evaluating the influence of the temperature on the mechanical behaviour of the structure. In particular, the temperature rise due to resistive heating of the embedded electrical conductors is characterized experimentally and numerically.
A methodology of characterization of the thermo-mechanical behaviour of multi-layered and multi-material structures is then developed. The constituents of a sandwich structure used as a role model are characterized through DMA testing to analyse their temperature-dependent stiffness. These experimental data are then used in the Timoshenko beam theory to account for the temperature-dependent bending stiffness of the structure. These analytical predictions also take into account a temperature-dependent shear correction factor to model the temperature-dependent shear effects. Finally, the DMA data are used in a Finite Element (FE) code to perform structural and stress analyses.

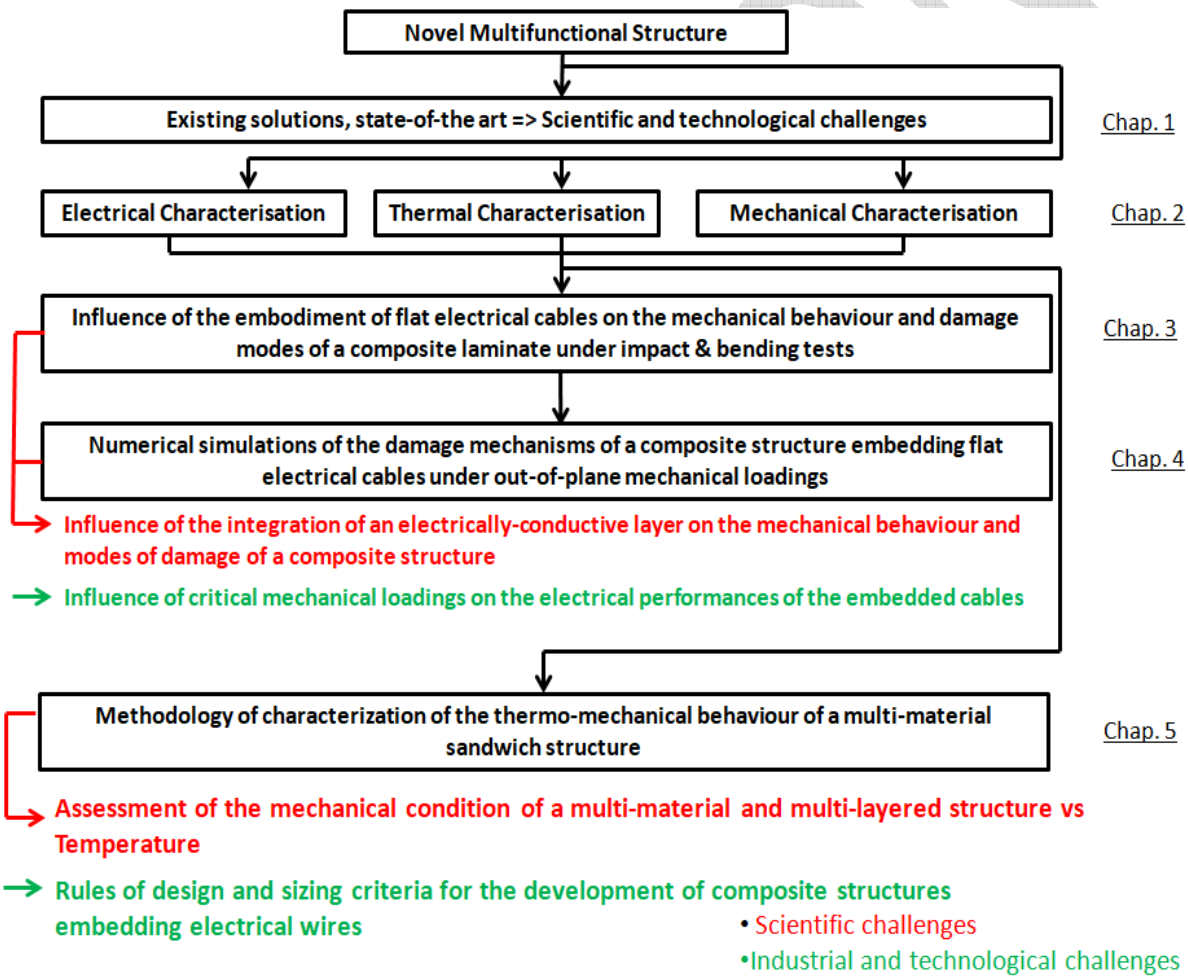

BROUILLON

Chapter 1 : Literature Review

BROUILLON

Chapter 1 : Literature Review

1. Composite Materials 11

1.1. Roles of matrix and reinforcement 11

1.2. Laminated and sandwich composites 12

1.3. Mechanics of composite materials 12

1.4. Damage mechanisms 14

1.6. Advantages and drawbacks 16

2. Multifunctional Composite Structures 16

2.1. Classification of multifunctional structures 16

2.2. Example of composite structures embedding electrical devices 17

2.3. Challenges of element integration into structures 19

2.3.1. Manufacturing process 19

2.3.2. Guaranteeing optimal mechanical performances 20

2.3.3. Multi-physics couplings 21

3. Aerospace Wiring Practices (Requirements & Specifications) 28

3.1. Generalities 28

3.1.1. Definitions 28

3.1.1.1. Dielectric strength (breakdown voltage) 28

3.1.1.2. Dielectric permittivity 28

3.1.1.3. Characteristic impedance 28

3.1.2. Wires and cables 29

3.1.3. American Wire Gauge (AWG) system 30

3.1.4. Flat cables 30

3.2. Operating environment and damage 30

3.3. Wires and insulation design 32

3.3.1. Wire design 32

3.3.2. Insulation design 33

3.3.3. ESA Specifications & Requirements 34

3.4. Concluding remarks 35

4. Definition of the scientific and technological challenges 35

BROUILLON

This literature review is divided into 3 parts. The first one presents an overview on composite materials and some of their disadvantages leading to the development of multifunctional composite structures. The second part exposes some multifunctional structures, patents, and applications encountered in various industries (automotive, aerospace, energy). This helps unveiling existing sizing criteria and limitations to be dealt with in the frame of this work. Finally, some specifications and requirements of the aerospace industry in terms of wiring practices are presented and help identifying the limitations and common modes of failure of conventional wiring technologies.

1. Composite Materials

The objectives of this part are not to deliver a complete state of the art on composite materials, but rather to present a brief overview of their composition, manufacturing, advantages and disadvantages. For a deeper insight into composite materials, work of Gay [1] or Berthelot [2] may be consulted.

A composite material may basically be defined as a combination of two or more constituents with different properties that, once combined, remain distinct and separate while forming a material with better properties than the ones of the single constituents considered separately. A third constituent, the interface between the reinforcement and the matrix is often distinguished since its properties (mechanical, chemical, thermal, etc.) have a significant influence on the macroscopic behaviour of the composite structure.

In the aeronautical and aerospace industry, most of the composite materials are fibre-reinforced polymer (FRP) composites which are mainly developed for their load-bearing capabilities and low weight as compared to metals.

1.1. Roles of matrix and reinforcement

In fibre-reinforced polymer composites, the reinforcement is fibrous in nature: natural (such as flax or hemp fibres) or synthetic (such as glass and carbon fibres) while the second constituent is a polymer matrix. The fibres act as the key structural component while the matrix serves as a binder to shape the material.

Short fibre-reinforced and continuous (long) fibre-reinforced composite materials can be distinguished with different existing pattern (unidirectional tapes, plain weave, harness satins, braided, stitched, etc.), cf. Figure 1.1.

Similarly, depending on the type of polymer matrix used, a distinction is made between thermoplastic composites (for instance including a PEEK: PolyEther Ether Ketone resin) and thermoset composites (such as including an epoxy or vinylester resins). Thermoset are currently more used than thermoplastic resins due to their low viscosity and low crosslinking/polymerisation temperature. However, their toxicity and non-recyclability remain their main inconvenients.

BROUILLON

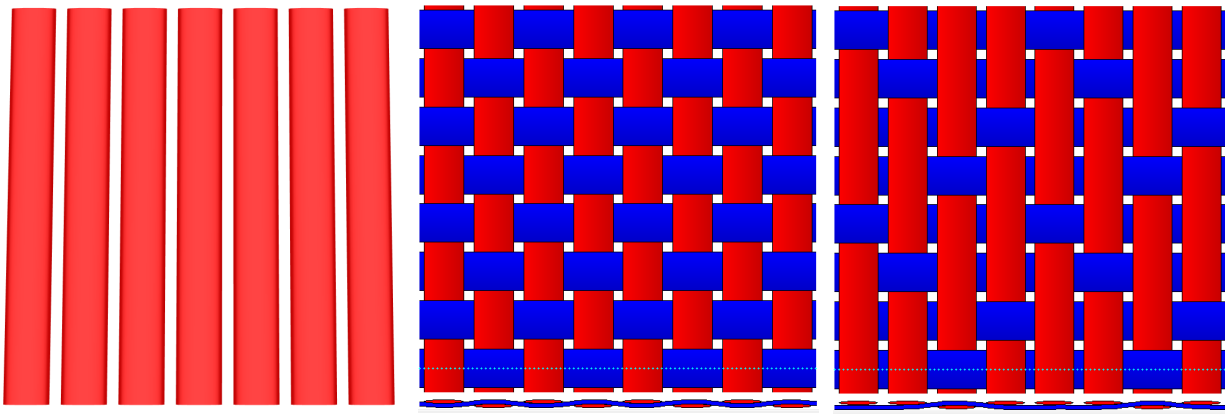

(a) (b) (c)

Figure 1. 1 Schemes of (a) unidirectional, (b) plain weave, and (c) 4 harness-satin weave reinforcements

1.2. Laminated and sandwich composites

A composite structure is made of several laminated composite plies and may be manufactured according to various processes depending on the application, the material properties, the shape of the part, etc. As a composite ply is usually highly anisotropic due to the orientations of the fibres, the composite plies are combined together with various orientations so as to obtain a cross-plied laminate with the required properties in the different directions, cf. Figure 1.2 (a).
A second common type of composite structure is sandwich composite where a honeycomb-like structure is interposed between several layers of fibrous laminate. These structures generally offer an excellent weight to flexural stiffness ratio as well as good thermal insulation properties, cf. Figure 1.2 (b).

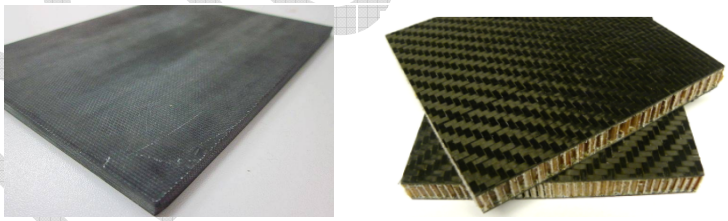

(a) (b)

Figure 1. 2 (a) Composite laminate and (b) honeycomb-core sandwich structure

1.3. Mechanics of composite materials

This part aims at briefly introducing the fundamental notions and notations relative to composite materials mechanics in order to ease the understanding of the work presented hereafter. Further insights into composite materials mechanics can be found in the work of Gay [1] or Berthelot [2].

Composite materials mechanics is based on continuum mechanics principles. Therefore, their mechanical behaviour is described with differential equations derived from fundamental physical laws such as the conservation of mass, the conservation of momentum, and the conservation of energy.

Due to the anisotropic nature of composite materials, second-order Cartesian tensors are used to define the state of stress and strain at a point. In addition, due to the symmetry of stresses and strains, the strains and stresses tensors have six stress components (σ_{11}, σ_{22}, σ_{33}, σ_{13}, σ_{23}, σ_{12}) denoted σ_{ij} and six strains components denoted ε_{ij} (ε_{11}, ε_{22}, ε_{33}, ε_{13}, ε_{23}, ε_{12}) [1]. The first index i indicates that the stress acts on a plane normal to the e_i-axis, and the second index j denotes the direction in which the stress acts, cf. Figure 1. 3.

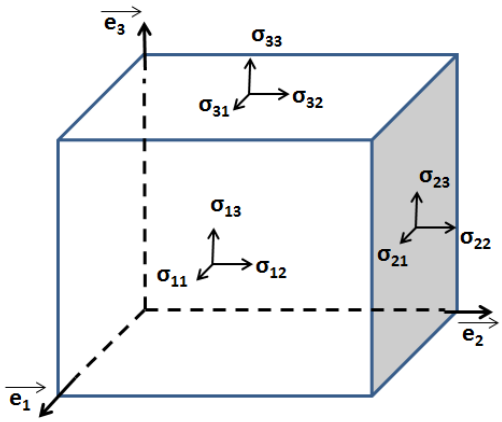

Figure 1. 3 Scheme of the stresses acting on a material element

In the case of small strains (linear theory of elasticity), the Cauchy stress tensor is used for stress analysis of composite materials, and strains are linearly and homogeneously related to the stresses according to the 3-D Hooke's law [1]. A total of 21 material constants are needed to fully describe these stress-strain relations as shown by (Eq.1. 1) where stresses are related to strains through the stiffness matrix.

$$\begin{Bmatrix} \sigma_{11} \\ \sigma_{22} \\ \sigma_{33} \\ \sigma_{23} \\ \sigma_{13} \\ \sigma_{12} \end{Bmatrix} = \begin{bmatrix} C_{11} & C_{12} & C_{13} & C_{14} & C_{15} & C_{16} \\ sym & C_{22} & C_{23} & C_{24} & C_{25} & C_{26} \\ sym & sym & C_{33} & C_{34} & C_{35} & C_{36} \\ sym & sym & sym & C_{44} & C_{45} & C_{46} \\ sym & sym & sym & sym & C_{55} & C_{56} \\ sym & sym & sym & sym & sym & C_{66} \end{bmatrix} \begin{Bmatrix} \varepsilon_{11} \\ \varepsilon_{22} \\ \varepsilon_{33} \\ \varepsilon_{23} \\ \varepsilon_{13} \\ \varepsilon_{12} \end{Bmatrix} \quad \text{(Eq.1. 1)}$$

Planes of symmetry or of isotropy may reduce this number. Composite materials are often orthotropic (elastic homogeneous material whose mechanical behaviour has two planes of symmetry, orthogonal to each other), which reduces this total to 9 different constants. These 9 constants are the 3 elasticity moduli (E_{11}, E_{22}, E_{33}), the 3 shear moduli (G_{23}, G_{13}, G_{12}) and the three Poisson's ratios (v_{12}, v_{13}, v_{23}). Relating stresses and strains through the compliance matrix, this yields [1]:

$$\begin{Bmatrix} \varepsilon_{11} \\ \varepsilon_{22} \\ \varepsilon_{33} \\ \varepsilon_{23} \\ \varepsilon_{13} \\ \varepsilon_{12} \end{Bmatrix} = \begin{bmatrix} 1/E_{11} & -v_{21}/E_{22} & -v_{31}/E_{33} & 0 & 0 & 0 \\ -v_{12}/E_{11} & 1/E_{22} & -v_{32}/E_{33} & 0 & 0 & 0 \\ -v_{13}/E_{11} & -v_{23}/E_{22} & 1/E_{33} & 0 & 0 & 0 \\ 0 & 0 & 0 & 1/G_{23} & 0 & 0 \\ 0 & 0 & 0 & 0 & 1/G_{13} & 0 \\ 0 & 0 & 0 & 0 & 0 & 1/G_{12} \end{bmatrix} \begin{Bmatrix} \sigma_{11} \\ \sigma_{22} \\ \sigma_{33} \\ \sigma_{23} \\ \sigma_{13} \\ \sigma_{12} \end{Bmatrix} \quad \text{(Eq.1. 2)}$$

1.4. Damage mechanisms

Due to the structure and anisotropy of composite materials, damage mechanisms are numerous, and occur at various scales. Among the most significant damage mechanisms, one would note at the microscopic scale fibre/matrix debonding and plastic deformation of the resin matrix, at the mesoscopic scale intra-laminar matrix and fibre crackings (transverse and longitudinal crackings), and at the macroscopic scale delaminations [2]–[5]. These damage mechanisms are coupled. They are functions of the reinforcement type, the orientation of the fibres, the lay-up, the resin type, the environmental and loading conditions, the geometry, etc.

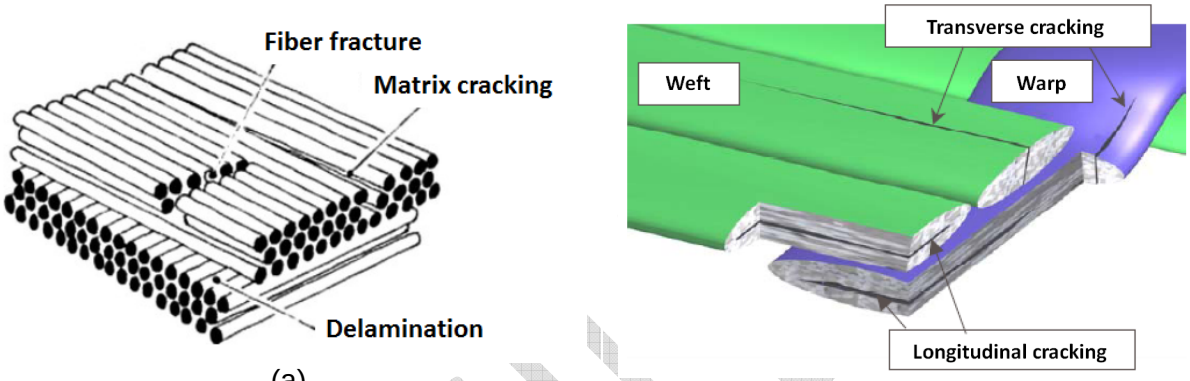

Figure 1. 4 Main damage modes on (a) a unidirectional laminates and (b) a woven fabric

Composite structures are significantly weaker in the transverse direction, and more generally in any directions where the load is carried by the matrix material. Hence, impact loadings due to foreign objects are known to be harmful to composite materials and have been extensively studied for understanding the damage mechanisms [6]–[8], the effects of temperature [9], [10] and impact parameters [11], [12], and resin and fibres properties [13]. The resulting damage mechanisms are not necessarily showy, but are likely to degrade the mechanical properties of the structure such as its load bearing capacity.
As out-of-plane loadings will be shown to be particularly damaging to the multifunctional structure studied in this work, some experimental and numerical details on low energy impact tests are given below.

1.5. Low Energy Impact Tests

Several experimental setup may be used to characterise the impact response of composite laminates: for low to medium impact energies (< 300J), the usage of pendulums like the ones used in the Charpy impact tests [14], [15] are often encountered. In the aerospace industry, standards have been issued by ASTM [16] and Airbus [17] to determine the low speed impact resistance characteristics of fibre reinforced plastics. The methods consist in impacting a composite plate with a drop-weight tower and submitting it to a post-impact compression test.

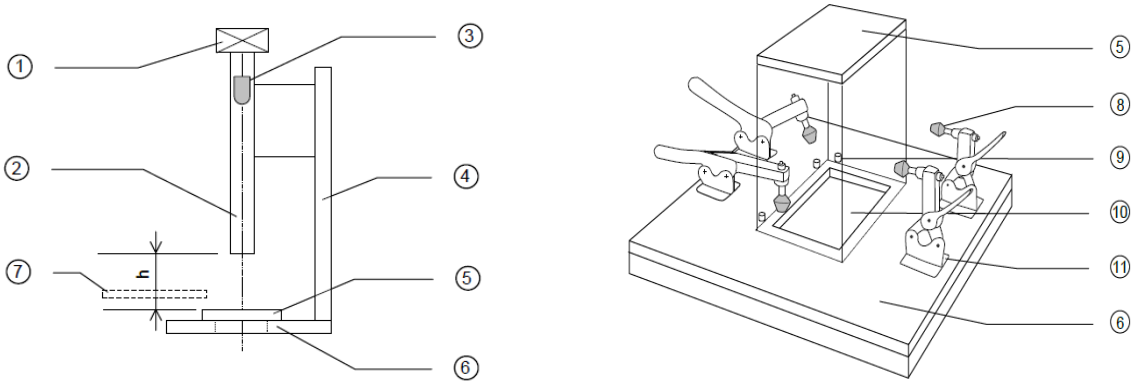

(1) Release system (2) Guide tube (3) Impactor (4) Support beam (5) Specimen (6) Steel base
(7) Anti-bounce device (8) Rubbers (9) Guide pins (10) Window 75 mm x75 mm (11) Clamping system

Figure 1. 5 Impact test equipment recommended by the normative reference AITM1-0010 [17]

In parallel, many efforts have been done towards the prediction of the impact behaviour and damage mechanisms of composite structures under low energy impacts, see for instance [8], [18], [19]. Impact-induced damage of composite laminates may be numerically treated at various scales through different approaches, but the most widely used rely on continuum damage mechanics. Actually, two distinct formulations are used: a continuum damage-based model to address fibre and matrix cracking within a ply (intra-laminar damage) and cohesive damage models to account for delaminations (inter-laminar damage).

These fibre and matrix crackings are often modelled with strain- or stress-based failure criterion implemented in finite element (FE) codes. Most of the time, they consist in quadratic (or more generally, polynomial) stress-based or strain-based functions which allows modelling the initiation of intra-ply damage, such as the Tsai-Wu or Tsai-Hill criteria. At the ply level, the most widely used failure criteria is the Hashin criteria [20] which takes into account four different failure modes. Besides Hashin's failure criterion, other failure criterion and theories have been developed to account for particular geometries, loading conditions, composite materials, etc.... Among the most widespread, one would note the Puck failure theory [21], and the LaRC04 three-dimensional failure criteria for laminated fiber-reinforced composites [22].

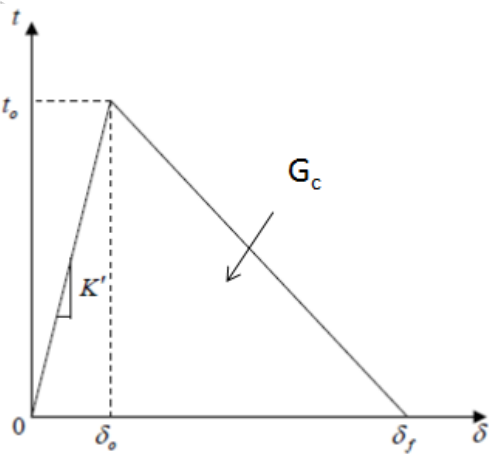

Figure 1. 6 Schematic of traction-separation relationship

On the other hand, inter-laminar damage (delaminations) in composite materials is often dealt with separately with cohesive plies and cohesive damage models [23]–[25]. This

procedure also involves two steps: damage initiation and damage propagation which is eventually controlled by the fracture toughness G_C of the material.

1.6. Advantages and drawbacks

The main advantages of using composite materials as compared to conventional metals such as aluminium is their lightness, and more particularly their high specific modulus and strength. Hence the possibility to manufacture composite parts with mechanical properties equivalent to the ones of metals but with a reduced weight. Among others advantages of composite materials, one could also note their high levels of fatigue strength, their corrosion, resistance due to their polymeric external surface, their design flexibility (can be tailored to many specific application), and their multi-functionality.

Indeed, if composite materials exhibit some drawbacks as compared to metals (low thermal and electrical conductivities for instance), they also offer the opportunity to control all the components that form the structure, hence giving the possibility to add mechanical, thermal and electrical properties to the structure. Additionally, completely new functions may be embedded within a composite lay-up, as detailed below.

2. Multifunctional Composite Structures

To counter the drawbacks resulting from the use of composite materials in structures and systems, researchers have been working on solutions to develop composite structures combining both structural functions (strength, stiffness, fracture toughness…) and non-structural functions (electrical and thermal conductivity, electromagnetic shielding, recyclability…) [26]. Indeed, the increasing number of publications on these topics underlines the growing interest of many industries (avionic, space, automotive, infrastructure) for the development of such structures [27]–[29].
In particular, integration of systems and structures in a multi-disciplinary approach (integration of wires into composites [30], structural batteries [31], integrated supercapacitors [32]) is a key technological challenge for the aeronautical and aerospace industry [33]. While enabling the future of electric and hybrid flight, these structures also have the potential to save weight and volume as well as to reduce lead time for system installations.

2.1. Classification of multifunctional structures

Matic [34] proposes a classification of multifunctional structures in terms of dimensional scales. According to his denomination, a Type I structure is a structure made of elements in which one function is simply coated or laminated on a second phase (usually a structural component), cf. Figure 1. 7 (a).

BRUNEL

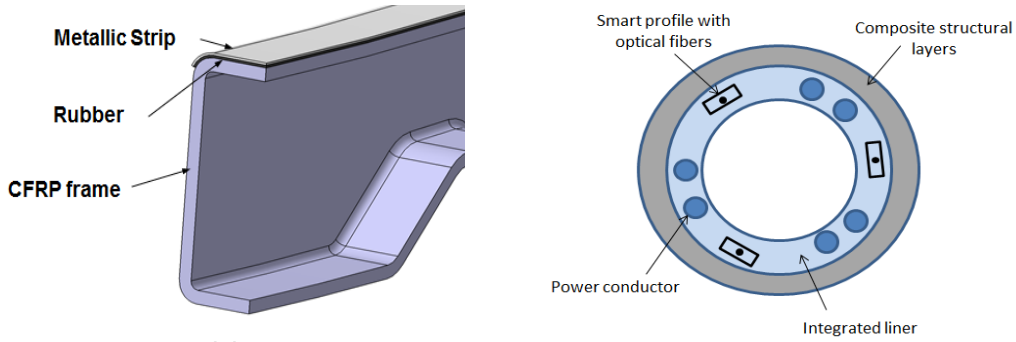

(a) (b)

Figure 1. 7 (a) Type I structure of a metallic strip laminated on a CFRP frame [35] and (b) Type II structure with power conductors integrated in a composite laminate [30]

Type II structure are made of distinct elements in which one function is embedded in another (usually a structural element), cf. Figure 1. 7 (b). Type II structures are used for various applications such as de-icing [36], structural health monitoring purposes [36], [37], electromagnetic shielding [38], power and data transmission [30], [33], [39]–[41], energy-storage [31], [42]–[44], etc. All these applications are based on the embodiment of a functional element inside a structural element. Some of these examples are further detailed in the following sub-section.

Type III materials are truly integrated materials in which the phases of each material are intermeshed, hence blurring the physical distinction between them. Nano-composites based fibre reinforced polymer (FRP) structures are a good example of such materials [45], [46].

2.2. Example of composite structures embedding electrical devices

As this work will deal with the study of a Type II multifunctional structure, some examples of existing Type II multifunctional structures are further detailed here to give a brief overview of existing technologies.

Nino, et al. [36] proposed a design strategy for a multifunctional composite structure integrating Heat Emitting Layers (HELs). They underlined that the composite part needs to be chosen first according to stiffness and strength requirements, followed by the choice of metal fibres based on properties such as electrical conductivity, chemical resistance and thermal conductivity. In addition, these two elements also need to be chosen carefully so as to avoid coupled phenomena such as electrochemical corrosion. Finally, the spacing between the fibres depends on the functionality requirements (such as the maximum allowable temperature inside the laminate) and manufacturing issues.

The multifunctional composite structure developed by Murtola et al. [30] consists in integrating electrical conductors into the wall of a spoolable fatigue-resistant thermoplastic composite tube for electric drilling application, cf. Figure 1. 7(b). Similarly, a patent which deals with embedded electrical conductors in a well hose has been deposited [39], cf. Figure 1. 8. In this application, the electrical conductors were embedded in an adhesive on the outer surface of a polyurethane tube. The polyurethane tube was then inserted in a woven outer jacket, and pressurized from the inside with steam. The application concerns the transmission of signals and power supply, but the electrical conductors were also used to provide stiffness against torque, therefore resulting in a multifunctional structure combining electrical functions and a load-bearing capacity.

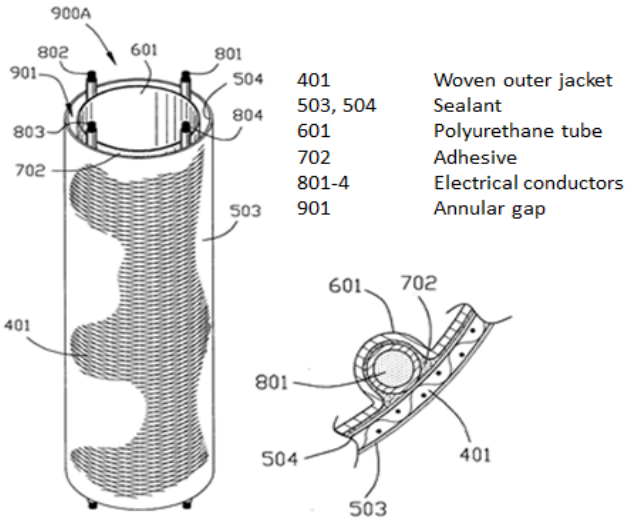

Figure 1. 8 Well hose embedding electrical conductors [39]

The aerospace industry is also very interested in developing such structures. In [33], Noor et al. discuss various structures technology for future aerospace systems, among which structures embedding antennas and other electronics are presented as advantageous so as to lower costs, eliminate electrical chassis, and save mass and volume. The interest of the space industry for such multifunctional structures is further underlined by Jang, et al. [40] since these structures "enable to considerably increase the ratio of electrical functionality to spacecraft volume and can lead to significant mass savings". The same authors [40] embedded flexible circuitry and miniaturized components on a sandwich structural panel consisting of an aluminium honeycomb core and CFRP facesheets, cf. Figure 1. 9. It allowed the integration of structural, thermal, radiation shielding, and electronics functions into a single multifunctional composite structure.

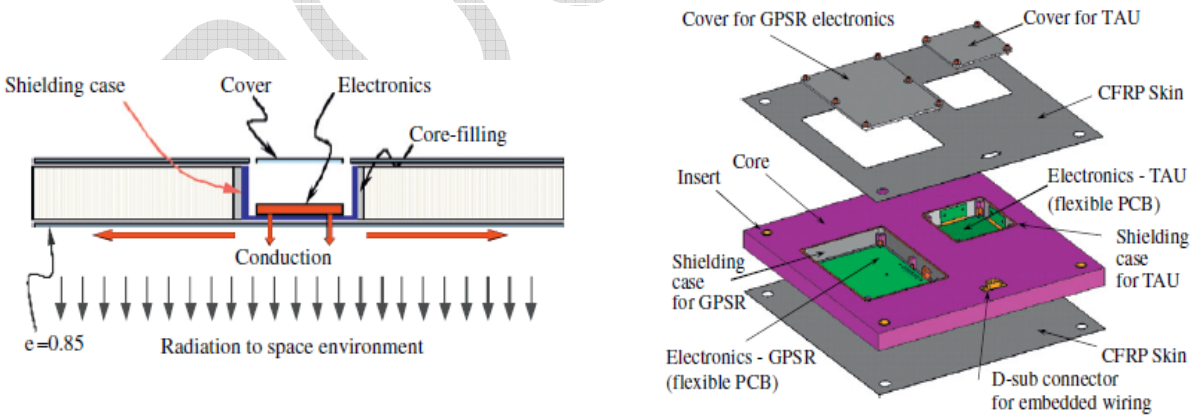

Figure 1. 9 Exploded schematic view of the multifunctional structure designed by Jang, et al. [40]

The shielding case aims at providing available space for embedding electronics, but also to transfer the heat generated by the electronic devices to the outer skins (thermally conductive pitch-based CFRP). Similarly, Hahn, et al. [28] developed a multifunctional spacecraft structure concept with electrical and thermal functions by embedding electronic modules between the faces of sandwich structural panels.

Finally, Bf1 systems has developed a new composites technology known as Wire in Composites Technology (WiC TECH™) which consists in printed electrical tracks on a flexible circuit board sandwiched between two layers of composite material [41].

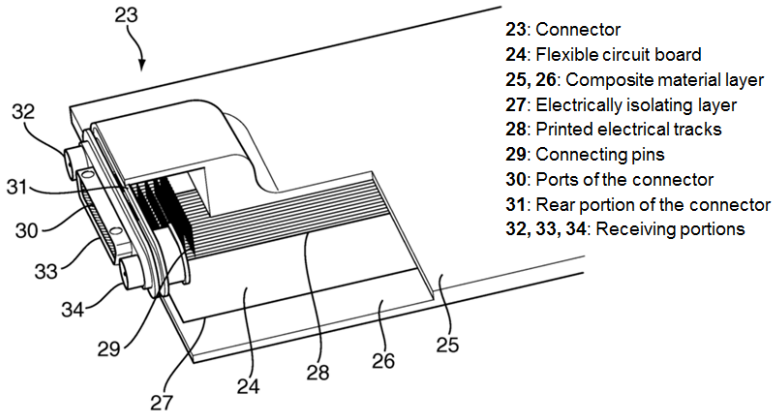

Figure 1. 10 Scheme of the Wire in Composite Technology™ developed by Bf1 Systems [41]

All these applications consist in embedding electrical devices in a composite structure and have shown promising results. Yet, they all faced similar issues as detailed in the next section.

2.3. Challenges of element integration into structures

When designing such structures, it must be ensured that every function of the structure is maintained during its lifespan. It is challenging as they undergo multi-physics couplings, present manufacturing issues due to the combination of different materials and highly non-linear and heterogeneous mechanical behaviours.

2.3.1. Manufacturing process

Whatever the technique (resin transfer moulding [47], printing [26], [48], [49], autoclave/oven curing [43], [50], moulding [51], etc.), manufacturing of such multi-materials structures is challenging as it requires implementing elements of different natures, sizes and geometry within the same structure. This is likely to induce resin rich regions and favours the appearance of residual stresses [52]–[54], or voids, in particular when the embedded parts are impermeable [47], cf. Figure 1. 11.

Yet, keeping the void content to a minimum is mandatory since it is known to negatively affect the mechanical properties of composite materials [55], [56]. It is all the more crucial to keep it to a minimum when manufacturing a multifunctional structure embedding electronic components. Indeed, as air has a lower dielectric constant than most of the dielectrics commonly used, presence of voids will locally reduce the isolative properties of the surrounding material [43].

Several techniques might help in reducing the void content and optimising the mechanical properties of the structure such as pre-curing of the pre-preg [48], increasing the curing pressure [57], or altering the moment of applying the pressure [55].

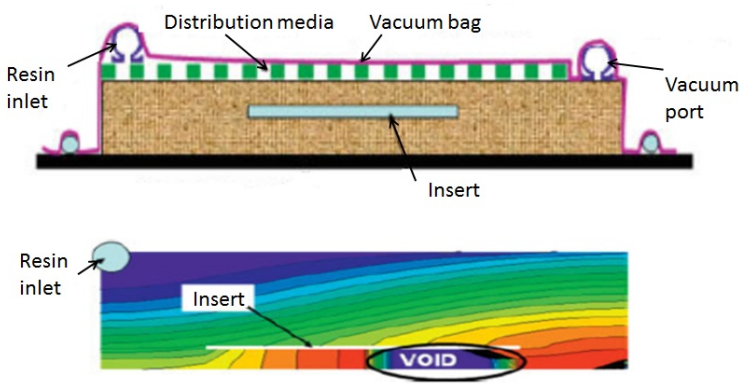

Figure 1. 11 Flow distribution around an impermeable insert during a vacuum-assisted resin transfer moulding (VARTM) process [47]

Cutkosky, et al. [53] investigated several techniques such as selective material deposition and selective material removal (use of a sacrificial material that can be chemically removed) to embed flexible components among host rigid structures. They relate that the main issues arising from the fabrication of such structures are to define and control the shapes and locations of the flexible materials during processing, and to add the host material around the flexible components without damaging them or being hindered by them. In addition, compatibility of the various materials between each other, as well as their stability throughout the manufacturing process needs to be considered.

2.3.2. Guaranteeing optimal mechanical performances

Once a manufacturing process has been selected, the main issue remains to manufacture good interface properties between the host structure and the embedded elements so as to ensure optimal performances (mechanical, electrical, thermal, etc.) of the structure. Indeed, most of the studies show that the interface between the structure and the embedded components is critical to the global performances of the structure.
For instance, Kim et al. [50] embedded copper strips in a composite laminate and noticed that copper crack growth under tensile cyclic loadings was strongly influenced by the interface bond strength between the copper and composite. They were able to improve the fatigue life of the structure by strengthening the interfacial bond with an adhesive film, cf. Figure 1. 11.

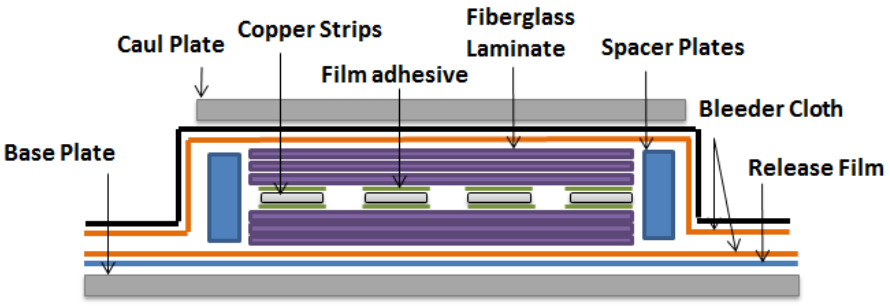

Figure 1. 12 Manufacturing of composite test specimens with embedded copper strips as made by Kim et al. [58]

Similarly to what was noticed by Kim et al. [50], [58], Xiao et al. [59] investigated damage evolution of carbon/epoxy laminates embedding thin film of lithium energy cells for energy

storage purposes. They found out that delamination at the interface between the composite and the integrated device is a significant damage mechanism under tensile loading.

Structural performances of glass fibre-vinyl ester composites with inter-laminar copper inserts, were investigated by A.Obaid and Yarlagadda [60]. They studied the process-induced strains and static mechanical properties as a function of the insert size and copper surface treatment. It was found that under tension, the presence of inserts causes a small reduction in modulus and elastic strain, but an increase in failure strength and strain. Tensile properties were not impacted by the size of the insert, or by the surface treatment. On the contrary, compression properties were impacted since they highly depend on the adhesion between the copper surface and the composite. The same observation was drawn in terms of flexural properties: significant degradation in elastic stress/strain values and failure properties were observed as the size of the insert was increased. Both flexural and compression properties were increased back up to the nominal values (without insert) with adequate surface treatment, thus underlining the crucial role of the interface between the insert and the composite host structure.

Gresil [65] observed that the integration of a metallic weave inside a glass/vinyl-ester woven fabric could decrease the flexural resistance of the structure by 20% and induce stress gradients at the interface between the composite structure and the embedded metallic layer. In addition, tensile tests realised on test specimens integrating various metallic weavings showed a slightly lower Young's modulus (diminution of about 5%), lower ultimate tensile stress (diminution of about 20%) and lower ultimate tensile strains (of about 7%). The same observations were made as regards to the inter-laminar shear strength, which was decreased by approximately 15%.

As shown by these examples, the embodiment of a functional element inside a composite structure is likely to degrade its mechanical properties (in terms of stiffness and strength). This is especially true for the out of plane properties (ILSS, flexural modulus, flexural strength), and depends on the size of the embedded layer, the surface treatments, and on the type of loadings it is submitted to (fatigue, compression, tension, bending).

2.3.3. Multi-physics couplings

Multi-physic considerations are also required as elements of different nature and functions are integrated within the same structure and interact with each other. Therefore, compatibility of the various materials between each other [36], as well as their stability throughout the lifespan of the structure needs to be considered [53]. This part aims at briefly presenting the main multi-physic couplings that are likely to occur during the lifespan of the structure.

2.3.3.1. Electro-Mechanical

As a part of the structure, the embedded conductive elements have to withstand the same mechanical strains as the composite host structure. Hence, the sizing of the structure must ensure that neither structural failure of the composite, nor failure of the embedded electrical conductors can occur within the lifespan of the structure.

Electrical degradation of the embedded elements can be monitored through various parameters such as: the electrical resistance, the insulation resistance, the breakdown voltage, the dielectric permittivity and the characteristic impedance. All of these properties refer to a specific component within the cable (conductor, insulator, jacket).

The electrical resistance will allow looking at the electrical conductor integrity while the insulation resistance, permittivity, and dielectric strength will provide insight on the insulation degradation. The characteristic impedance mainly depends on the geometry and arrangement of the conductors inside the structure.

Kim et al. [50], [58] observed that under monotonic tensile loadings, the host composite structure fractured well before the embedded copper strips, hence leaving an intact electrically conductive path despite structural failure of the composite. Yet, as copper has a shorter fatigue life than the composite, it was found that under cyclic loadings through-width cracks developed on the copper conductors, hence resulting in electrical failure of the structure despite the composite remaining mechanically intact.

Murtola, et al. [30] ensured that both mechanical operations and repeated bending cycles had no influence on the conductor through electrical resistance measurements. Similarly, Zhao [48] and Kim et al. [49] measured resistance changes of printed electrodes under static loadings, cf. Figure 1. 13.

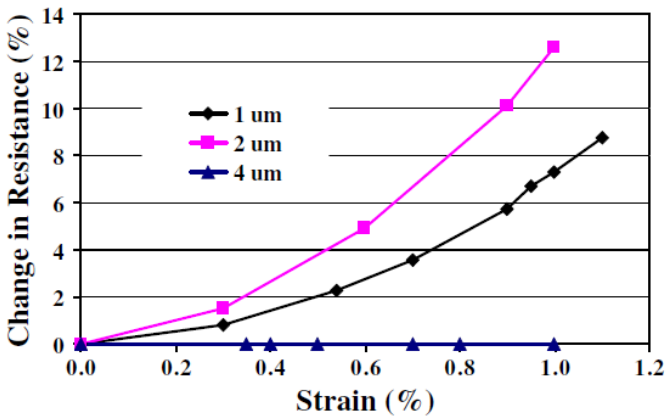

Figure 1. 13 Percentage of resistance change of the printed electrodes with respect to the electrode thickness and the applied strain [49]

Generally, an increase of electrical resistance will be observed with increasing strains since the resistance (R) is linked to the length (L) and cross-section (S) of the conductor according to (Eq.1. 3), with ρ_{elec} the electrical resistivity.

$$R = \rho_{elec}\frac{L}{S} \qquad \text{(Eq.1. 3)}$$

Murtola, et al. [30] monitored partial discharge levels to get information about the insulation degradation. The effect of mechanical strains on the wiring insulation may also be monitored with the real permittivity. For instance, the real permittivity of PTFE has been shown to decrease by approximately 19% under 150% tensile strain [61], cf. Figure 1. 14, hence indicating a degradation of the insulation.

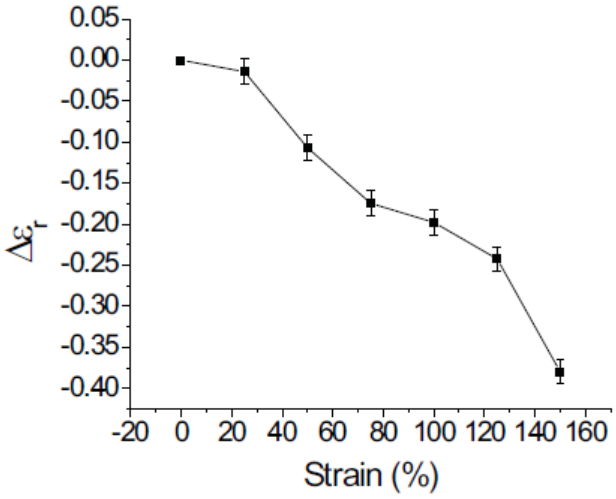

Figure 1. 14 Effect of tensile strain on the real permittivity of PTFE [61]

The performance of an electrical insulation is related to its dielectric strength, which is the maximum electric field that a pure material can withstand under ideal conditions without breaking. Hence, to design properly an insulator its thickness needs to be adapted to withstand these electrical constraints.

$$e_{elec} > \frac{U_{max}}{E_{max}} \quad \text{(Eq.1. 4)}$$

With e_{elec} the required thickness of the insulator considering the electrical requirements (in m), U_{max} the maximum voltage that the line will have to transmit (in V), and E_{max} the dielectric strength of the insulator (in $V.m^{-1}$).

2.3.3.2. Thermo-mechanical couplings

Thermo-mechanical couplings may arise at different levels of the multifunctional structure: at the fibre/matrix interface within a composite ply, between two composite plies of different orientations, and between the various materials being part of the multifunctional structure.

i. Thermo-mechanical behaviour of composite materials

As regards to the host composite structure, curing of thick parts induces thermal gradients, the formation of residual stresses and polymer degradation [62]. In particular, the polymer matrix is more affected as it undergoes volume shrinkage during cross-linking [63] resulting in waviness and dimensional inaccuracy. Besides, temperature and degree of cure gradients, chemical shrinkage, and the anisotropy of composite materials all lead to the development of residual stresses which directly affect the mechanical performances of the structure [52], [62]–[65].

Zhao, et al. [54] underlined the need to investigate the deformation behaviour of woven glass/epoxy composite substrate under thermo-mechanical loadings. Indeed, they showed that viscoelastic effects dominate the material response near the glass transition temperature

BROUILLON

of woven glass/epoxy composite materials, in particular since its load bearing capabilities are considerably decreased.

These temperature-dependencies of the mechanical properties (and in particular, of the elastic modulus) of polymer reinforced composites may be characterized through Dynamic Mechanical Analysis (DMA) testing. Indeed, correlations have been observed between complex dynamic modulus yielded by DMA measurements and elastic modulus of fibre-reinforced polymer [66]–[69]. Recent studies also consisted in developing relations for modelling the temperature-dependent modulus of fibre-reinforced polymers [70], [71].

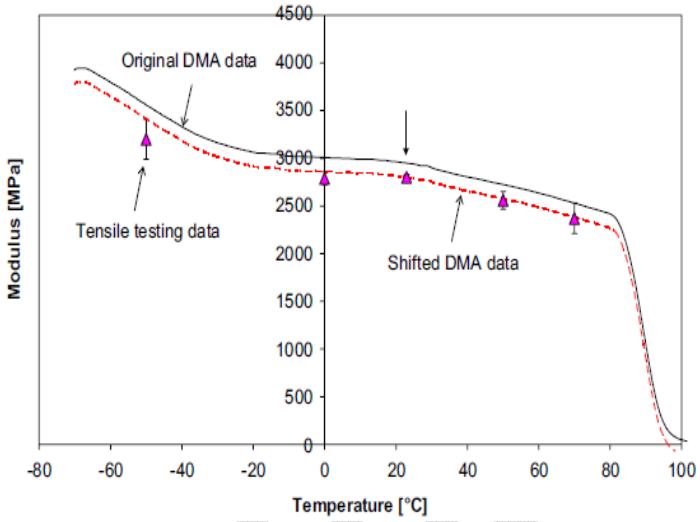

Figure 1. 15 DMA data under tensile mode need to be slightly corrected to fit quasi-static mechanical testing data [68]

The typical variation of elastic modulus versus temperature for a polymer exhibiting a secondary relaxation is shown by Figure 1. 16.

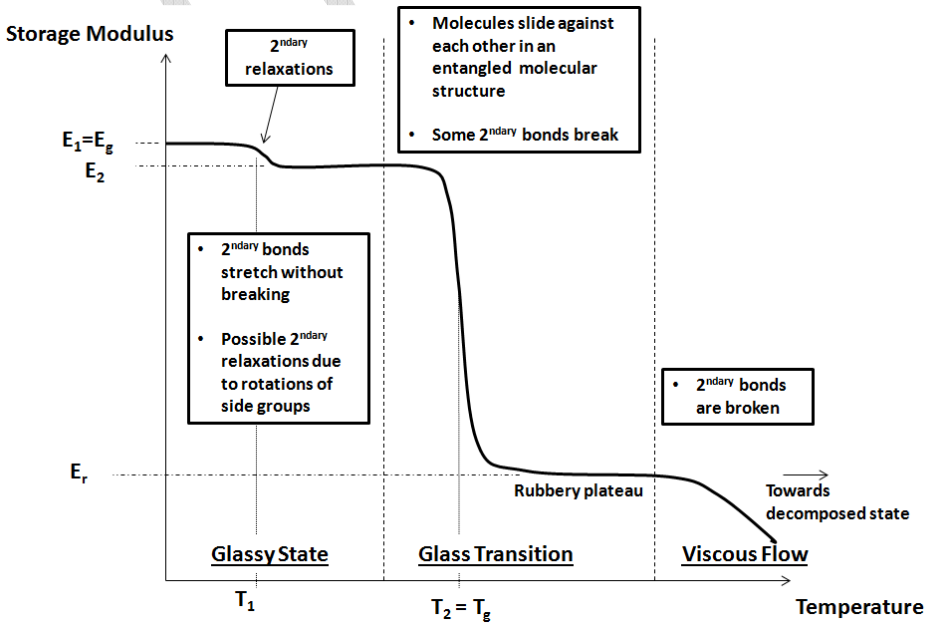

Figure 1. 16 Storage Modulus versus temperature for a typical polymer

This temperature dependence is strongly related to molecular motions, and in particular to the inter- and intra-molecular bonds [72]. In the lower temperature range the polymer is in the glassy state with intact primary and secondary bonds. As temperature increases, secondary bonds stretch without breaking resulting in a quasi-elastic behaviour of the polymer. In some cases secondary relaxations can occur if the thermal energy is high enough to allow rotation of side groups [72].
As the temperature is raised further, a much more noticeable relaxation occurs, known as the alpha transition or the glass transition which results in a dramatic drop of the storage modulus until the rubbery plateau where the material state comprises intact primary bonds and broken secondary bonds. At even higher temperature, the primary bonds are also broken and the material is decomposed which is noticeable by a new drop of the storage modulus (viscous flow).

These evolutions result in a decrease of the material's strength and stiffness with increasing temperature, in particular in terms of out-of-plane properties (which are matrix-dominated) such as the flexural and shear strengths and stiffness [73]. It also affects the modes of failure of the structure as the glass transition may favours non-linear behaviours, and the initiation and propagation of indentation and matrix crushing during mechanical testing [73].

ii. Thermo-mechanical behaviour of multifunctional and sandwich structures

All these phenomena are accentuated when manufacturing a multifunctional structure due to the implementation of elements of different nature and thermal expansion behaviours inside the same structure. In particular, a type II multifunctional structure (i.e. a composite structure embedding electrical cables) may be reduced to a sandwich structure embedding a viscoelastic layer. Hence, this work will also be inspired from previous observations made on the thermo-mechanical behaviour of sandwich composite structures.

For instance, Manalo et al. [74] observed that the flexural behaviour of a GFRP skin/phenolic core/GFRP skin sandwich system was governed by the GFRP skins up to 80°C (significant contribution to the sandwich stiffness and strength), and by the phenolic core beyond 80°C. They evidenced that the fibre/matrix interface was affected by an increase of T°C near the Tg of the GFRP skins, hence reducing the load transfer through the matrix and modifying the modes of failures of the GFRP skins. In particular, the bending strength was observed to be more affected by an increase of T°C than the stiffness.

Similarly, Zhang et al. [75] investigated on the failure modes of polymer foam cored sandwich structures and revealed that high temperatures induce losses of stiffness of the core material and promote unstable failure modes at smaller loads than those predicted by classical material failure.

These issues will need to be addressed in this thesis, especially as the multifunctional structure is submitted to internal heating due to the resistive heating of the embedded electrical conductors, combined to the thermal environment of the structure.

2.3.3.3. Thermo-electrical couplings

i. Joule Effect

Indeed, in addition to its exposure to the external thermal environment, a multifunctional structure embedding electrical conductors will generate internal heating due to resistive heating of the embedded wires.

The Joule effect bounds the electrical and the thermal fields due to the resistance of any electrical conductors against the flow of the electric current, which results in heat release. This heat release needs to be taken into account during the design of a multifunctional structure as the resulting temperature increase should not exceed the maximum allowable temperature of the surrounding materials (insulation, jacket and polymer matrix) [30]. This is further detailed in Chapter 5 of the present thesis.

ii. De-rating

Another thermo-electrical coupling known as the de-rating phenomenon affects the current-carrying capacity of an electrical conductor, which decreases when temperature increases. To take this phenomenon into account, the part needs to be operated at lower values than rated specifications, as specified by the ESA specification No.3901 [76], cf. Figure 1.17.

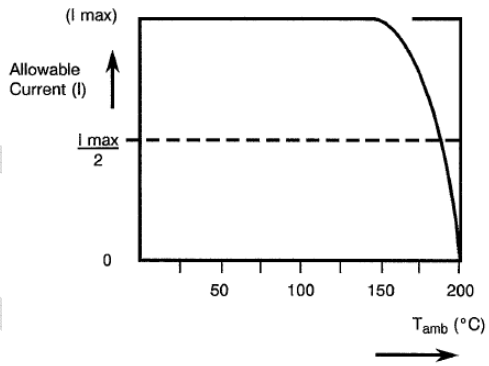

Figure 1. 17 Allowable Current versus Temperature according to ESA/ESCC No 3901 [76]

In particular, the electrical conductivity σ of a wire is related to its specific resistivity ρ_0 and to the temperature T through (Eq.1.5):

$$\sigma = \frac{1}{\rho_0(1+\alpha(T-T_0)} \qquad \text{(Eq.1.5)}$$

Hence, the higher the temperature, the lower the conductivity of the cable, and the higher its resistivity. This coupled electro-thermal effects induces further ohmic loss and resistive heating of the electrical conductors.

iii. Skin Effect

The skin effect is an effect of electromagnetic nature which makes that at high frequency, the current tends to circulate around the border of a conductor (instead of being homogeneously distributed). This results in an increase of the electrical resistance.

The skin depth is characterised with the skin depth δ and defined as the distance at which the current density decreases $\frac{1}{e}$ of its initial value.

$$\delta = \sqrt{\frac{2}{w\mu\sigma}} \qquad \text{(Eq.1. 4)}$$

With w the angular frequency (in rad.s^{-1}), σ the electrical conductivity (in Ω^{-1}m^{-1} or S.m^{-1}) and μ the magnetic permeability (in H.m^{-1}).

Copper wire	
Frequency (kHz)	**Skin depth (mm)**
0,05	9,22
0,06	8,42
0,4	3,26
1	2,06
10	0,65
1000	0,21

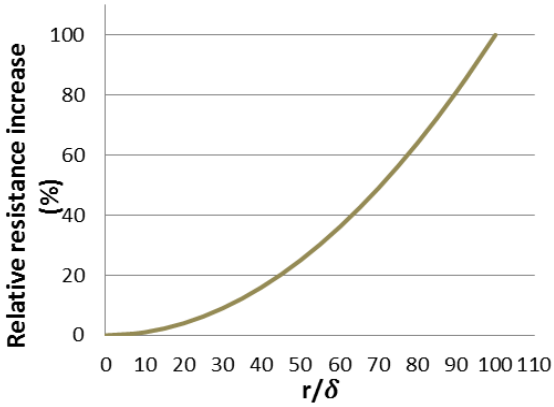

Figure 1. 18 Resistance increase in a copper wire due to the skin effect [77]

For a circular conductor, the resistance variation depends on the ratio between the radium of the conductor and the skin depth [77]. For instance, the skin depth of a copper wire at 400Hz is δ=3,26mm. Which means that the resistance increase due to the skin depth is negligible up to a radium of conductor of about 30mm. Indeed, according to Figure 1.18, the resistance increase due to the skin effect is negligible if r/δ < 10.

iv. Proximity Effect

When two or more conductors are placed near each other, the magnetic field induced between the conductors modify the electric field: this is called the Proximity effect, cf. Figure 1.19. It results in a resistance increase at very high frequencies. The higher the frequency, the stronger the proximity effect.

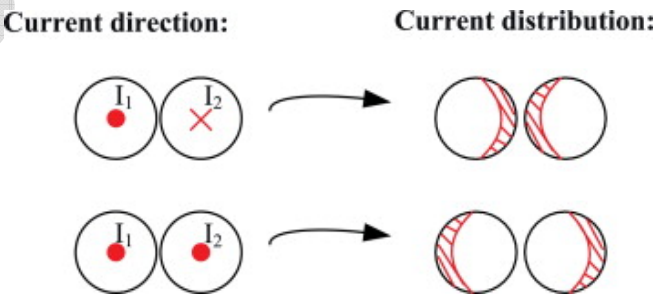

Figure 1. 19 Current distribution because of proximity effect for two adjacent conductors as a function of the current direction

These high frequencies effects will not be considered in the present thesis.

3. Aerospace Wiring Practices (Requirements & Specifications)

A wide range of wires and cables are used by the aerospace industry according to their specific application: thermocouple cables, radio-frequency cables, airframe wires, data bus cables, etc. Wiring has become a complex system that not only distributes power, but also links multiple systems; hence failure of any component of the wiring system may lead to catastrophic damage of an aircraft [78]. The complexity of the electrical system in itself is also increasing due to the increasing number of electrical loads, such that the regulation authorities FAA (Federal Aviation Administration) and EASA (European Aviation Safety Agency) now require to consider aircrafts' electrical wiring systems as a system on its own, named EWIS (Electrical Wiring Interconnection System) [2–4].

A wire is actually chosen for an application based upon a number of factors, including the electrical needs of the circuit (current, voltage, signal loss allowable, voltage drops, etc.), the environmental conditions (temperature, moisture, contamination, etc.), the physical requirements for the application (vibration, flexing, abrasion, etc.), and other factors such as how long the wire should be able to perform its intended function, or whether it will be part of inspections. Once chosen, the wire needs to be installed properly (proper supports, spacing, protection from other systems, etc.). Finally, the maintenance operations play an important role as regards to the wiring integrity. Indeed, if they are performed inappropriately, the ability of the wire to perform adequately after being disturbed may be negatively affected [2, 5].

3.1. Generalities

3.1.1. Definitions

At this point, it is necessary to define some typical electrical and dielectrical properties of an electrical cable that will be referred to in this report.

3.1.1.1. Dielectric strength (breakdown voltage)

The dielectric strength of an insulating material is the maximum electric field that an insulating material can withstand without breaking down (expressed in kV/mm). The voltage at which the material breaks down is called the breakdown voltage (expressed in V).

3.1.1.2. Dielectric permittivity

The dielectric permittivity is a fundamental parameter that relates to the propagation of electric fields: it is a measure of how electric field behaves/interacts with any material. It can also be seen as how easily an electric field will polarize a given dielectric material. The relative permittivity (or dielectric constant) ε_r is related to the dielectric permittivity ε and to the dielectric permittivity of vacuum ε_0 by $\varepsilon = \varepsilon_0\varepsilon_r$.

3.1.1.3. Characteristic impedance

The characteristic impedance is the ratio of the magnitude of the forward travelling voltage wave to the magnitude of the forward travelling current wave. Characteristic impedance depends on the geometry and materials of the transmission line.

3.1.2. Wires and cables

The words “wire” and “cable” are often interchanged. Yet, a wire is formed from a single solid conductor, contained within insulation and protective sheath material whereas a cable can be defined as two or more wires contained within the same insulation and protective sheath, twisted together, or simply covered by a sheath.

Two types of cables may be encountered: single strands cables or multi-strands cables (bundles). Multi-stranding is often used to offer more flexibility and to make it easier for the cable to withstand vibrations. In addition, cables may be shielded or screened, cf. Figure 1. 20. Some cables are shielded since they carry high power signals and should not cause any electromagnetic interference to their environment. On the contrary, some cables are screened to prevent their signals from being affected by external electromagnetic interferences. The role of the sheath is mainly to protect the conductors from any external contaminants. Finally, the strands generally have a plating (tin, silver or nickel depending on the operating temperature) to prevent oxidation of the conductor.

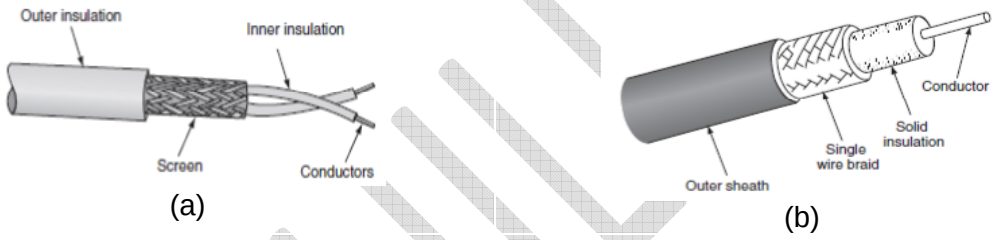

Figure 1. 20 (a) screened cable, (b) Shielded cable (example of a coaxial cable)

Component	Property
Flexible strand **Multi-strands**	To ease the installation To withstand the vibrations
Screen	To prevent the signals from being affected by electromagnetic interferences
Shield	To prevent the signals from causing any electromagnetic interferences
Sheath	To protect against any external contaminants
Plating	To prevent oxidation
Insulator	To ensure electrical and thermal insulation

Table 1.1 Main component of an aerospace cable and their associated functions

Two main conductors are used: aluminium and copper. The choice of any of these two conductors depends upon the application and is a trade-off, cf. Table 1. 2. Yet, the majority of current applications use copper conductors for its low resistivity, high ductility and tensile strength, and for its ease of soldering.

Material	Advantage	Inconvenient
Aluminium	▪ 60% lighter than copper ▪ Self-oxidizing (no need for plating)	▪ More expensive than copper
Copper	▪ More ductile ▪ Can be easily soldered ▪ Lower resistivity than aluminium	▪ Individual strands need to be coated to prevent oxidation

Table 1. 2 Advantages and inconvenient of Copper and Aluminium as electrical conductors

3.1.3. American Wire Gauge (AWG) system

The American Wire Gauge (AWG) is mainly used as the standardized wire gauge system to characterize the diameters and cross-sectional areas of round wires [83]. The higher the gauge number, the lower the wire diameter and the current-carrying capacity. The AWG tables are for a single, solid, round conductor. Hence the AWG of a stranded wire is determined by the cross-sectional area of the equivalent solid conductor. As there exist small gaps between the strands, it is likely that a stranded wire will have a slightly larger overall diameter than a solid wire with the same AWG.

Wire Size AWG	Nominal Section (mm²)
18	0,93
20	0,6
22	0,38

Table 1. 3 AWG classification

3.1.4. Flat cables

The development of flat cables began in the late 1950s, especially due to requirements of the aerospace industry not only in terms of performance and reliability but also in terms of packaging and manufacturing. Flat cables are particularly interesting due to their better flexibility and space efficiency, cf. Figure 1.22.

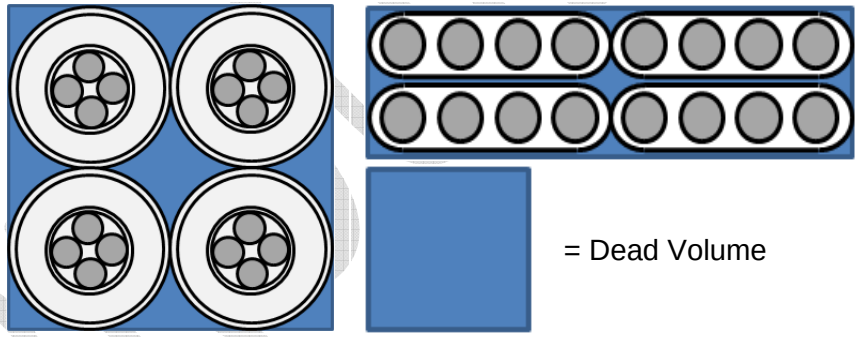

Figure 1. 21 Space efficiency of flat cables as compared to round cables

3.2. Operating environment and damage

Aerospace wiring needs to withstand the harsh environment it is exposed to: vibrations, extreme temperatures, humidity, electromagnetic interferences, shocks, maintenance operations, chafing, etc. are as many examples of physical, chemical, and electrical mechanisms that may damage the wire insulation polymers and conductors [81].

According to Jerome H. Collins [84], the Naval Air Systems Command (NAVAIR) has identified three common causes for electrical wiring system failure: unqualified components being used on aircrafts, improper installation, and poor or non-existent maintenance and repair. Among the most recurrent damages are circuit breakers (protective devices) that do no function properly and connectors that are corroded beyond repair.

Similarly, NASA [79] has classified the different kind of cable defects according to their origin, cf. Figure 1. 22. Among them, chafing, short-circuits and broken cables are the most common. Theses defects can be classified as “hard” defects (short-circuits, open circuits) which characterize defects that prevent any signal from going further away [85], or as “softs” defects such as chafing which accounts for more than 30% of wire defects found in Aircrafts [2, 8].

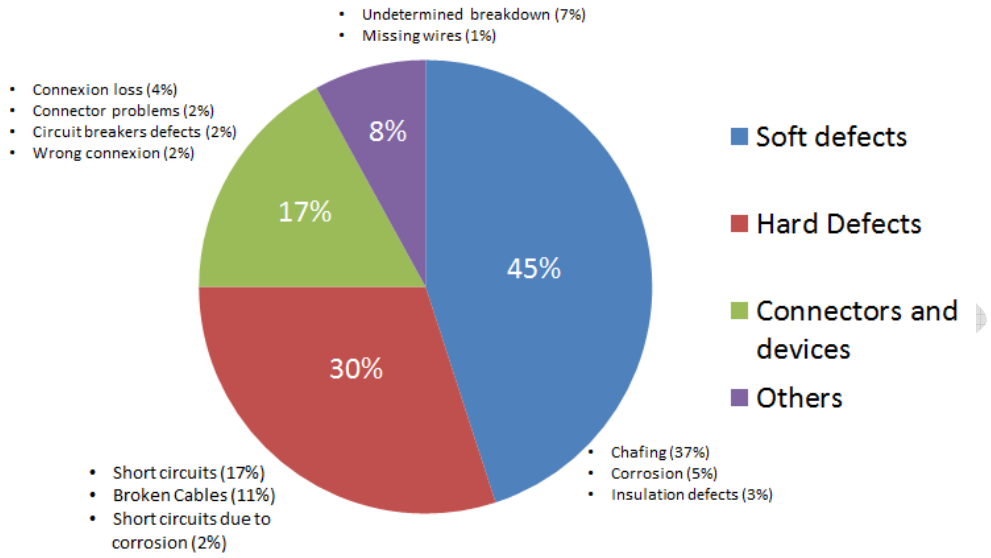

Figure 1. 22 Classification of wire defects found in aircrafts (NASA), according to [79]

Further information can also be found in [82], where some aircraft wiring practices are presented: installation, maintenance, industry practices, primary factors associated with wire degradation etc.

Therefore, based on this review, the different causes of wiring degradations are:

- **Vibration:** accelerates degradation over time and exacerbates any existing problem with wire insulation cracking
- **Moisture:** accelerates corrosion processes on terminals, pins, sockets and conductors
- **Maintenance:** when improperly done (including repairs), contributes to long term problems and wiring degradation
- **Indirect damage:** the surrounding wire needs to be safe
- **Chemical contamination:** hydraulic fluid, battery electrolytes, fuel, cleaning agents… contribute to degradation of wiring
- **Heat:** accelerates degradation, insulation dryness and cracking
- **Installation:** improper installation accelerates the wiring degradation process

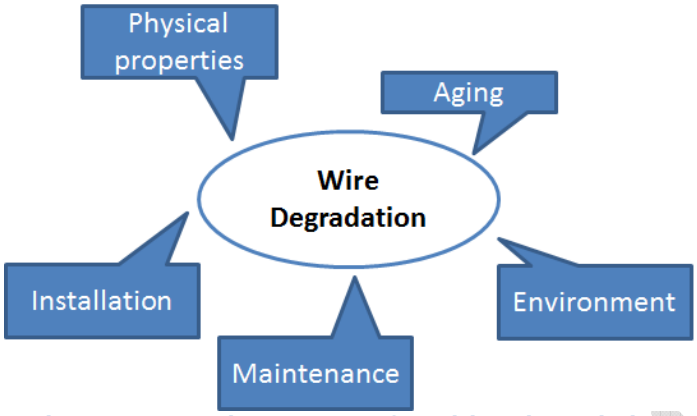

Figure 1. 23 Various causes for wiring degradation

Among all these defects, one of the most critical is the electrical arcing, which occurs when a power wire makes intermittent contact with an object, or wire, of a different voltage potential [27]. Indeed, an arc between two conductors is likely to pyrolize the surrounding environment (in particular the insulation) and propagates along the wire, hence causing significant damage.

To protect devices against arc tracking, or against any increase of current beyond the current-carrying capacity of the conductors, the insulator needs to be chosen carefully, and circuit protections such as fuse, circuit-breaker and limiting resistor need to be used.

3.3. Wires and insulation design

3.3.1. Wire design

Performance requirements of wires are measured in terms of: ease of removing the insulation, ease of soldering, dielectric testing, elongation and tensile strength, high and low temperature testing, life cycle testing, flammability, smoke emission etc. In addition, wire system design should be made to ensure that the maximum ambient temperature that the wires will be subjected to, plus the rise of temperature due to the current loads, does not exceed the maximum allowable temperature in the conductor [82].

Wires sizes are defined by the American Wire Gauge (AWG), and depend mainly on the current intensity to be transmitted, cf. Table 1.4. Larger diameter wires, despite resulting in heavier cables, offer less voltage drop for a given length, and lower heating effect due to the Joule Effect.

AWG	Conductor Diameter (mm)	Section (mm²)	Electrical resistance (Ω/km)	Maximum Current (A)
16	1.29	1.31	13.20	13.0
18	1.02	0.823	20.90	10.0
20	0.812	0.518	33.30	7.5
22	0.644	0.326	52.95	5.0

Table 1. 4 Some copper wire gauge and current limits

Further specifications can be found in the normative reference NF-EN-ISO 3475: Aerospace series – Cables [86] which specifies methods to measure and validate aeronautic cables: electrical (insulation resistance, resistance to arc propagation, attenuation, characteristic impedance, etc.), mechanical (tensile strength, flexure endurance, cut-through resistance, etc.), and thermal (thermal shock, fire resistance, thermal stability, etc.) methods are detailed.

3.3.2. Insulation design

The wire insulation selection should be made to ensure [82]:

- Abrasion, arc, fluid, and corrosion resistance
- Dielectric, Mechanical and Cut-through strength
- Smoke emission and flame resistant
- Heat distortion
- Withstand the applied voltage

Many polymeric materials exist and are good candidate for such wire insulation. Nevertheless, they do not gather all these properties at the same time, cf. Table 1. 5. Among them, the Poly Tetra Fluoro Ethylene (PTFE, or Teflon FEP) is a plastic which is flexible up to -200°C and stable up to 200°C. It has excellent high temperature properties and is non-flammable; yet, it has a poor cut-through resistance and is susceptible to solar radiation. The Ethylene Tetra Fluoro Ethylene (Tefzel ETFE) can withstand physical abuse during and after installation, has good high (up to 150°C) and low temperature properties, and exceeds the mechanical properties of PTFE; yet, insulation tends to soften at high temperature and it is susceptible to flammability in a 30% oxygen environment. Finally, an Aromatic Polyimide (PI) such as Kapton has good abrasion and cut-through properties, excellent radiation resistance, but has limited resistance to arc propagation (such as wet arc and dry arc arising from abrasions and cuts), low flexibility, and absorbs moisture.

	(1) Most desirable => (3) Least desirable		
Relative ranking	**1**	**2**	**3**
Weight	PI	ETFE	PTFE
Temperature	PTFE	PI	ETFE
Cut-through Resistance	PI	ETFE	PTFE
Chemical Resistance	PTFE	ETFE	PI
Flammability	PTFE	PI	ETFE
Smoke Generation	PI	PTFE	ETFE
Flexibility	PTFE	ETFE	PI
Arc propagation Resistance	PTFE	ETFE	PI

Table 1. 5 Comparative properties of some polymeric materials used as wire insulation systems, taken from [3]. PTFE: Poly Tetra Fluoro Ethylene, ETFE: Ethylene Tetra Fluoro Ethylene, PI: Aromatic polyimide (e.g.: Kapton)

Therefore, the best balance needs to be found between electrical, mechanical, chemical and thermal (plus non-flammability and low smoke) properties.

3.3.3. ESA Specifications & Requirements

As regards to a spatial environment, the detail specifications are given by the ESA (European Space Agency) normative reference ESCC No 3901 (European Space Components Coordination) [76], [87]. which specifies “the ratings, physical and electrical characteristics, test and inspection data for Polyimide Insulated Wires and Cables, Low Frequency, 600V, -100 to +200°C”, in conjunction with MIL-W-81381.

Figure 1. 24 presents the qualification tests of standard electronic components for space application, applicable to wires and cables, 600V, low frequency. More details about these tests can be found in Ref. [76]. Among the given requirements, it is noted that:

- The electrical conductors must have an elongation at break higher than 10%
- The maximum ratings current for an AWG20 conductor is 7.5A to ensure that the total temperature of the wire (ambient + rise) does not exceed the continuous operating temperature of the wire in a vacuum environment
- Finally, the electrical requirements are listed in Table 1. 6 below.

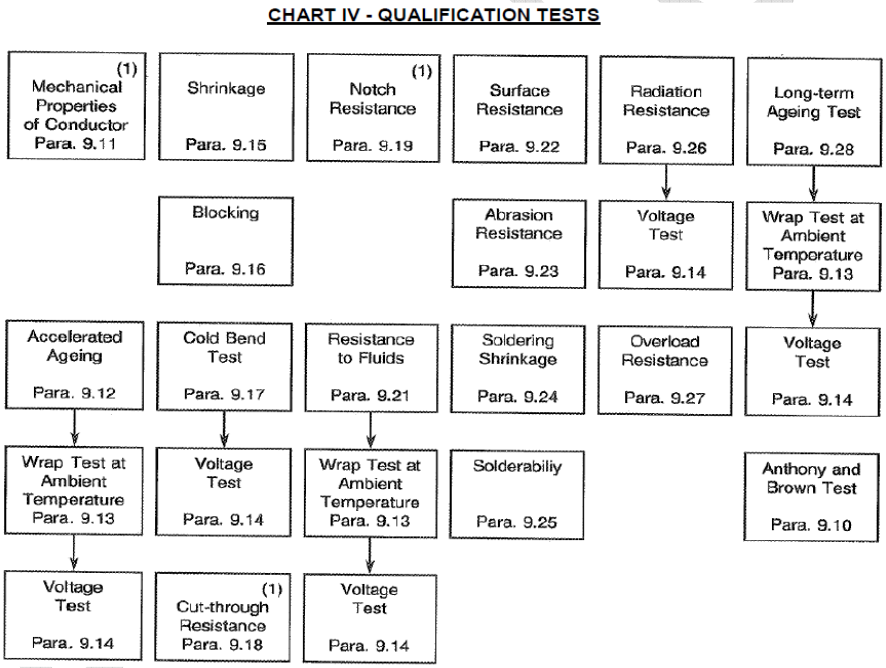

Figure 1. 24 Qualification tests as given by the ESCC Generic Specification No. 3901 [87]

No.	CHARACTERISTICS	SPEC. AND/OR TEST METHOD	LIMITS	UNIT
1	Conductor Resistance	ESA/SCC No. 3901, Section9	Table 1(a)	Ω/km
2	Spark Test	ESA/SCC No. 3901, Section9	Insulation: 3 Jacket: 1.5	kV
4	Insulation Resistance	ESA/SCC No. 3901, Section9	Insulation: 750 Jacket: 30	MΩ.km
5	Surface Resistance	ESA/SCC No. 3901, Section9	: 125	MΩ.mm

Table 1. 6 Electrical requirements at room temperature, according to the ESCC Detail Specification No. 3901/001 [76]

3.4. Concluding remarks

A brief review on common aerospace wiring was presented. It unveiled the damage mechanisms likely to be encountered by the wires and some key rules to properly design a cable. Among the presented damage mechanisms, aging (mechanical fatigue, thermal cycling, corrosion, etc.) and electrical arcing seem to be the most critical.

These specifications and failure modes consider conventional wiring technologies where the electrical cables run alongside structural parts. Therefore, when designing a multifunctional structure embedding electrical conductors, it is likely that these failure modes will differ. That's why it seems mandatory to investigate on the influence of a multifunctional architecture on the modes of failure of the embedded cables and to sort out the critical failure scenarios.

4. Definition of the scientific and technological challenges

Based on this literature review, it has been shown that the design and development of a multifunctional composite structure embedding a functional layer is challenging for numerous reasons.
First of all, the mechanical performances of the host structure are likely to be degraded due to the weak interface between the embedded layer and the host structure. Indeed, placing dissimilar materials may lead to early delaminations and debondings due to a poor interface adhesion, especially when the structure is submitted to out-of-plane deformations such as bending and low energy impacts. A loss of adhesion at this interface could not only lead to a reduction of the mechanical performances of the structure, but also to a loss of electrical performances due to the degradation of the embedding cables. Hence the need to address the following question:
What is the influence of the embodiment of an electrically conductive layer on the mechanical behaviour and damage modes of a composite laminate?
From an industrial point of view, these investigations will allow defining electrical degradation criteria under low energy impact tests for such structures embedding electrical wires.

These considerations are likely to be greatly influenced by multi-physics couplings. Indeed, the integration of an electrically conductive layer among a composite structure results in coupled electrical, thermal and mechanical mechanisms. Among other, it appears mandatory to study the effect of the temperature on the mechanical properties of the multifunctional structure; and to ensure that the temperature due to resistive heating of the conductors, combined to the external temperature, does not exceed the maximum allowable temperature of any component. This constitutes the definition of the second scientific challenge to be broached during this work:
How to accurately assess the mechanical condition of a multi-material sandwich composite beam as a function of temperature?

PROTOTYPE

References

[1] D. Gay, *Matériaux Composites*, 5th ed. Paris: Lavoisier, 2005.
[2] J.-M. Berthelot, *Matériaux composites - Comportement mécanique et analyse des structures*, H.-. Lavoisier. 660. .
[3] M. Asaad, 'Damage Accumulation in Hybrid Woven Farbic Composites', Bournemouth University, 2002.
[4] M. Kollegal, S. N. Chatterjee, and G. Flanagan, 'Progressive failure analysis of plain weaves using damage mechanics based constitutive laws', *Int. J. Damage Mech.*, vol. 10, no. 4, pp. 301–323, 2001.
[5] Y. Thollon and C. Hochard, 'A general damage model for woven fabric composite laminates up to first failure', *Mech. Mater.*, vol. 41, no. 7, pp. 820–827, Jul. 2009.
[6] J.-K. Kim and M.-L. Sham, 'Impact and delamination failure of woven-fabric composites', *Compos. Sci. Technol.*, vol. 60, no. 5, pp. 745–761, 2000.
[7] H. Ullah and V. V. Silberschmidt, 'Analysis of impact induced damage in composites for wind turbine blades', in *Power Generation System and Renewable Energy Technologies (PGSRET), 2015*, 2015, pp. 1–6.
[8] R. C. Batra, G. Gopinath, and J. Q. Zheng, 'Damage and failure in low energy impact of fiber-reinforced polymeric composite laminates', *Compos. Struct.*, vol. 94, no. 2, pp. 540–547, Jan. 2012.
[9] Y. Hirai, H. Hamada, and J.-K. Kim, 'Impact Response of Woven Glass-Fabric Composites - II. Effect of Temperature', *Composites Science and Technology*, pp. 119–128, 1998.
[10] C. Suresh Kumar, V. Arumugam, H. N. Dhakal, and R. John, 'Effect of temperature and hybridisation on the low velocity impact behavior of hemp-basalt/epoxy composites', *Compos. Struct.*, vol. 125, pp. 407–416, Jul. 2015.
[11] H. Zabala, L. Aretxabaleta, G. Castillo, J. Urien, and J. Aurrekoetxea, 'Impact velocity effect on the delamination of woven carbon–epoxy plates subjected to low-velocity equienergetic impact loads', *Compos. Sci. Technol.*, vol. 94, pp. 48–53, Apr. 2014.
[12] B. M. Icten, B. G. Kıral, and M. E. Deniz, 'Impactor diameter effect on low velocity impact response of woven glass epoxy composite plates', *Compos. Part B Eng.*, vol. 50, pp. 325–332, Jul. 2013.
[13] D. D. R. Cartié and P. E. Irving, 'Effect of resin and fibre properties on impact and compression after impact performance of CFRP', *Compos. Part Appl. Sci. Manuf.*, vol. 33, no. 4, pp. 483–493, Apr. 2002.
[14] W. Hufenbach, F. M. Ibraim, A. Langkamp, R. Böhm, and A. Hornig, 'Charpy impact tests on composite structures – An experimental and numerical investigation', *Compos. Sci. Technol.*, vol. 68, no. 12, pp. 2391–2400, Sep. 2008.
[15] M. A. Caminero, G. P. Rodríguez, and V. Muñoz, 'Effect of stacking sequence on Charpy impact and flexural damage behavior of composite laminates', *Compos. Struct.*, vol. 136, pp. 345–357, Feb. 2016.
[16] 'ASTM D7137/D7137M - 12 Standard Test Method for Compressive Residual Strength Properties of Damaged Polymer Matrix Composite Plates', *http://www.astm.org/Standards/D7137.htm*.
[17] 'AITM1-0010 - Airbus Test Method. Fiber Reinforced Plastics - Compression Strength After Impact', pp. 1–15, Oct-2005.
[18] T. Mitrevski, I. H. Marshall, R. S. Thomson, and R. Jones, 'Low-velocity impacts on preloaded GFRP specimens with various impactor shapes', *Compos. Struct.*, vol. 76, no. 3, pp. 209–217, Nov. 2006.
[19] H. Fang, M. Gutowski, M. DiSogra, and Q. Wang, 'A numerical and experimental study of woven fabric material under ballistic impacts', *Adv. Eng. Softw.*, vol. 96, pp. 14–28, Jun. 2016.
[20] Z. Hashin, 'Failure criteria for unidirectional fibre composites', *Journal of Applied Mechanics*, pp. 329–334, 1980.

BROUILLON

[21] A. Puck and H. Schürmann, 'Failure analysis of FRP laminates by means of physically based phenomenological models', *Composite Science and Technology*, vol. 58, pp. 1045–1067, 1998.
[22] S. T. Pinho, C. G. Dàvila, P. P. Camanho, L. Iannucci, and P. Robinson, 'Failure models and criteria for FRP under in-plane or three-dimensional stress states including shear non-linearity', 2005.
[23] T. Diehl, 'On using a penalty-based cohesive-zone finite element approach, Part I: Elastic solution benchmarks', *Int. J. Adhes. Adhes.*, vol. 28, no. 4–5, pp. 237–255, Jun. 2008.
[24] C. S. Lopes, P. P. Camanho, Z. Gürdal, P. Maimí, and E. V. González, 'Low-velocity impact damage on dispersed stacking sequence laminates. Part II: Numerical simulations', *Compos. Sci. Technol.*, vol. 69, no. 7–8, pp. 937–947, Jun. 2009.
[25] P. P. Camanho, C. G. DáVila, and S. T. Pinho, 'Fracture analysis of composite co-cured structural joints using decohesion elements: Composite co-cured structural joints', *Fatigue Fract. Eng. Mater. Struct.*, vol. 27, no. 9, pp. 745–757, Oct. 2008.
[26] S. Nemat-Nasser, S. Nemat-Nasser, T. Plaisted, A. Starr, and A. V. Amirkhizi, 'BIOMIMETICS: Biologically Inspired Technologies Edited by Yoseph Bar-Cohen CRC Press (2005)'.
[27] R. F. Gibson, 'A review of recent research on mechanics of multifunctional composite materials and structures', *Compos. Struct.*, vol. 92, no. 12, pp. 2793–2810, Nov. 2010.
[28] S. Hahn, R. Usami, and T. Ozaki, 'Multifunctional structure spacecraft bus technology', in *22nd AIAA International Communications Satellite Systems Conference & Exhibit 2004 (ICSSC)*, 2004, p. 3135.
[29] D. M. Barnett and S. P. Rawal, 'Multifunctional Structures Technology Demonstration on New Millenium Program (NMP) Deep Space 1 (DS1) Technology Validation Report', Lockheed Martin, Astronautics Division, Denver, CO.
[30] E. Murtola, S. M. Neuhold, and P. Anliker, 'Hyperelastic high voltage conductor for electric drilling', in *Proc. 4th Int. Conf. CMOO*, 2005, pp. 1–11.
[31] M. S. Qidwai, J. Thomas, and W. Pogue, 'Structure-battery composites for UUVs: multifunctional interaction effects', in *50th AIAA/ASME/ASCE/AHS/ASC Structures, Structural Dynamics, and Materials Conference 17th AIAA/ASME/AHS Adaptive Structures Conference 11th AIAA No*, 2009, p. 2341.
[32] E. S. Greenhalgh, L. E. Asp, A. Bismarck, and M. Wienrich, 'Mechanical, electrical and microstructural characterisation of multifunctional structural power composites', *Journal of Composite Materials*, vol. 49 (15), pp. 1823–1834, 2015.
[33] A. K. Noor, S. L. Venneri, D. B. Paul, and M. A. Hopkins, 'Structures technology for future aerospace systems', *Comput. Struct.*, vol. 74, no. 5, pp. 507–519, 2000.
[34] P. Matic, 'Overview of Multifunctional Materials', *Proc. SPIE 5053, Smart Structures and Materials 2003: Active Materials: Behavior and Mechanics*, 2003.
[35] R. Perraud *et al.*, 'Metallic Strip Concept: Overview and Results', presented at the SARISTU Final Project Meeting and Conference, Moscow, Russia, 2015.
[36] G. F. Nino, T. J. Ahmed, and H. E. N. Bersee, 'Design and Manufacturing of a Multifunctional Thermoplastic Composite Leading Edge', 2009.
[37] A. Orlowska, J. Biczyk, and P. Kolakowski, 'Using Embedded Electrical Grid for Active Thermography Diagnostics of Composite Structures'.
[38] M. Grésil, 'Contribution à l'étude du contrôle de santé intégré associé à une protection électromagnétique pour les matériaux composites', École normale supérieure de Cachan-ENS Cachan, 2009.
[39] R. Harcourt and M. Lockhart, 'Well Hose with Embedded Electrical Conductors', US20050247362 A1.
[40] T. Seong Jang, D. Soo Oh, J. Kyu Kim, K. In Kang, W. Ho Cha, and S. Woo Rhee, 'Development of multi-functional composite structures with embedded electronics for space application', *Acta Astronaut.*, vol. 68, no. 1–2, pp. 240–252, Jan. 2011.
[41] J. M. Bailey, 'A connector and electrical tracks assembly', US Patent 20110014803 A1.
[42] E. D. Wetzel, D. J. O'Brien, J. F. Snyder, R. H. Carter, and J. T. South, 'Multifunctional structural power and energy composites for US army applications', DTIC Document, 2006.

PROJECTION

[43] T. Carlson, D. Ordéus, M. Wysocki, and L. E. Asp, 'Structural capacitor materials made from carbon fibre epoxy composites', *Compos. Sci. Technol.*, vol. 70, no. 7, pp. 1135–1140, Jul. 2010.
[44] J. P. Thomas, M. A. Qidwai, W. R. Pogue III, and G. Pham, 'MULTIFUNCTIONAL STRUCTURE-BATTERY MARINE COMPOSITES'.
[45] D. Fritsch, C. Viets, E. Mannov, K. Schulte, and B. Fiedler, 'Nanocomposite Based Structural Health Monitoring Approaches for Fibre Reinforced Polymers-On Doorstep to Industrial Relevance after Two Decades of Intense Research?', in *EWSHM-7th European Workshop on Structural Health Monitoring*, 2014.
[46] T. A. J. Plaisted, C. Santos, and A. V. Amirkhizi, 'Self-healing structural composites with electromagnetic functionality', presented at the 14th ICCM Conference, San Diego, CA, 2003.
[47] J. M. Lawrence, P. Frey, A. A. Obaid, S. Yarlagadda, and S. G. Advani, 'Simulation and validation of resin flow during manufacturing of composite panels containing embedded impermeable inserts with the VARTM process', *Polym. Compos.*, vol. 28, no. 4, pp. 442–450, Aug. 2007.
[48] D. Zhao, 'Study of a New Manufacturing Technology for Multi-Functional Composite Structures with Aerosol-Jet Printing', Electronic Theses, Treatises and Dissertations.
[49] H. S. Kim, J. S. Kang, J. S. Park, H. T. Hahn, H. C. Jung, and J. W. Joung, 'Inkjet printed electronics for multifunctional composite structure', *Compos. Sci. Technol.*, vol. 69, no. 7–8, pp. 1256–1264, Jun. 2009.
[50] H. Kim, M. Park, and K. Hsieh, 'Fatigue fracture of embedded copper conductors in multifunctional composite structures', *Compos. Sci. Technol.*, vol. 66, no. 7–8, pp. 1010–1021, Jun. 2006.
[51] J. Di Palma, J. Preble, M. Schoenoff, and S. Motoyama, 'Applications of Multifunctional Structures to Small Spacecraft', presented at the 18th Annual AIAA/USU Conference on Small Satellites.
[52] Y. Nawab, F. Jacquemin, P. Casari, N. Boyard, Y. Borjon-Piron, and Y. Subotka, 'Stud of variation of thermal expansion coefficients in carbon/epoxy laminated composite plates', *Composites: Part B*, 2013.
[53] M. Hatanaka and M. R. Cutkosky, 'Process planning for embedding flexible materials', presented at the ASME Design Engineering Technical Conferences and Computers and Information in Engineering Conference, Chicago, Illinois USA, 2003.
[54] Z. Zhao, X. Chen, and X. Wang, 'Deformation behavior of woven glass/epoxy composite substrate under thermo-mechanical loading', *Mater. Des.*, vol. 82, pp. 130–135, Oct. 2015.
[55] L. Liu, B.-M. Zhang, D.-F. Wang, and Z.-J. Wu, 'Effects of cure cycles on void content and mechanical properties of composite laminates', *Compos. Struct.*, vol. 73, no. 3, pp. 303–309, Jun. 2006.
[56] M. L. Costa, S. frascino M. De Almeida, and M. C. Rezende, 'The influence of porosity on the interlaminar shear strength of carbon/epoxy and carbon/bismaleimide fabric laminates', *Compos. Sci. Technol.*, vol. 61, no. 14, pp. 2101–2108, 2001.
[57] P. Olivier, J. P. Cottu, and B. Ferret, 'Effects of cure cycle pressure and voids on some mechanical properties of carbon/epoxy laminates', *Composites*, vol. 26, no. 7, pp. 509–515, 1995.
[58] H. Kim and K. Hsieh, 'Measurement and prediction of embedded copper foil fatigue crack growth in multifunctional composite structure', *Compos. Part Appl. Sci. Manuf.*, vol. 43, no. 3, pp. 492–506, Mar. 2012.
[59] Y. Xiao, W. Qiao, H. Fukuda, and H. Hatta, 'The effect of embedded devices on structural integrity of composite laminates', *Compos. Struct.*, vol. 153, pp. 21–29, Oct. 2016.
[60] A. Abu Obaid and S. Yarlagadda, 'Structural performance of the glass fiber–vinyl ester composites with interlaminar copper inserts', *Compos. Part Appl. Sci. Manuf.*, vol. 39, no. 2, pp. 195–203, Feb. 2008.
[61] N. Bowler, M. R. Kessler, L. Li, P. R. Hondred, and T. Chen, 'Electromagnetic Nondestructive Evaluation of Wire Insulation and Models of Insulation Material Properties', 2012.

PROQUEST

[62] Y. Abou Msallem, F. Jacquemin, N. Boyard, A. Poitou, D. Delaunay, and S. Chatel, 'Material characterization and residual stresses simulation during the manufacturing process of epoxy matrix composites', *Compos. Part Appl. Sci. Manuf.*, vol. 41, no. 1, pp. 108–115, Jan. 2010.
[63] Y. Nawab, X. Tardif, N. Boyard, V. Sobotka, P. Casari, and F. Jacquemin, 'Determination and modelling of the cure shrinkage of epoxy vinylester resin and associated composites by considering thermal gradients', *Composite Science and Technology*, p. Pages 81-87, 2012.
[64] Y. A. Msallem, F. Jacquemin, N. Boyard, A. Poitou, D. Delaunay, and S. Chatel, 'Characterisation of an aeronautic epoxy resin during the manufacturing process – simulation of residual stresses in epoxy matrix composites', 2008.
[65] E. Ruiz, C. Billotte, F. M. Bernard, F. Carra, and H. Baurier, 'Chemical Shrinkage and Thermomechanical Characterization of an Epoxy Resin During Cure by a Novel In Situ Measurement Method', in *18th International Conference on Composite Materials (ICCM18)*, 2011.
[66] Y. Rao, S. H. Shi, and C. P. Wong, 'An improved methodology for determining temperature dependent moduli of underfill encapsulants', *IEEE Trans. Compon. Packag. Technol.*, vol. 23, no. 3, pp. 434–439, 2000.
[67] T. Hobbiebrunken, B. Fiedler, M. Hojo, S. Ochiai, and K. Schulte, 'Microscopic yielding of CF/epoxy composites and the effect on the formation of thermal residual stresses', *Compos. Sci. Technol.*, vol. 65, no. 10, pp. 1626–1635, Aug. 2005.
[68] S. Deng, M. Hou, and L. Ye, 'Temperature-dependent elastic moduli of epoxies measured by DMA and their correlations to mechanical testing data', *Polym. Test.*, vol. 26, no. 6, pp. 803–813, Sep. 2007.
[69] S. Ropers, M. Kardos, and T. A. Osswald, 'A thermo-viscoelastic approach for the characterization and modeling of the bending behavior of thermoplastic composites', *Compos. Part Appl. Sci. Manuf.*, vol. 90, pp. 22–32, Nov. 2016.
[70] J. Feng and Z. Guo, 'A New Temperature-Dependent Storage Modulus Model of Epoxy Resin', in *Challenges in Mechanics of Time Dependent Materials, Volume 2*, B. Antoun, A. Arzoumanidis, H. J. Qi, M. Silberstein, A. Amirkhizi, J. Furmanski, and H. Lu, Eds. Cham: Springer International Publishing, 2017, pp. 195–201.
[71] C. A. Mahieux, 'A systematic stiffness-temperature model for polymers and applications to the prediction of composite behavior', Ph.D. Dissertation, Virginia Polytechnic Institute and State University, 1999.
[72] M. F. Ashby and D. R. H. Jones, *Engineering materials 2: An introduction to microstructures, processing and design*, 3. ed., Reprinted. Amsterdam: Elsevier, 2008.
[73] A. Manalo, G. Maranan, S. Sharma, W. Karunasena, and Y. Bai, 'Temperature-sensitive mechanical properties of GFRP composites in longitudinal and transverse directions: A comparative study', *Compos. Struct.*, vol. 173, pp. 255–267, Aug. 2017.
[74] A. Manalo, S. Surendar, G. van Erp, and B. Benmokrane, 'Flexural behavior of an FRP sandwich system with glass-fiber skins and a phenolic core at elevated in-service temperature', *Compos. Struct.*, vol. 152, pp. 96–105, Sep. 2016.
[75] S. Zhang, J. M. Dulieu-Barton, and O. T. Thomsen, 'The effect of temperature on the failure modes of polymer foam cored sandwich structures', *Compos. Struct.*, vol. 121, pp. 104–113, Mar. 2015.
[76] ESA, 'ESCC Detail Specification No. 3901/001, Polyimide insulated wires and cables, Low frequency, 600V, -100 to +200°C'. Issue 3, Jan-1996.
[77] M. M. Al-Asadi, A. P. Duffy, A. J. Willis, K. Hodge, and T. M. Benson, 'A simple formula for calculating the frequency-dependent resistance of a round wire', *Microw. Opt. Technol. Lett.*, vol. 19, no. 2, pp. 84–87, Oct. 1998.
[78] G. A. Slenski and M. F. Walz, 'Novel Technologies for improving wire system integrity'. .
[79] G. Millet *et al.*, 'Aircraft electrical wiring monitoring system', *Embed. Real Time Softw. Syst. Toulouse*, 2014.
[80] M. Tooley and D. Wyatt, *Aircraft electrical and electronic systems: principles, operation and maintenance*, 1. ed. Amsterdam: Elsevier/Butterworth-Heinemann, 2009.

BROUILLON

[81] J. Kurek *et al.*, *Aircraft wiring degradation study*. US Department of Transportation, Federal Aviation Administration, 2008.
[82] B. Portwood and M. Sadeghi, *Aircraft Wiring Practices, An interactive Training and Self-Study Course - Participant Guide*. Federal Aviation Administration, 2001.
[83] *ASTM B258 - 14. Standard Specification for Standard Nominal Diameters and Cross-Sectional Areas of AWG Sizes of Solid Round Wires Used as Electrical Conductors. West Conshohocken: ASTM International. Retrieved 23 August 2018.* .
[84] J. Collins, 'The challenges facing US navy aircraft electrical wiring systems', in *Proceedings of the 9th Annual Aging Aircraft Conference*, 2006.
[85] F. Auzanneau, 'Wire troubleshooting and diagnosis: Review and perspectives', *Prog. Electromagn. Res. B*, vol. 49, pp. 253–279, 2013.
[86] 'NF-EN-ISO 3475: Aerospace series - Cables, Electrical, Aircraft use'. .
[87] ESA, 'ESCC Generic Specification No. 3901, Wires and Cables, Electrical, 600V, Low Frequency'. Issue 2, May-2013.

BROUILLON

Chapter 2 : Presentation of the materials and characterizations of the constituents of the multifunctional structure

Chapter 2 : Presentation of the materials and characterizations of the constituents of the multifunctional structure

1. Presentation of the multifunctional structure 43

1.1. Industrial context 43

1.2. Flat electrical cable 44

1.3. Host composite structure 45

2. Manufacturing of the multifunctional structure 45

3. Mechanical characterization of the host composite structure 48

3.1. Mechanical properties of a yarn 48

3.2. Geometrical modelling 50

3.3. Mechanical properties of the woven fabric 50

4. Mechanical characterization of the flat electrical cable 51

4.1. Material Properties 51

4.2. Tensile testing 52

4.2.1. Longitudinal direction 52

4.2.2. Transverse direction 53

4.2.3. Through-the-thickness direction 54

4.2.4. Mechanical properties of the flat electrical cable 55

5. Critical defaults to the electrical performances of the electrical cable 56

5.1. Broken wires 56

5.2. Insulation defects 58

5.2.1. Nominal breakdown voltage 59

5.2.2. Breakdown voltage of a damaged cable 60

5.2.2.1. Adjacent wires 60

5.2.2.2. Non-adjacent wires 60

6. Concluding remarks 61

This chapter aims at presenting the multifunctional structure studied in the frame of this work and its constitution. The host composite structure and flat electrical cables used to manufacture the multifunctional structure are presented and characterised through mechanical and electrical testing. This allows the determination of the mechanical properties of the composite and cable, as well as the identification of the failure modes of the cable.

1. Presentation of the multifunctional structure

1.1. Industrial context

AIRBUS GROUP has been working for a few years on the development of new, innovative, and more robust avionics technologies so as to reduce the costs associated with wired networks installation. In this framework, the integration of electrical wires within composite structures has become a major industrial stake. Indeed, The main advantage of embedding electrical wires inside a composite structure is to reduce time on the line as the installation and segregation of the wiring has already been pre-completed. Besides, it confers a protection to the electrical systems from environmental conditions and enables increasing the ratio of electrical functionality to volume, hence leading to significant mass and volume savings.

This PhD aims at studying such a structure, and has been motivated by a specific use case designed for launcher applications. Indeed, ARIANE GROUP wished to investigate the replacement of conventional wiring solutions for space launcher applications. Such a technology would also offer the potential to carry synergies for other applications on civil and military aircrafts (pax floor, seat rails, replacement of electrical harnesses, etc.).

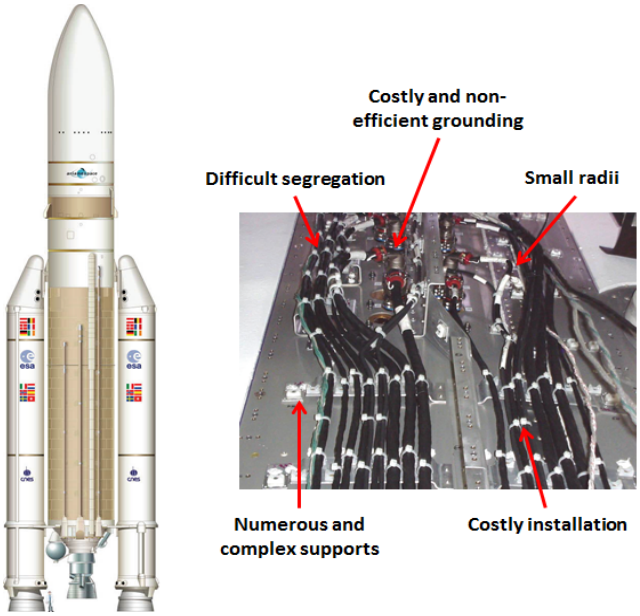

Figure 2. 1 Installation and segregation of the wires is time-consuming

The foreseen multifunctional structure should consist in a composite beam embedding flat electrical cables mainly composed of wire gauges AWG22, AWG20 and AWG18 for power and data transmission. During its lifespan, it will be submitted to:

- Manufacturing and inspections operations

- Transport, delivery, storage, and assembly on the launcher
- Waiting on the launching site
- Take off and flight

Before take-off, the structure is likely to be submitted to mechanical shocks which may occur during transport and handling operations (drop tools for instance). They may also occur due to the ignition of the boosters or during stages separation (pyrotechnics shocks). Besides, during the take off and flight, the structure endures a harsh vibratory environment (sinusoidal, random, acoustic, constant). All of these environmental conditions do not enter in the frame of this work but need to be taken into account in the design phase. In particular, this work aims at investigating the influence of mechanical shocks and temperature on the mechanical behaviour and failure modes of such a structure.

The components, architecture, and manufacturing process of this multifunctional structure are presented hereafter.

1.2. Flat electrical cable

A flat cable technology has been selected and designed to replace the conventional solution and ease the integration of the electrical wires inside the composite structure, cf. Figure 2. 2

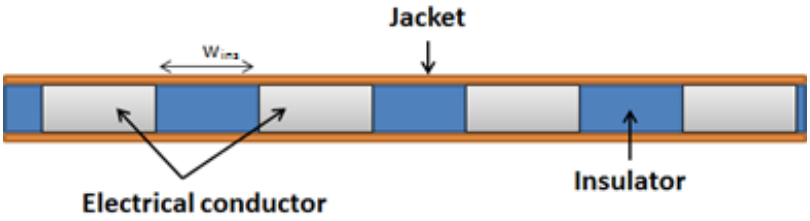

Figure 2. 2 Scheme of the flat electrical cable

The design of these flat electrical cables is based on electromagnetic and electrical considerations which define the segregation (thickness of the insulation w_{ins}) between the wires to ensure sufficient insulation [1], cf. Table 2. 1.

Characteristics	Normative Reference	Minimum Value	Unit
Spark Test	ESA/SCC No. 3901, Section9	Insulation: 3 Jacket: 1.5	kV
Insulation Resistance	ESA/SCC No. 3901, Section9	Insulation: 750 Jacket: 30	MΩ.km

Table 2. 1 ESA/SCC No. 3901 insulation requirements

The chosen materials were a polyimide tape for the jacket, a fluorocarbon resin for the insulator, and AWG20 copper braided conductors for the wires. Some of their main mechanical, electrical, and thermal properties are listed in Table 2. 2 below.

Property	Jacket: Polyimide Tape	Insulator: fluorocarbon resin
Tensile Strength (MPa)	200	27
Elongation (%)	25	300
Dielectric Constant (at 1 kHz)	3	2.06
Dielectric strength (kV/mm)	108	80
Thermal Conductivity (W/mK)	0.12	0.25

Table 2. 2 Main mechanical, electrical and thermal properties of the jacket and insulator

The electrical cables have a nominal width of about 85mm containing 17 AWG20 electrical conductors with a width of about 3mm each once laminated inside the cable. Besides, it is worth noticing that in order to ensure the flatness of the electrical cable, the fluorocarbon resin sections were filled with two glass-fibres between every electrical wire, as shown by Figure 2. 3 (a).

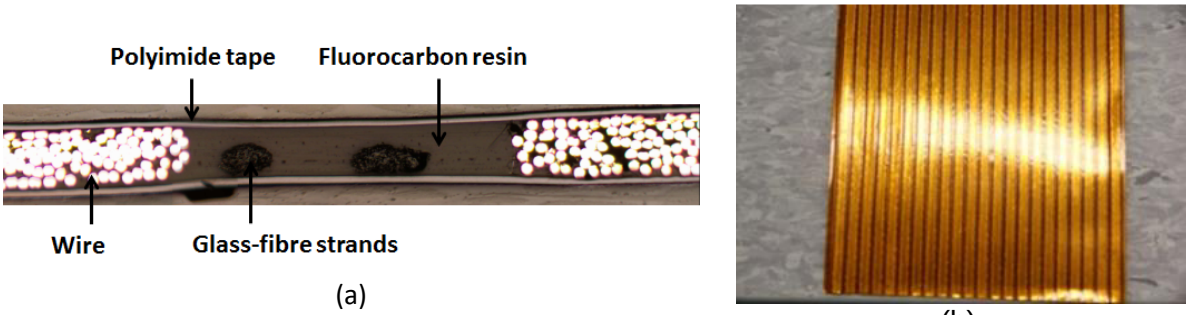

Figure 2. 3 (a) Microscopic observation of a cross-section of the flat electrical cable and (b) picture of a sample of electrical cable

1.3. Host composite structure

The chosen host composite structure is a woven glass fabric filled with an epoxy resin. The pattern is a 4-harness satin: the fill yarn passes over three warp yarns and under one. Besides, the reinforcement pattern is quasi-equilibrated with 51% fibres in the warp direction and 49% in the weft direction. The choice of this composite material was first motivated by the nature of the reinforcement (glass fabric) which offer good electrical insulation properties and galvanic protection (as compared to carbon fabric), and by its low cost. Further characterisations and details about this composite materials are given in section 3 of the present chapter.

2. Manufacturing of the multifunctional structure

The solution investigated consists in superposing two flat electrical cables so as to have sufficient electrical wires for power and data transmission, and return current functions. Hence, two flat electrical cables are laid one above the other within the composite structure. The distance between them is chosen according to the required characteristic impedance of the line. This divides the composite structure into three lay-ups of thickness h, with h=1.5mm. Additionally, two copper foils are laminated on the outer surfaces of the multifunctional structure for electromagnetic shielding purposes. The mechanical behaviour of these copper foils, and their influence on the mechanical behaviour of the structure will not be detailed in

this report. Nevertheless, they were not altered when manufacturing the test specimens so as not to deviate from the industrial manufacturing process.

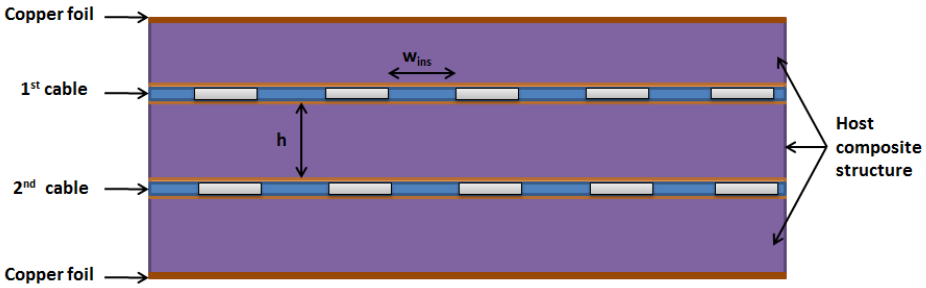

Figure 2. 4 Scheme of the multifunctional structure to be manufactured

The composite plies are glass prepregs, i.e. pre-impregnated woven sheets of glass fiber with epoxy resin, that require a cure cycle of 180min at 160°C under a pressure between 1 and 5 bar according to manufacturer's datasheet. Several curing parameters were tested on this composite material, and an autoclave curing cycle of 180min under 160°C, 1 bar vacuum and 7 bars pressure was finally chosen with a heating rate of 2°C/min, cf Figure 2.6. Additionally, the moment of applying the pressure was shifted so as to reduce the void content to a minimum [2], cf. Figure 2. 5.

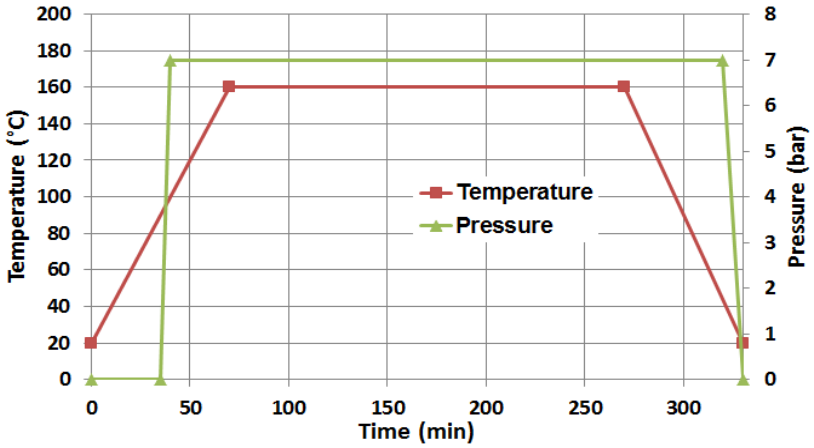

Figure 2. 5 Temperature and pressure of the curing cycle

Composite plates without embedded electrical cables were first manufactured and resulted in an average cured ply thickness of 0,125mm which corresponds to a resin content of 50% and a fibre volume content of 33% according to manufacturer's datasheet, cf. Figure 2. 6. Therefore, in order to get h=1,5mm, 12 plies of woven glass fabric were needed.

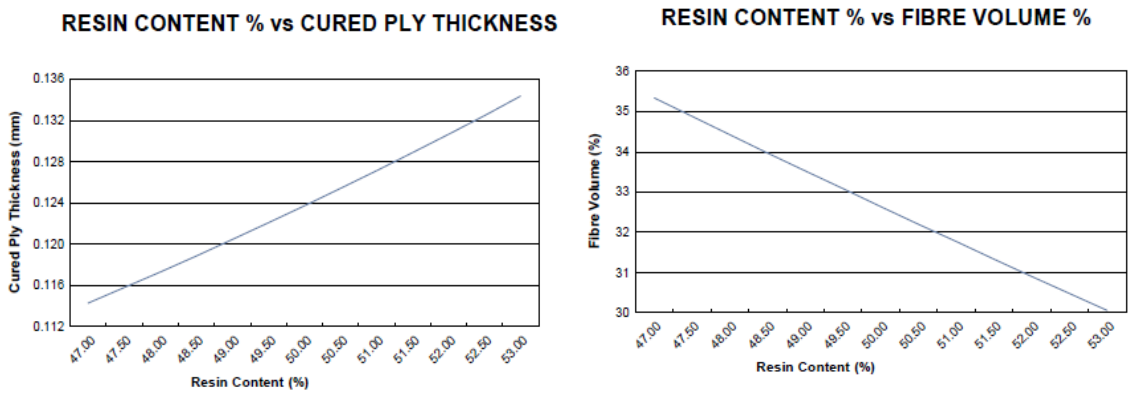

Figure 2. 6 Fibre Volume (%) as a function of the cured ply thickness (mm) and Resin content (%), according to manufacturer's datasheet

The curing environment is presented in Figure 2. 7. The outer stacking sequences of composite plies are $[0/45/0/-45/45/0]_s$ and the inner stacking sequence is $[-45/0/45/0/-45/0]_s$. The composite plies, flat electrical cables and copper foils were manually laid up in this configuration while performing intermediate compacting and suitable surface treatment of the electrical cables (such as dry-cleaning) to ensure good interface properties between the composite and the cables.

This manufacturing process was used to manufacture every plate and test specimens presented in this report.

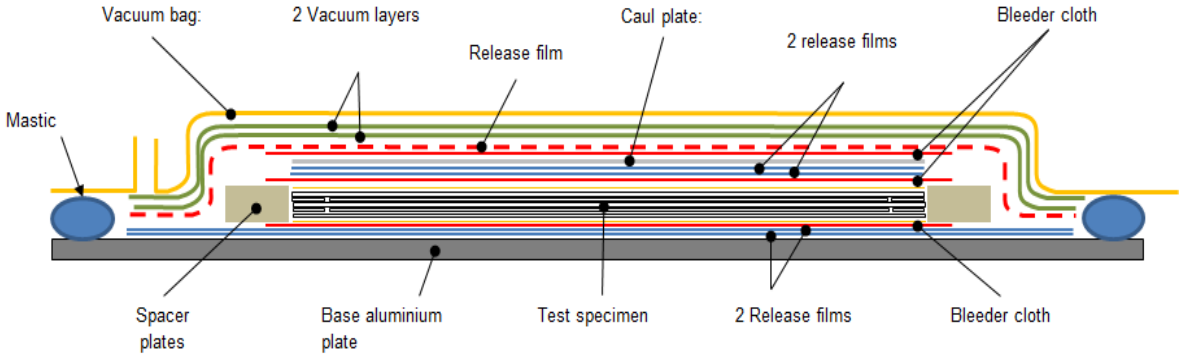

Figure 2. 7 Curing environment

The resulting part thickness is approximately 5,6 mm, corresponding to the three composite sequences (1,5mm each), two embedded electrical cables (0,45mm each) and two copper foils (0,1mm each), cf. Figure 2. 8.

Figure 2. 8 Microscopic observation of a cross-section of the multifunctional structure

As this thesis aims at investigating the mechanical behaviour, multi-physics couplings and damage modes of such a structure, it requires the knowledge of some engineering and elastic properties. Hence, the next sections aim at determining the elastic properties of the host composite structure and flat electrical cables.

3. Mechanical characterization of the host composite structure

The mechanical properties of woven fabric composite materials depend on many factors such as the yarn spacing, yarn size, fibre volume fraction, yarn stacking sequence, etc. Hence, determining the elastic properties and engineering constants of such composites is challenging and requires many experimental tests and numerical investigations [3], [4]. Yet, in the past few years, researches have shown that the effective macro mechanical properties of woven fabric textile composites may be easily determined through the analysis of periodic unit cells and micro mechanical methods [5]. In particular, the University of Notthingham (UK) has been developing an open source code known as TexGen [6] to ease the geometric modelling of a unit cell of woven fabric and to estimate its elastic properties. The proposed modelling method includes modelling the unit cell with the appropriate geometric and material properties (yarn spacing, yarn mechanical properties, volume ratio of fibres, number of strands per yarn, etc.) under TexGen and determining the macro mechanical properties of the woven fabric with help of Finite Element Method (FEM) based simulations under the software ABAQUS. The scheme of this method is depicted in Figure 2.9.

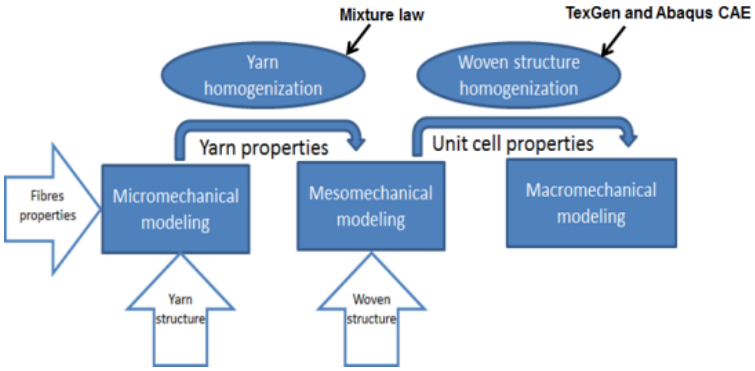

Figure 2. 9 Scheme of the methodology used to determine the elastic properties of the woven fabric

The mechanical properties of a yarn are first calculated. Then the geometrical modelling of a unit cell is created under TexGen, and finally the computation of the elastic properties of the woven fabric is performed under ABAQUS.

3.1. Mechanical properties of a yarn

Data about the yarn micro-structure, such as the number of fibres per yarn, the yarn width and spacing, the total fibre area etc. need to be known and implemented in TexGen. The yarn reference is ECD 450 ½ where “E” stands for the glass composition, “C” for the type of yarn (Continuous), “D” for the filament diameter (equivalent to 5.0 microns) and “450” for the strand count. The manufacturer’s datasheet further informs about the linear density: $5.6.10^{-6}$

kg/m, and fibre density: 2600 kg.m^{-3}. All these information are required for completion of the method.

The dimensions of the elliptical yarns are determined from microscopic observations on cured plies, manufactured according to the manufacturing process detailed above. The measurement of the width and height are averaged over ten yarns and yield a width of 335 µm and a height of 60µm.

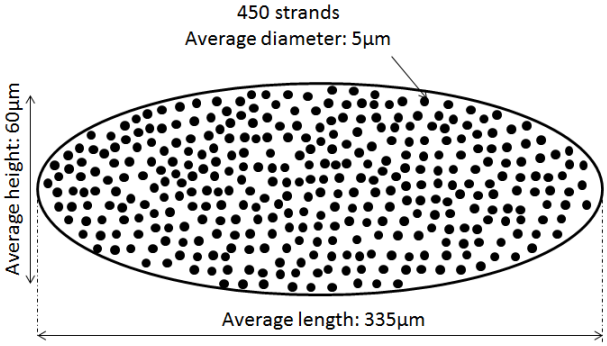

Figure 2. 10 Scheme of a yarn

Assuming that a yarn has an elliptical shape, the cross-sectional area of a yarn S_{yarn} is equal to $\pi \frac{0,335}{2} \frac{0,06}{2}$ = 1.58.10^{-2} mm². As there are 450 glass-fibre strands per yarn with an average diameter of 5µm per strand, the total area covered by the glass-fibres is $S_{fibres}=450*\pi*\left(\frac{0,005}{2}\right)^2$ which yields S_{fibres} = 7.85.10^{-3} mm².

The volume ratio of fibre V_f within a yarn is then computed as the ratio S_{fibres}/S_{yarn}, which yields $V_f \approx 0,56$. It is further assumed that a yarn behaves like a unidirectional orthotropic solid body whose longitudinal direction is aligned with the fibres direction, denoted as 11. The transverse directions are denoted as 22 and 33. The mechanical properties of a yarn are then determined by applying classical rules of mixtures presented in Appendix 1 with the mechanical properties of Table 2.3, and a volume ratio of fibres V_f=0,56.

Property	E-Glass fibre	Epoxy resin
Young Modulus (GPa)	72	3.8
Shear Modulus (GPa)	30	1.6
Poisson's Ratio	0.20	0.40

Table 2. 3 Mechanical properties of the fibres and matrix composing a yarn

In addition to the equations of the rules of mixtures, arbitrary transverse Poisson's ratios v_{13} and v_{23} were chosen based on the work of Craig and Summerscales [7].

V_f	E_{11} (GPa)	E_{22} (GPa)	E_{33} (GPa)	G_{12} (GPa)	G_{13} (GPa)	G_{23} (GPa)	v_{12}	v_{13}	v_{23}
0.56	42	11	6.2	4.90	1.61	1.61	0.30	0.35	0.42

Table 2. 4 Mechanical properties of a yarn

3.2. Geometrical modelling

The Representative Elementary Volume (REV) of the 4 harness satin weave is created under TexGen, cf. Figure 2. 11, with the geometrical properties listed in Table 2. 5 and Table 2. 6.

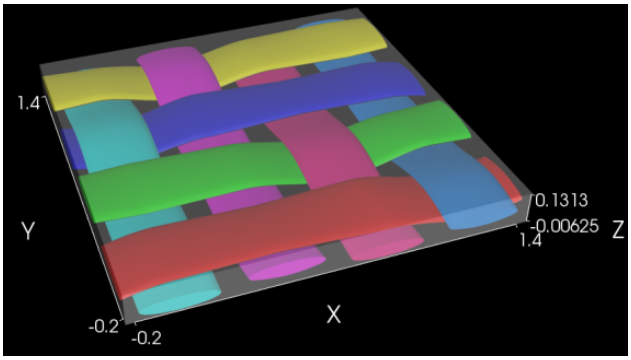

Figure 2. 11 Unit cell for 4 harness-satin weave fabric

Length (mm)	Width (mm)	Thickness (mm)	Volume (mm^3)
1.60	1.60	0.14	0.35

Table 2. 5 Unit cell size

Yarn spacing (mm)	Yarn width (mm)	Yarn thickness (mm)	Fabric thickness (mm)	Number of strands per yarn
0.4	0.3	0.060	0.125	450

Table 2. 6 Input data for the yarn geometrical modelling

3.3. Mechanical properties of the woven fabric

Once the geometrical modelling has been completed and the material properties filled, TexGen generates a voxel meshing [8] file which needs to be exported to ABAQUS for completion of the method. The unit cell is then subjected to periodic boundary conditions and pre-written Python scripting codes (provided with the open software) are executed to compute the elastic properties of the woven fabric [9]. The results are presented in Table 2.7.

E_{11} (GPa)	E_{22} (GPa)	E_{33} (GPa)	G_{12} (GPa)	G_{13} (GPa)	G_{23} (GPa)	ν_{12}	ν_{13}	ν_{23}
12.04	12.04	5.59	2.36	1.53	1.53	0.18	0.48	0.48

Table 2. 7 Mechanical properties of the woven fabric

This approach results in lower elastic moduli values than the values typically encountered in the literature, cf. Table 2.7. This kind of result was expected as a volume ratio of fibre of 33% has been determined, which is rather low compared to typical structural aerospace composite materials which usually exhibit a fibre volume ratio of about 50% to 60%, cf. Table 2.8.

	8HS balanced glass/epoxy [10]	Plain weave balanced glass/epoxy [11]	Plain weave balanced glass/epoxy [12]
V_f (%)	50	40	50
E_{11} (GPa)	20.5	18.1	20
E_{22} (GPa)	21.5	18.1	20
G_{12} (GPa)	3.5	3.94	2.85
v_{12}	0.15	0.19	0.13

Table 2. 8 Typical in-plane elastic properties of glass/epoxy woven fabric

Besides, these properties will be shown to yield reasonably good correlations between experimental and numerical data in the forthcoming chapters.

4. Mechanical characterization of the flat electrical cable

Three materials make up the cable: the jacket (polyimide tape) and the insulator (fluorocarbon resin) for which the mechanical properties are known, cf. Table 2. 9, and the wires (copper braided AWG20). Yet, for engineering and numerical analyses it will also be necessary to know the mechanical properties of the overall cable. Determining these mechanical properties is the purpose of the following section.

4.1. Material Properties

Among the three materials that compose the cable, the jacket and the insulator are isotropic materials while the wire may be assumed orthotropic since it is an assembly of copper strands embedded by the insulator resin.

	Jacket (polyimide tape)	Insulator (fluorocarbon resin)
Young's Modulus (GPa)	2.50	0.48
Poisson's Ratio	0.48	0.48
Shear Modulus (GPa)	0.84	0.16

Table 2. 9 Elastic properties of the jacket and insulator according to manufacturer's datasheet

As these materials are isotropic, their shear modulus was computed thanks to equation (Eq.2. 1) below:

$$G = \frac{E}{2(1+\vartheta)} \qquad \text{(Eq.2. 1)}$$

In principle, no numerical or experimental methods exist to efficiently characterise the mechanical properties of such an assembly. Hence, quasi-static tensile tests were performed on all three directions (longitudinal, transverse, through-the-thickness) so as to get insights into the mechanical behaviour of the electrical cables. As for now, the mechanical properties of the cable will be considered with the longitudinal direction taken aligned with the direction of the wires, denoted 11, and the transverse directions denoted 22 and 33.

4.2. Tensile testing

Quasi-static tensile tests were performed on at least 4 electrical cables test specimens per orientation (longitudinal, transverse and through-the-thickness) using an INSTRON 1196 testing machine with a load capacity of 50kN. The crosshead speed and specimens dimensions are detailed in Table 2.9 below.

Orientation of the cable	Dimensions (mm)	Crosshead speed (mm/min)	Scheme of the test specimens
Longitudinal	80x45x0.42	2	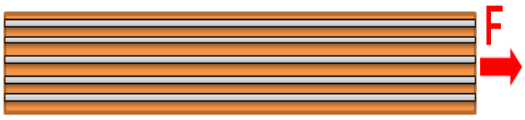
Transverse	28x45x0.42	4	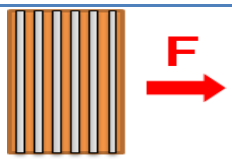
Through-the-thickness	cf. 4.2.3	1	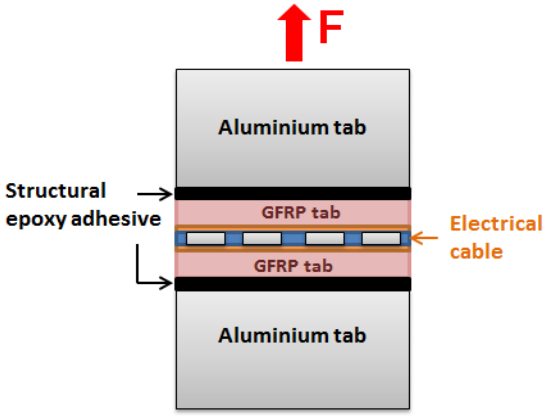

4.2.1. Longitudinal direction

Specimens were 45mm wide by 80mm long with an average thickness of 0.42mm, and were equipped with strain gauges, cf. Figure 2. 12. The resulting tensile stress-strain curves are also presented in Figure 2. 12 up to the failure of the first copper braids which occurred at an average strain of 2.97%.

The analysis of the initial linear part of these curves allowed determining an average longitudinal elasticity modulus for the electrical cable: E_{11} = 19.5GPa associated to an elasticity limit of approximately 0.2%.

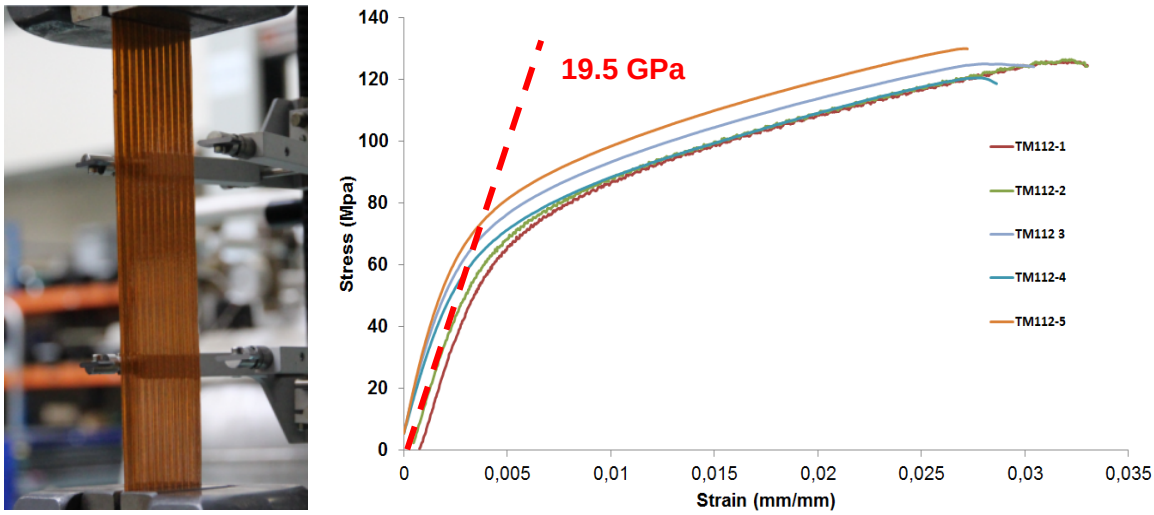

Figure 2. 12 Longitudinal tensile tests on the electrical cable

The highly nonlinear behaviour is mainly attributed to the complex nature and geometry of the electrical wires (braided geometry), which provide most of the stiffness under tensile load, cf Figure 2. 13.

While accurate characterisations of the mechanical behaviour of such a conductor do not enter in the frame of this work, it is easily imaginable that under tension phenomena such like friction between the copper strands, and re-organisation of the strands occur, thus leading to a highly nonlinear mechanical behaviour.

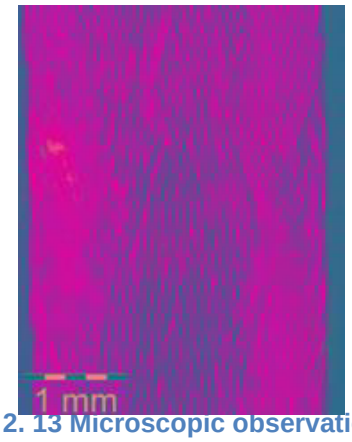

Figure 2. 13 Microscopic observation of a copper braid

4.2.2. Transverse direction

The test specimens were 45mm wide by 28mm in length with an average thickness of 0.42mm and the crosshead speed was set to 4mm/min.

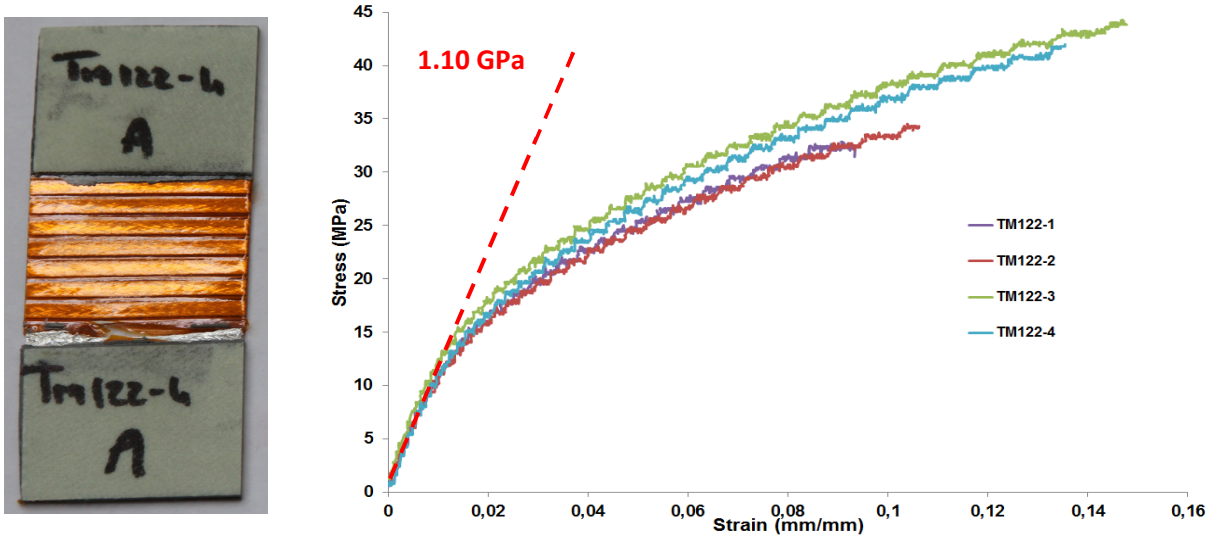

Figure 2. 14 Transverse tensile tests on the electrical cable

In the transverse direction, the stiffness is mostly provided by the polyimide jacket. The analysis of the initial linear part of stress-strain curves allowed determining an average transverse elasticity modulus for the electrical cable: E_{22} = 1.10GPa associated with an elasticity limit of approximately 0.1%.

4.2.3. Through-the-thickness direction

The purpose of this test is not to determine any proper elastic properties, but rather to determine the weakest interface among the multifunctional sandwich structure, cf. Figure 2. 15, and to start investigating on its behaviour under out-of-plane deformations.

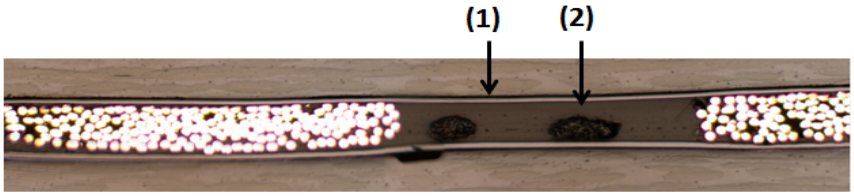

(1) Interface composite/jacket
(2) Interface jacket/insulator

Figure 2. 15 Interfaces within the multifunctional structure

The test specimens consisted in one layer of flat cable co-bonded to 1mm thick GFRP tabs according to the manufacturing process detailed previously. This assembly was then bonded to aluminium tabs with an epoxy structural adhesive on which the load was applied with a crosshead speed of 1mm/min. Picture of the test as well as the recorded force-displacement curves are presented in Figure 2. 16.

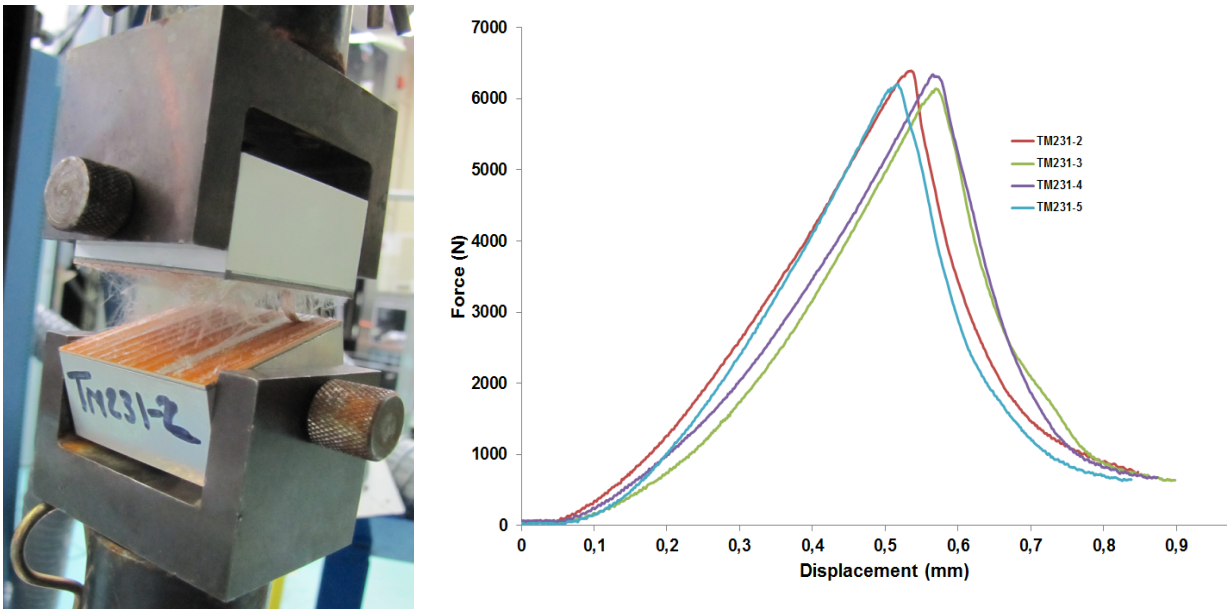

Figure 2. 16 Through-the-thickness tensile test

As shown by Figure 2. 16, the failure occurred inside the cable within the fluorocarbon resin (insulator). Therefore, the weakest interface is inside the cable itself, meaning that the out-of-plane mechanical behaviour of the electrical cable is mainly governed by the insulator. This observation will be further supported by the results of the short 3 point bend tests presented in the next chapter where it is shown that the orientations of the electrical wires inside the structure have no influence on the bending behaviour of the structure. Besides, it indicates that any out-of-plane loading submitted to the multifunctional structure is likely to degrade the insulation properties of the cable and lead to a decrease of its electrical performances. These issues are further addressed in the forthcoming chapters.

4.2.4. Mechanical properties of the flat electrical cable

Despite the highly non-linear behaviour of the cable and the relatively low elasticity limits, these observations motivated the following assumptions that were made to estimate the engineering elastic properties of the flat cables:

- The longitudinal and transverse elasticity moduli of the cable are set to E_{11}=19.5 GPa and E_{22}=1.1 GPa
- The in-plane shear modulus of the cable is computed from a rule of mixtures between the different components of the cable (insulator and jacket). This yields G_{12} = 0.43 GPa.
- The through-the-thickness elasticity modulus of the cable is equal to the elastic modulus of the insulator resin E_{33} = 0.48 GPa
- The out-of-plane shear moduli of the cable are equal to the shear modulus of the insulator resin G_{13} = G_{23} = 0.16 GPa
- The in-plane and out-of-plane Poisson's Ratios of the cable are taken equal to the Poisson's ratio of the jacket and insulator v_{12}=v_{13}=v_{23}=0.48.

E_{11} (GPa)	E_{22} (GPa)	E_{33} (GPa)	G_{12} (GPa)	G_{13} (GPa)	G_{23} (GPa)	ν_{12}	ν_{13}	ν_{23}
19.50	1.10	0.48	0.43	0.16	0.16	0.48	0.48	0.48

Table 2. 10 Mechanical properties of an electrical cable

At this stage, the engineering constants and elastic properties of the composite laminate and electrical cable are known. The modes of failure of the composite laminate are also assumed to be known from the literature [10], [11], [13]. What is unknown however, are the modes of electrical and mechanical failure of the electrical cable. Hence, before studying the modes of failure of the overall multifunctional structure, it appears necessary to investigate the failure modes of the electrical cable.

5. Critical defaults to the electrical performances of the electrical cable

It has been seen (cf. Chapter 1: Literature Review, section 3: Aerospace Wiring Practices) that the main defects affecting the electrical performances of aeronautical wires are short-circuits, broken cables, chafing, corrosion, connexion losses and insulation defects. Among the various causes of these wiring degradations, moisture, chafing, corrosion and chemical contamination are unlikely to occur with the multifunctional architecture presented previously due to the embodiment of the electrical cables within the composite structure. Nevertheless, other critical loadings remain, or appear due to this new wiring architecture. In particular, this work will focus on two types of electrical damage: broken wires and insulation defects (damage of the jacket and/or insulation).

Broken cables remain one of the critical scenarios to be avoided, and will occur due to excessive tensile strains on the electrical wires. In terms of electrical performances, this will induce an increase of the electrical resistance of the line, and ultimately a loss of data and power transmission.

Insulation defects also appear to be critical since it has been shown that the insulator resin is the weakest interface inside the multifunctional structure. Indeed, insulation properties within the multifunctional structure are both a key design criterion and a major concern since a loss of insulation between two wires is likely to result in significant reduction of the breakdown voltage, and ultimately in short-circuits and electrical arcing.

5.1. Broken wires

Under a longitudinal tensile test, the first wires break from a strain of approximately 3% (cf 4.2.1). From then, all load is distributed on the remaining copper braids which break progressively, followed by the polyimide tape, cf. Figure 2. 17 where the results of the tensile tests presented previously are shown.

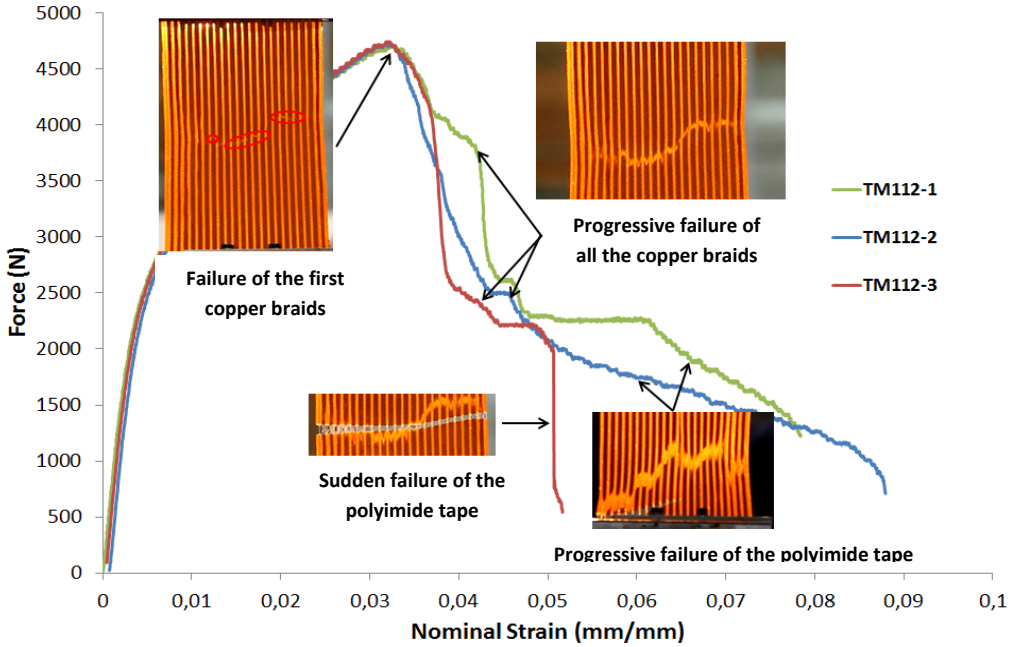

Figure 2. 17 Scenario of failure of the electrical cable under a longitudinal tensile test

The influence of this failure mode on the electrical performances of the cable has been characterised in terms of electrical resistance. Further investigations on the influence of such tensile strains on the electrical signal transmission are presented in Chapter 3.

Electrical resistance measurements were carried out with a 4-wire (Kelvin) resistance measurement setup, suited for measuring low resistances. The 4-wire measurement technique consists in applying a constant current of I=1A at the terminals of the device whose resistance needs to be measured, and to measure the resulting voltage across the device (for instance with a multimeter), cf. Figure 2. 18. Indeed, Ohm's law states that volts (V) equal current (I) times resistance (R): V=IR. Therefore, with a current of I = 1A, the voltage measured across the device is directly equal to the electrical resistance of the device. It also allows neglecting the resistance of the test cables and alligator clips.

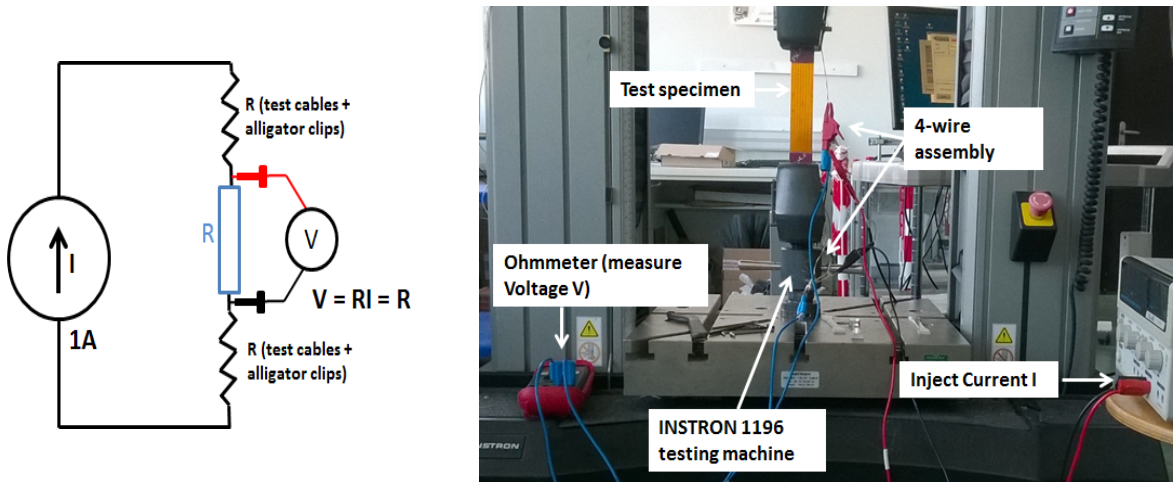

Figure 2. 18 4-wires (Kelvin) assembly for electrical resistance monitoring during a tensile test

Tensile tests were performed on the same INSTRON 1165 testing machine as presented previously, with a crosshead speed of 2mm/min. The test specimens were 250mm in length (including 50mm GFRP tabs on each extremity) and 40mm in width. Among the wires composing the electrical cable, only one was used for electrical resistance measurements. Three test specimens were used to monitor the electrical resistance as a function of the tensile strains. Among them, the two more representative results are presented in Figure 2. 19 below.

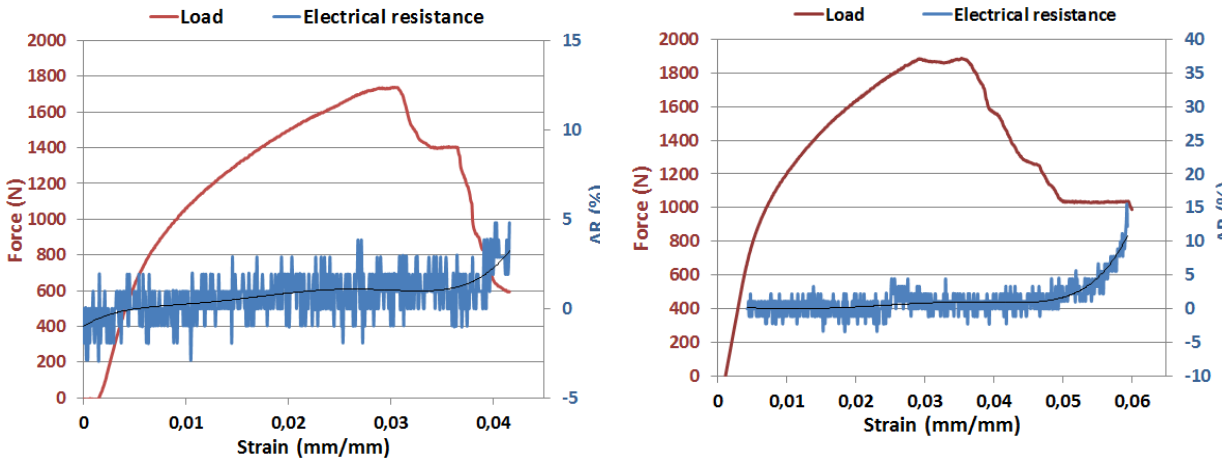

Figure 2. 19 Electrical resistance measurements during a longitudinal tensile test on an electrical cable

Figure 2. 19 shows that only a small resistance increase (<5%) is recorded before ultimate failure of the wire, which tends to show that the wire failure is quasi-brittle: most of the copper strands break simultaneously. Therefore, it is considered that under longitudinal tensile strains the mechanical and electrical failures of the cable occur simultaneously at 3% of strain (failure of the first copper braids).

5.2. Insulation defects

Insulation defects can be monitored with various testing methods such as insulation resistance, dielectric permittivity, and dielectric strength measurements. In this work, dielectric strength tests have been selected to characterise insulation defects within the electrical cables.

The dielectric strength of an insulating material is the maximum electric field that a pure material can withstand under ideal conditions without breaking down (i.e., without experiencing failure of its insulating properties).
Hence a dielectric strength test consists in measuring the breakdown voltage of a device under test while applying a differential of potential across the dielectric. A dielectric strength tester (also called hipot tester, flash tester, or high voltage tester) is used to measure this current. In this work, the system used for the measurements was a SEFELEC PR12NN with a maximum capacity of 12kV, cf. Figure 2. 20.

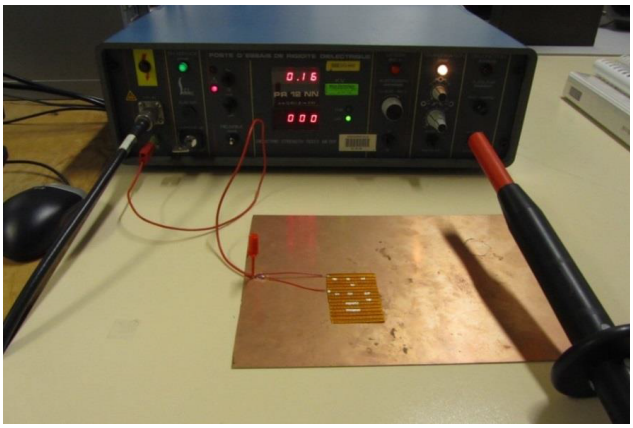

Figure 2. 20 Picture of the setup with the SEFELEC PR12NN dielectric strength tester at the back and sample at the front

5.2.1. Nominal breakdown voltage

The objective of this test was to measure the breakdown voltage between two copper braids (i.e the breakdown voltage of the insulator between two wires). Samples were prepared as shown in Figure 2. 21: the jacket was stripped in two locations so that one braid was connected to the SEFELEC PR12NN ground port via a soldered wire, and a second one was used to apply the voltage. The ends of the line were insulated with a Teflon adhesive rubber so as to avoid breakdown at the edges.

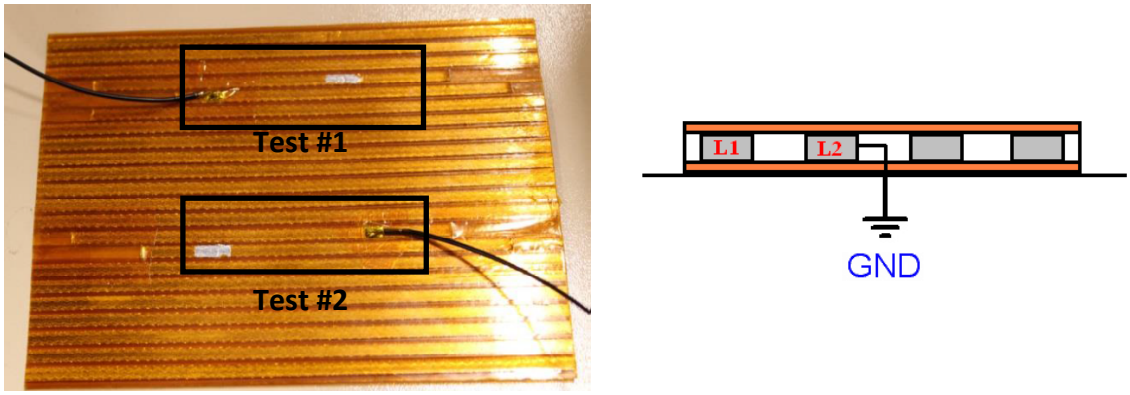

Figure 2. 21 Picture of a sample used to measure the breakdown voltage between two adjacent wires

The obtained breakdown voltages are listed in Table 2. 11.

	Test 1	Test 2	Test 3	Test 4	Test 5
Breakdown Voltage (kV)	11.68	>12	11.70	11.32	>12

Table 2. 11 Results of the dielectric strength tests on two adjacent braids

In all cases, electrical shorting occurred at the edges, for voltage higher than 11 kV and in two cases no breakdown was observed in the voltage range available with the SEFELEC PR12NN (0-12 kV). When breakdown occurred, it appeared at the ends of the line within the Teflon adhesive rubber. Hence, it is concluded that the flat cable is able to withstand at least 12kV insulation between every wires.

5.2.2. Breakdown voltage of a damaged cable

5.2.2.1. Adjacent wires

In order to investigate on the defaults that are likely to alter insulation properties of the electrical cable, a worst-case scenario has been considered where the insulation between two wires is removed, cf. Figure 2. 22. This insulation defect is then characterised through dielectric strength tests.

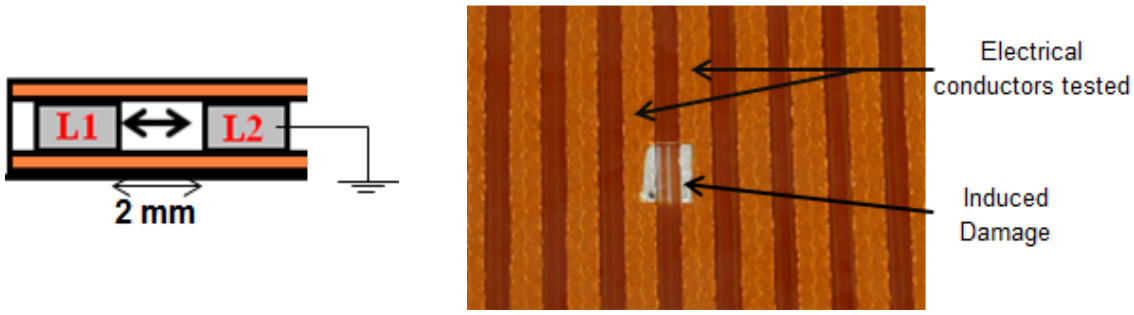

Figure 2. 22 Dielectric strength characterisation on damaged electrical cables

The test method and testing machine were identical to the dielectric strength characterisations presented previously. Results are listed in Table 2.11.

Test Specimens	Breakdown Voltage (kV)
Reference (cf. 5.1)	>12
Test specimen 1	6.35
Test specimen 2	4.17
Test specimen 3	3.24
Test specimen 4	7.91

Table 2. 12 Results of the dielectric strength characterisations on damaged electrical cables

The dielectric strength tests all resulted in a spark localized at the area where the jacket had been removed and accompanied by a drop of the breakdown voltage as low as 3.24kV. Hence, dielectric strength tests allow detecting insulation defects between adjacent wires.

5.2.2.2. Non-adjacent wires

Similar tests were conducted to estimate the influence of a defect on the insulation properties between two non-adjacent wires. The configurations investigated (3 test specimens per configurations were tested) are presented in Figure 2. 23.

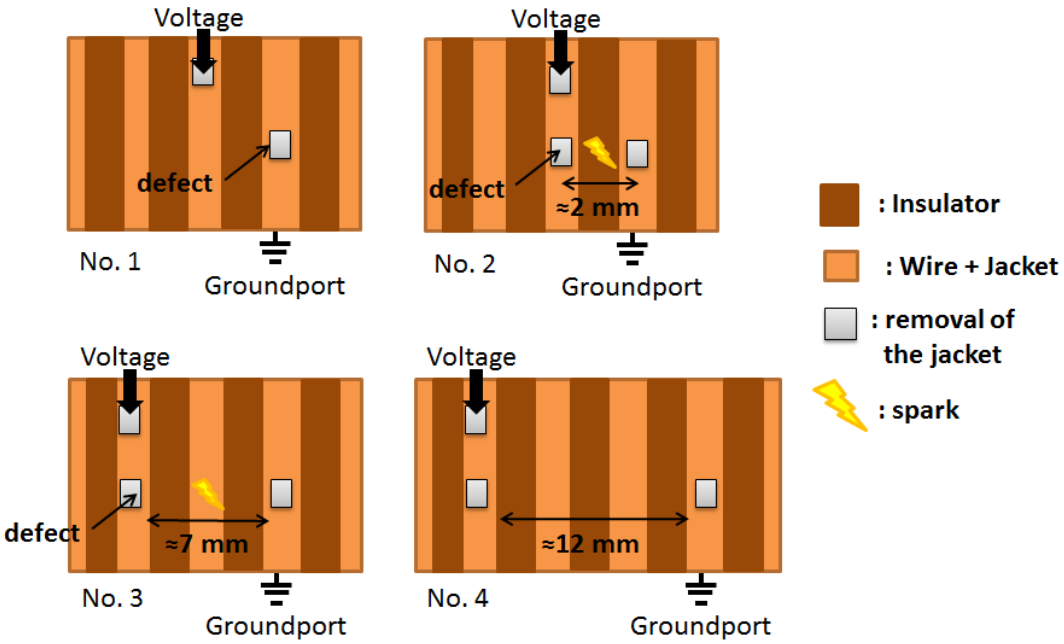

Figure 2. 23 Configurations investigated for the dielectric strength characterisation of non-adjacent wires on damaged electrical cables

Breakdown voltage occurred only for configurations No.2 (which corresponds to the case of adjacent wires presented previously) and No.3, respectively at an average voltage of approximately 6kV and 11kV. No breakdown occurred for configurations No.4 since the maximum capacity of the SEFELEC PR12NN test machine is 12kV. The results are listed in Table 2. 13.

	No.1	No.2	No.3	No.4
Test specimen 1	>12 kV	6.12 kV	11.41 kV	>12 kV
Test specimen 2	>12 kV	7.97 kV	>12 kV	>12 kV
Test specimen 3	>12 kV	6.34 kV	11.37 kV	>12 kV

Table 2. 13 Results of the dielectric strength characterisations on non-adjacent wires

5.2.3. Concluding remarks on insulation defects

These tests have shown that the electrical cable is able to withstand at least 11kV insulation between every wire. Besides, it showed that dielectric strength tests offer the opportunity to detect insulation degradation between wires, provided that the wires are not separated by more than 2 insulator sections. Hence, such characterizations will be used in the forthcoming chapters to investigate on the influence of out-of-plane mechanical loadings on the electrical performances of the embedded cables.

6. Concluding remarks

The multifunctional structure and its components have been presented. Some experimental and analytical tools have been used to characterise the mechanical properties of the host composite structure and flat electrical cable. These engineering properties will be further used for numerical purposes in the forthcoming chapters.

Tensile tests on the electrical cable revealed that structural and electrical failure of the cable occur simultaneously under a longitudinal tensile strain of approximately 3%. Through-the-thickness tensile testing unveiled that the insulator resin within the cable is the weakest interface of the structure. Therefore, it seems likely that out-of-plane mechanical loadings could induce insulation degradation within the cables, and lead to a loss of electrical performances. In addition, dielectric strength tests have been performed to estimate the insulation properties of the cables. It was also shown that this kind of test allows detecting insulation defects.

This drives the need for further testing on samples of the multifunctional structure to investigate on its robustness with regards to out-of-plane loadings. In particular, it appears mandatory to study not only the influence of such mechanical loadings on the damage modes of the structure, but also to investigate on their influence on the electrical performances of the embedded cables.

References

[1] ESA, 'ESCC Detail Specification No. 3901/001, Polyimide insulated wires and cables, Low frequency, 600V, -100 to +200°C'. Issue 3, Jan-1996.

[2] L. Liu, B.-M. Zhang, D.-F. Wang, and Z.-J. Wu, 'Effects of cure cycles on void content and mechanical properties of composite laminates', *Compos. Struct.*, vol. 73, no. 3, pp. 303–309, Jun. 2006.

[3] J. J. Crookston, A. C. Long, and I. A. Jones, 'A summary review of mechanical properties prediction methods for textile reinforced polymer composites', *Proceedings of the Institution of Mechanical Engineers, Part L: Journal of Materials Design and Applications*, vol. 219, p. 91, 2005.

[4] J. J. Crookston, W. Ruijter, A. C. Long, N. A. Warrior, and I. A. Jones, 'A comparison of mechanical property prediction techniques using conformal tetrahedra and voxel-based finite element meshes for textile composite unit cells', *Proc. Finite Elem. Model. Text. Text. Compos.*, pp. 26–28, 2007.

[5] M. Sherburn, 'Geometric and mechanical modelling of textiles', University of Nottingham, 2007.

[6] M. Sherburn, A. C. Long, I. A. Jones, and C. D. Rudd, 'TexGen: geometric modelling schema for textile composites', presented at the Proc. 8th Int. Conference on Textile Composites (TEXCOMP 8), Nottingham, UK, 2006, vol. Paper T19.

[7] P. D. Craig and J. Summerscales, 'Poisson's ratios in glass fibre reinforced plastics', *Composite Structures*, vol. 9(3), pp. 173–188, 1988.

[8] H. J. Kim and C. C. Swan, 'Voxel-based meshing and unit-cell analysis of textile composites', *International Journal for Numerical Methods in Engineering*, vol. 56, pp. 977–1006, 2003.

[9] A. Dixit, H. S. Mali, and R. K. Misra, 'Unit Cell Model of Woven Fabric Textile Composite for Multiscale Analysis', *Procedia Eng.*, vol. 68, pp. 352–358, 2013.

[10] T. Lisle, C. Bouvet, M. L. Pastor, P. Margueres, and R. Prieto-Corral, 'Damage assessment of thin woven composite subjected to quasi-static tensile loading using infrared thermography', in *Proceedings of 15th European conference on composite materials, Venice, Italy*, 2012.

[11] N. K. Naik, Y. C. Sekher, and S. Meduri, 'Damage in woven-fabric composites subjected to low-velocity impact', *Compos. Sci. Technol.*, vol. 60, no. 5, pp. 731–744, 2000.

[12] D. Gay, *Matériaux Composites*, 5th ed. Paris: Lavoisier, 2005.

[13] M. Asaad, 'Damage Accumulation in Hybrid Woven Farbic Composites', Bournemouth University, 2002.

[14] E. Jacquet, F. Trivaudey, and D. Varchon, 'Calculation of the transverse modulus of a unidirectional composite material and of the modulus of an aggregate. Application of the rule of mixtures', *Compos. Sci. Technol.*, vol. 60, no. 3, pp. 345–350, 2000.

[15] M. A. Mbacke, 'Caractérisation et modélisation du comportement mécanique des composites tressés 3D: Application à la conception de réservoirs GNV', Ecole Nationale Supérieure des Mines de Paris, 2013.

Chapter 3 : Influence of the embodiment of flat electrical cables on the mechanical behaviour and damage modes of a composite laminate

Chapter 3 : Influence of the embodiment of flat electrical cables on the mechanical behaviour and damage modes of a composite laminate

1. Tensile tests 68

1.1. Composite Laminate 68

1.2. Composite laminate with embedded cable 70

1.3. Concluding remarks on the tensile tests 71

2. Quasi-static Short 3 Point Bend Tests 71

2.1. Host Composite Structure 72

2.2. Multifunctional Structure 74

2.3. Comparison with the Timoshenko beam theory 76

2.4. Concluding remarks on the quasi-static S3PB tests 78

3. Dynamic Short 3 Point Bend Tests 78

4. Impact tests 87

4.1. Host Composite Structure 87

4.2. Multifunctional Structure 89

4.3. Concluding remarks 91

5. Post-impact electrical performances 92

Concluding remarks 95

The integration of electrical devices and functional layers inside composite structures causes a geometric discontinuity which is likely to weaken the host laminate's structural performances, in particular in the transverse direction. Actually, a few studies can be found in the literature about the effect of embedded devices on the structural performances of composite laminates [1]–[3]. Most of the time, such investigations consist in performing mechanical tests under tensile and/or flexural loading to study the effects of the embodiment on the structural stiffness and strength of a composite structure [4]–[6]. In particular, adhesion and interface strength between the embodiment and the composite host structure play a major role in maintaining not only good out-of-plane properties such as inter-laminar shear strength and compression properties [2], but also tensile properties up to an optimum [3].
What is at stake is to ensure that neither structural failure of the composite, nor failure of the embedded electrical conductors can occur within the lifespan of the structure. Therefore, such investigations need to be completed with in-situ or post-tests electrical measurements.
This chapter deals with such investigations. It especially focuses on the damage modes of the structure under out-of-plane loadings (bending, impact). To start with, the influence of the embodiment of a cable on the tensile behavior of a composite laminate is characterized through quasi-static tensile tests. Then, the bending behavior of the multifunctional structure is characterized under quasi-static short 3 point bend tests (S3PB) which is expected to ease the understanding of the response of the structure under impact loadings. Dynamic bending tests and drop-weight impact tests are finally performed on both the composite laminate and on multifunctional test specimens. The post-impact electrical performances of the embedded cables are characterized through dielectric strength tests and reveal electrical insulation degradation within the embedded cables due to the impact event.

Such considerations allow addressing the following issues:

- What is the influence of the embodiment of a flat electrical cable on the mechanical behavior and damage modes of a composite laminate?
- What are the critical mechanical loadings and damage mechanisms as regards to the electrical performances of the embedded cables?

1. Tensile tests

Quasi-static tensile tests were performed on an INSTRON 1196 testing machine with a load capacity of 250kN at a crosshead speed of 2mm/min. Two kinds of test specimens were manufactured according to the process detailed in Chapter 2 so as to compare the strength and stiffness of a quasi-isotropic layup of the composite laminate $[(-45,0,45,0,-45,0)]_s$, cf. Figure 3. 1(a), with a composite laminate embedding an electrical cable, cf. Figure 3. 1 (b).

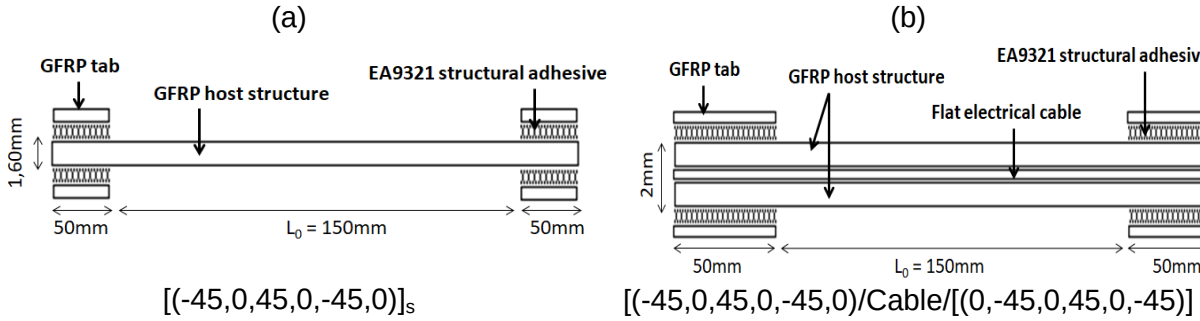

$[(-45,0,45,0,-45,0)]_s$ $[(-45,0,45,0,-45,0)/Cable/[(0,-45,0,45,0,-45)]$

Figure 3. 1 Schemes of the tensile test specimens

In addition, the embedded cables were equipped with soldered wires (one per electrical wire in the cable) which were connected to an electrical connector board and luminous diodes, cf. Figure 3. 2. There was one luminous diode per electrical wire to allow monitoring the electrical signal transmission of every wire during the test.

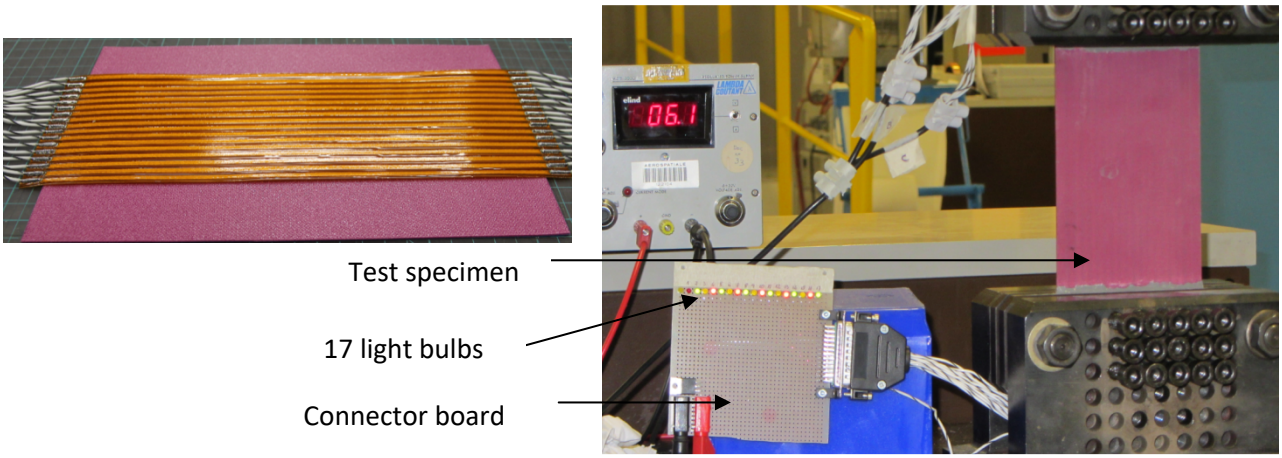

Figure 3. 2 Monitoring of electrical transmission during a tensile test

1.1. Composite Laminate

Results of the tensile tests performed on 4 quasi-isotropic layups of the composite laminate are presented in Figure 3. 3. Every test specimens exhibited a brittle failure.

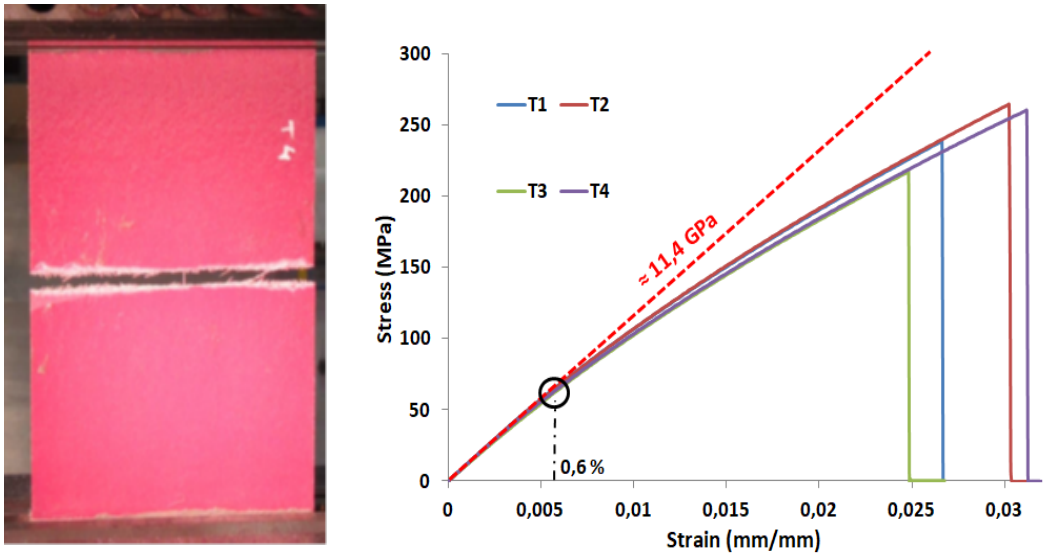

Figure 3. 3 Results of the tensile tests performed on a quasi-isotropic layup

The stress-strain curves show a good reproducibility in terms of modulus (≈11.4GPa). Yet, test specimens T1 and T3 failed prematurely between the jaws of the test machine, hence the average ultimate tensile stress and strain were only calculated based on the two test specimens T2 and T4. This yielded an average ultimate tensile strain of 3.1% and average ultimate tensile strength of 255MPa.

A non-linear behaviour is observed from a strain of approximately 0,6%. This is attributed to geometric and material nonlinearities of the yarns and surrounding matrix, in particular in the 45° plies due to shear softening (and failure) of the matrix in the yarns [7], and friction effects [8]. In addition, transverse tensile failure of the matrix in the fill of the 0° plies is known to occur on such woven fabric composites [9]. Indeed, when a tensile load is applied on the warp fibre bundle, it induces local bending deformations on the weft fibre bundle, and ultimately, crack initiation on the tensile side of the weft bundle, cf. Figure 3. 4.

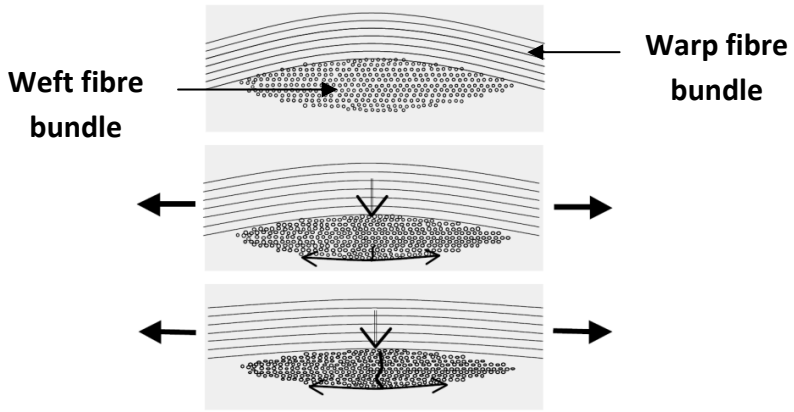

Figure 3. 4 Transverse tensile failure of the matrix in the weft bundle under tensile loading of a warp bundle [9]

1.2. Composite laminate with embedded cable

The results of the tensile tests performed on the same composite layup, embedding a flat electrical cable are presented in Figure 3. 5. Among the test specimens tested, TX2 exhibited failure between the jaws. The others TX1-3 and 4 exhibited simultaneous brittle failures of both the composite laminate and embedded cable. This observation was further confirmed by the observations of the electrical monitoring system. Indeed, the luminous diodes were lit during the whole duration of the tests, and all turned off when the ultimate failure occurred. This indicates that the electrical signal transmission is not altered before structural failure of the composite laminate occurs.

In terms of stiffness and strength, the average ultimate tensile stress and strain of the composite laminate embedding an electrical cable were computed based on the three test specimensTX1, TX3 and TX4. This yielded 224MPa and 3.2% respectively. In addition, an elastic stiffness of 11.9GPa was determined up to an elongation of 0.2%.

Therefore, the embodiment of an electrical cable reduced the ultimate tensile stress down by approximately 12%, and induced further nonlinear behaviour. This was expected as the electrical cable showed a highly nonlinear behaviour under tension (cf. Chapter 2). On the contrary, no noticeable influence on either the elastic stiffness, or the ultimate tensile strain was observed.

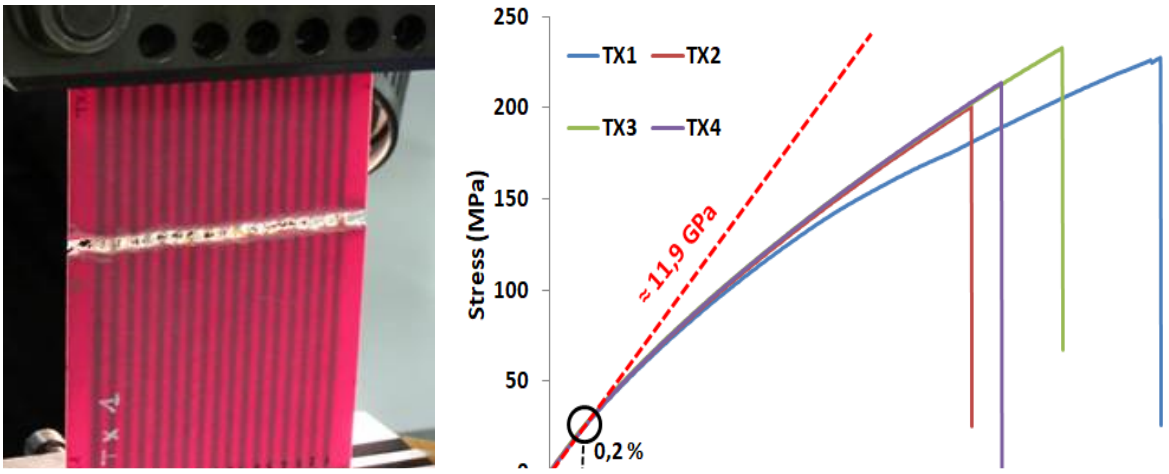

Figure 3. 5 Results of the tensile tests on a composite laminate embedding an electrical cable

These experiments showed that under tension, there are no risks of electrical failure (in terms of electrical signal transmission and electrical resistance, cf. Chapter 2) before structural failure. Nonlinear effects are predominant, especially due to the nonlinear behaviour of both the electrical wires (complex braided structure) and composite material.

1.3. Concluding remarks on the tensile tests

Quasi-static tensile loads do not appear to be critical to the electrical performances of the structure, especially since electrical failure does not occur before structural failure of the host composite structure.

2. Quasi-static Short 3 Point Bend Tests

This section investigates on the influence of the integration of two flat electrical cable on the damage and mechanical behaviours of the composite laminate under short 3 point bend tests. This is expected to pave the way for a better understanding of the structure behaviour under impact loadings where inter-laminar shear strains are expected to be critical.

Experimental results on test specimens with and without embedded cables are compared. The architecture of the multifunctional structure is presented in Figure 3. 6 and presents a thickness of approximately 5,6mm. As a reminder, the manufacturing process provided a ply thickness of approximately 0.125mm.
So as to compare the bending behaviour of this assembly with a reference composite structure, composite plates composed of 45 plies with a layup $[(0/45)_{11}/0/(45/0)_{11}]$ were manufactured with an identical manufacturing process. This resulted in composite test specimens approximately 5,6mm thick.

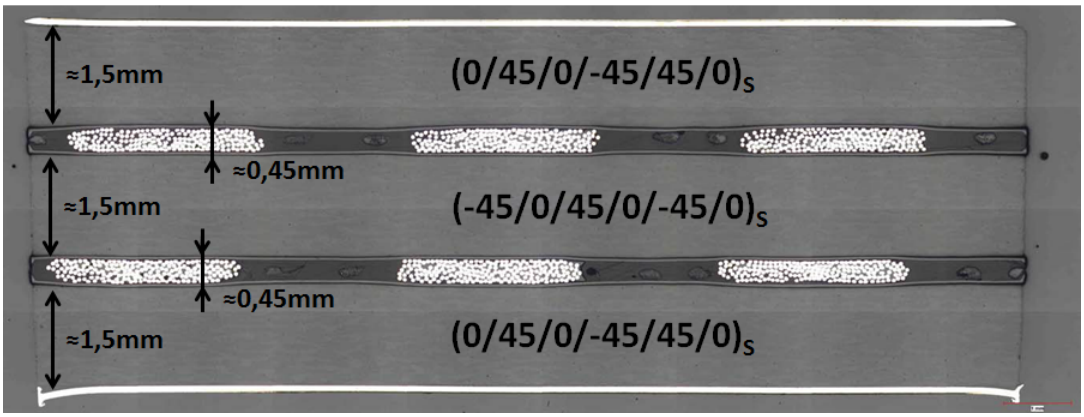

Figure 3. 6 Microscopic observation of the composite laminate embedding two electrical cables

As much as possible, the short 3 point bend tests (S3PB) were carried out according to the normative reference ISO14130 which is used for the determination of the apparent interlaminar shear strength of fibre-reinforced plastic composites by the short beam method. Hence, the width of the test specimens is chosen as 5 times the thickness and the length as 10 times the thickness as specified in the test method. Besides, the electrical wires were either oriented in the transverse, or longitudinal direction to investigate on their influence on the bending stiffness of the structure.

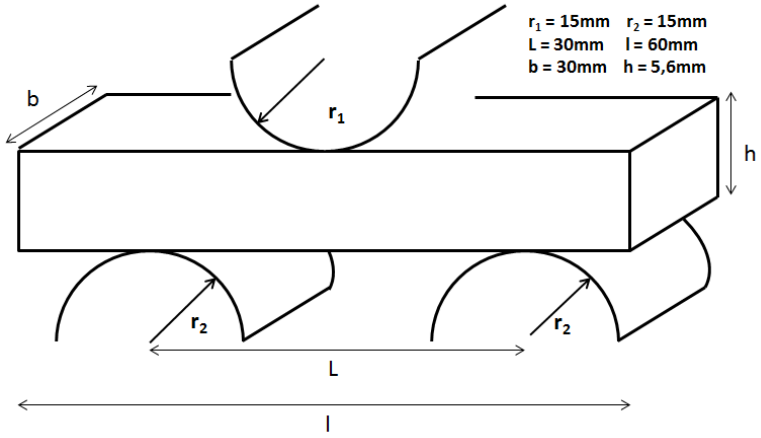

Figure 3. 7 Configuration of the Short 3 Point Bend Tests (S3PB)

Two test specimens per configuration and three blank test specimens were used: reference test specimens (x3), transverse multifunctional test specimens (x2) and longitudinal multifunctional test specimens (x2).

	Reference (FDV1)	Reference (FDV2)	Reference (FDV3)	Transverse (Trans1)	Transverse (Trans2)	Longitudinal (Long1)	Longitudinal (Long2)
h (mm)	5,62	5,64	5,64	5,61	5,58	5,60	5,62
b (mm)	29,7	30,4	30,4	31,9	29,7	30,1	29,9
l (mm)	61,2	60,6	60,6	60,3	60,5	60,2	61,1

Table 3. 1 Short 3 Point Bend Tests - Test specimens dimensions



(a)



(b)

Figure 3. 8 Picture of (a) a transverse multifunctional S3PB test specimens and (b) a longitudinal S3PB multifunctional test specimen

The choice has been made to perform these tests at iso-thickness between the various samples. Yet, one must keep in mind that the flexural rigidity of the multifunctional test specimens is 16% lower than the flexural rigidity of the reference (composite) samples as detailed in section 2.3 of the present chapter.

2.1. Host Composite Structure

Short 3 point bend tests results (load-displacement curve) of the reference test specimens FDV1 and FDV2 are presented in Figure 3. 9 and Table 3. 2.

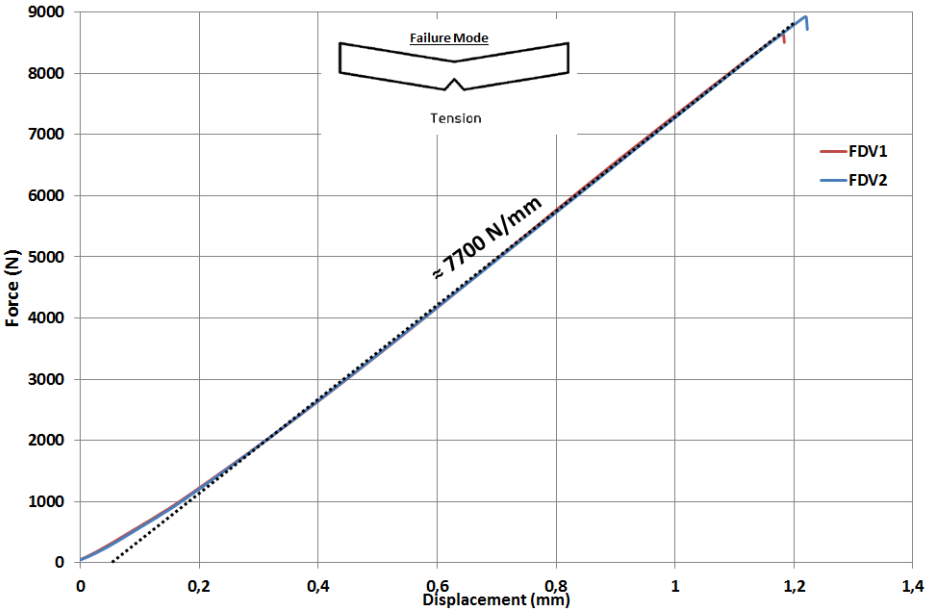

Figure 3. 9 Short 3 Point Bend Tests Results - Reference test specimens

Both curves are almost identical, with a maximum load of approximately 8,750N, a maximum displacement of approximately 1.22mm, and an overall linear behaviour up to failure with a bending stiffness of 7,700N/mm. Failure occurred on the side under tension, cf. Figure 3. 10.

	Maximum Load (N)	Maximum Displacement (mm)
FDV1	8,600	1.20
FDV2	8,900	1.25

Table 3. 2 Results of the S3PB tests on the reference test specimens



Figure 3. 10 Post Short 3 Point Bend Test picture of the blank test specimen FDV2

Test specimen FDV3 was tested under charge/discharge loadings with increments of 1,500N, cf. Figure 3. 11 in order to compare to the results of the short 3 point bend tests on the multifunctional test samples, presented hereafter.

Small hysteresis loops are observed and indicate energy-dissipative mechanisms which increase with increasing load. This may witness friction between the test specimen and the test machine supports, or creep and damage mechanisms within the composite structure (viscosity of the matrix or friction between the warp and weft fibres, and fibre/matrix debonding [10]). In particular, the back face of the test specimen is loaded under tension (where failure occurs) and such a quasi-isotropic layup is known to exhibit a nonlinear behavior under tension (cf. Chapter 2, 1.1), especially due to the 45° plies.

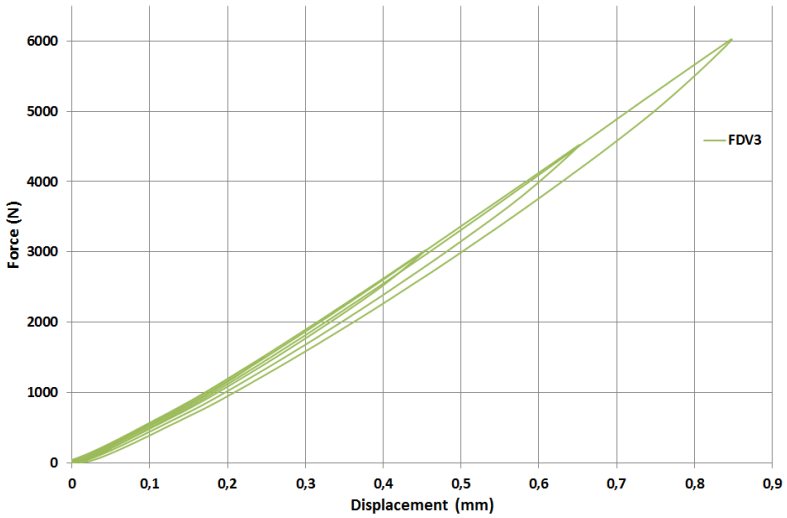

Figure 3. 11 Charge/Discharge S3PB force-displacement curve – Blank test specimen

2.2. Multifunctional Structure

The results of the short 3 point bend tests on the multifunctional test specimens are presented in Figure 3. 12. For comparison purposes, the force-displacement curve of the reference test specimen FDV3 was also plotted. These tests were also performed under charge/discharge conditions with increments of 1,500N.

The first observation that can be drawn is the highly non-linear behaviour of the multifunctional test specimens as compared to the blank test specimens. Indeed, the hysteresis loops are much bigger than the ones observed previously. This underlines the presence of other energy-dissipative mechanisms, apart from the damage mechanisms inherent to the composite structure or to the contacts between the test specimens and the test machine. In particular, it is worth mentioning that inter-laminar shear strains occurring within the embedded cables could be visually seen during the test.

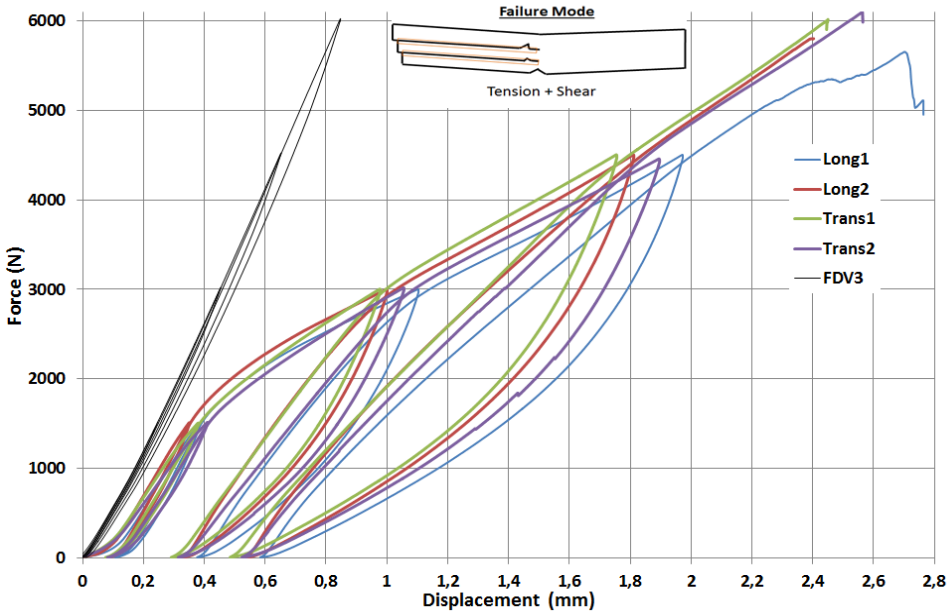

Figure 3. 12 Short 3 Point Bend Test results - Multifunctional test specimens

These inter-laminar shear strains were also revealed through Digital Image Correlations (DIC), cf. Figure 3. 13 where a qualitative measure of the inter-laminar strains is presented for a displacement of the crosshead of d=0.5mm and d=2.0mm. Measuring accurately the deformations of such samples under DIC is challenging, especially due to the heterogeneity of the cables. It appears that the inter-laminar strains within the cables reach approximately 8.0% at the onset of slipping/debonding (displacement of the cross-head of 0.5mm).

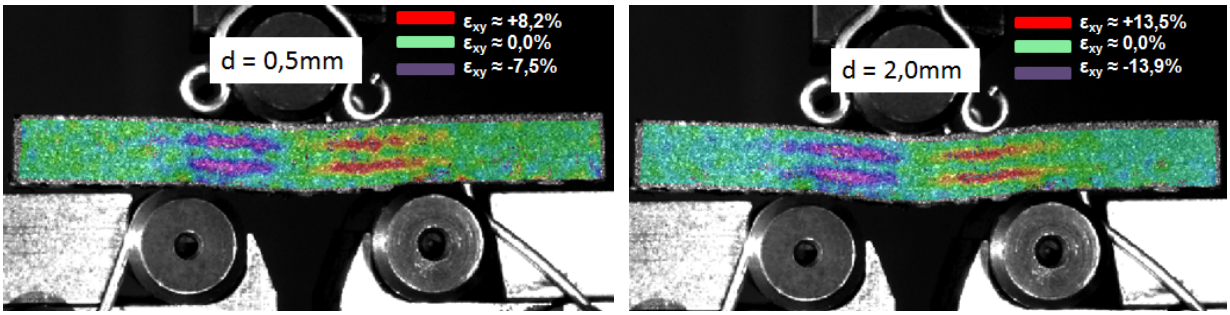

Figure 3. 13 Interlaminar shear strains εxy observed through DIC on a multifunctional test specimen under S3PB test

Hence the embodiment of the two electrical cables results in a highly discontinuous load transfer between the three composite layups and in a highly non-uniform distribution of the shear stresses through the thickness of the test specimen.
As a consequence, tensile strains and stresses arise on every bottom composite plies interfacing with the embedded cables. Ultimately, this results in internal tension- shear fibre failure of those composite plies, as depicted in Figure 3. 14.

It is further noticed that as compared to the reference composite test specimens, the maximum displacement is significantly increased (by approximately 100%) and the maximum load significantly decreased (by approximately -30%), cf. Table 3. 3.

	Maximum Load (N)	Maximum Displacement (mm)
Trans1	5,991	2.44
Trans2	5,912	2.36
Long1	5,360	2.44
Long2	5,841	2.40

Table 3. 3 Results of the S3PB tests on the multifunctional test specimens

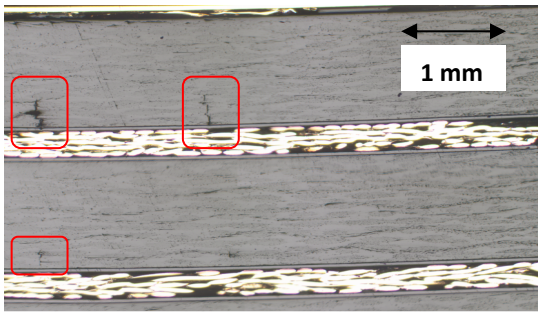

Figure 3. 14 Tensile-shear failure of the composite plies at the interface with the embedded cables and on the back face

The second main observation that can be drawn is the non-influence of the orientation of the wires on the mechanical response of the structure. This further confirms the assumption that the out-of-plane strains are mainly transmitted through the insulator resin within the cables. Indeed, this is consistent with the observation made on Chapter 2 (section 4.2.3) where

through-the-thickness tensile tests revealed that the weakest interface within the structure was the insulator resin.

2.3. Comparison with the Timoshenko beam theory

In order to get further insights into the bending behaviour of the structure, the Timoshenko beam theory will be used to analytically predict and compare the bending stiffness of the reference composite and multifunctional composite test specimens with the experimental data.

Hence, Figure 3. 15 below presents the experimental bending stiffness of the multifunctional test specimens determined from the initial linear part of the force-displacement curves. It is noticed that after the first loading cycle, the bending stiffness decreases at each loading cycle with a knee point appearing for smaller loads. The initial bending stiffness of the composite beams embedding two layers of flat electrical cable varies between 5,000 and 6,000 N/mm which is lower than the bending stiffness of the reference composite beams which was measured at 7,700 N/mm.

	Long 1	Long 2	Trans 1	Trans 2
S_1 (N/mm)	5200	5800	5300	5000
S_2 (N/mm)	5700	6000	5500	5200
S_3 (N/mm)	5000	5000	4700	4500
S_4 (N/mm)	4400	4800	4300	4150

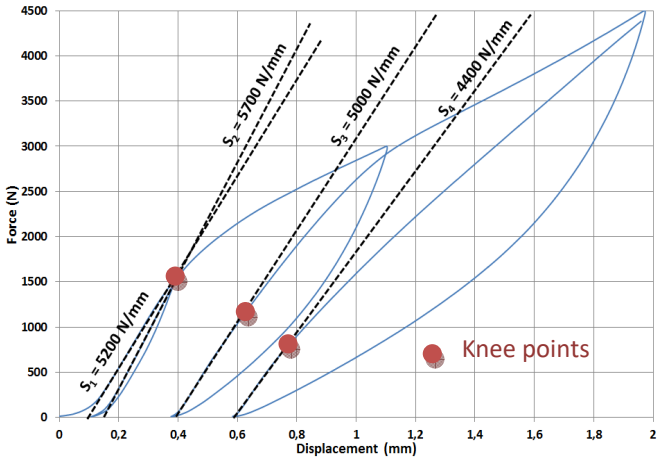

Figure 3. 15 Measurements of the bending stiffness of the multifunctional test specimens under S3PB tests

The Timoshenko beam theory expresses the total deflection of a beam (Δ) under 3 point bending as a sum of flexural (Δ_f) and shear (Δ_s) deformations, cf. Figure 3. 16. In the contribution of the shear deformations, Timoshenko introduced a shear area factor (k) and originally proposed that k=3/2 [11]. Since then, many investigations have been performed to predict the influence of the transverse shear deformations on the deflection and flexibility of a beam [11]–[14] and a value of k=6/5 is the value widely used today.

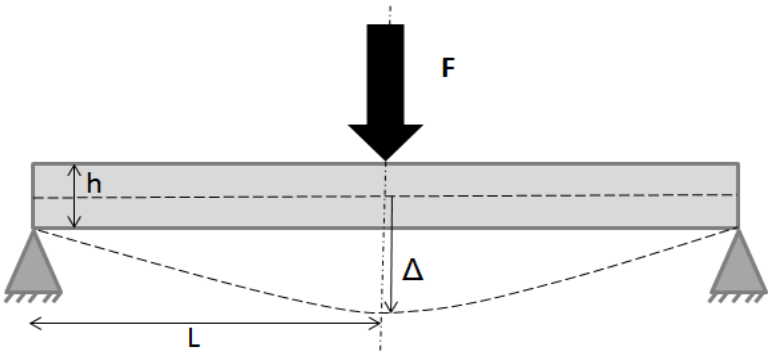

$$\Delta = \Delta_f + \Delta_s = \frac{FL^3}{6\langle EI\rangle} + \frac{FL}{2}\frac{k}{\langle GS\rangle}$$

$$K_s = \frac{F}{\Delta}$$

K_s: Bending stiffness
F: load at midspan
Δ: Deflection of the beam
$\langle EI\rangle$: Flexural Rigidity
$\langle GS\rangle$: Shear rigidity
k: shear correction factor

Figure 3. 16 Scheme of the S3PB tests used in the Timoshenko Beam Theory

As the wires seemed to have no influence on the bending stiffness of the assembly, two values of the cables stiffness (denoted as the core stiffness E_c) were assumed when calculating the flexural rigidity <EI> of the multifunctional test specimens, cf. Figure 3. 17. The flexural rigidity is computed considering the sum of the equivalent flexural rigidity of the facings and core according to their own centroidal axis (first and second term). In addition, the stiffness of the two external faces and core about the centre of the beam are also added using the parallel axis theorm (third and fourth term). The equivalent shear rigidity of the beam is simply the sum of the shear stiffness of each cross section: <GS> = $3*G_p*S_p$ + $2*G_c*S_c$.

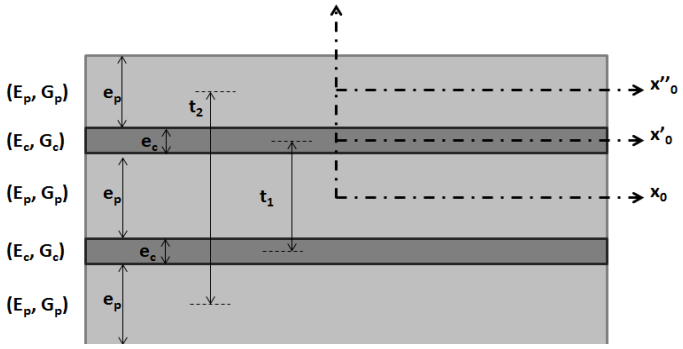

$$< EI > = 3E_p\frac{be_p{}^3}{12} + 2E_c\frac{be_c{}^3}{12} + 2E_c be_c(\frac{t_1}{2})^2 + 2E_p be_p(\frac{t_2}{2})^2$$

Figure 3. 17 Scheme of the sandwich multifunctional structure and associated flexural rigidity

The core stiffness was first taken equal to E_c=19,5GPa (as determined through tensile tests, cf. Chapter 2), and then to E_c=0,48GPa (which corresponds to the elastic modulus of the insulator resin). Yet, both assumptions resulted in an over-estimate of the bending stiffness, cf. Table 3. 4. On the contrary, the bending stiffness of the reference test specimens is well correlated with the experimental bending stiffness.

	Experimental (Reference Composite)	Timoshenko (Ref. Composite)	
Ks (N/mm)	7,700	7,750	
	Experimental (Multifunctional Composite)	Timoshenko (Multifunctional Composite)	
Ks (N/mm)	5,325	With E_c = 19.5 GPa	7,000
		With E_c = 0.48 GPa	6,500

Table 3. 4 Comparison between the experimental and analytical bending stiffness under S3PB condition

An explanation to these results resides in the assumption of the shear area factor, taken equal to 6/5. This value is commonly used to account for the non-uniform shear stress distribution through the thickness of isotropic beams under bending [15], [16]. If this value is well-suited for the reference composite beam, it is likely that it is under-estimated in the case of the multifunctional test specimens where the contribution of the shear deformations to the total deflection of the beam is expected to be much higher. In addition, it has been observed through DIC that the embodiment of the two cables induces significant gradients in the distribution of the shear strains across the thickness of the beam.

It is found that increasing the shear area factor up to 2.7 yields a bending stiffness of the multifunctional test specimens of 5,330 N/mm, in better agreement to experimental data. With such a shear correction factor, shear strains contribute to more than 30% of the total deflection of the beam. As a comparison, they only account for 15% of the total deflection of the reference composite test specimens. These considerations are only qualitative as accurately determining the shear area factor of a sandwich composite beam is a challenging task [14], [15]. This will be further developed in Chapter 5 of the present dissertation where the influence of the temperature on the bending stiffness of a sandwich structure is investigated by taking a temperature-dependent shear area factor into account.

2.4. Concluding remarks on the quasi-static S3PB tests

Test specimens have been compared at iso-thickness, knowing that the reference samples (only composite) have a flexural rigidity <EI> of 5.27×10^6 N.mm² and the multifunctional samples have a flexural rigidity of 4.42×10^6 N.mm² (16% lower).

In the light of experimental and analytical considerations under short 3 point bend tests, it has been observed that the embodiment of the two cables:

- Reduces the maximum load and bending stiffness by approximately -30%
- Leads to a highly non-uniform shear stress distribution through the thickness of the test specimens. To account for these shear effects in the Timoshenko beam theory, a shear correction factor of 2.7 was used. This resulted in a contribution of the shear deformations to the total deflection of the beam two times higher in the presence of electrical cables as compared to the reference composite test specimens.
- Induces tensile strains on the composite plies at the upper interface with the embedded cables, which leads to internal damage in the form of tension-shear fibre failure.

3. Dynamic Short 3 Point Bend Tests

This section presents dynamic bending tests performed on similar both blank and multifunctional test specimens. Dimensions of the test specimens were identical to the ones

presented previously (width of 30mm, thickness of 5,6mm) and the distance between the bottom support was kept at 30mm.

3.1. Test setup

To perform such dynamic bending tests, a specific impact bending test setup was designed, cf. Figure 3. 18. The setup was directly mounted on an Imatek IM10-30 drop-weight impact tester with two screwed connectors. Impactor and cylindrical test supports had cylindrical heads of 10mm diameter, and the impactor total weight was 11,07 kg.

Impact energies were chosen based on the damage threshold which is considered as the impact energy at which first ply failure occurs on the back face of test specimens: this resulted in impact tests between 12Joules and 13Joules. As the weight of the impactor was kept constant (m=11,0kg), these energies were achieved by adjusting the height of the impactor. For instance, to obtain an impact energy of 12 Joules with a mass of 11,0kg the height of the striker needs to be at 0,11m. This is determined thanks to (Eq.3.1) and (Eq.3.2) which links the impact velocity V_0 to the kinetic energy E, the weight of the impactor m, the height of the striker z_0, and the gravitational constant (g=9,81m.s^{-2}).

$$E = \frac{1}{2} m V_0^2 \qquad \text{(Eq.3.1)}$$

$$V_0 = \sqrt{2 g z_0} \qquad \text{(Eq.3.2)}$$

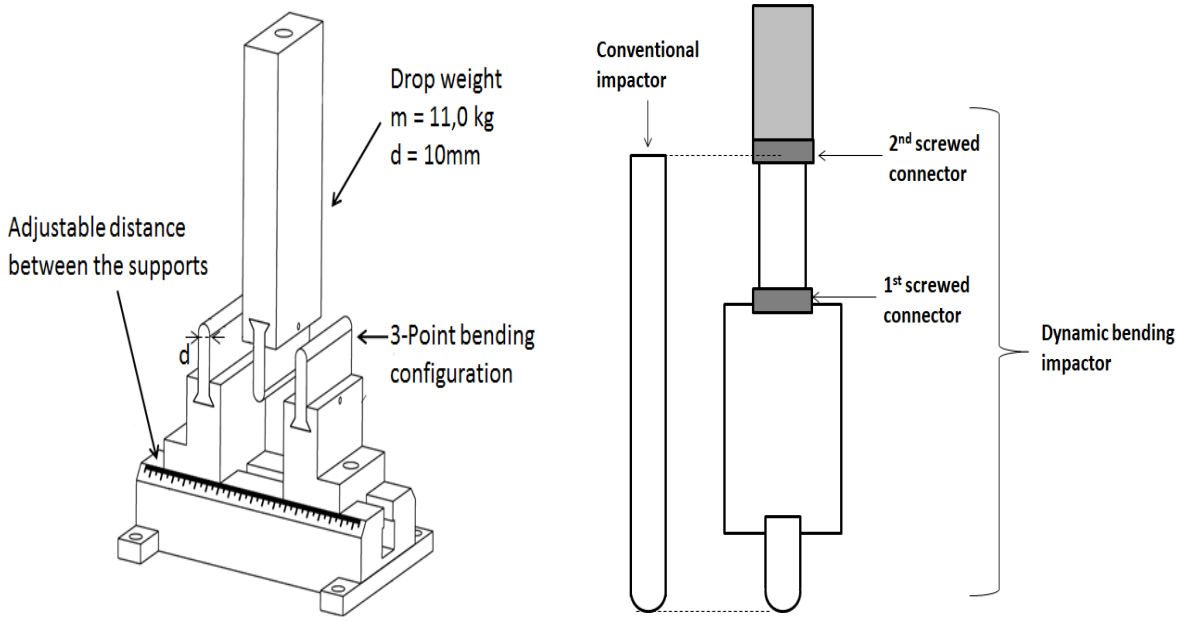

Figure 3. 18 Dynamic bending test setup

In addition, this test setup allows observing the side of the test specimens during impact event and performing Digital Image Correlations [17]. Hence, the test specimens were painted with a stochastic pattern composed of black dots on a white background and illuminated via two lighting systems. The impact events were recorded in 2D via a ultra-high speed camera at 12,000 pictures/sec from the side section of the specimens and post-treated with the software VIC 3D.



Figure 3. 19 Dynamic Bending Test Setup

In the literature, such test setups are not often encountered as impact analysis of composite laminates are mainly performed on fully clamped specimens during drop weight impact tests [18]–[22]. Yet, some studies deal with the study of the dynamic flexural behaviour of woven composites [17], [23], [24]. Such a configuration is especially expected to provide a better understanding of the influence of boundary conditions on the dynamic response of the structure [25], and to allow performing Digital Image Correlations (DIC).

3.2. Results of the dynamic bending tests on blank test specimens

3.2.1. Contact force history

The contact force history of 4 blank test specimens impacted at 12J are presented in Figure 3. 20 below. Several periodic load drops are observed and occur approximately every 0.85 to 0.90ms but are not associated with any damage mechanisms.

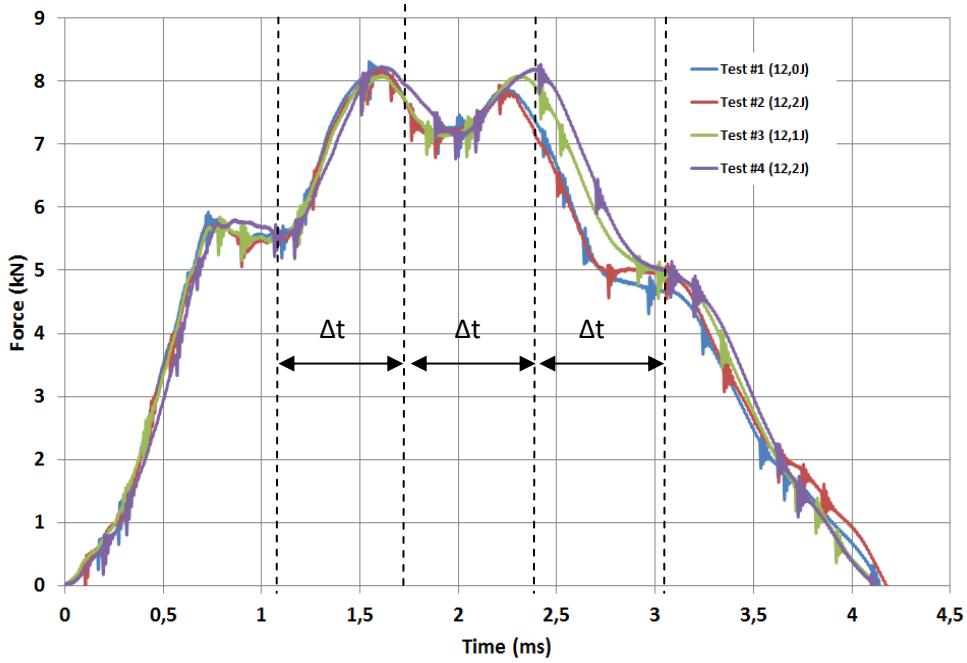

Figure 3. 20 Contact force histories of 4 blank test specimens showing periodic oscillations with Δt≈0,8-0,9ms

Indeed, visual observations and digital image correlations (shown latter) did not reveal any significant damage mechanisms apart from ply failure on the back face of the test specimens at the peak contact force, cf. Figure 3. 21.

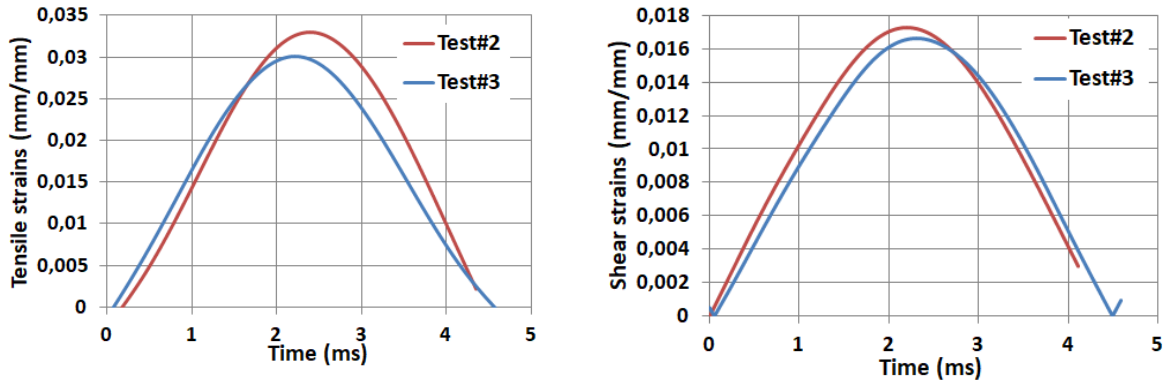

(a) (b)

Figure 3. 21 (a) Maximum tensile strains and (b) maximum shear strains as a function of time on blank test specimens

Several complementary tests were performed on various specimens, including metallic test specimens and they all revealed these instabilities with the same periodic oscillations at intervals of 0.80 to 0.90ms. In addition, these discontinuities do not occur when the conventional impactor (spherical impactor normally used with the Imatek IM10-30 impact tester) is mounted on the drop weight tower, cf. Figure 3. 18.

These observations are further supported by the two FFT diagrams plotted in Figure 3.21. They correspond to the FFT diagrams of two accelerometers placed on the impactor (accelerometer 2) and near the force sensor of the drop weight tower (accelerometer 1). It is observed that the measure near the force sensor is much more disturbed than the signal of the second accelerometer, and exhibit three resonance peaks at approximately 610Hz, 830Hz and 1,070Hz. This last frequency corresponds to the periodic oscillations observed in the contact force histories. Hence, these discontinuities seem to be an artefact of the measuring system and are most likely due to instabilities and impedance discontinuities between the newly developed impactor and the drop weight tower on which it is mounted through the two screwed connectors.

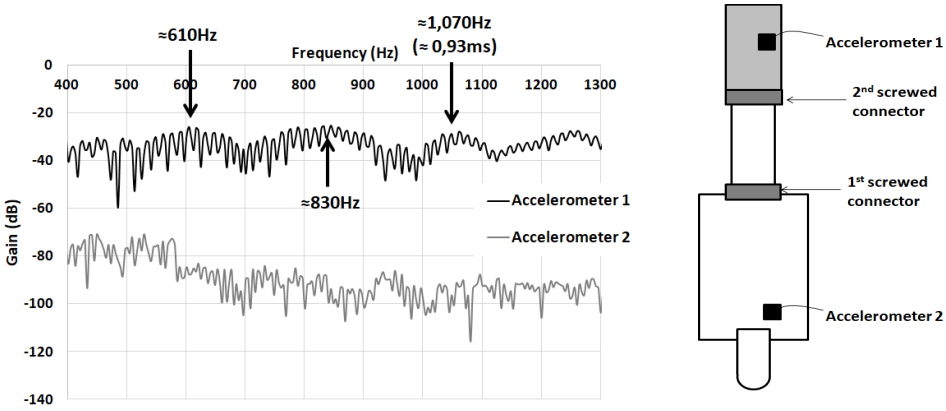

Figure 3. 22 FFT diagrams of the two accelerometers No.1 and No.2

3.2.2. Force-displacement curves

As a consequence, the force-displacement curves presented below were plotted “piece-by-piece” to reproduce as accurately as possible the expected experimental measurements. For comparison purposes, the force-displacement curves of the quasi-static short 3 point bend test specimens was also plotted. In general, a good correlation is found between the dynamic and quasi-static results in terms of stiffness and peak contact force. From 0 to 0.6mm the load seem to be non-homogeneously distributed across the surface of the test specimens due to a non-parallelism and thickness variations. Due to the uncertainties in the recorded data, further comparisons would be senseless. The test specimens all failed under tension (ply fracture on the back face) apart from test specimen No.1 which did not exhibit any significant signs of failure.

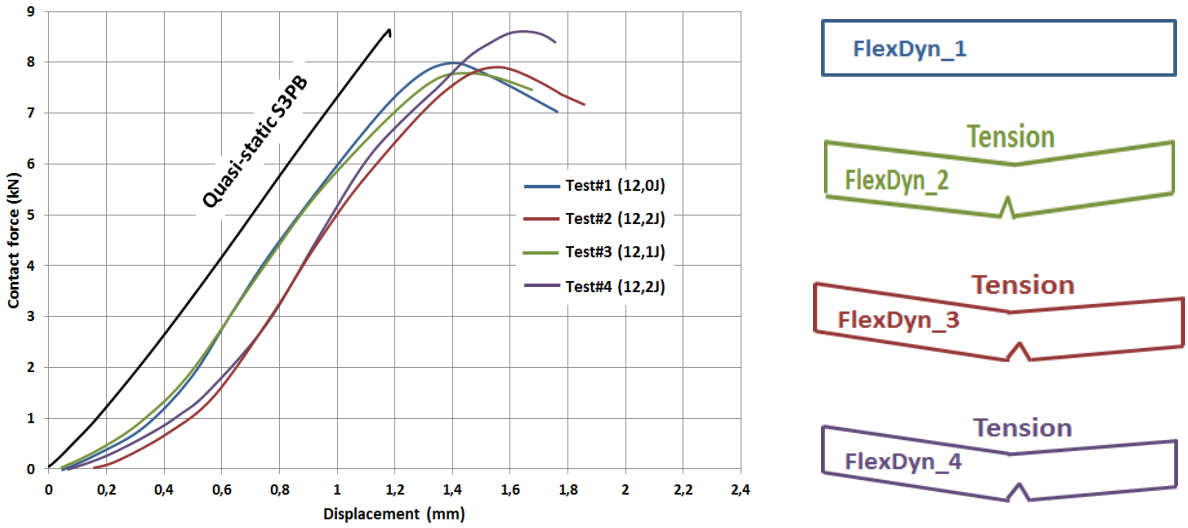

Figure 3. 23 Contact force-displacement curve and failure modes of the blank test specimens under dynamic bending at 12J

3.2.3. Digital Image Correlations

Results of the Digital Image Correlations (DIC) analyses are also consistent with the observations made during the quasi-static short 3 point bend tests as a tensile strain of approximately 3.2% is measured on the back face of the test specimens, cf. Figure 3. 24, at the moment of failure.

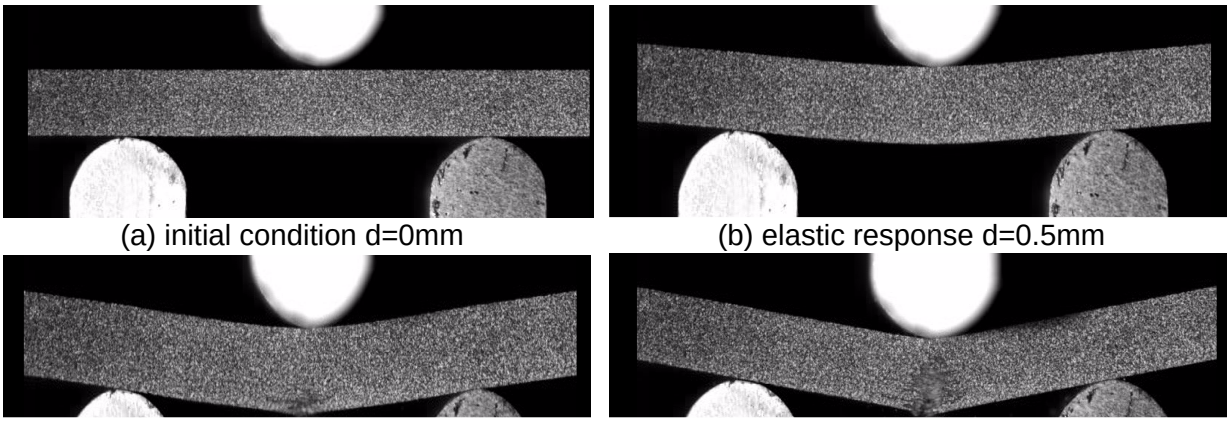

(a) initial condition d=0mm (b) elastic response d=0.5mm

(c) first ply failure d=1.4mm (d) total failure of the test specimen d=1.6mm

(e) Interlaminar shear strains at d=1.4mm (f) Tensile strains at d=1.4mm

Figure 3. 24 Failure scenario and DIC of the blank test specimens under dynamic bending

3.3. Multifunctional Structure

The dynamic bending tests on the multifunctional test specimens were performed with the cables oriented in the transverse direction: the wires were oriented perpendicular to the length of the test specimen, in the direction of the high-speed camera.

3.3.1. Force-displacement curves

The force-displacement curves of the dynamic bending tests performed on the multifunctional tests specimens are presented in Figure 3. 25 up to the peak contact load and compared with the experimental data of the quasi-static short 3 point bend tests presented previously. It is interesting to note that the damage threshold occurred between 13J and 14J (impact energies at which tensile failure occurred on the back face), which is slightly higher than the energy required for the blank test specimens.

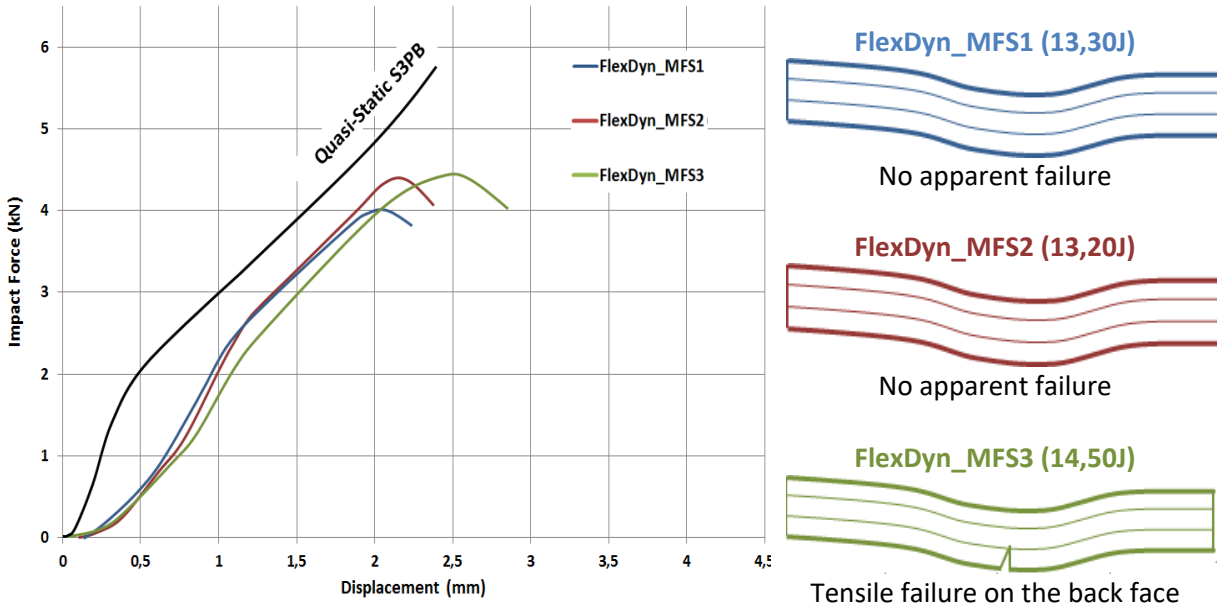

Figure 3. 25 Contact force-displacement curve and failure modes of the blank test specimens under dynamic bending at 12J

Similarly to the quasi-static measurements, the force-displacement curves can be divided into two parts: the initial loading up to slipping/cohesive damage within the cables, and loading up to ultimate failure. Similarly to the blank test specimens, the experimental load-displacement curve seem to be altered due to a non-homogeneous distribution of the load up to 1.0mm.

3.3.2. Digital Image Correlations

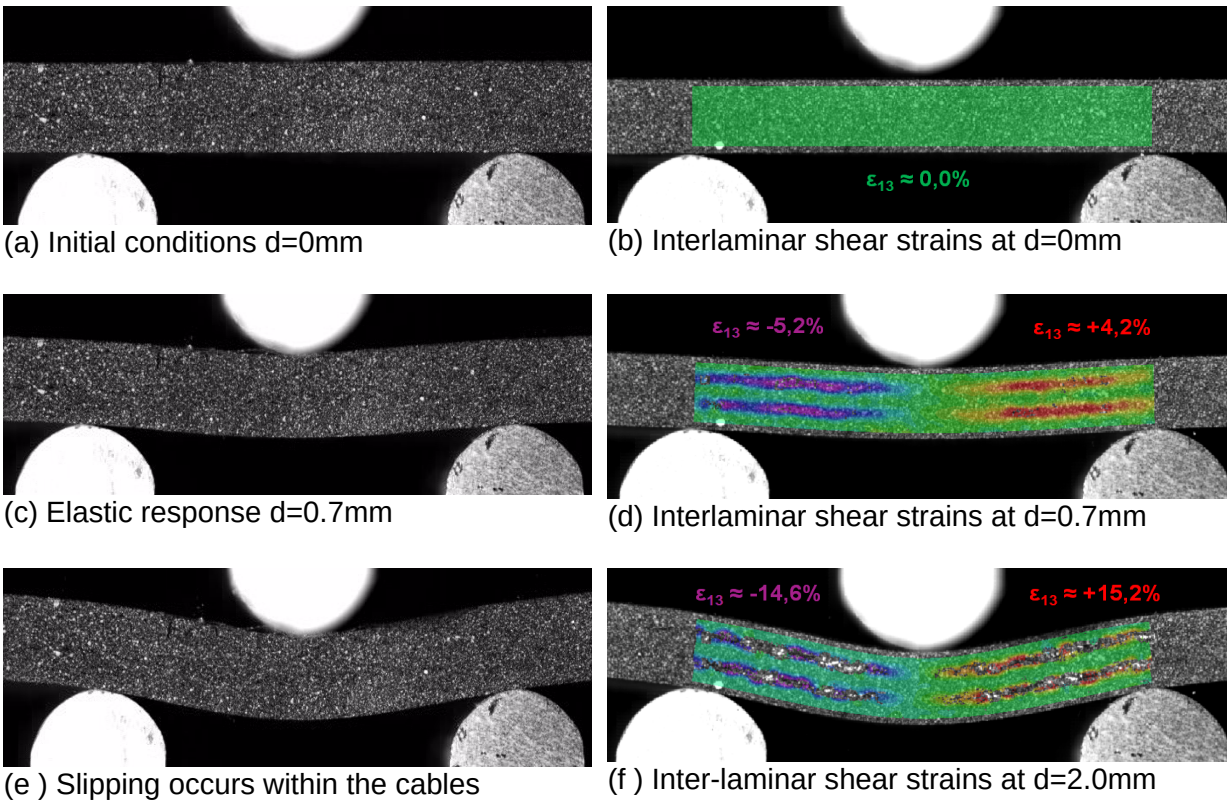

(a) Initial conditions d=0mm

(b) Interlaminar shear strains at d=0mm

(c) Elastic response d=0.7mm

(d) Interlaminar shear strains at d=0.7mm

(e) Slipping occurs within the cables

(f) Inter-laminar shear strains at d=2.0mm

Figure 3. 26 Digital Image Correlations on a multifunctional test specimen under dynamic bending

Tensile strains on the back face of the test specimens are recorded and plotted in Figure 3. 27 (a). Ply fracture on the back face occurred on test specimen No.3 under a tensile strain of 3,0 to 3,5%.

Inter-laminar strains within the cables versus time (the most representative data were selected) are also plotted in Figure 3. 27 (b) even though their measurements was challenging due to the heterogeneity of the cables and the initiation of decohesion. It shows an increase of the inter-laminar shear strains up to approximately 10% before reaching a plateau between 10 and 14%.

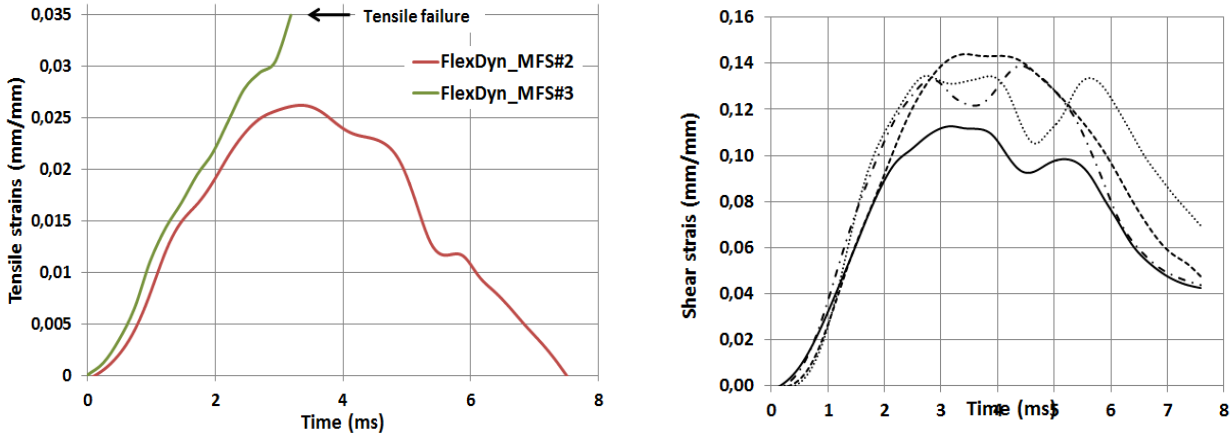

(a) (b)

Figure 3. 27 (a) Maximum tensile strains (back face) and (b) maximum shear strains (cables) as a function of time on multifunctional test specimens

In addition to ply fracture on the back face and slipping/decohesion within the cables that could be visually observed, post-test microscopic observation revealed the same kind of internal fibre failures as observed on the quasi-static short 3 point bend tests, cf. Figure 3. 28. Indeed, without occurrence of ply fracture on the back face, fibre failure could be observed on the composite plies at the interface with the upper cable. Figure 3.28 also reveals clear debondings between the wires that were not observed on the quasi-static test specimens.

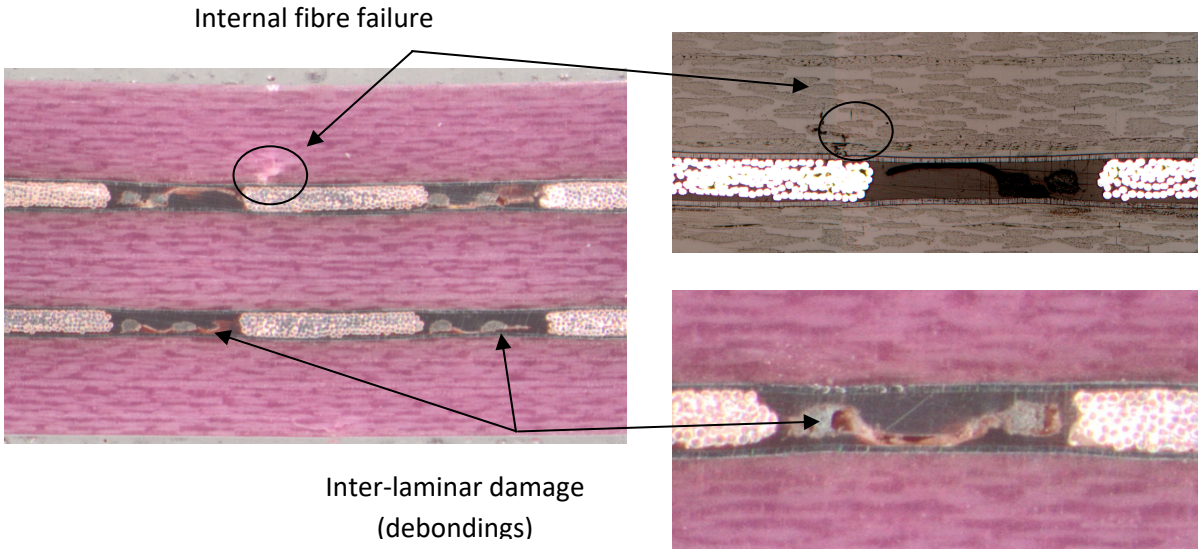

Figure 3. 28 Post dynamic bending microscopic observations of a multifunctional test specimen impacted at 10J

Therefore, at lower impact energies two main damage mechanisms are observed:

- Debonding within the cables between the wires
- Fibre failure within the composite plies at the upper interface with the embedded cables

These data are expected to ease the analysis and understanding of the impact behaviour of the structure under conventional impact test conditions, as presented hereafter.

4. Impact tests

Drop weight impact tests were performed on 60x60mm² test specimens pneumatically clamped to the fixture by means of circular grips, cf. Figure 3. 29. These tests were conducted with a constant impact mass of 9.067kg at impact energies of 10J, 15J and 20J.

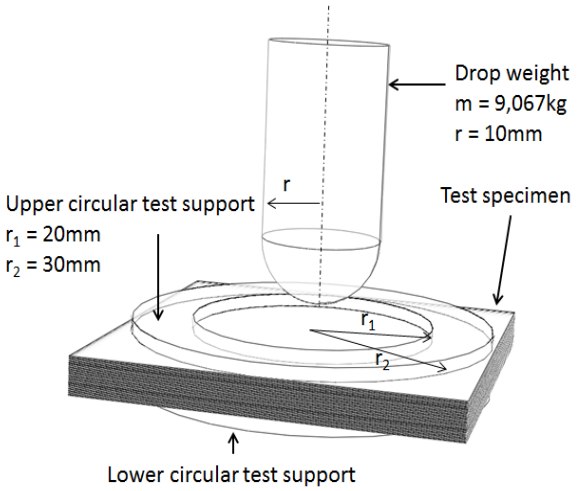

Figure 3. 29 Drop weight impact test setup

4.1. Host Composite Structure

The contact force history of three test specimens impacted at 10J, 15J and 20J is plotted in Figure 3. 30. At 10J and 15J the curves exhibit a dome shape, while at 20J a more severe discontinuity appears at approximately 1,2ms.

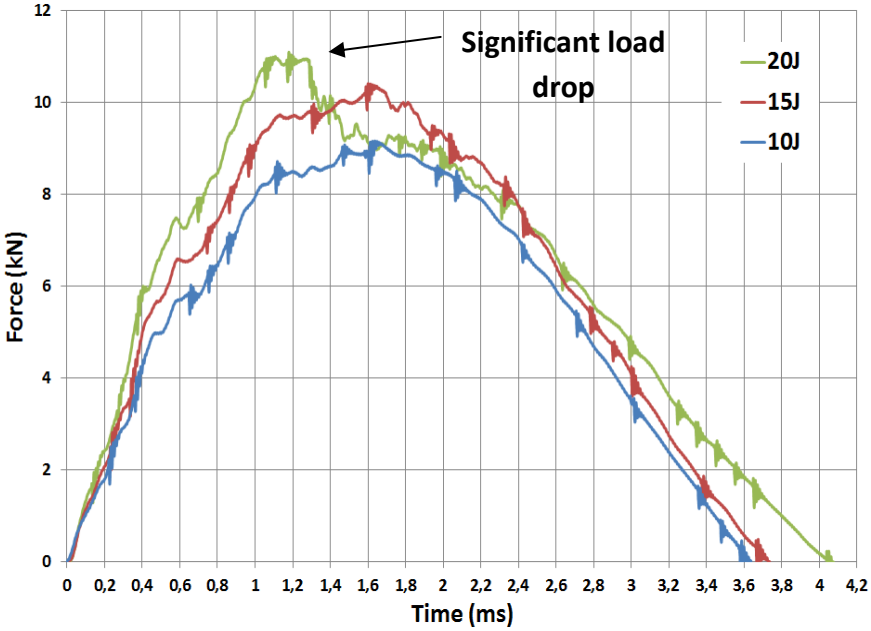

Figure 3. 30 Contact force history of the blank test specimens submitted to drop weight impacts between at 10J, 15J and 20J

In addition, it turns out that the impact response (contact force history and damage mechanisms) observed is very similar to what is described in the work of Xiao, et al. [19] where thick laminates have been impacted with a similar impactor and boundary conditions.

Indeed, as depicted in Figure 3. 31, a bi-linear behaviour can be deduced from the contact force history, where the initial linear behaviour (slope K_e) is followed by a slight drop and another linear behaviour (with a slope K_d and $K_d<K_e$ indicating losses of flexural and shear stiffness). This is likely to be associated with local matrix cracks followed by initiation of delamination in a ring shape through the thickness of the laminates as observed in Figure 3. 32. Indeed, delamination initiation is mainly due to high transverse shear which are localized around the impact zone, hence resulting in a ring shape and propagating through the laminate due to the transverse shear loading. Once the delamination has propagated, fibre failure begins to occur on the back face of the test specimens at 15J and 20J.

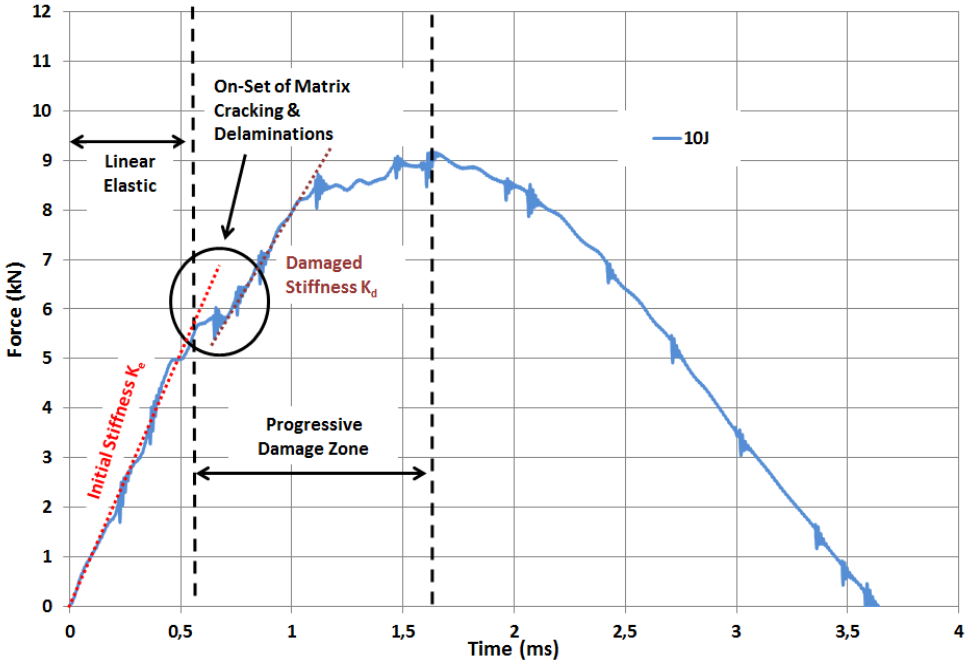

Figure 3. 31 Analysis of the contact force history

Post-impact microscopic observations did not reveal any visible damage for the test specimens impacted at 10J. On the contrary, cracks and delaminations could be noticed on the bending area (back face) of the test specimens impacted at 15J and 20J, as described in [26]. Delaminations through the thickness of the laminate are clearly visible at 20J.

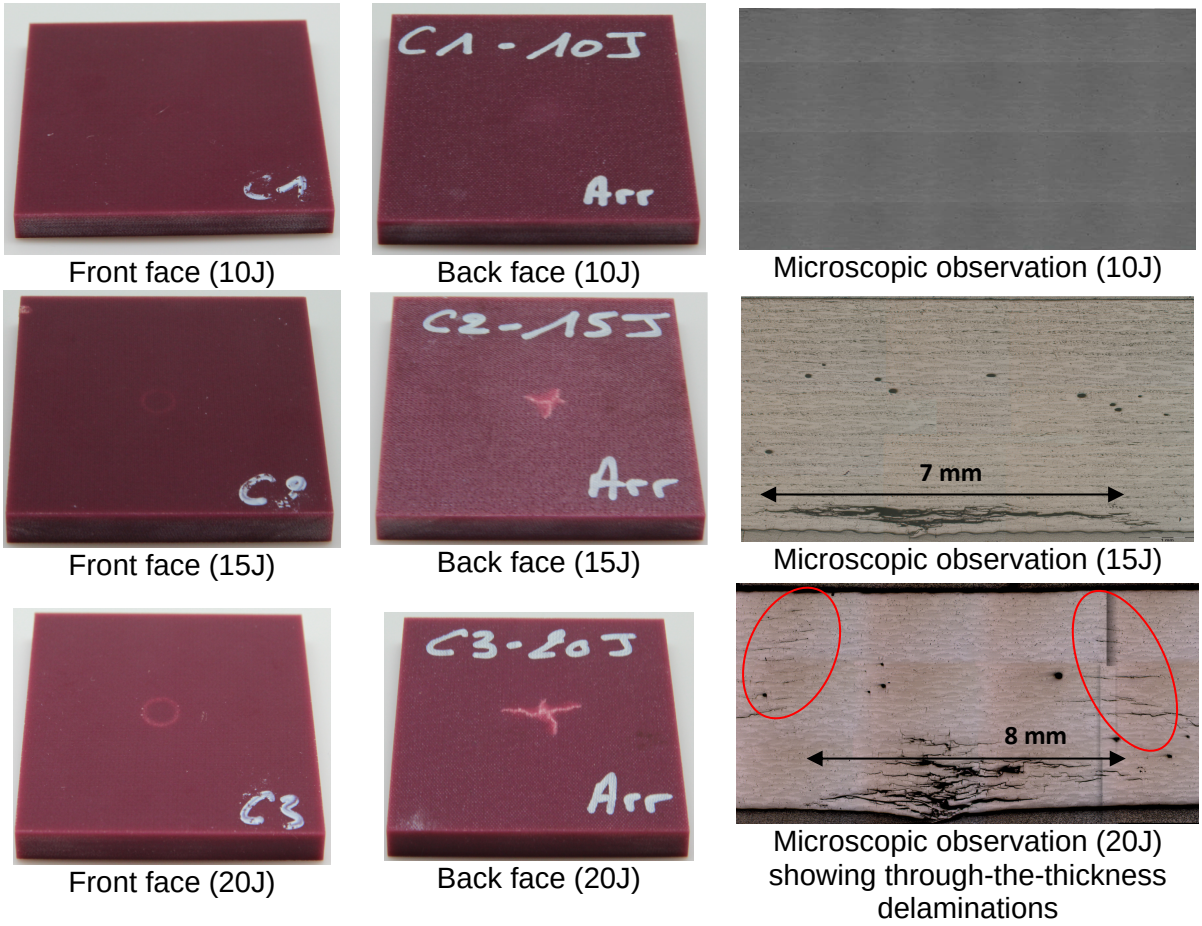

Front face (10J) | Back face (10J) | Microscopic observation (10J)

Front face (15J) | Back face (15J) | Microscopic observation (15J)

Front face (20J) | Back face (20J) | Microscopic observation (20J) showing through-the-thickness delaminations

Figure 3. 32 Pictures of the front faces, back faces, and post-impact microscopic observations of the blank test specimens

Hence, the main damage modes identified are:

- Delamination initiation & propagation through-the-thickness of the laminate
- Fibre tension and shear failure on the back face

4.2. Multifunctional Structure

The contact force history of three test specimens with two layers of embedded cables impacted at 10J, 15J and 20J are plotted in Figure 3. 33. As compared to the test specimens without embedded cables, these test specimens show a much more dissipative behaviour with lower peak contact forces and higher impact durations.

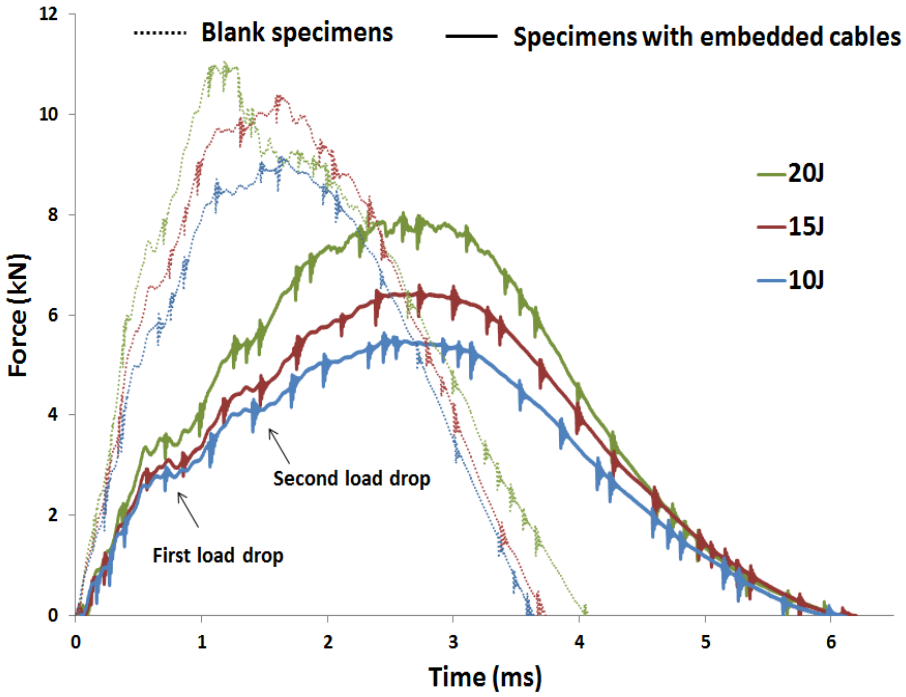

Figure 3. 33 Comparison between the contact force histories of the multifunctional and blank test specimens impacted at 10J, 15J and 20J

In particular, the multifunctional test specimens seem to exhibit a tri-linear behaviour (similarly to the bilinear behaviour observed previously), with two noticeable load drops. This tri-linear behaviour is most probably associated to both slipping and inter-laminar damage among the two embedded cables (as was observed during quasi-static short 3 point bend tests), and to initiation of matrix cracking and delamination among the host composite structure as observed previously.

As regards to the damage mechanisms, up to 15J no external damage can be visually detected either on the front face (no ring shape), nor on the back face (no ply fracture) of the test specimens, cf. Figure 3. 34. Yet, microscopic observations revealed fibre breakage inside the test specimens, at the interface with the embedded cables, as depicted by Figure 3. 34. These fibres failures are perpendicular to the embedded cables, oriented towards the impact location. At higher impact energies, ply fracture and delaminations occur on the back face, similarly to what was observed on the blank test specimens.

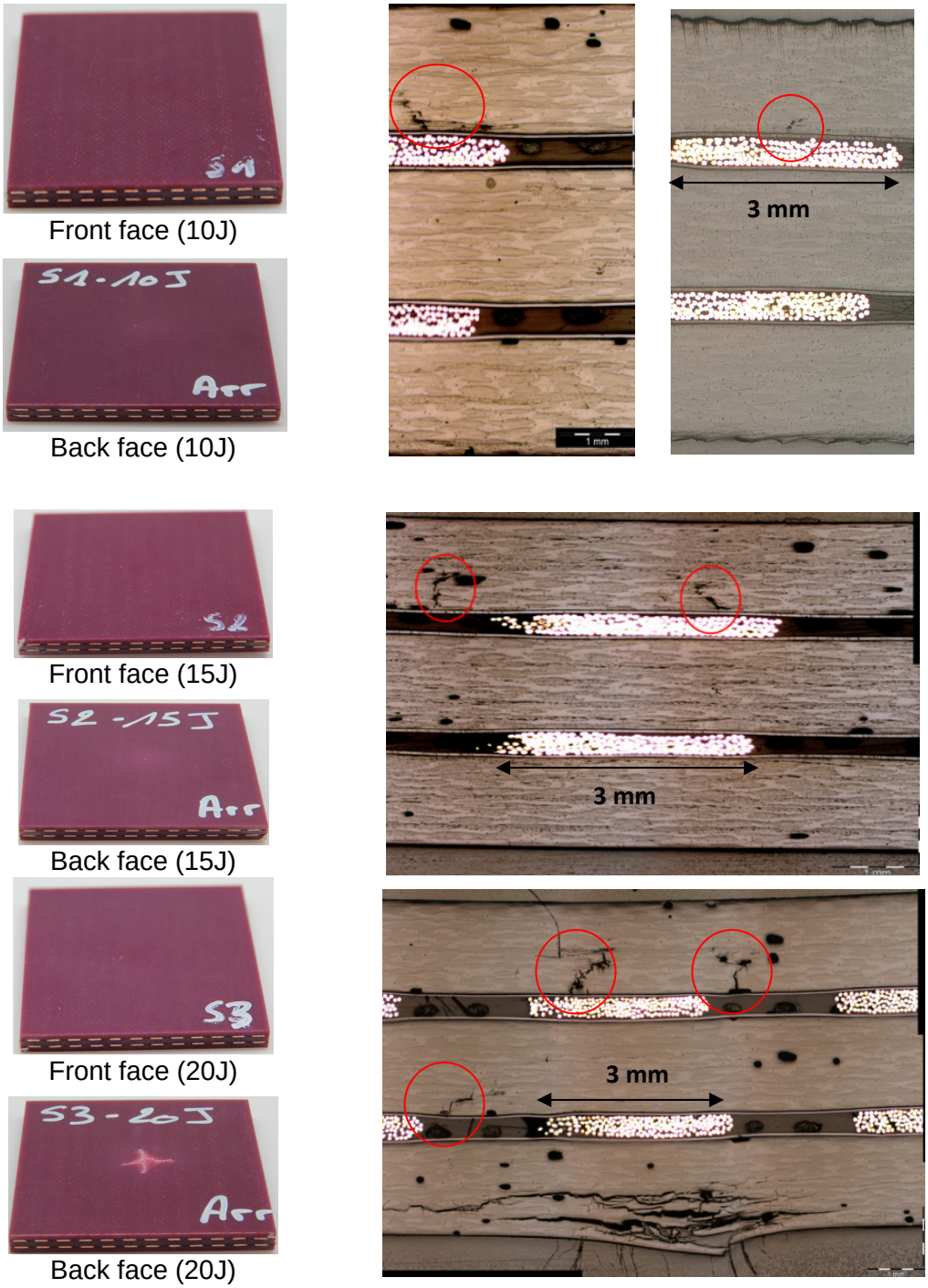

Figure 3. 34 Post-impact pictures of the front faces, back faces, and microscopic observations of the multifunctional test specimens

4.3. Concluding remarks

These experimental testings revealed two main damage mechanisms that potentially hinder the electrical functionality of the structure:

- Slipping within the cables (observed under transverse dynamic bending)
  - Eventually leading to debondings within the cables (observed under transverse dynamic bending test)

- Tension-shear fibre failure of the composite plies at the interface with the embedded cables

In addition, as compared to blank test specimens, the multifunctional test specimens seemed to exhibit better energy absorption and slightly higher damage thresholds.

Apart from the induced mechanical damage and potential loss of load-bearing capability of the structure, it is mandatory to investigate on the influence of these damage mechanisms on the electrical functionality of the embedded cables. Hence, post-impact dielectric strength measurements were performed, as detailed in the next section.

5. Post-impact electrical performances

In order to study the influence of such damage mechanisms on the electrical functionality of the structure, post-impact dielectric strength tests were performed. These measurements are expected to provide qualitative information about the insulation degradation of the cables [11, 12].

5.1. Test specimens

In order to perform post-impact dielectric strength measurements, the test specimens have to be adapted to allow testing the wires. The manufacturing process was kept unchanged, but the plates were directly manufactured according to the dimensions of the test specimens. Besides, the length of the embedded cables was longer than the dimensions of the composite structure, as shown in Figure 3. 35. This resulted in thickness variations, in particular near the edges, which was held responsible for the non-linear behaviour observed under dynamic bending tests in the previous section.

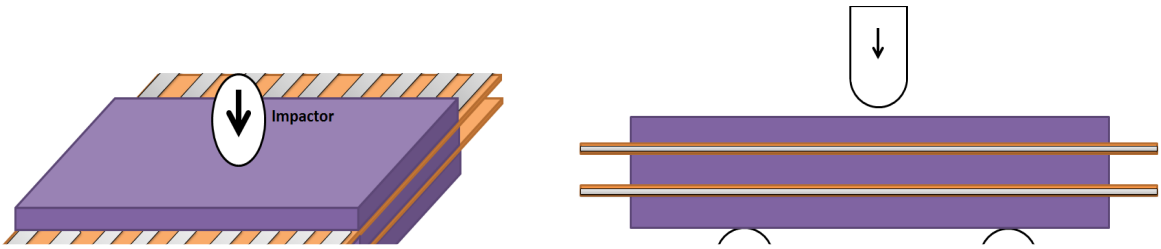

Figure 3. 35 Scheme of the test specimens used for post-impact dielectric strength measurements

Once manufactured, these multifunctional test specimens were impacted both under conventional impact test conditions, and under dynamic bending conditions, between 10J and 25J. The experimental conditions were kept identical to the experiments presented in the previous sections. Once impacted, the polyimide jacket was stripped in various locations so as to allow soldering wires (for grounding) and applying high voltage, cf. Figure 3.36. In

addition, the edges of the cables were insulated with an insulating glue having a dielectric strength of at least 60kV/mm.

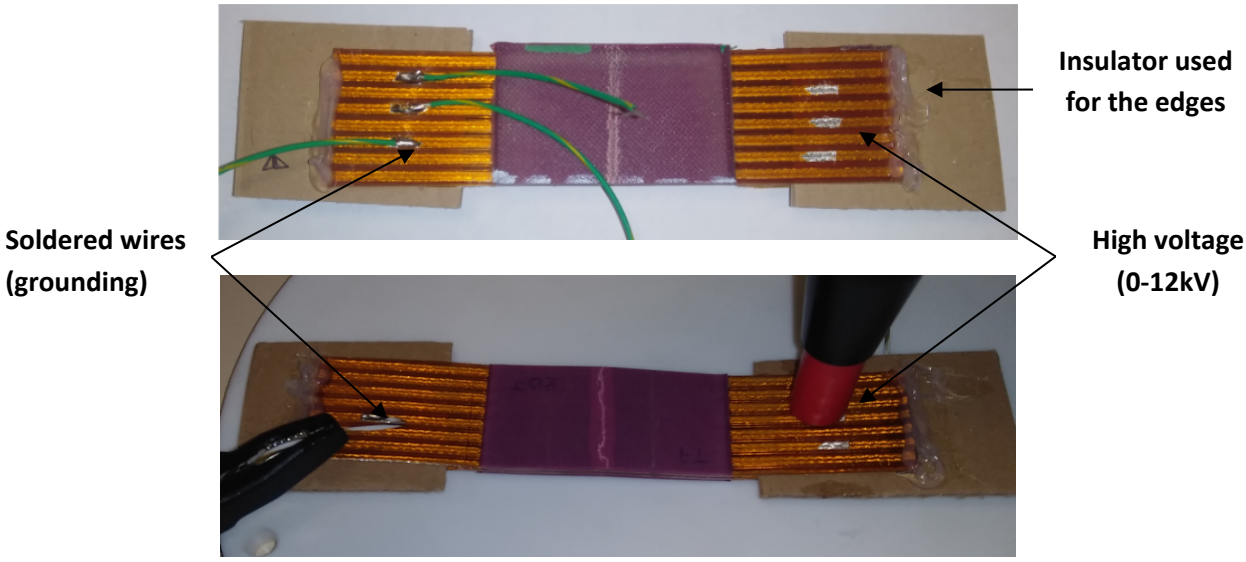

Figure 3. 36 Pictures of an impacted test specimen equipped with soldered wires to perform dielectrical strength measurements

5.2. Dielectric strength measurements

Different circuitry configurations were tested according to Figure 3. 37(c) below:

- No.1: between every adjacent wires: 1-2/2-3/3-4/4-5 and 1'-2'/2'-3'/3'-4'/4'-5'
- No.2: between every two wires 1-3/2-4/3-5 and 1'-2'/2'-4'/3'-5'
- No.3: between the upper and lower adjacent wires 1-1'/2-2'/3-3'/4-4'/5-5'

This resulted in 19 dielectric strength measurements per test specimens. Among all these tests, electrical shorting only occurred between the adjacent wires (configuration No.1) numbered 2, 3 and 4. When electrical shorting occurred, it was detected by a spark within the composite structure, as shown by Figure 3. 37 (b).

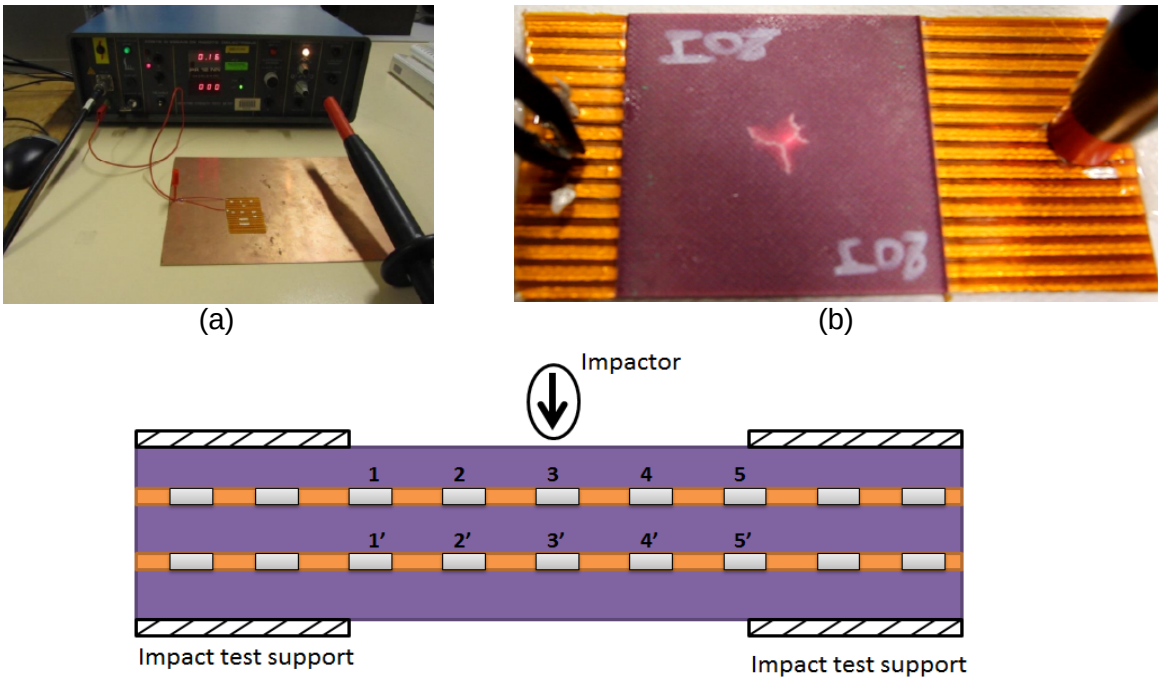

Figure 3. 37 (a) SEFELEC PR12NN dielectric strength tester, (b) spark localized in the damaged area and (c) configuration of the embedded wires within the impacted test specimens

These considerations led to the results presented in Figure 3. 38 (conventional impact test conditions) and Figure 3. 39 (dynamic bending conditions) where the dielectric strength (breakdown voltage in kV) is plotted versus the impact energy.

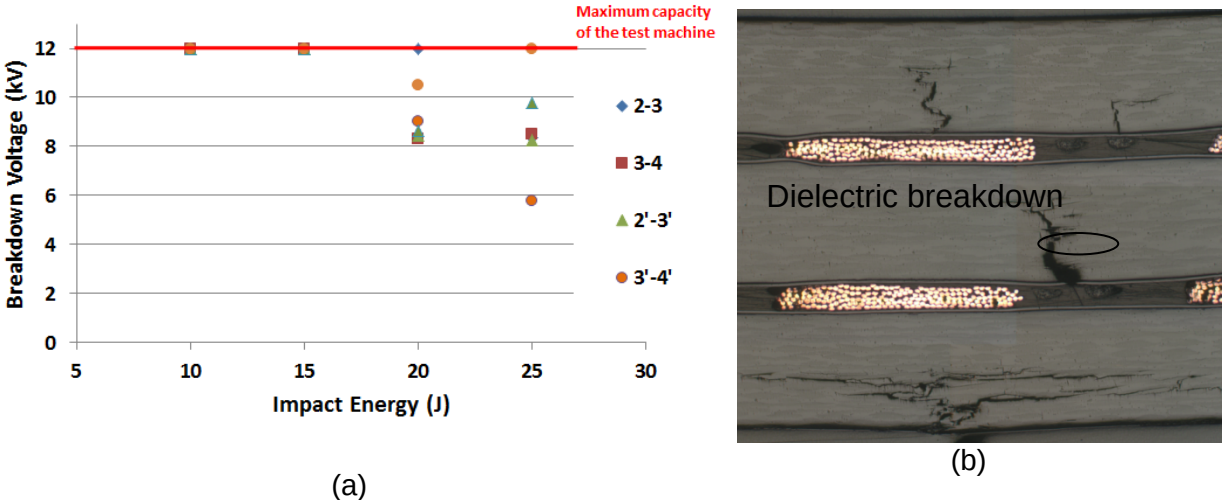

Figure 3. 38 (a) Results of the post-impact dielectric strength tests and (b) Post-dielectric strength test microscopic observation (conventional impact test conditions)

Electrical shorting started occurring within the embedded cables for test specimens impacted at 20J under conventional impact test conditions, and at 15J for the test specimens impacted under dynamic bending conditions. It always occurred between two conductors of the same cable (adjacent conductors of the top or bottom cable) on the conductors numbered 2&3

(resp. 2'&3') or 3&4 (resp. 3'&4'). Results of the dielectric strength tests involving the conductors numbered 1 and 5 are not presented since it never resulted in any electrical shorting. Post-impact post-dielectric strength tests microscopic observations revealed that the electrical shorting occurred due to the internal tension-shear fibre failure observed previously, cf. Figure 3. 38(b) and Figure 3. 39(b), and resulted in a small burnt out area between the wires. It is further interesting to highlight that the resulting degradation was confined to the adjacent wires and did not spread to the other wires. The burnt out area was also confined to the 3 to 4 adjacent composite plies and did not initiate any flame nor smoke emission.

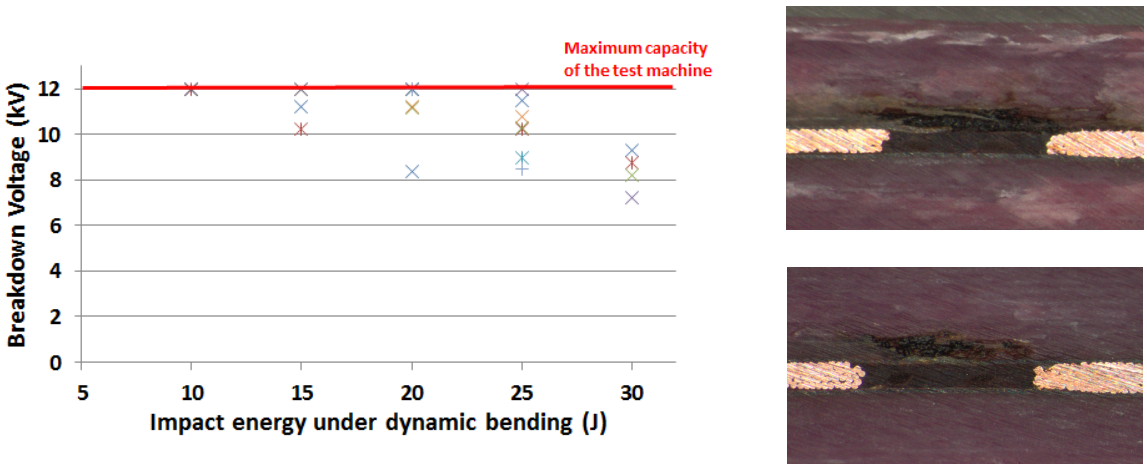

Figure 3. 39 (a) Results of the post-impact dielectric strength tests and (b) Post-dielectric strength test microscopic observation (dynamic bending test specimens)

Concluding remarks

The purpose of this chapter was to present the investigations performed to characterise the influence of the embedded cables on the damage mechanisms of the structure, and to investigate on potential degradation of the electrical functionality of the cables under critical mechanical loadings.

Due to the embodiment of the cables, this architecture was expected to be particularly weak under out-of-plane and shear loadings. In addition, impact loadings due to foreign objects (such as drop tools) are known to be harmful to composite materials. This led to further investigate on the behaviour of the structure under short 3 point bend tests and impact tests. To develop a full understanding of the induced damage mechanisms, test specimens were first tested under quasi-static short 3 point bend conditions, then under dynamic short 3 point bend conditions, and finally under conventional impact conditions. In an effort to quantitatively characterise damage onset, Digital Image Correlations (DIC) were performed. These analyses were challenging due to the heterogeneity of the cables and need to be further improved.

A highly heterogeneous distribution of shear strains through the thickness of the laminate due to the presence of the two embedded cables was revealed. Under these short bending conditions, damage was shown to occur in the form of internal tensile fibre failure of the composite plies at the interface with the embedded cables. This damage mechanism is most

likely coupled to slipping and debonding within the cables under inter-laminar shear strains. In particular, the weakest interface of the structure was shown to be inside the cables, hence leading to the conclusion that the out-of-plane strain distribution was mainly disturbed by the insulator within the cables.
This was further confirmed by microscopic observation made on test specimens impacted under dynamic bending conditions which showed clear debondings between adjacent wires.

Given the nature of the observed damage mechanisms, the post-impact electrical performances of the structure were characterized in terms of dielectric strength tests. It revealed that such damage leads to a drop of the dielectric strength between two adjacent wires. This means that the main risk of electrical degradation depends on the insulation degradation between two wires.

Therefore, these investigations provide a first step towards the elaboration of electrical degradation criteria for such multifunctional composite structures embedding electrical cables. These observations are further expected to pave the way for the choice of an adequate non-destructive testing technique prior to the use of such a structure. In particular, it seems mandatory to be able to detect insulation potential failures, for instance through insulation resistance testing.

References

[1] Y. Xiao, W. Qiao, H. Fukuda, and H. Hatta, 'The effect of embedded devices on structural integrity of composite laminates', *Compos. Struct.*, vol. 153, pp. 21–29, Oct. 2016.

[2] A. Abu Obaid and S. Yarlagadda, 'Structural performance of the glass fiber–vinyl ester composites with interlaminar copper inserts', *Compos. Part Appl. Sci. Manuf.*, vol. 39, no. 2, pp. 195–203, Feb. 2008.

[3] H. Kim, M. Park, and K. Hsieh, 'Fatigue fracture of embedded copper conductors in multifunctional composite structures', *Compos. Sci. Technol.*, vol. 66, no. 7–8, pp. 1010–1021, Jun. 2006.

[4] W. Hufenbach, F. Adam, W.-J. Fischer, A. Kunadt, and D. Weck, 'Effect of Integrated Sensor Networks on the Mechanical Behaviour of Textile-Reinforced Thermoplastics', *Procedia Mater. Sci.*, vol. 2, pp. 153–159, 2013.

[5] M. Grésil, 'Contribution à l'étude du contrôle de santé intégré associé à une protection électromagnétique pour les matériaux composites', École normale supérieure de Cachan-ENS Cachan, 2009.

[6] J.-C. Walrick, M. Grésil, and P. Parneix, 'Influence sur la tenue mécanique de l'insertion d'une fonction de protection électromagnétique au sein de composites à renforts de fibres de verre= Strength mechanical influence of electromagnetic shield function embedded in laminated glass composite', in *JNC 16*, 2009, p. 10–p.

[7] M. Kollegal, S. N. Chatterjee, and G. Flanagan, 'Progressive failure analysis of plain weaves using damage mechanics based constitutive laws', *Int. J. Damage Mech.*, vol. 10, no. 4, pp. 301–323, 2001.

[8] S. Treutenaere, F. Lauro, B. Bennani, T. Matsumoto, and E. Mottola, 'Modelling of the intralaminar matrix damage with friction effects of fabric reinforced polymers', *Compos. Part B Eng.*, vol. 111, pp. 60–73, Feb. 2017.

[9] T. Osada, A. Nakai, and H. Hamada, 'Initial fracture behavior of satin woven fabric composites', *Compos. Struct.*, vol. 61, no. 4, pp. 333–339, Sep. 2003.

[10] M. Asaad, 'Damage Accumulation in Hybrid Woven Farbic Composites', Bournemouth University, 2002.

[11] S. P. Timoshenko, 'On the correction for shear of the differential equation for transverse vibrations of prismatic bars', *Philosophical Magazine*, pp. 742–746, 1921.

[12] E. Reissner, 'The effect of transverse shear deformation on the bending of elastic plates', *ASME Journal of Applied Mechanics*, no. 12, pp. A69–A77, 1945.

[13] G. R. Cowper, 'The shear coefficient in Timoshenko's beam theory', *ASME Journal of Applied Mechanics*, no. 33, pp. 335–340, 1966.

[14] T. Kaneko, 'On Timoshenko's correction for shear in vibrating beams', *Journal of Physics D: Applied Physics*, vol. 8, no. 16, pp. 1927–1936, 1975.

[15] V. Birman and C. W. Bert, 'On the Choice of Shear Correction Factor in Sandwich Structures', *J. Sandw. Struct. Mater.*, vol. 4, no. 1, pp. 83–95, Jan. 2002.

[16] S. B. Dong, C. Alpdogan, and E. Taciroglu, 'Much ado about shear correction factors in Timoshenko beam theory', *Int. J. Solids Struct.*, vol. 47, no. 13, pp. 1651–1665, Jun. 2010.

[17] O. T. Topac, 'Experimental and Numerical Investigation of Damage Process in Composite Laminates under Low-Velocity Impact', Middle East Technical University, 2016.

[18] 'AITM1-0010 - Airbus Test Method. Fiber Reinforced Plastics - Compression Strength After Impact', pp. 1–15, Oct-2005.

[19] J. R. Xiao, B. A. Gama, and J. W. Gillespie, 'Progressive damage and delamination in plain weave S-2 glass/SC-15 composites under quasi-static punch-shear loading', *Compos. Struct.*, vol. 78, no. 2, pp. 182–196, Apr. 2007.

[20] R. C. Batra, G. Gopinath, and J. Q. Zheng, 'Damage and failure in low energy impact of fiber-reinforced polymeric composite laminates', *Compos. Struct.*, vol. 94, no. 2, pp. 540–547, Jan. 2012.
[21] M. A. Hassan, S. Naderi, and A. R. Bushroa, 'Low-velocity impact damage of woven fabric composites: Finite element simulation and experimental verification', *Mater. Des.*, vol. 53, pp. 706–718, Jan. 2014.
[22] N. R. Mathivanan and J. Jerald, 'Experimental investigation of woven E-glass epoxy composite laminates subjected to low-velocity impact at different energy levels', *J. Miner. Mater. Charact. Eng.*, vol. 9, no. 07, p. 643, 2010.
[23] H. Ullah, A. R. Harland, and V. V. Silberschmidt, 'Dynamic bending behaviour of woven composites for sports products: Experiments and damage analysis', *Mater. Des.*, vol. 88, pp. 149–156, Dec. 2015.
[24] I. Ivañez, C. Santiuste, and S. Sanchez-Saez, 'FEM analysis of dynamic flexural behaviour of composite sandwich beams with foam core', *Compos. Struct.*, vol. 92, no. 9, pp. 2285–2291, Aug. 2010.
[25] H. Ullah, A. R. Harland, and V. V. Silberschmidt, 'Evolution and interaction of damage modes in fabric-reinforced composites under dynamic flexural loading', *Compos. Sci. Technol.*, vol. 92, pp. 55–63, Feb. 2014.
[26] H. Ullah, A. R. Harland, and V. V. Silberschmidt, 'Damage and fracture in carbon fabric reinforced composites under impact bending', *Compos. Struct.*, vol. 101, pp. 144–156, Jul. 2013.
[27] 'NF-EN-ISO 3475: Aerospace series - Cables, Electrical, Aircraft use'. .
[28] ESA, 'ESCC Detail Specification No. 3901/001, Polyimide insulated wires and cables, Low frequency, 600V, -100 to +200°C'. Issue 3, Jan-1996.
[29] D. Gay, *Matériaux Composites*, 5th ed. Paris: Lavoisier, 2005.

Chapter 4: Numerical simulations of the mechanical behaviour and damage modes of a composite structure embedding flat electrical cables

Chapter 4: Numerical simulations of the mechanical behaviour and damage modes of a composite structure embedding flat electrical cables

1. Damage modelling of woven fabric composite laminates 102

1.1. Intralaminar damage 102

1.2. Interlaminar damage 103

1.2.1. Stiffness of a cohesive-zone elements 103

1.2.2. Size of the cohesive elements 104

1.3. Approach chosen to model the failure modes of the multifunctional structure 105

2. Damage of the multifunctional structure under quasi-static short 3 point bend tests 108

2.1. Modelling of the composite host structure 108

2.1.1. Geometrical modelling 109

2.1.2. Material properties 109

2.1.3. Mesh 110

2.1.4. Results and discussion 111

2.2. Modelling of the composite laminate embedding flat electrical cables 113

2.2.1. Stiffness of the cohesive-zone interface 113

2.2.2. Delamination initiation 114

2.2.3. Cohesive zone meshing 114

2.2.4. Delamination propagation 115

2.2.5. Results and discussion 116

3. Failure of the multifunctional structure under impact tests 119

3.1. Calibration of the progressive damage model 119

3.1.1. Crush strength, punch-shear strength and inter-laminar shear strength 119

3.1.2. Softening parameters m_j 120

3.2. Results 122

3.2.1. Blank test specimens 122

3.2.2. Multifunctional test specimens 123

4. Concluding remarks 125

The purpose of this chapter is to identify and use available failure theories and modelling techniques to predict the failure modes of the multifunctional structure identified in Chapter 3. In particular, the study focuses on the modelling of damage mechanisms leading to a degradation of the electrical performances of the embedded cables, namely: the tension-shear fibre failures of the composite plies at the interface with the embedded cables, and the inter-laminar damage (slipping, de-cohesion) within the cables.

To do so, a progressive failure analysis is performed with the ABAQUS software. The model uses a progressive damage model coded in a VUMAT subroutine to account for damage of the composite plies, and cohesive-zone elements to account for damage within the cables.

The parameters of the cohesive-zone elements are first estimated based on experimental and numerical correlations of the quasi-static short 3 point bend tests. Then, the impact tests presented in Chapter 3 are modelled. This approach allows capturing damage initiation of the aforementioned damage mechanisms and characterising the coupling between slipping within the cables and internal tension-shear fibre failures of the composite plies.

1. Damage modelling of woven fabric composite laminates

Two types of damage are often distinguished when dealing with damage of composite laminates: intra-laminar damage and inter-laminar damage. Intra-laminar damage refers to damage mechanisms occurring within a composite ply (such as fibre breakage and matrix cracking) while inter-laminar damage refers to damage occurring between the composite plies (mainly delaminations). Modelling such damage mechanisms is challenging and every damage models faces similar issues in terms of sensitivity of the predicted progressive failure behaviour to assumptions about geometric nonlinearity, mesh dependency, strain localization, and the property degradation model [1]–[3].

1.1. Intralaminar damage

Due to their relatively high geometrical and micro-structural complexity, failure modelling of woven fabric composite materials is all the more challenging [4]. Most of the current numerical and analytical methodologies used to characterize textile composites assume that the textile is a homogeneous material at the macroscopic scale. Engineering failure criteria for unidirectional composite materials such as the maximum stress criterion, maximum strain criterion, or quadratic interaction criterion such as the Tsai-Wu and Tsai-Hill failure theories [5], [6] applied or adapted to woven fabric are used to model damage initiation.
Other models based on continuum damage mechanics principles have been developed at the ply scale, such as the model developed by Hochard et al.[7], [8] which accounts for the loss of stiffness in the warp, weft and shear directions under static and fatigue loadings. This model is based on thermodynamic expressions and internal variables where the plies are assumed to be homogeneous and orthotropic. In addition, it is assumed that a woven ply may be replaced by two stacked unidirectional plies corresponding to the warp and weft thicknesses. Another common approach is based on the micromechanics of textile composites where unit cells of the woven fabric are used with appropriate periodic boundary conditions to examine the behaviour of the entire textile subjected to various loading conditions [9], [10].
When the textile is not treated as homogeneous, the mechanical behaviour of the fibre and matrix are separated, such as in the semi-continuous approach used by Navarro, et.al [11] and Pascal et al. [12].

These various approaches have also been applied to dynamic and impact analysis of composite laminates by using stress-based criteria such as Hashin [13], [14], Tsai-Hill [5], LaRC04 [15], or Puck [3] criterion to capture damage initiation. Such simulations also require to take strain-rate effects into account which have a significant influence on the material response under dynamic loading [16], [17].
Damage propagation is mostly based on energetic-based relations, or empirical relations such as proposed by Matzenmiller, Lubliner and Taylor [14], [18]. In addition, under such out-of-plane loadings, one of the most dominant failure mode is delamination [19]–[22], even though woven fabric are known to offer a better resistance to delaminations than unidirectional composites [20], [23]. Hence, modelling woven fabric impacts not only requires modelling the fibre and matrix damage mechanisms within plies, but also the inter-laminar damage mechanisms.

1.2. Interlaminar damage

Inter-laminar damage may also be modelled according to stress- or interface strength-based failure criterion such as proposed by Brewer and Lagace [24]. Yet, the use of cohesive elements inserted between the plies [3], [13], [15], [25]–[27] is mostly encountered in the literature. Two approaches are mainly encountered: the CCZM (Continuous Cohesive Zone Method) which relies upon a continuum element type and a traction-separation relationship, cf. Figure 4. 1, and the DCZM (Discrete Cohesive Zone Method) which is based on a discrete spring formulation. Such approaches also offer the possibility to take into account visco-plastic effects and different behavior in tension and compression [28].

When treated with a traction-separation relationship, damage initiation is related to the maximum traction on the load – displacement curve, cf. Figure 4. 1, and is followed by a softening phase that simulates the progressive decohesion of the interface with increasing damage. The softening phase might be modelled with linear, trapezoidal (elasto-plastic material) or polynomial laws. Several stress- or strain-based criteria may be used to account for damage initiation while damage propagation is usually monitored by the fracture toughness and shape of the traction-displacement curve.

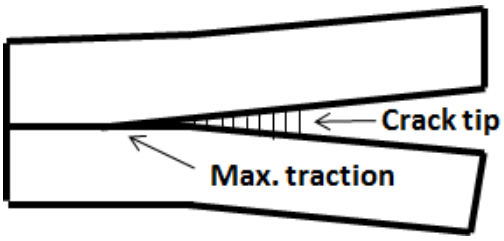

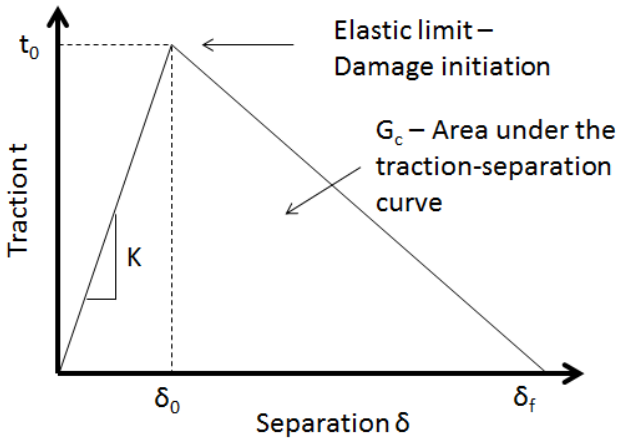

t: traction
δ: displacement
K : initial stiffness
δ_0 : separation at damage initiation
δ_f : separation at failure
G_c : Fracture Toughness

Figure 4. 1 Traction-displacement curve of a cohesive zone element

With such an approach, there are three main parameters governing the cohesive behavior: the fracture toughness (G_c), initial stiffness (K) and strength of the interface (t_0). Among them, only the fracture toughness can be reliably and easily measured experimentally [29]. The other properties are difficult to determine and may be treated as penalty (or fitting) parameters [30].

1.2.1. Stiffness of a cohesive-zone elements

Several authors have pointed out the necessity to choose a sufficiently high value of the initial stiffness (K) so as not to affect the overall compliance of the model before the damage initiation criterion is met [30], [31]. On the contrary, a very high value may lead to

convergence difficulties of FE calculations. Therefore, an optimum value needs to be chosen to overcome these difficulties.

Several methods may be used to determine this elastic stiffness. It can be based on experiments [32]–[34], or determined according to the elastic modulus and thickness of the surrounding region [31], [35]. This latter approach states that the normal interface stiffness may be chosen according to Equation (Eq.4.1) below:

$$K_n = \alpha \frac{E}{h} \qquad \text{(Eq.4.1)}$$

with α >> 1 (α greater than 50 has been found to be suitable for most cases [31]), E the Young's modulus of the sublaminate, and h its thickness. Similar expressions may be used for shear modes with G the shear modulus of the surrounding region:

$$K_s = \alpha_s \frac{G}{h} \qquad \text{(Eq.4.2)}$$

1.2.2. Size of the cohesive elements

The choice of the cohesive mesh size has a significant effect on the computational performances of a model [30], [31], [36]. As a matter of fact, accurately capturing delamination with cohesive elements usually requires mesh elements of a few tenths of millimetres.
Some methods and numerical tools have been developed to characterise the mesh size influence on the accuracy of the results. For instance, it was shown by Turon et al. [31] that lowering the interfacial strengths allows using a coarser mesh which leads to computational time saving. It was also observed by Panettieri et al. [36] that unlike tests in which the opening mode is predominant, problems for which shearing modes are predominant may be modelled with greater mesh sizes and higher maximum shearing loads.

More generally, the cohesive element size needs to be less than the cohesive zone length which is defined as the distance from the crack tip to the point where the maximum cohesive strength is reached. This distance is usually noted l_{cz} and expressed as [37]:

$$l_{cz} = ME \frac{G_c}{(t_0)^2} \qquad \text{(Eq.4.3)}$$

$$N_e = \frac{l_{cz}}{l_e} \qquad \text{(Eq.4.4)}$$

With E the Young's modulus of the material, G_c the fracture energy release rate, t_0 the maximum interfacial strength, M a parameter which is problem dependent ranging from 0.2 to 1 [37], l_e the mesh size and N_e the number of elements in the cohesive zone. Generally, the minimum number of elements needed in the cohesive zone to accurately capture the fracture energy tends to revolve between 2 and 5. Over-meshing the cohesive zones by more than 5 cohesive elements per surrounding elements is usually useless and do not improve the solution accuracy [30].

1.3. Approach chosen to model the failure modes of the multifunctional structure

As observed experimentally (cf. Chapter 3), there are mainly two damage mechanisms likely to degrade the electrical performances of the embedded cables that need to be captured: slipping and de-cohesion within the embedded cables (inter-laminar damage), and fibre failure at the interface with the embedded cables. In this study, a progressive failure analysis will be used to model damage of the composite laminate while cohesive-zone elements will be used to model the inter-laminar damage within the cables, cf. Figure 4. 2.



Figure 4. 2 Damage mechanisms to be captured

The progressive damage model is presented hereafter. It is initially developed by Matzenmiller, Lubliner and Taylor [18] and enables modelling the elastic-brittle damage of fiber-reinforced composites based on a homogenized continuum approach and internal variables to describe the evolution of damage state.

Recently, it has been adapted to model progressive damage and delamination in plain weave composites under punch-shear loading [38], as well as damage of composite structures under lightning strikes [39].

As regards to damage of woven fabrics, it takes into account seven damage modes related to the damage thresholds $r_{j\ (j=1..7)}$. Damage is initiated once any of these damage thresholds exceeds 1 ($r_j \geq 1$).

The fiber failure criteria of Hashin is used and generalized to characterize the fiber damage in terms of strain components for a plain weave layer.

- The warp (Eq.4.5) and weft (Eq.4.6) tensile/shear fibre breakage are calculated as the quadratic interaction between the axial and through the thickness shear stresses:

$$\left(\frac{E_{11}\langle\varepsilon_{11}\rangle}{X_{1T}}\right)^2 + \left(\frac{G_{13}\varepsilon_{13}}{S_{\mathrm{FS}}}\right)^2 - \mathrm{r}_1^2 = 0 \qquad \text{(Eq.4.5)}$$

$$\left(\frac{E_{22}\langle\varepsilon_{22}\rangle}{X_{2T}}\right)^2+\left(\frac{G_{23}\varepsilon_{23}}{S_{\mathrm{FS}}}\right)^2-\mathrm{r}_2^2=0 \qquad \text{(Eq.4.6)}$$

with <.> the Macaulay brackets, X_{1t} and X_{2t} the axial tensile strengths in the fill and weft directions and S_{FS} the laminar shear strength due to fibre shear failure.

- The in-plane compressive damage in the warp (Eq.4.7) and weft (Eq.4.8) directions is given by the maximum strain criterion. These expressions takes into account the effect of through the thickness compressive strain on the in-plane compressive damage:

$$\left[\frac{E_{11}\langle-\varepsilon_{11}-\langle-\varepsilon_{33}\rangle\frac{E_{33}}{E_{11}}\rangle}{X_{1C}}\right]-\mathrm{r}_3^2=0 \qquad \text{(Eq.4.7)}$$

$$\left[\frac{E_{22}\langle-\varepsilon_{22}-\langle-\varepsilon_{33}\rangle\frac{E_{33}}{E_{22}}\rangle}{X_{2C}}\right]-\mathrm{r}_4^2=0 \qquad \text{(Eq.4.8)}$$

with X_{1c} and X_{2c} the axial compressive strengths in the fill and warp directions.

When a composite material is subjected to transverse impacts by projectile, high compressive stresses will generally occur in the impact area with high shear stresses, taken into account by the following criterion.

- Crush damage due to through the thickness compressive stresses:

$$\left(\frac{E_{33}\langle-\varepsilon_{33}\rangle}{X_{3\mathrm{C}}}\right)^2-\mathrm{r}_5^2=0 \qquad \text{(Eq.4.9)}$$

with X_{3C} the fibre crush strength.

- In-plane matrix damage mode under in-plane shear stresses without occurrence of fibre breakage:

$$\left(\frac{G_{12}\varepsilon_{12}}{S_{12}}\right)^2-\mathrm{r}_6^2=0 \qquad \text{(Eq.4.10)}$$

with S12 the shear strength due to matrix shear failure

- Delamination due to the through-the-thickness matrix failure is taken into account by the quadratic interaction between the transverse strains:

$$S^2\left[\left(\frac{\langle\sigma_{33}\rangle_+}{\mathrm{Z}_T}\right)^2+\left(\frac{G_{23}\varepsilon_{23}}{S_{23}+S_{SR}}\right)^2+\left(\frac{G_{13}\varepsilon_{13}}{S_{13}+S_{SR}}\right)^2\right]-\mathrm{r}_7^2=0 \qquad \text{(Eq.4.11)}$$

Where Z_T is the through-the-thickness tensile strength for tensile normal strain ($\varepsilon_{33}>0$) and S_{SR} stands for an additional damage strength under compressive through the thickness strain ($\varepsilon_{33} < 0$) [38], where damaged surface (delamination) is closed. It is expressed as $S_{SR}=-\varepsilon_{33}E_{33}\tan(\varphi)$ according to the Mohr-Coulomb theory with φ the Coulomb friction angle. A scale factor S is also considered and is determined by fitting the analytical and experimental data as regards to the delamination area.

Damage variables $w_{i(i=1..6)}$ are then defined to relate the onset and damage growth to stiffness losses in the material. Stiffness losses are applied to the elastic constants of the materials through a coupling matrix Q_{ij} presented in Table 4. 1 and a scalar damage function $\varphi_{j\ (j=1..7)}$ which monitors damage propagation. Thus, as the r_j values varies from 1 to infinity with increasing strains, the damage variables w_i vary from 0 to 1.

$$w_i = max\{\varphi_j Q_{ij}\} \quad \text{(Eq.4.12)}$$

and,

$$\varphi_j = 1 - exp\left(\frac{1}{m_j}\left(1 - r_j^{m_j}\right)\right), r_j \geq 1 \quad \text{(Eq.4.13)}$$

(Eq.4.13) shows that damage propagation is function of strain softening parameters m_j which expresses that the higher the damage parameters, the more brittle the damage is, cf. Figure 4. 3.

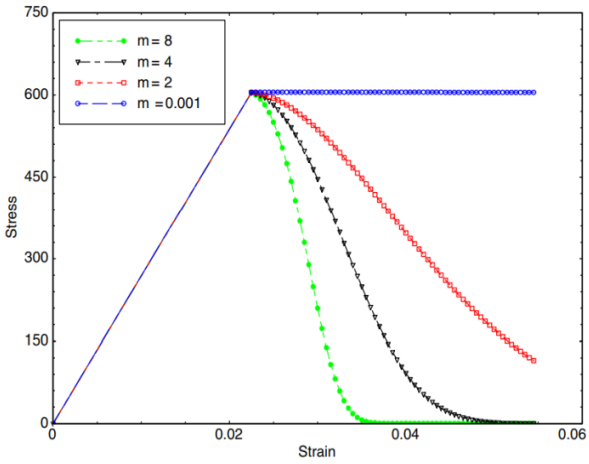

Figure 4. 3 Tensile stress–strain relationships with different damage parameters [38]

Damage Types / Affected Moduli	Fibre Damage Modes					Matrix Damage Modes	
	Mode 1 (j=1)	Mode 2 (j=2)	Mode 3 (j=3)	Mode 4 (j=4)	Mode 5 (j=5)	Mode 6 (j=6)	Mode 7 (j=7)
E_{11}	1	0	1	0	1	0	0
E_{22}	0	1	0	1	1	0	0
E_{33}	0	0	0	0	1	0	1
G_{12}	1	1	1	1	1	1	0
G_{23}	0	1	0	1	1	0	1
G_{13}	1	0	1	0	1	0	1

Table 4. 1 Damage coupling matrix Q_{ij}

The compliance matrix [S] is related to the damage variables [18], [38] as:

$$[S] = \begin{bmatrix} \frac{1}{(1-w_1)E_{11}} & \frac{-v_{21}}{E_{22}} & \frac{-v_{31}}{E_{33}} & & & \\ \frac{-v_{12}}{E_{11}} & \frac{1}{(1-w_2)E_{22}} & \frac{-v_{32}}{E_{33}} & & [0] & \\ \frac{-v_{13}}{E_{11}} & \frac{-v_{32}}{E_{22}} & \frac{1}{(1-w_3)E_{33}} & & & \\ & & & \frac{1}{(1-w_4)G_{12}} & 0 & 0 \\ & [0] & & 0 & \frac{1}{(1-w_5)G_{23}} & 0 \\ & & & 0 & 0 & \frac{1}{(1-w_6)G_{13}} \end{bmatrix} \quad \text{(Eq.4.14)}$$

This damage scheme is implemented in a VUMAT subroutine under the software Abaqus according to the scheme described in Figure 4. 4.

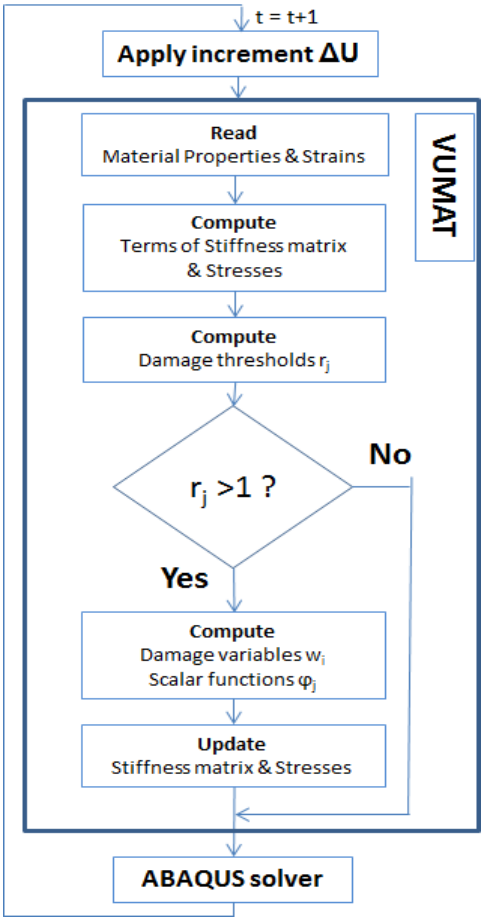

Figure 4. 4 Scheme of the VUMAT subroutine

Yet, besides implementing this progressive damage model in the FE code, the parameters of the cohesive-zone elements, used to model the inter-laminar damage within the cables need to be identified. This is done in the next section through numerical and experimental correlations on the quasi-static short 3 point bend tests.

2. Damage of the multifunctional structure under quasi-static short 3 point bend tests

Numerical correlations on the quasi-static S3PB tests are used to determine the best set of parameters to model the inter-laminar damage (parameters of the cohesive zone interactions) within the embedded cables. To do so, this section starts by modelling the quasi-static short 3 point bend tests performed on the blank test specimens. These first simulations are used to verify the accuracy of the model in terms of material properties and boundary conditions. No damage is taken into account and the material behaviour is assumed to be linear elastic.

Then, the study goes on with the numerical modelling of the quasi-static short 3 point bend tests performed on the multifunctional test specimens. For these simulations, cohesive-zone interactions are implemented at the interface between the embedded cables and the composite plies. Numerical correlations with experimental data help defining the best set of parameters to be used in cohesive zones.

2.1. Modelling of the composite host structure

2.1.1. Geometrical modelling

A 3D modelling of the quasi-static short 3 point bend test was done under ABAQUS CAE. Only a quarter of the test specimens (30mm in length and 15mm in width) was modelled in accordance with the experimental test specimen (cf. chapter 3). and was given symmetry conditions, cf. Figure 4. 5. The contacts between the test specimens and the rigid supports were defined with a normal (default hard contact) and tangential component (with an arbitrary friction coefficient of 0.1). Each composite ply was modelled and meshed with one element through the thickness of the ply and the interfaces between the plies were assumed to be perfect. The layup consisted of 45 plies: $[(0/45)_{11}/0/(45/0)_{11}]$, with a ply thickness of 0,125mm.

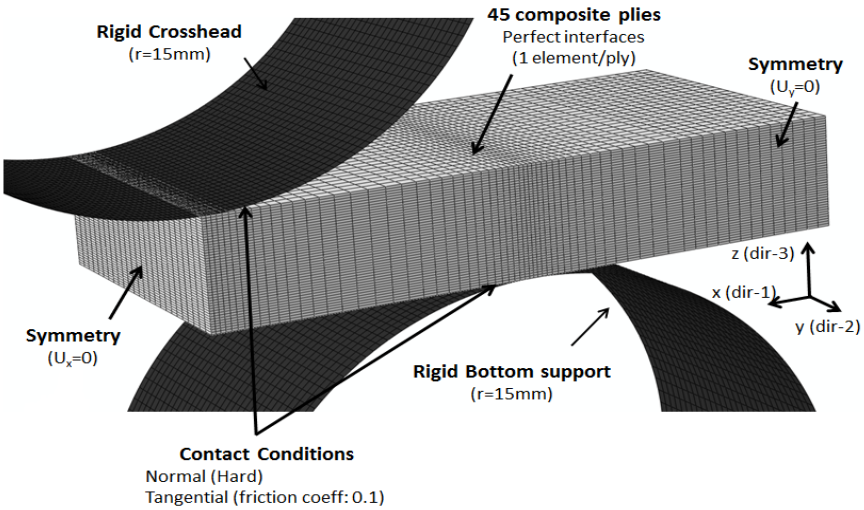

Figure 4. 5 3D modelling of the quasi-static short 3 point bend tests

2.1.2. Material properties

The mechanical properties of the woven fabric were determined in Chapter 2, and are listed in Table 4.2

Properties	E_{11}	E_{22}	E_{33}	ν_{12}	ν_{13}	ν_{23}	G_{12}	G_{31}	G_{23}
Value	12.04	12.04	5.59	0.18	0.48	0.48	2.36	1.53	1.53

Table 4. 2 Mechanical properties of a composite ply, all moduli values are given in GPa

No damage is taken into account in this model and the behaviour of a composite ply is assumed to be linear elastic. Hence, the model is expected to over-estimate the experimental data, especially due to the non-linear behaviour of the composite laminate under tension as observed experimentally in Chapter 3, cf. Figure 4.5. It is further assumed that the behaviour of the material is the same under tension or compression.

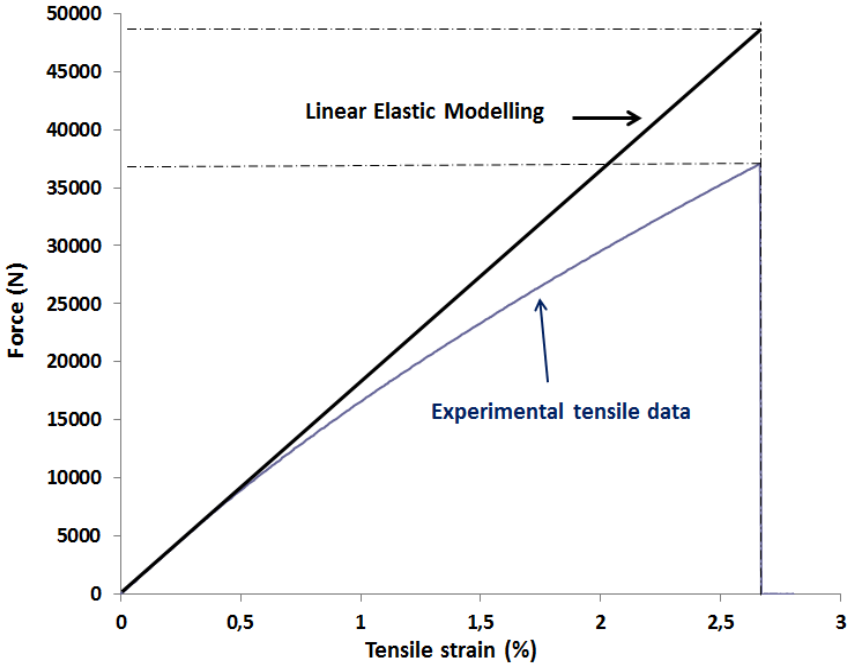

Figure 4. 6 Linear elastic modelling of the tensile behaviour of the composite plies

2.1.3. Mesh

With the FE software ABAQUS, several elements may be used to mesh structures under bending deformations. Choosing the best element is a trade-off between computational time and accuracy of the results. Generally, first order elements are used with either a fully-integrated integration (C3D8), or a reduced integration formulation (C3D8R). While fully-integrated elements undergo a 'shear-locking' phenomenon due to an overly stiff behaviour, the reduced-integration elements are sensitive to 'hourglassing'. To reduce the hourglass effect, more elements are needed through the thickness of the parts experiencing bending deformations.
In addition, there exist 'incompatible' mode elements which consist in fully-integrated elements with added internal degrees of freedom to eliminate shear locking phenomena. Thus, they can capture bending as accurately as second-order elements with reduced runtime.

These elements were compared with various mesh size to assess the convergence of the model as regards to the reaction force measured on the crosshead, cf. Figure 4. 7.

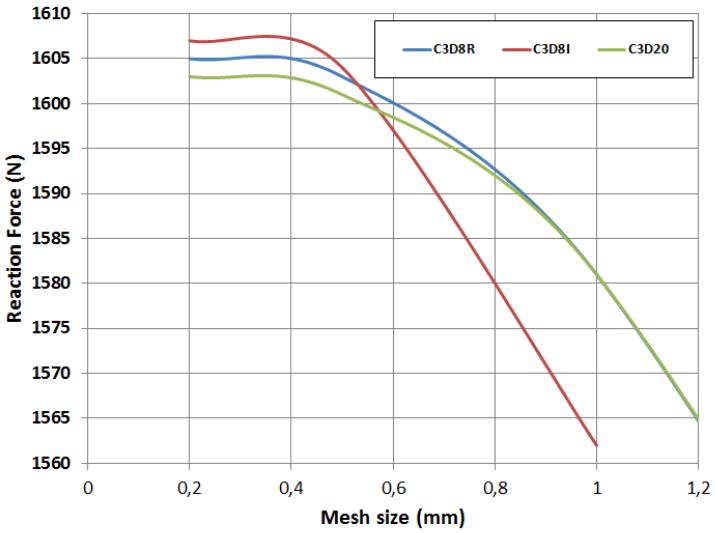

Figure 4. 7 Mesh convergence according to the reaction force

A convergence seems to be achieved for element size of approximately 0.4mm, which is mainly due to the element size needed to capture the stress gradients near the contact zones. Hence, a biased mesh was chosen starting with a mesh size of 0.2mm near the contact zones, and increasing up to 0.7mm, cf. Figure 4. 5. Quadratic elements (C3D20) are expected to be more accurate but are much more costly than the linear elements with reduced integration (C3D8R) or incompatible modes (C3D8I). Hence, C3D8R elements were chosen. The model is finally composed of 1,980 discrete rigid elements R3D4 (a 4-node 3-D bilinear rigid quadrilateral element) on the rigid supports and 56,000 solid elements C3D8R (an 8-node doubly curved thick shell element with reduced integration) for the composite laminate.

2.1.4. Results and discussion

The numerical results are obtained by imposing a displacement of 1.2mm, they are compared with the experimental force-displacement curve from the test specimen FDV1 and FDV2, cf. Figure 4. 8.

It is observed that the numerical simulations over-estimate the experimental data with a maximum relative error of approximately 10%. This over-estimation was expected due to:

- The assumed linear elastic behaviour of the material (damage prior to ultimate failure of a ply is not taken into account).
- The assumed identical behaviour of the material under tension and compression

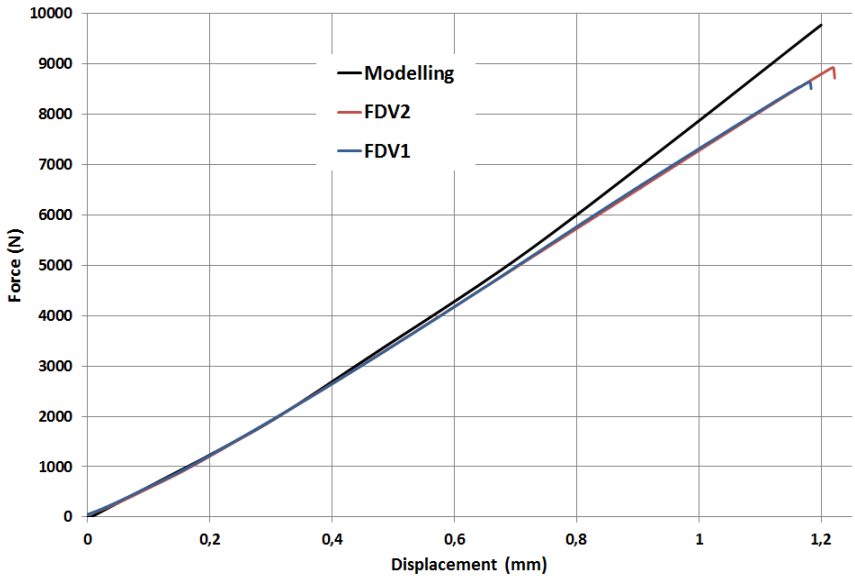

Figure 4. 8 Correlation between S3PB numerical and experimental data on the blank test specimens

For a displacement of the crosshead of 1.2mm (where failure occurs experimentally under tension on the back face), the numerical tensile and inter-laminar strains reach respectively 3.5% and 3.7%, cf. Figure 4.8. These values also seem over-estimated since failure of the composite laminate is expected to occur under tensile strains of approximately 3.1% (cf. Chapter 3, 1.1). The associated inter-laminar shear stresses reach 56MPa, which is close to the inter-laminar shear strength of the material (>55MPa according to manufacturer's datasheet).

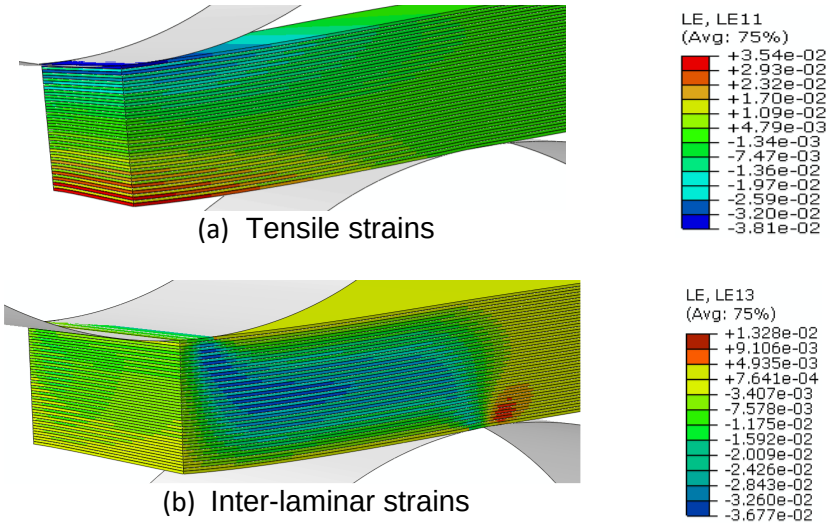

Figure 4. 9 Numerical (a) tensile and (b) inter-laminar shear strains on a blank test specimens under S3PB test for a displacement of the crosshead of 1,20mm

Despite these discrepancies and the assumptions made, the model is considered accurate enough to perform numerical simulations on the multifunctional test specimens under quasi-static short 3 point bend tests. This will help defining the parameters of the cohesive-zone elements required to model inter-laminar-damage within the cables.

2.2. Modelling of the composite laminate embedding flat electrical cables

A similar 3D geometry is created under ABAQUS CAE to model the multifunctional test specimens, cf. Figure 4. 10.

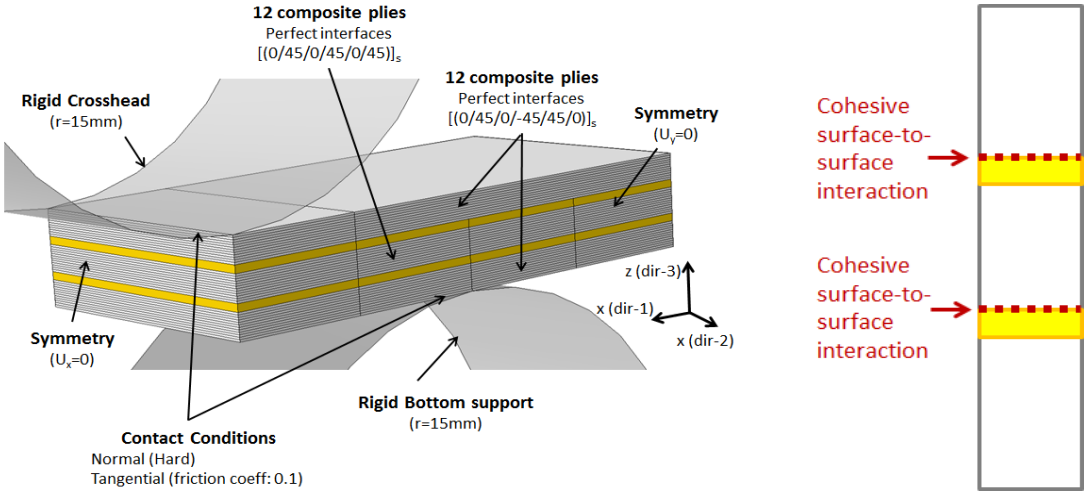

Figure 4. 10 Geometrical modelling of the S3PB test on the multifunctional test specimens

Cables are modelled as 0,45mm thick homogeneous and anisotropic layers with the elastic properties determined in Chapter 2, cf. Table 4. 3. Similarly to composite plies, the mechanical behaviour of an electrical cable is assumed to be linear elastic. Given their highly heterogeneous composition and non-linear behaviour, this is a strong assumption of the model.

E_{11} (GPa)	E_{22} (GPa)	E_{33} (GPa)	G_{12} (GPa)	G_{13} (GPa)	G_{23} (GPa)	ν_{12}	ν_{13}	ν_{23}
19.50	1.10	0.48	0.43	0.16	0.16	0.48	0.48	0.48

Table 4. 3 Mechanical properties of an electrical cable

In addition, a surface-to-surface cohesive interaction is defined at the upper interfaces between the cables and the composite host structure, as shown by Figure 4. 10. The master surface is chosen as the upper composite ply, and the slave surface is chosen as the adjacent cable surface. With such an interaction property, there is no need to choose any proper cohesive elements. Yet, the cohesive contact interactions still needs to be defined with the same set of parameters: the initial stiffness of the interface (K), the fracture toughness (G_c) and the interface strength (t_0).

All other material properties, loading, and boundary conditions are similar to those used in the previous modelling of the blank test specimens.

2.2.1. Stiffness of the cohesive-zone interface

As a 3D model is used, the initial (un-damaged) stiffness of the interface is defined by three stiffness parameters in the three directions: n (normal to the plane of the interface, ie thickness direction), s (first in-plane shear direction) and t (second in-plane shear direction).

Based on the paper by Turon, et al.[31], it is recommended to choose the stiffness value K_{nn} (thickness direction) so that:

$$K_{nn} = \alpha \frac{E_{33}}{t} \quad \text{(Eq.4.15)}$$

with α greater than 50, E_{33} the through-the-thickness Young's modulus of the surrounding material and t the thickness of an adjacent sublaminate. The shear stiffnesses $K_{ss}=K_{tt}$ is chosen by replacing E_{33} with the shear modulus G_{12} of the surrounding material.

In this study, we choose α=50, E_3 = 5,730MPa, t = 0.125mm and G_{12}=2,670MPa which are the constant related to an adjacent composite ply. These considerations yield **K_{nn} = 2.3x10^6 N.mm^{-3}** and **$K_{ss}=K_{tt}$=1.1x10^{6}N.mm^{-3}**. Such values are consistent with common stiffness of cohesive elements encountered in the literature.

2.2.2. Delamination initiation

Under quasi-static short 3 point bend tests, slipping within the cables has been observed to occur under inter-laminar strains of approximately 8.0% (Cf. Chapter 3). Assuming a linear behaviour of the insulator within the cables with a shear modulus G=0.16GPa, the onset of damage within the cables should occur under inter-laminar stresses of 12.80MPa.

The initiation of the cohesive damage within the cables is modelled with a maximum stress criterion, cf. (Eq.4.16).

$$max\left\{\frac{\langle S_{33}\rangle}{S_{33}^0}, \frac{S_{13}}{S_{13}^0}, \frac{S_{23}}{S_{23}^0}\right\} = 1 \quad \text{(Eq.4.16)}$$

With S_{33}^0, S_{13}^0 S_{23}^0 the peak values of the contact stresses respectively in the normal direction or in the first shear and second shear directions. Several values of the inter-laminar shear stresses $S_{13}=S_{23}$ are tested (12MPa, 13MPa and 14MPa) and $S_{13}=S_{23}$=14MPa offers the best fit with experimental data. Hence, a maximum stress damage initiation criterion is chosen to stand for damage initiation within the cohesive elements with $S_{13}^0 = S_{23}^0$=14MPa and S_{33}^0=14MPa. This latter value of S_{33}^0 is chosen as a numerical parameter rather than as a material property. In addition, under S3PB tests the test specimens are mainly loaded under mode II shear, hence the influence of mode I is negligible.

2.2.3. Cohesive zone meshing

The composite plies were meshed with C3D8R elements identically to the meshing used for the blank test specimens (with an element size of approximately 0.7mm and a biased mesh near the contact zones). The cables were meshed with C3D8I elements which were found more efficient to bypass hourglass effects due to high shear deformations, and the rigid bodies were meshed with R3D4 elements. In addition, the C3D8I element sizes were reduced as compared to the C3D8R element sizes so as to get a proper interaction between the master surfaces (composite plies) and slave surfaces (cables) in the cohesive zones. Four different mesh densities were tested and yielded the same results in terms of resulting

reaction force vs displacement since the reference mesh used for meshing the blank test specimens was already refined enough.

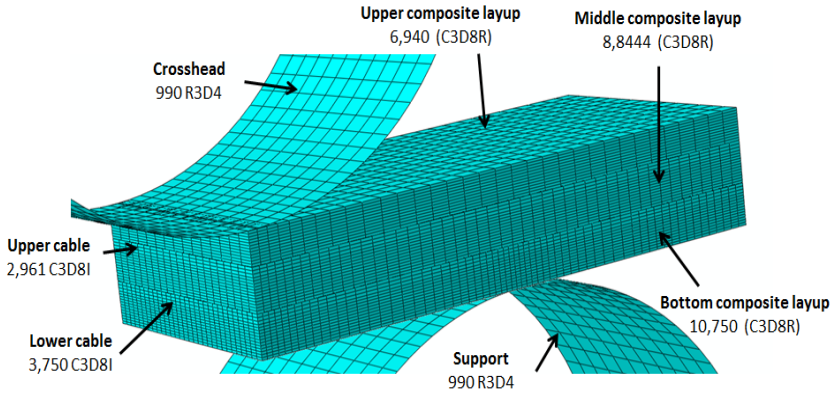

Figure 4. 11 Meshing of the S3PB multifunctional test specimens with cohesive surface-to-surface interactions

The choice of the element sizes was then made according to the accuracy of the delamination initiation and propagation within the cohesive contact zones. This resulted in 1,980 R3D4 elements, and approximately 7,000 C3D8I elements and 46,500 C3D8R elements.

2.2.4. Delamination propagation

Once the damage threshold is reached, stiffness degradation occurs. This damage degradation process is governed by the fracture energies G_{Ic} (=G_n), G_{IIc} (=G_s) and G_{IIIc} (=G_t), cf. Figure 4. 12 with $G_{IIc} = G_{IIIc}$.

Damage propagation is usually defined either in terms of displacement or energy. Here, the energy-based damage propagation process is chosen with a linear softening behavior which was found to fit well experimental data in this particular study. The power law criterion proposed by Benzegagh and Kenane [29] is used to monitor the delamination propagation.

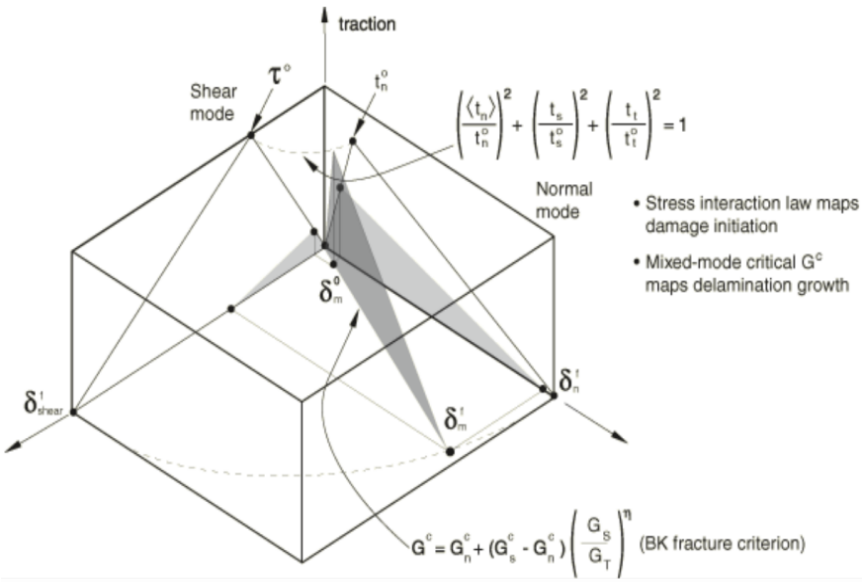

Figure 4. 12 Mixed-mode response in cohesive elements, from ABAQUS User's Manual

As the fracture energy G_{IIc} governing the delamination under mode II remains an unknown, it is treated as a penalty parameter. Several fracture energy values were successively tried on, cf. Figure 4. 13. As expected, the higher the fracture energy, the smoother the degradation of the interface (higher area under the load displacement curves). It was found that a fracture energy of **G_{IIc}=1,000 N/mm** yielded a good correlation with experimental data.

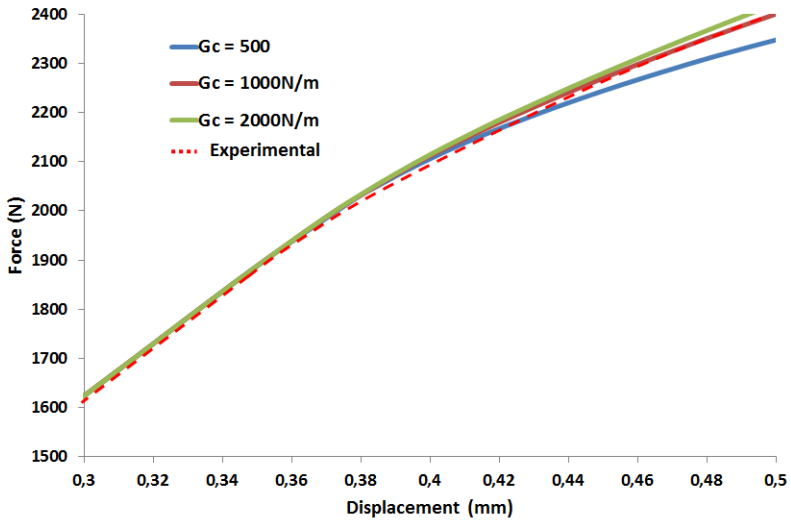

Figure 4. 13 Value of Gc needed to fit the experimental data

The fracture energy G_{Ic} is then chosen according to Turon, et al. [35] who defined a methodology to accurately predict delamination propagation using cohesive elements under mixed-mode fracture. They have shown that under mixed-mode conditions, the values of the interfaces strengths have an effect on the energy dissipated during delamination propagation. Hence, a relation between the interlaminar strengths and the fracture toughness must be imposed to ensure accurate predictions of delamination propagation under mixed-mode conditions:

$$\tau_{sh}^{0} = \tau_{3}^{0}\sqrt{\frac{G_{IIc}}{G_{Ic}}} \qquad \text{(Eq.4.17)}$$

where τ_{sh}^{0} is the interface shear strength, τ_{3}^{0} the interface strengths in mode I, G_{Ic} the fracture toughness under pure mode I and G_{IIc} the fracture toughness under pure mode II. As it was assumed that τ_{3}^{0}=τ_{sh}^{0}=14MPa, **G_{Ic}= G_{IIc}= G_{IIIc}=1,000N/mm.**

The parameters that have been determined are therefore a nominal shear stress **S_{13}^{0}=14MPa** and a fracture energy of **G_c = 1,000N/mm** with a **linear softening behaviour**. The damage initiation criteria chosen is the maximum stress criteria with **S_{33}^{0}=S_{13}^{0}=S_{23}^{0}=14MPa**, and the cohesive zones have initial stiffnesses of **K_{nn}=2.3x10^6 N/mm^3** and **K_{ss}=K_{tt}=1.1x10^6 N/mm^3**.

2.2.5. Results and discussion

The comparison between the resulting force-displacement curve (for an imposed displacement of 2.3mm) and the experimental data is plotted in Figure 4. 14. The

experimental force-displacement curve of the test specimen Long2 has been taken as the reference experimental data.

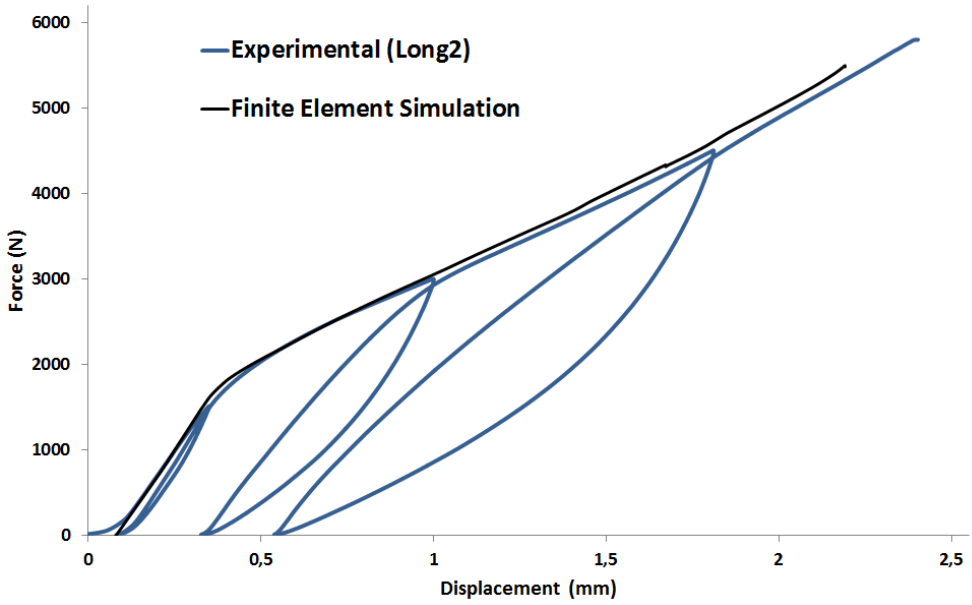

Figure 4. 14 Numerical correlations with experimental data

The identified cohesive parameters allow a good correlation between experimental and numerical data. In particular, the choice of the fracture energy G_c allows to correlate the post-interlaminar damage bending stiffness and the experimental test response. This still relies on a linear elastic behaviour of the composite laminate and embedded cables whereas these materials are known to exhibit a highly non-linear behaviour. Hence, a linear elastic model should over-estimate the experimental data as observed in the previous section with the blank specimens. It is then likely that the actual fracture energy may be higher than 1,000 N/mm.

Nevertheless, this allows us to get further insights into the tensile and inter-laminar strains distribution within the multifunctional test specimens as a function of the displacement of the crosshead as presented in Figure 4. 15.

It illustrates the coupling between slipping within the cables and fibre breakage observed experimentally at the interfaces with the embedded cables. Indeed, it is shown that once slipping/delamination is initiated in the cohesive zones, it induces a non-uniform distribution of the tensile strains through the thickness of the test specimens. As a consequence, every composite layup behaves like a single composite laminate beam under bending, with the back face composite plies loaded in tension. This ultimately leads to fibre failure of those composite plies under tensile strains.
In particular, tensile strains higher than 3.5% (when failure occurs numerically according to the modelling of the blank test specimens) appear from a displacement of the cross-head of 2.0mm (against approximatively 2.4mm experimentally). Hence, the numerical model tends to predict a lower ultimate failure load than the experimental values.

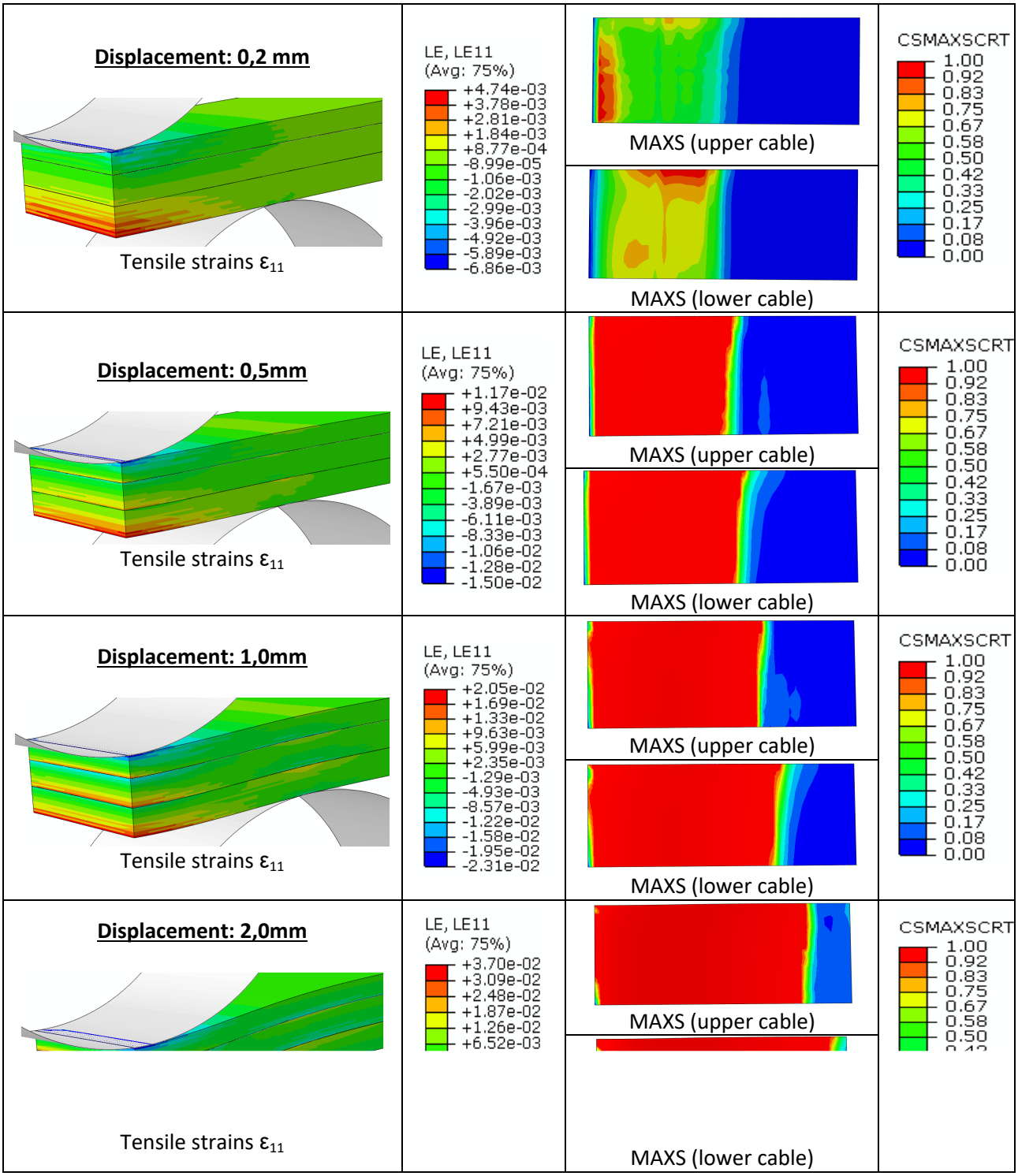

Figure 4. 15 Distribution of tensile strains as a function of the displacement of the cross-head and associated damage initiation (MAXS) within the cohesive zones

2.2.6. Concluding remarks: failure of the structure under shear loadings

A finite element model was developed under ABAQUS CAE to model the inter-laminar damage (slipping and de-cohesion) which occurs within the flat cables under out-of-plane deformations. Cohesive zones were defined to account for this damage mechanism. The parameters of these cohesive zones have been fitted to experimental data, which yielded a

good correlation. In particular, it highlighted the coupling between slipping occurring within the cables and the resulting internal fibre breakage of composite plies.

The next section presents numerical and experimental correlations on the damage modes of the structure under impact loads with the use of a progressive damage model.

3. Failure of the multifunctional structure under impact tests

In an effort to reproduce the damage mechanisms observed experimentally under impact testing, numerical modelling of the impact tests was performed under ABAQUS/explicit.

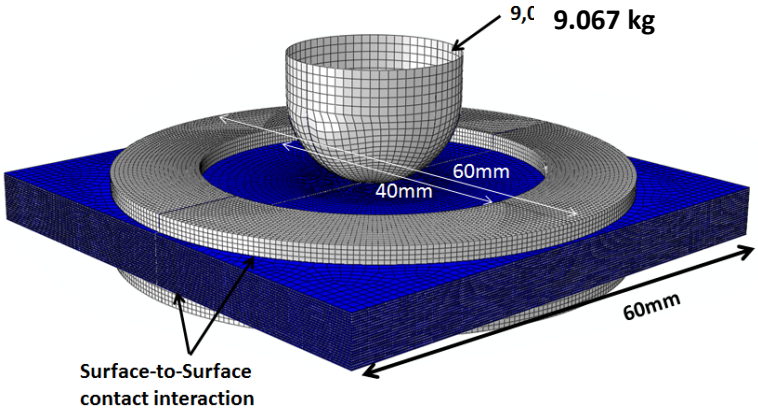

Figure 4. 16 Finite element model of the test specimens

Similar geometry, mesh and contact interactions (including cohesive interactions) were used to build this model. The 3D geometry is detailed in Figure 4. 16. To model the impact event, the impactor was modelled as a rigid body with a mass of 9.067kg and an initial speed of 1,490m.s^{-1} for a 10J impact and 1,820 m.s^{-1} for a 15J impact. Hence, the impact energy is provided to the model in the form of kinetic energy.
In addition, a user-defined constitutive law was used to model the mechanical behaviour of the composite plies thanks to a VUMAT subroutine based on the progressive damage model detailed in the previous section.

3.1. Calibration of the progressive damage model

The user-defined VUMAT subroutine is based on the model referenced MAT162 implemented in LS-DYNA [38] which is based on the principle of progressive failure of Hashin [40] and damage mechanics of Matzenmiller et al. [18]. The complete model uses a set of seven quadratic failure criteria related to fibre fracture, fibre crush, fibre shear, in-plane matrix crack and delamination.

3.1.1. Crush strength, punch-shear strength and inter-laminar shear strength

The parameters used are listed in Table 4. 4. In particular, the crush strength X_{3c} and punch-shear strength S_{FS} are unknown for this material. Yet, Xiao et al. [38] relate a series of tests performed by Materials Science Corporation on a plain weave E-glass using laterally constrained transverse compressive testing fixture. These tests yielded a crush strength between 607-758MPa and a fibre shear strength between 228-310 MPa. In this work, X_{3c}=650MPa and S_{FS}=300MPa (as used by Xiao et. al [38]). The inter-laminar shear strengths (S_{13} and S_{23}) and tensile strengths (X_{1T} and X_{2T}) are provided by the manufacturer.

The in-plane shear strength is assumed equal to 75MPa, which neglects the in-plane shear softening effects.

E_{11} (GPa)	E_{22} (GPa)	E_{33} (GPa)	v_{12}	v_{13}	v_{23}	G_{12} (GPa)
12.04	12.04	5.59	0.18	0.48	0.48	2.36 GPa
G_{13} (GPa)	G_{23} (GPa)	X_{1T} (MPa)	X_{2T} (MPa)	X_{3C} (MPa)	S_{12} (MPa)	S_{13}=S_{23} (MPa)
1.53	1,53	450	450	850	75	55
S_{FS} (MPa)	φ	m_1	m_2	m_3	m_4	S
300	10	2	2	1	1	1.5

Table 4. 4 Mechanical properties used to model the glass/epoxy woven fabric

3.1.2. Softening parameters m_j

As related by Xiao et al. [38], smaller values of the strain softening parameters result in a more ductile behavior of the material while higher values give the material a more brittle behavior. Here, these damage parameters are calibrated according to the damage sequence which has been identified experimentally as:

- Delamination initiation & propagation (Damage mode No.7), monitored by the parameter m_4
- Fibre tension and shear failure (Damage modes No.1 and No.2), monitored by the parameters m_1 & m_2

It is important to notice that the model was run without activation of the damage modes No.3 and No.4 which corresponds to the in-plane fibre compressive failure modes. This choice was motivated by both the lack of knowledge on the damage of this material under in-plane compressive strains, and by the supposed low influence of such a failure mode on the overall impact response of the material.

The model is first applied by only activating the No.7 damage mode (delamination failure mode) for an impact energy of 10J and 15J with different values of m_4, cf. Figure 4.16.

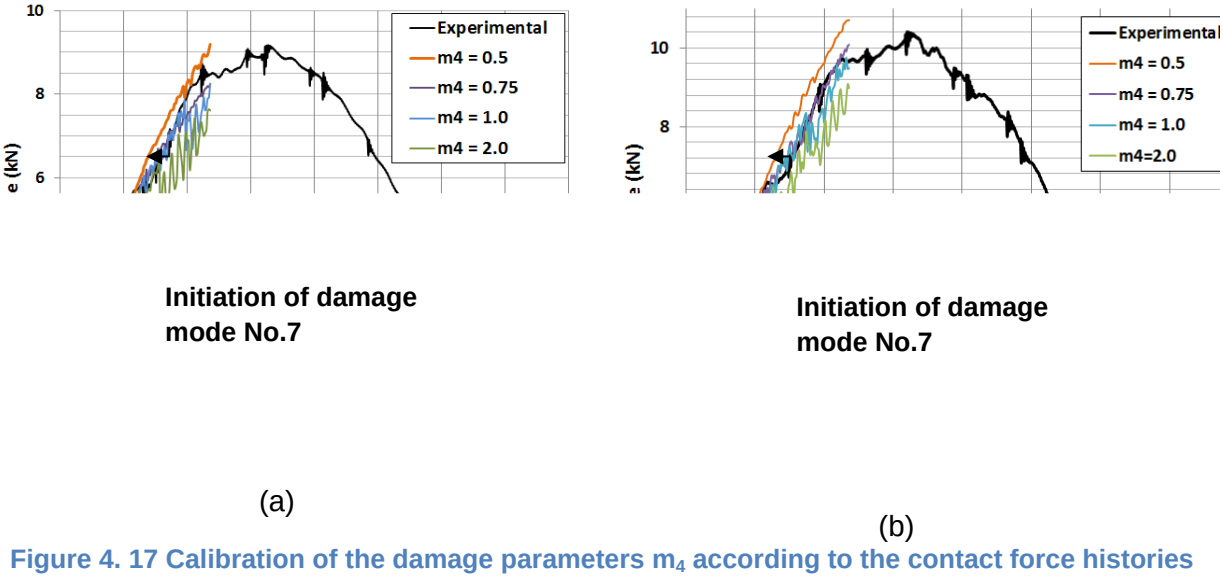

Figure 4. 17 Calibration of the damage parameters m_4 according to the contact force histories of the test specimens impacted at (a) 10J and (b) 15J

The initiation of damage mode No.7 seems to fit reasonably well with the first experimental load drop observed on the contact force histories. A value of m_4=0.5 is found to have barely any influence at all, while a value m_4=2 seems to underestimate the damage threshold. A value of m_4=0.75 is chosen as it provides an excellent prediction as regards to the test specimens impacted at 15J.

The model is then run with the damage modes No.1, No.2 (tension-shear fibre failures) and No.6 (in-plane shear failure mode) activated for which damage propagation and softening behaviours are controlled by the softening parameters m_1 and m_2 (it is assumed that m_1=m_2 since the composite material is a quasi-equilibrated woven fabric).

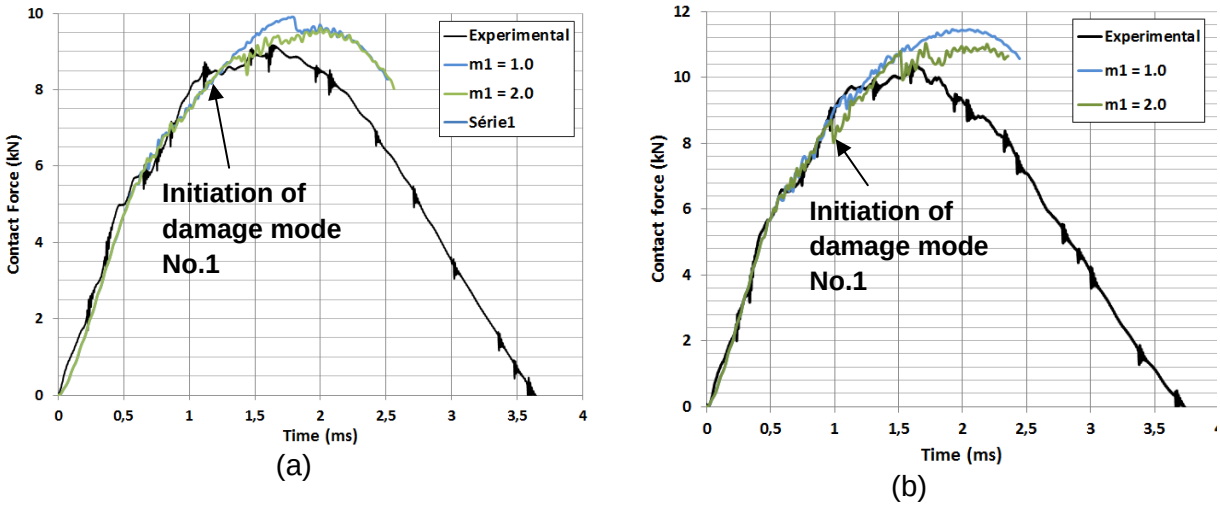

Figure 4. 18 Calibration of the damage parameters m_1 and m_2 (m_1=m_2) according to the contact force histories of the test specimens impacted at (a) 10J and (b) 15J

It is observed that tensile failure is predicted near the peak contact force for an impact energy of 10J, cf. Figure 4. 18 (a). On the contrary, it is predicted earlier for an impact energy of 15J, which seems to be under-estimated as regards to the experimental contact force history, cf. Figure 4. 18 (b). Based on these observations, a strain softening parameter m_1=m_2=2.0 is chosen.

Figure 4. 19 further illustrates that such parameters yield reasonably good correlations between the maximum displacement and peak contact forces. Yet, as the area under the load-displacement curve is under-estimated, this seems to indicate that damage propagation is not well-correlated (some energy-dissipative mechanisms are not modelled).

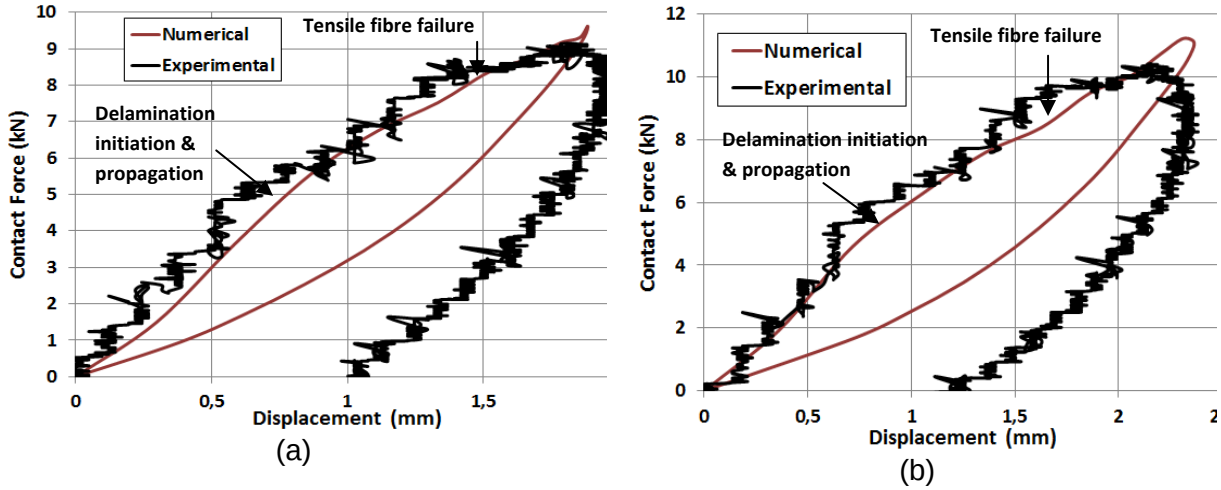

Figure 4. 19 Numerical and experimental correlations on the force-displacement curves of test specimens impacted at (a) 10J and (b) 15J

Modelling accurately damage propagation and the associated energy-dissipative mechanisms is challenging and would require much more effort in terms of experimental testing and numerical modelling. In addition, as damage initiation is well-correlated, the model looks promising in predicting the damage within the structure under low energy impact tests.

3.2. Results

Once calibrated, the model allows modelling the damage modes observed experimentally on the blank and multifunctional test specimens.

3.2.1. Blank test specimens

As noted previously, the first damage modes observed are delamination initiation and propagation in the shape of a ring shape through the thickness, cf. Figure 4.18.

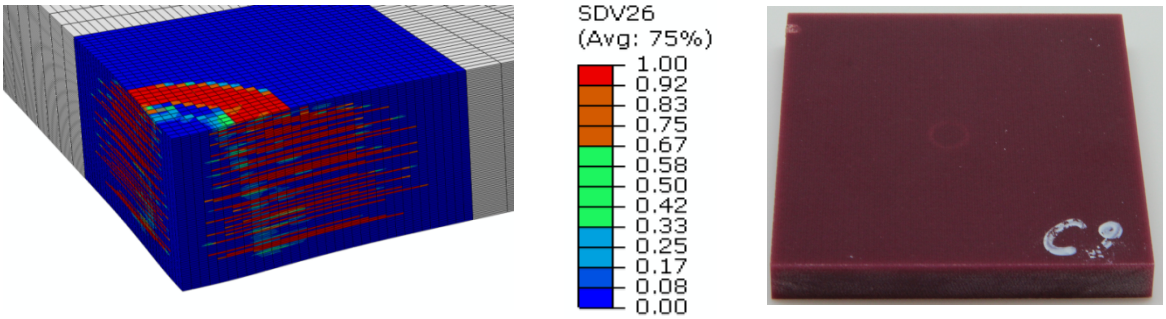

Figure 4. 20 Delamination initiation (damage mode No.7 stored in the state variable SDV26) in the form of a ring shape

This is followed by the tensile-shear fibre failures on the back face of the test specimens, cf. Figure 4. 21.

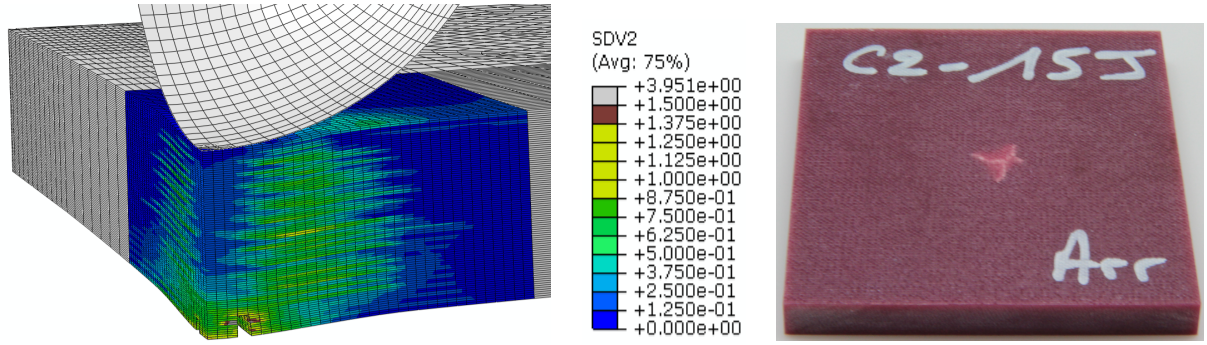

Figure 4. 21 Initiation of damage mode No.1 (stored in the state variable SDV2) on the back face

However, what is not represented in the model is the associated delamination that arise in the bending area on the back face due to the ply fractures, cf. Figure 4. 22. Indeed, the delamination failure mode included in the model allows capturing the inter-laminar damage but does not lead to proper de-cohesion between the plies since it does not take any physical interface into account.



Figure 4. 22 Microscopic observation of a test specimen impacted at 15J showing the intra-laminar (ply fracture) damage and inter-laminar (delamination) damage

3.2.2. Multifunctional test specimens

The model is then run with the same set of parameters and an identical mesh size on a multifunctional architecture integrating cohesive interactions at the interface with the cables, as determined in section 2 of the present chapter.

From numerical simulations, it is confirmed that the first load drop observed is due to the initiation of the maximum stress criterion within the cohesive elements, followed by damage propagation. The initiation and propagation of this inter-laminar damage matches well with the experimental contact force history, cf. Figure 4. 23. This is followed by the initiation of tensile-shear fibre failure at approximately t=1,5ms, which corresponds to the second load drop observed experimentally. As the displacement of the impactor increases, the peak contact force is over-estimated by the model, as well as the unloading part of the curve, similarly to what was noticed on blank test specimens (the model lacks accuracy in terms of energy dissipation and damage propagation).

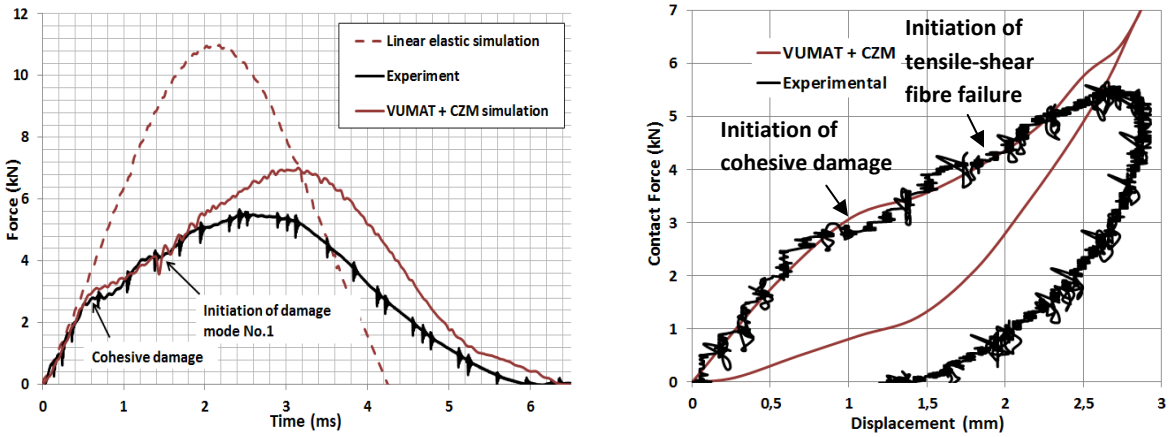

Figure 4. 23 Numerical and experimental contact force history and force-displacement curve of a multifunctional test specimen impacted at 10J (CZM: Cohesive Zone Model)

Figure 4. 24 and Figure 4. 25 illustrate the difference of damage mechanisms between the two kind of test specimens. While the transverse shear strains result in delamination initiation and propagation through-the-thickness of the blank test specimens, they only seem to initiate inter-laminar damage within the first composite sequence of the multifunctional test specimens, cf. Figure 4. 24.

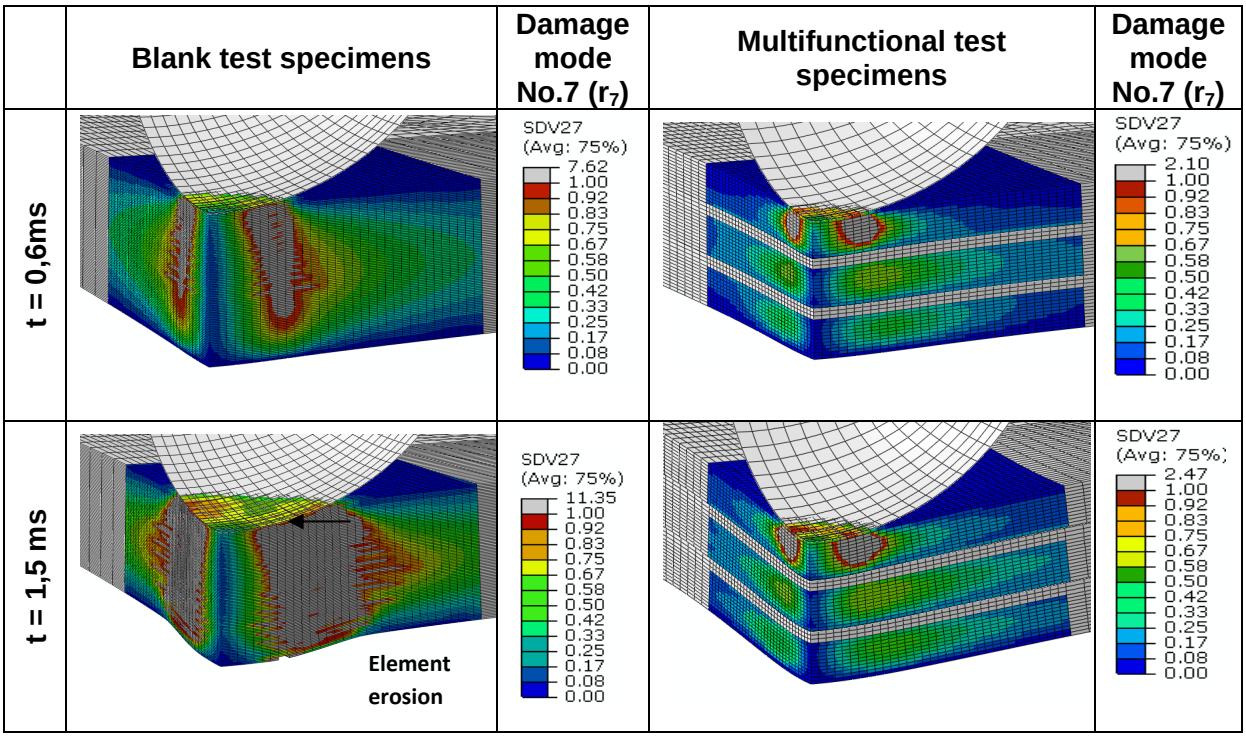

Figure 4. 24 Delamination initiation criteria (SDV27=r_7>1) on the blank and multifunctional test specimens impacted at 10J at t=0.6ms and t=1.5ms

As observed experimentally, this result in internal tension-shear fiber failure of the composite plies at the upper interface with each cable, cf. Figure 4. 25.

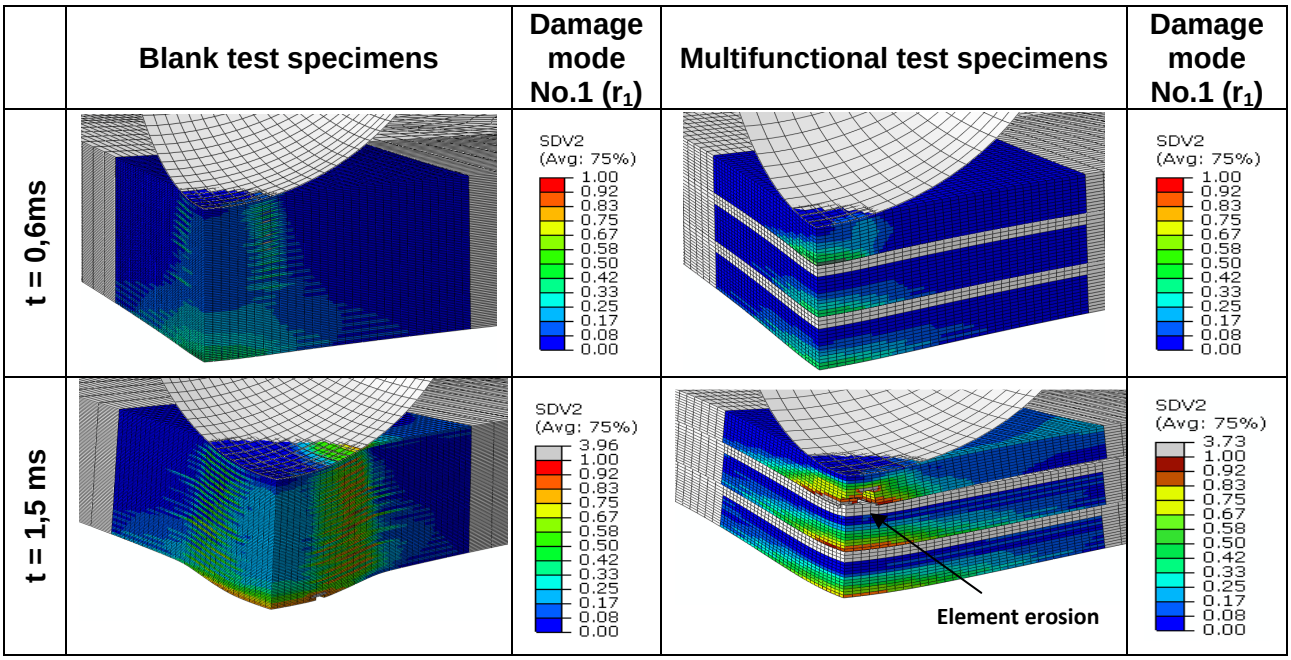

Figure 4. 25 Initiation of tension-shear fibre failure (SDV2=r1>1) on the blank and multifunctional test specimens impacted at 10J at t=0.6ms and t=1.5ms

4. Concluding remarks

A progressive damage model, coupled to cohesive interactions, was implemented in a finite element model thanks to a VUMAT subroutine under ABAQUS to model the failure of the multifunctional test specimens under impact tests.

The cohesive interactions constitutive parameters were first determined by fitting the numerical data with the experimental data resulting from the quasi-static short 3 point bend tests. Then, the parameters of the progressive damage model were determined by fitting the experimental and numerical data on impacted blank test specimens.

Applied the multifunctional test specimens, the model successfully captured the initiation of the two main damage modes observed experimentally and leading to a degradation of the electrical performances of the embedded cables. However, some discrepancies were observed between the simulated results and the experimental force-displacement curves, especially regarding the unloading phase and the extent of damage. This is mainly attributed to the strong assumptions made about the modelling of the embedded cables, which were treated as homogeneous layers with an elastic behaviour, and about the parameters of the progressive damage model which requires further experimental testing to accurately capture all the damage mechanisms that occur during the impact. Generally, the extent of damage seemed to be over-predicted by the numerical simulations, in particular as regards to delaminations.

However, such an approach allowed reasonably good correlations with the experimental data and seems promising to estimate the robustness of such multifunctional sandwich structures with regards to low energy impacts.

References

[1] J. Whitcomb and K. Srirengan, 'Effect of various approximations on predicted progressive failure in plain weave composites', *Compos. Struct.*, vol. 34, no. 1, pp. 13–20, 1996.

[2] M. Donadon, C. V, S. de Almeida, rgio F. M, M. A. Arbelo, and A. R. de Faria, 'A Three-Dimensional Ply Failure Model for Composite Structures', *Int. J. Aerosp. Eng.*, vol. 2009, p. e486063, Sep. 2009.

[3] G. Perillo, N. P. Vedvik, and A. T. Echtermeyer, 'Numerical analyses of low velocity impacts on composite. Advanced modelling techniques', in *Proceedings of the Simulia customer conference–2012*, 2012.

[4] R. Karkkainen, 'A Stress Gradient Failure Theory for Textile Structural Composites', University of Florida, 2006.

[5] A. Mishra and N. K. Naik, 'Failure initiation in composite structures under low-velocity impact: Analytical studies', *Compos. Struct.*, vol. 92, no. 2, pp. 436–444, Jan. 2010.

[6] C. Menna, D. Asprone, G. Caprino, V. Lopresto, and A. Prota, 'Numerical simulation of impact tests on GFRP composite laminates', *Int. J. Impact Eng.*, vol. 38, no. 8, pp. 677–685, 2011.

[7] C. Hochard and Y. Thollon, 'A generalized damage model for woven ply laminates under static and fatigue loading conditions', *Int. J. Fatigue*, vol. 32, no. 1, pp. 158–165, Jan. 2010.

[8] Y. Thollon and C. Hochard, 'A general damage model for woven fabric composite laminates up to first failure', *Mech. Mater.*, vol. 41, no. 7, pp. 820–827, Jul. 2009.

[9] M. Kollegal, S. N. Chatterjee, and G. Flanagan, 'Progressive failure analysis of plain weaves using damage mechanics based constitutive laws', *Int. J. Damage Mech.*, vol. 10, no. 4, pp. 301–323, 2001.

[10] S. Daggumati, W. Van Paepegem, J. Degrieck, J. Xu, S. V. Lomov, and I. Verpoest, 'Local damage in a 5-harness satin weave composite under static tension: Part II – Meso-FE modelling', *Compos. Sci. Technol.*, vol. 70, no. 13, pp. 1934–1941, Nov. 2010.

[11] P. Navarro *et al.*, 'Semi-continuous approach for the study of impacts on woven composite laminates: Modeling interlaminar behavior with a specific interface element', *Int. J. Impact Eng.*, vol. 75, pp. 184–193, Jan. 2015.

[12] F. Pascal, P. Navarro, S. Marguet, and J.-F. Ferrero, 'On the modelling of low to medium velocity impact onto woven composite materials with a 2D semi-continuous approach', *Compos. Struct.*, vol. 134, pp. 302–310, Dec. 2015.

[13] A. Qiu, K. Fu, W. Lin, C. Zhao, and Y. Tang, 'Modelling low-speed drop-weight impact on composite laminates', *Mater. Des.*, vol. 60, pp. 520–531, Aug. 2014.

[14] R. C. Batra, G. Gopinath, and J. Q. Zheng, 'Damage and failure in low energy impact of fiber-reinforced polymeric composite laminates', *Compos. Struct.*, vol. 94, no. 2, pp. 540–547, Jan. 2012.

[15] O. T. Topac, 'Experimental and Numerical Investigation of Damage Process in Composite Laminates under Low-Velocity Impact', Middle East Technical University, 2016.

[16] M. R. Karim, 'Constitutive modeling and failure criteria of carbon-fiber reinforced polymers under high strain rates', The University of Akron, 2005.

[17] S. Treutenaere, F. Lauro, B. Bennani, G. Haugou, T. Matsumoto, and E. Mottola, 'Constitutive modelling of the strain-rate dependency of fabric reinforced polymers', *Int. J. Impact Eng.*, vol. 108, pp. 361–369, Oct. 2017.

[18] A. Matzenmiller, J. Lubliner, and R. . Taylor, 'A constitutive model for anisotropic damage in fiber-composites', *Mechanics of Materials*, pp. 125–152, 1995.

[19] H. Ullah, A. R. Harland, T. Lucas, D. Price, and V. V. Silberschmidt, 'Finite-element modelling of bending of CFRP laminates: Multiple delaminations', *Comput. Mater. Sci.*, vol. 52, no. 1, pp. 147–156, 2012.

[20] J.-K. Kim and M.-L. Sham, 'Impact and delamination failure of woven-fabric composites', *Compos. Sci. Technol.*, vol. 60, no. 5, pp. 745–761, 2000.
[21] H. Fang, M. Gutowski, M. DiSogra, and Q. Wang, 'A numerical and experimental study of woven fabric material under ballistic impacts', *Adv. Eng. Softw.*, vol. 96, pp. 14–28, Jun. 2016.
[22] G. A. O. Davies, D. Hitchings, and G. Zhou, 'Impact damage and residual strengths of woven fabric glass/polyester laminates', *Compos. Part Appl. Sci. Manuf.*, vol. 27, no. 12, pp. 1147–1156, 1996.
[23] L. Karaoglan, A. K. Noor, and Y. H. Kim, 'Frictional contact/impact response of textile composite structures', *Composite Structures*, pp. 269–280, 1997.
[24] J. Brewer and P. Lagace, 'Quadratic stress criterion for initiation of delamination', *Journal of Composite Materials*, pp. 1141–1155, 1988.
[25] C. Lopes and Z. Gürdal, 'Simulation of Low-Velocity Impact Damage on Composite Laminates', presented at the 50th AIAA/ASME/ASCE/AHS/ASC Structures, Structural Dynamics, and Materials Conferences, Palm Springs, California, 2009.
[26] K.-H. Jung, D.-H. Kim, H.-J. Kim, S.-H. Park, K.-Y. Jhang, and H.-S. Kim, 'Finite element analysis of a low-velocity impact test for glass fiber-reinforced polypropylene composites considering mixed-mode interlaminar fracture toughness', *Compos. Struct.*, vol. 160, pp. 446–456, Jan. 2017.
[27] C. S. Lopes, P. P. Camanho, Z. Gürdal, P. Maimí, and E. V. González, 'Low-velocity impact damage on dispersed stacking sequence laminates. Part II: Numerical simulations', *Compos. Sci. Technol.*, vol. 69, no. 7–8, pp. 937–947, Jun. 2009.
[28] D. Morin, B. Bourel, B. Bennani, F. Lauro, and D. Lesueur, 'A new cohesive element for structural bonding modelling under dynamic loading', *Int. J. Impact Eng.*, vol. 53, pp. 94–105, Mar. 2013.
[29] A. Turon, P. P. Camanho, J. Costa, and J. Renart, 'Accurate simulation of delamination growth under mixed-mode loading using cohesive elements: Definition of interlaminar strengths and elastic stiffness', *Compos. Struct.*, vol. 92, no. 8, pp. 1857–1864, Jul. 2010.
[30] P. P. Camanho, C. G. Dàvila, and M. F. Moura, 'Numerical Simulation of Mixed-Mode Progressive Delamination in Composite Materials', *Journal of Composite Materials*, p. 37 1415-1438, 2003.
[31] P. P. Camanho and C. G. Dàvila, 'Mixed-Mode Decohesion Finite Elements for the Simulation of Delaminations in Composite Materials', *Technical Memorandum*, NASA Langley Research Center, Hamton, 2002.
[32] M. L. Benzeggagh and M. Kenane, 'Measurement of mixed-mode delamination fracture toughness of unidirectional glass/epoxy composites with mixed-mode bending apparatus', *Compos. Sci. Technol.*, vol. 56, no. 4, pp. 439–449, 1996.
[33] T. Diehl, 'On using a penalty-based cohesive-zone finite element approach, Part I: Elastic solution benchmarks', *Int. J. Adhes. Adhes.*, vol. 28, no. 4–5, pp. 237–255, Jun. 2008.
[34] A. Turon, C. G. Dávila, P. P. Camanho, and J. Costa, 'An engineering solution for using coarse meshes in the simulation of delamination with cohesive zone models', 2005.
[35] Z. Zou, S. R. Reid, S. Li, and P. D. Soden, 'Modelling Interlaminar and Intralaminar Damage in Filament-Wound Pipes under Quasi-Static Indentation', *Journal of Composite Materials*, p. 36 (4):477-499, 2002.
[36] L. Daudeville, O. Allix, and P. Ladeveze, 'Delamination analysis by damage mechanics - some applications', *Composites Engineering*, p. 5 17-24, 1995.
[37] E. Panettieri, D. Fanteria, and F. Danzi, 'A sensitivity study on cohesive elements parameters: Towards their effective use to predict delaminations in low-velocity impacts on composites', *Compos. Struct.*, vol. 137, pp. 130–139, Mar. 2016.
[38] A. Turon, C. G. Dávila, P. P. Camanho, and J. Costa, 'An engineering solution for mesh size effects in the simulation of delamination using cohesive zone models', *Eng. Fract. Mech.*, vol. 74, no. 10, pp. 1665–1682, Jul. 2007.

[39] J. R. Xiao, B. A. Gama, and J. W. Gillespie, 'Progressive damage and delamination in plain weave S-2 glass/SC-15 composites under quasi-static punch-shear loading', *Compos. Struct.*, vol. 78, no. 2, pp. 182–196, Apr. 2007.
[40] F. Soulas, C. Espinosa, F. Lachaud, S. Guinard, B. Lepetit, and I. Revel, 'Damage of composite structures under lightning strikes', in *Compte Rendus des JNC 19*, Lyon, 2015.
[41] *ABAQUS (2011) 'Abaqus Documentation'*, Dassault Systèmes, Providence, RI, USA. .
[42] Z. Hashin, 'Failure criteria for unidirectional fibre composites', *Journal of Applied Mechanics*, pp. 329–334, 1980.
[43] H. Ullah, A. R. Harland, and V. V. Silberschmidt, 'Damage and fracture in carbon fabric reinforced composites under impact bending', *Compos. Struct.*, vol. 101, pp. 144–156, Jul. 2013.

Chapter 5: Temperature-dependent bending stiffness and shear effects of a sandwich composite beam

Chapter 5: Temperature-dependent bending stiffness and shear effects of a sandwich composite beam

1. Literature Background *132*

2. Internal heating of the core due to resistive heating of the embedded wires *134*

2.1. Experimental characterisations *134*
2.1.1. Test method and setup 134
2.1.2. Results and Discussion 135

2.2. Numerical characterisations *136*
2.2.1. Theoretical background 136
2.2.2. Finite element modelling 138

2.3. Concluding remarks *143*

3. Temperature-dependent stiffness of the constituents *143*

3.1. Materials and test method *144*

3.2. Results *145*

3.3. Modelling of the temperature-dependent stiffness *145*

4. Sandwich composite beam theory *147*

4.1. Experimental temperature-dependent bending stiffness under dual cantilever mode *149*

4.2. Analytical calculation of the sandwich beam's bending stiffness *150*

4.3. Discussion on the shear correction factor *151*

4.4. Parameters sensitivity *152*

5. Finite Element Modelling *153*

5.1. Material Parameters *153*

5.2. Model description *154*

5.3. Results *155*

6. Concluding remarks *157*

The previous chapters unveiled the failure modes occurring in composite laminates embedding flat electrical cables. In particular, it was shown that the out-of-plane stresses where mainly transmitted through the cable's insulator resin which could lead to a degradation of the electrical performances of the embedded cables when the insulator was damaged (loss of insulation between adjacent wires).
Besides, among the various design and technological issues faced by composite structures embedding electrical devices (cf. Chapter 1), the effect of temperature has not been dealt with yet. From the articles reviewed, it appeared that the additional temperature generated by the embedded components needed to be taken into account to ensure that no excessive heating may affect the strength of each material. In addition, it also appears mandatory for our particular study to investigate on the influence of the temperature on the out-of-plane behaviour of the multifunctional structure which has been shown to be a critical issue.

These issues are addressed in the forthcoming chapter which deals with:

- The characterisation of the internal heating of the structure due to the resistive heating of the embedded wires
- The characterisation of the thermo-mechanical elastic behaviour of the structure under bending deformations

In particular, a methodology has been developed to investigate on the temperature-dependent bending behaviour of a sandwich beam designed as a model structure.
It consists in three layers of materials, two skins made of GFRP and a core with epoxy adhesive. At first, the constituents were characterized separately. Then, these temperature-dependencies have been included in an analytical solution based on the Timoshenko beam theory. This allows taking temperature-dependent shear effects on the bending stiffness of the sandwich assembly into account. Characterization was performed by means of DMA (Dynamic mechanical Analysis). Finite element analysis and structural calculations were used to simulate the effect of temperature on the behaviour of the sandwich structure.

1. Literature Background

The influence of temperature on the flexural and shear moduli of pultruded GFRP composite laminates was studied by Manalo et al. [1] by means of three-point static bending test at various temperatures. Their study was completed with investigations on the flexural behaviour of a sandwich system made of glass-fibre skins and phenolic core, including DMA characterisation to determine the glass transition temperature of the constituents. In addition, the sandwich beam theory was proven useful in predicting the temperature-dependent strength and stiffness of the sandwich beam. Yet, as the phenolic core presented high shear modulus and strength, the contribution of shear strains on the bending stiffness were neglected.

Ropers et al. [2] used rheometer-based bending experiments and DMA to assess the temperature-dependent bending behaviour of thermoplastic composites. In addition, a non-linear viscoelastic material model was able to represent the actual material bending behaviour. Margossian et al. [3] used DMA device for the bending characterisation of a unidirectional carbon fibre reinforced polyamide 6 composite. Timoshenko's and Euler Bernouilli's beam theories were successfully used to predict the strain rate dependency of the out-of-plane bending modulus of the test specimens. Once again, the inter-laminar shear effects appeared to be negligible due to the large free span length to thickness ratio of the test specimens.

As the out-of-plane shear moduli G13 and G23 are partly responsible for the shear component of the deflection of composite beams, Nagatsuka et al. [4], [5] investigated on the influence of the temperature on the out-of-plane shear modulus of discontinuous carbon fibre mat reinforced thermoplastics based on a modified double notched compression method. The temperature dependency of the out-of-plane shear modulus was successfully correlated with DMA derived test results on the matrix resin according to (Eq.5.1) to (Eq.5.3).

In these equations, G_f is the fibre shear modulus, V_f the volume fraction of fibre, Gm the matrix resin shear modulus, E_m the matrix resin elastic modulus, ϑ the matrix resin Poisson's ratio, E'm the storage modulus of the matrix resin determined with DMA and $\tan\delta$ the loss tangent which represents the phase difference between the strain-input and stress-output under dynamic mechanical analysis.

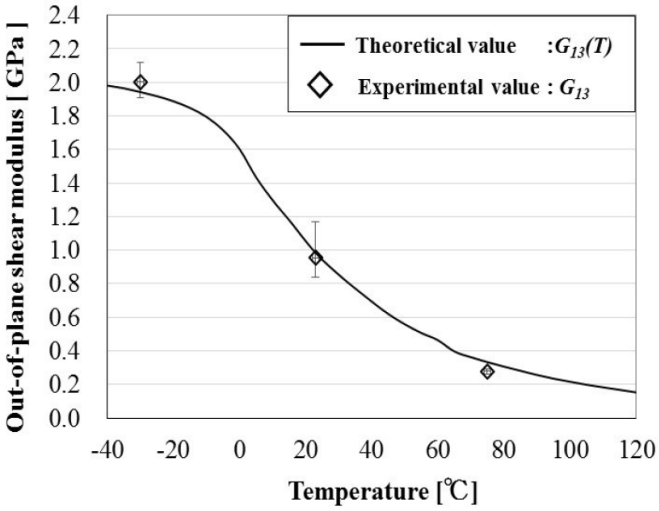

$$\begin{cases} G_{13}(T) = \dfrac{\alpha . G_f G_m(T)}{V_f G_m(T) + \alpha(1 - V_f) G_f} & (Eq.5.1) \\ G_m(T) = \dfrac{E_m(T)}{2(1+\vartheta)} & (Eq.5.2) \\ E_m(T) = E'_m(T).[(tan\delta)^2 + 1] & (Eq.5.3) \end{cases}$$

Figure 5. 1 Comparison of experimental G_{13} and theoretical $G_{13}(T)$ based on (Eq.5.1) to (Eq.5.3) as a function of temperature [15]

This seems to indicate a good correlation between DMA-derived mechanical properties and quasi-static testing-based mechanical properties. Actually, if similar trends are observed regarding temperature dependencies, discrepancies are often noted between DMA derived storage moduli and mechanical properties determined from quasi-static mechanical testing [6], [7], cf. Figure 5. 2.

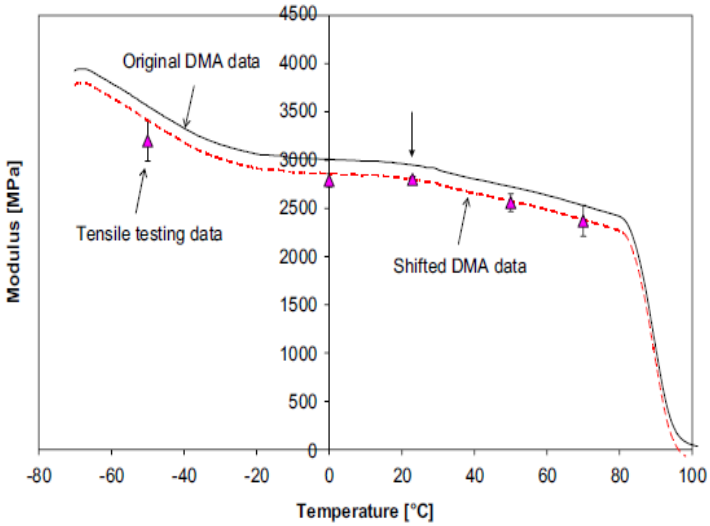

Figure 5. 2 DMA data under tensile mode need be corrected to fit mechanical testing data [16]

Hobbiebrunken et al. [7] calibrated their DMA moduli curves by shifting them to a lower temperature so as to match the static values obtained with tensile tests. This was also observed by Ropers, et al. [2] who had to apply a shift of 20K on their DMA measurement points to match the predicted bending stiffness of a woven textile reinforced thermoplastic prepreg (TPP) material. These discrepancies are attributed to the uncertainty on the exact temperature of the test samples, the instrumentation compliance, the boundary and experimental conditions, the test specimens dimensions, etc.

Yet, this seems to justify the transferability of the temperature dependency of the elastic moduli derived from DMA testing onto calculation of the bending stiffness of a sandwich system.

Therefore, it is proposed to address these issues through the study of a sandwich beam made of GFRP skins and an epoxy adhesive core where the contribution of shear strains are expected to be significant. Dynamic Mechanical Analysis (DMA) tests are performed to characterise separately the temperature-dependent stiffness of the skins and core, and implemented in an analytical and finite-element model to predict the temperature-dependent bending stiffness of the sandwich. The non-negligible temperature-dependent shear effects due to the low stiffness of the core as compared to the skins are also taken into account.

Yet, before presenting these investigations, the numerical and experimental characterisations of the internal heating of the structure (which motivated further studies on the temperature-dependent bending stiffness of the structure) are presented.

2. Internal heating of the core due to resistive heating of the embedded wires

This section investigates on the thermo-electrical coupling known as Joule effect which generates heat due to the resistive heating of an electrical conductor against the current flow. This additional temperature needs to be taken into account since the heat dissipation mechanisms within the multifunctional structure are different from the ones encountered in conventional wiring solutions. In particular, the total temperature near the cables has an influence on the choice and the design of the insulator [8], [9], and on the current-carrying capacity of the electrical conductors, cf. Table 5. 1.

Wire Size AWG	Nominal Section (mm²)	Max. Ohmic Resistance (Ω/km)	Maximum Current (A)
18	0.93	20.6	10
20	0.60	32.2	7.5
22	0.38	50.9	5.0

Table 5. 1 Current-carrying capacity of a round electrical conductor according to ESA/SCC No. 3901 [8]

2.1. Experimental characterisations

2.1.1. Test method and setup

A specific test specimen was manufactured to experimentally characterise the internal heating of the structure due to the resistive heating of the embedded wires. Previous to manufacturing, the middle conductor of each cable was removed and replaced by a thermocouple. In addition, two other thermocouples were embedded in the composite laminate on the edges of the test specimen, as depicted in Figure 5. 3. Every embedded wire was soldered between each other and linked to an intensity generator so that the same current intensity was implemented in every wire. In the meantime, thermocouples acquired the temperature within the test specimen. Currents of 5A, 6A, 7A and 8A were successively used until temperatures monitored by the embedded thermocouples showed a steady-state.

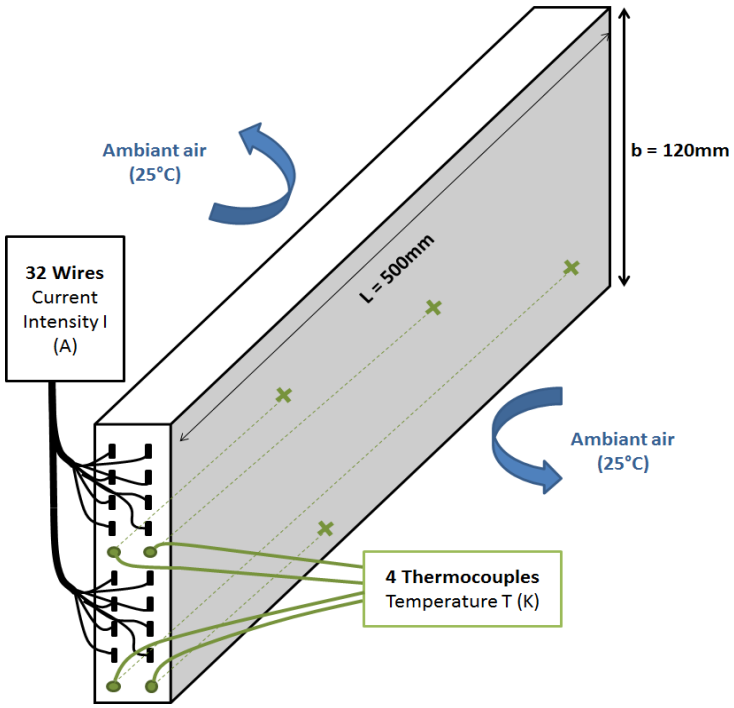

Figure 5. 3 Scheme of the experimental test setup to measure the temperature increase due to resistive heating of the embedded wires

2.1.2. Results and Discussion

The relative temperature increase $\Delta T = T - T_0$ (with a reference temperature taken as the initial temperature given by the thermocouples) as a function of time and current intensity is presented in Figure 5. 4. The results from thermocouple No.3 are not presented since it failed to provide any measurements.

It is observed that a current intensity of 5A induces a temperature increase of 9°C within the embedded cables (thermocouples 1 and 2) and 7.5°C within the composite laminate on the edges of the test specimen (thermocouple 4). The steady state is reached from approximatively 30'.The data recorded from the other current intensities are listed in Table 5.1.

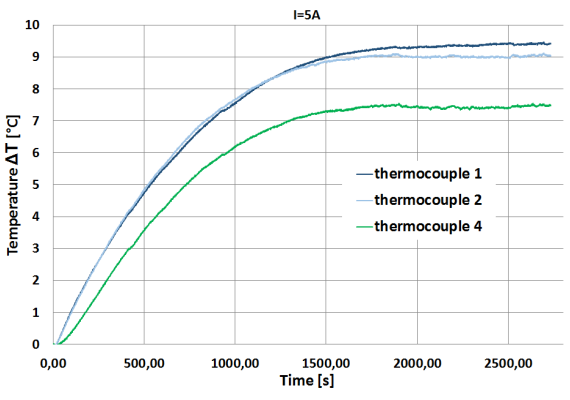

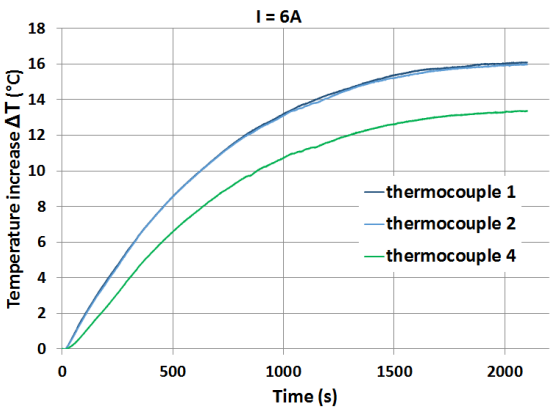

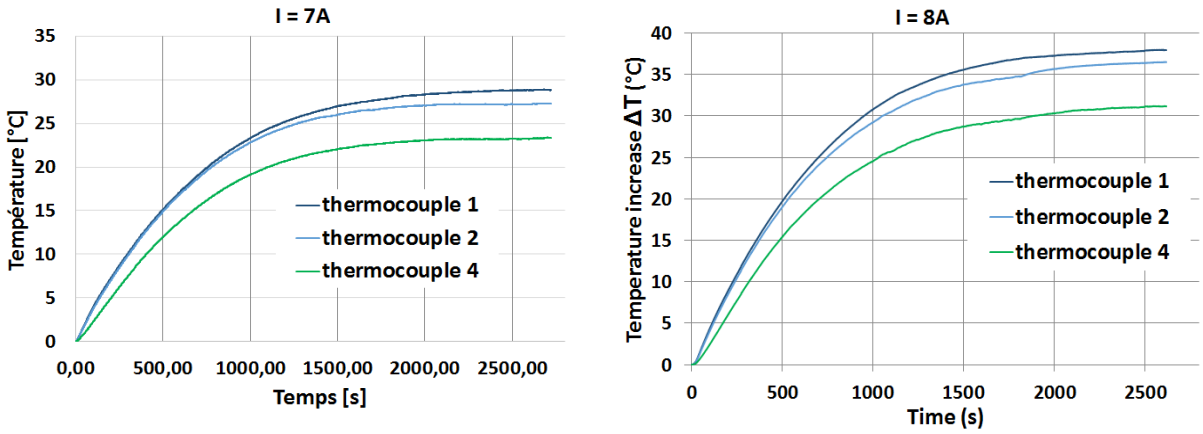

Figure 5. 4 Experimental increase of temperature as a function of the current intensity and position of the thermocouples

Up to a current intensity of 8A, the difference of temperature between the core of the cables and the surrounding composite laminate does not seem to exceed a few degrees (ΔT≈6°C at I=8A), cf. Figure 5. 5.

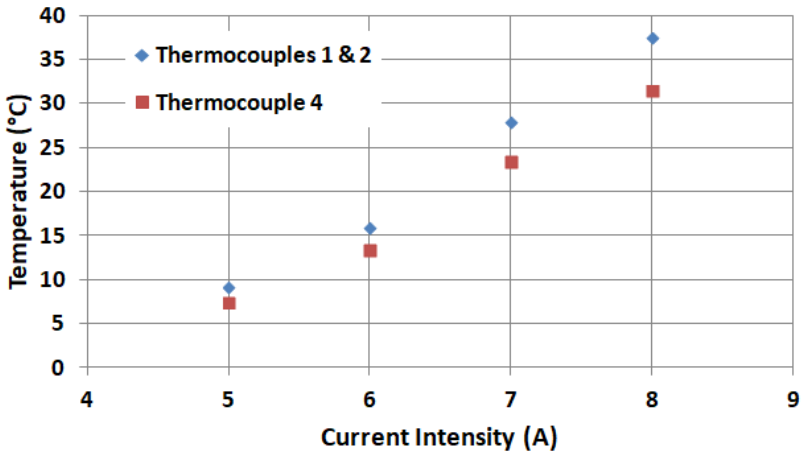

Figure 5. 5 Increase of temperature within the multifunctional structure as a function of current intensity in the permanent regime

2.2. Numerical characterisations

In order to get a better overview of the thermal field within the multifunctional structure, numerical simulations were carried out with a finite element mode.

2.2.1. Theoretical background

The numerical calculations are based on the traditional differential heat transfer equation, which is given in (Eq.5.1):

$$\nabla(k\nabla T) + W = \rho c \frac{\partial T}{\partial t} \qquad \text{(Eq.5.1)}$$

Where:

T : Temperature (K)
k : Thermal conductivity of the environment (W/m.K)
ρ : Density of the medium (kg/m^3)
c : Thermal capacity of the medium that transmits heat (J/kg.K)
W : Volumetric heat source intensity (W/m^3)
∇ : Gradient operator

The heat source intensity due to electrical current can be further expressed as a function of the electrical power according to (Eq.5.2) therefore defining a coupled electrical-thermal equation.

$$W = \vec{J}.\vec{E} \quad \text{(Eq.5.2)}$$

Where $\vec{J}$ is the current density ($\vec{J}$=σ$\vec{E}$) with σ the electrical conductivity in Ω^{-1}.m^{-1}) and $\vec{E}$ the electrical field intensity.

In addition, assuming a homogeneous distribution of the current through the copper braid section, the current density is equivalent to the current intensity divided by the cross section of the conductor:

$$\vec{J} = \frac{I}{A}\overrightarrow{e_x} \quad \text{(Eq.5.3)}$$

With $\overrightarrow{e_x}$ denoting the longitudinal direction of the conductor. Finally, the energy per unit volume in a 1D solid conductor is given by:

$$P_V = \vec{J}.\vec{E} = \vec{J}.\frac{1}{\sigma}\vec{J} = \frac{I^2}{\sigma A^2} \quad \text{(Eq.5.4)}$$

In addition, as the temperature of the cable increases due to Joule effect, the electrical conductivity decreases. This temperature-dependence of the electrical conductivity as a function of temperature can be expressed with equation (Eq.5.3):

$$\sigma = \frac{1}{\rho_0(1+\alpha(T-T_0)} \quad \text{(Eq.5.5)}$$

With ρ_0 the specific resistivity (=1.7x10^{-8} Ω.m) of the conductor at room temperature T_0 (T_0=20°C) and α a constant coefficient which is material-dependent. For a copper conductor, a typical value of α = 4.10^{-3} is commonly used.

Hence, the system of equations to be solved can be written as:

$$\begin{cases} \nabla(k\nabla T) + W_{HETVAL} = \rho c \frac{\partial T}{\partial t} \\ W_{HETVAL} = \frac{I^2}{\sigma A^2} \\ \sigma = \frac{1}{\rho_0(1+\alpha(T-T_0))} \end{cases} \quad \text{(Eq.5.6)}$$

This system of equation is applied to every electrical conductor and implemented in a subroutine in a finite element model under ABAQUS.

2.2.2. Finite element modelling

2.2.2.1. Geometrical modelling and meshing

A 2D geometrical modelling of the test specimen is created under ABAQUS CAE such as shown in Figure 5. 6 and Figure 5. 10.

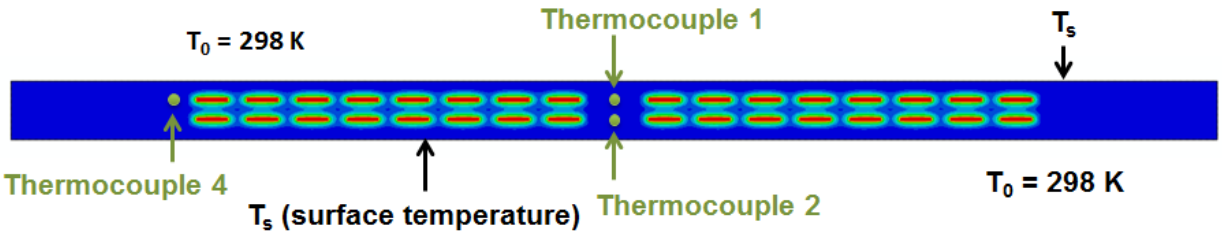

Figure 5. 6 Scheme of the experimental setup as modelled under ABAQUS

Every constituent of the multifunctional architecture is implemented (jacket, insulator, electromagnetic shielding, composite laminate), cf. Figure 5. 7. However, the composite host structure is treated as a homogeneous assembly (composite layers are not discretized) and the copper braided conductors are modelled as rectangular blocks of 3x0,35mm² (geometrical cross-section as given by the supplier). The analysis is only performed under thermo-electrical conditions, the mechanical properties of the materials are not implemented in the model. A fine mesh is required, in particular to mesh the 0,051mm thin jacket. In total, 21,745 DCC2D4 elements are used to mesh the part (4-nodes convection/diffusion quadrilateral elements).

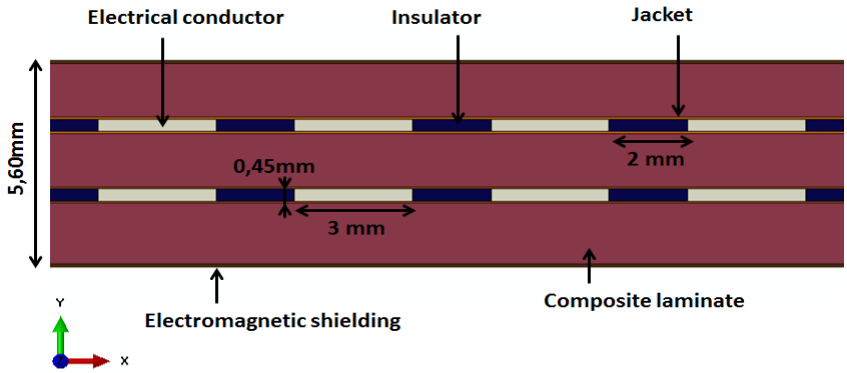

Figure 5. 7 Discretization of the constituents of the multifunctional structure in the coupled thermo-electrical finite element model

The thermal properties used in this model are listed in Table 5. 2.

	EM shielding	Insulator	Jacket	Electrical conductor	Composite laminate	
Conductivity (W/m.K)	392	0.25	0.12	392	X-axis 1.0	Y-axis 0.3
Specific heat (J/kg.K)	385.6	240	1090	385.6	900	
Density (kg/m3)	9,000	2,200	1,570	9000	1,930	

Table 5. 2 Material properties used in the thermo-electrical finite element model according to manufacturer's datasheet

2.2.2.2. Boundary and load conditions

The part is assumed to be exposed to the thermal environment of a room at ambient temperature (T_0=25°C). Therefore conductive heat transfer occurs inside the structure while convective and radiative heat transfers occur between the external surfaces of the test specimen and the surrounding environment. The convective heat transfer coefficients is calculated based on simplified equations for free convection of a vertical plane to air at atmospheric pressure in the laminar regime [10]:

$$h_c = 1.42\left(\frac{\Delta T}{b}\right)^{0.25} \quad \text{(Eq.5.7)}$$

with h_c the convective heat transfer coefficients (in W/m².K), ΔT the difference of temperature between the surface of the test specimen and the ambient air (in K) and b the vertical dimension (=0,12m). Besides, a radiative heat transfer coefficients is taken into account according to the standard UNI EN ISO 6946 [11] which recommends:

$$h_r = 4\varepsilon\sigma T_{av}^3 \quad \text{(Eq.5.8)}$$

with ε the surface emissivity (ε=0.07 for the electromagnetic shieldings and ε=0.9 for the composite), σ the Stefan-Boltzmann constant (in W/m².K^4) and T_{av} the average temperature between ambient air and the external surfaces. Numerically, a temperature-dependent heat transfer coefficients $H=h_r+h_c$ is implemented as a function of the test specimen's surface temperature, cf. Figure 5. 8. This is implemented as two interaction properties (one for the heat transfers occurring on the electromagnetic shieldings and one for the heat transfers occurring on the composite) with surface film conditions under ABAQUS.

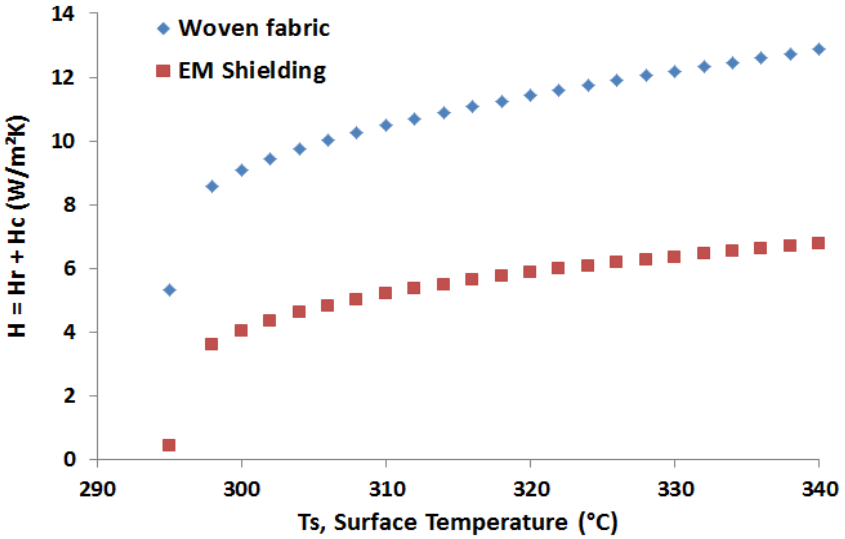

Figure 5. 8 Temperature-dependent heat transfer coefficients used in the FE model

2.2.2.3. Finite element implementation

The Joule Effect is implemented through a HETVAL subroutine, which permits to define a volumetric internal heat generation term in a material. Hence, the system of equations solved by Abaqus is written as:

$$\begin{cases} \nabla(k\nabla T) + W_{HETVAL} = \rho c \dfrac{\partial T}{\partial t} \\ W_{HETVAL} = \dfrac{I^2}{\sigma A^2} \\ \sigma = \dfrac{1}{\rho_0(1+\alpha(T-T_0))} \end{cases} \quad \text{(Eq.5.9)}$$

In addition, the volumetric heat source W_{HETVAL} applied to the electrical conductors is scaled based on the geometrical surface of the conductor (rectangle of 1,05mm²) and their effective heating surface (192 copper strands resulting in a surface of 0,6mm²). This scaling factor equals 0,57.

At each time step, the temperature inside a copper braid defines the electrical conductivity of the braid, which is used to compute the associated volumetric internal heating. The USDFLD subroutine is also used, and combined to the utility routine GETVRM to access the temperature at all copper material points, cf. Figure 5. 9. The state variables (initial temperature among the braids, and initial value of the volumetric internal heating) are initialized by the SDVINI subroutine. An initial temperature T0 of 298K is also implemented at all material points.

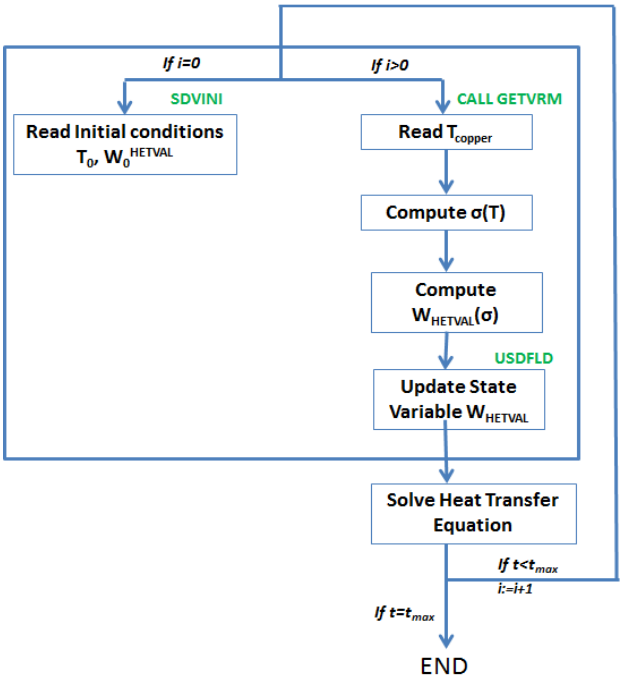

Figure 5. 9 Scheme of the coupled electro-thermal finite element analysis

2.2.2.4. Numerical results

Numerical and experimental correlations are presented in Figure 5. 10. Numerical predictions over-estimate the temperatures near the thermocouples for I=5A but tend to provide reasonably good correlations for the other currents considered (6A-8A). Therefore, such a coupled thermo-electrical model allows determining the temperature of any materials within the structure according to the amount of electrical current transmitted.

Such simulations are especially interesting to compare the difference of temperature increase between a conventional cable, and an embedded cable. Indeed, the normative reference ESA/ESCC No.3901 [8] specifies the maximum current allowable in a wire based on a “temperature rise of approximately 50°C above ambient temperature in a vacuum environment”, which yields I_{max} = 7.5A for an AWG20 conductor.

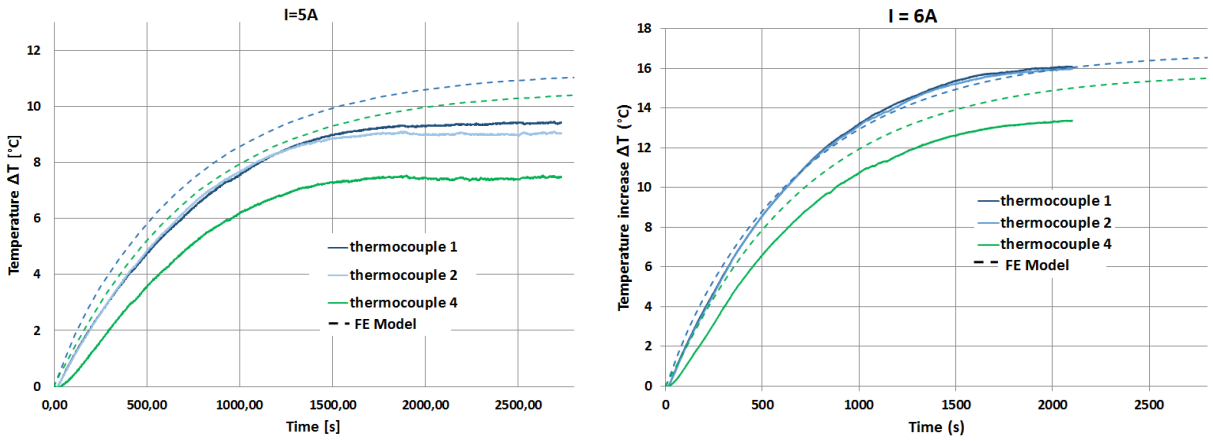

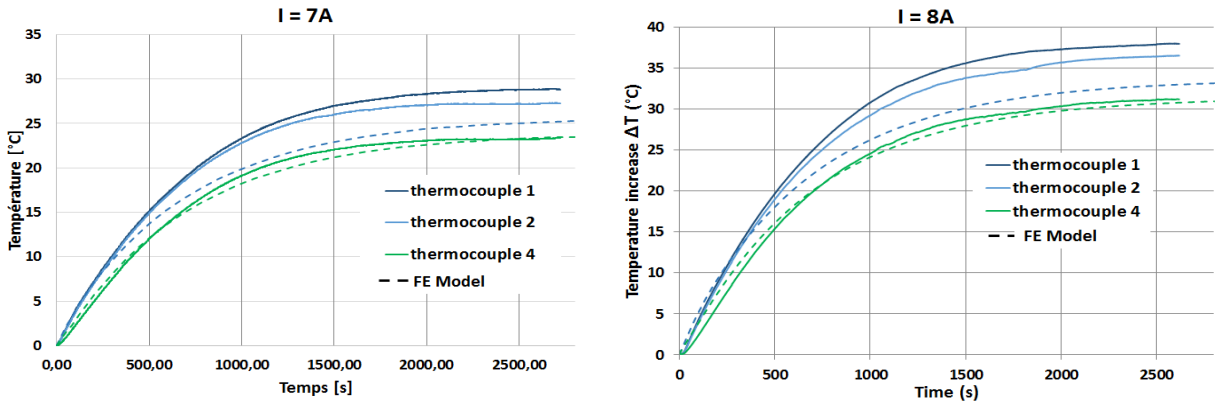

Figure 5. 10 Numerical and experimental correlations on the temperature increase within the structure as a function of the time and current intensity

The model developed previously can then be used to reproduce such conditions and to predict the maximum current allowable in an embedded cable composed of AWG20 conductors. Hence, the model was both run on a single flat cable and on the multifunctional structure. The convective heat coefficient was removed from the model so as to simulate a vacuum environment taking into account only radiative heat transfers at an ambient temperature of 293K. The emissivity of the electromagnetic shielding was kept at ε=0.07 while the emissivity of the polyimide jackets was fixed at 0.76 according to [12]. Several current intensities were implemented in both models so as to determine the threshold at which the temperature within the cables exceeded 50°C. This yielded I_{max}≈9A for a single cable and I_{max}≈3.5A for an embedded cable, cf. Figure 5.11.

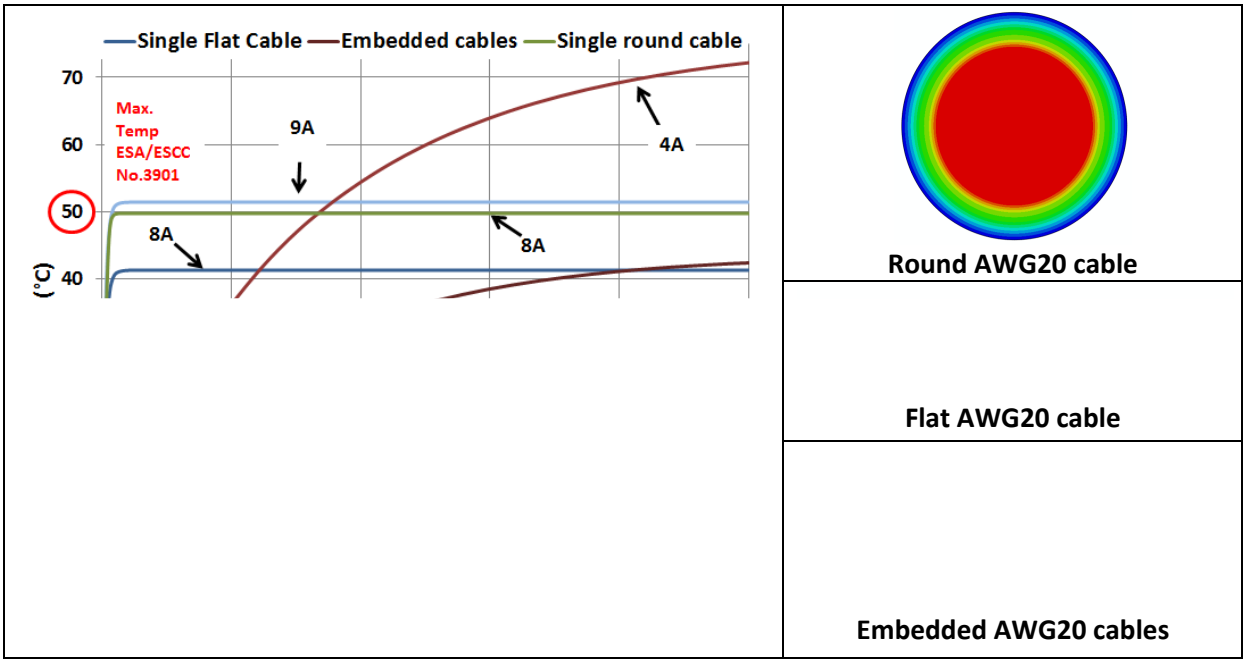

Figure 5. 11 Comparison of temperature increased due to Joule Effect between a single cable and an embedded cable, compared with the baseline of the normative reference ESA/ESCC No.3901

Hence, it is likely that due the embodiment of the cables and the associated temperature rise, such standards need to be reviewed and adapted to the multifunctional architecture.

2.3. Concluding remarks

A coupled thermo-electrical model has been developed to stand for the internal heating of the structure due to the resistive heating of the embedded wires. This allows determining the actual temperature of any materials and constituents within the multifunctional structure according to the electrical requirements of the system. In particular, it was underlined that the temperature rise within the embedded cables is likely to degrade the electrical performances of the cables since it induces a much greater temperature increase as regards to conventional wiring solution.

As it was presented previously, this motivated further investigations on the influence of the temperature on the mechanical behaviour of such sandwich-structured polymer composites, in particular under bending strains.

3. Temperature-dependent stiffness of the constituents

To investigate on the temperature-dependent bending of such assemblies, it is first proposed to characterize the temperature-dependent stiffness of the materials (skins and core) through Dynamic Mechanical Analysis. These temperature-dependencies will then be implemented in an analytical and finite element model. This will allow predicting the overall mechanical behaviour of the sandwich structure as a function of temperature. The method is developed based on a sandwich model made of GFRP composite skins and an epoxy adhesive core, as shown in Figure 5. 12.

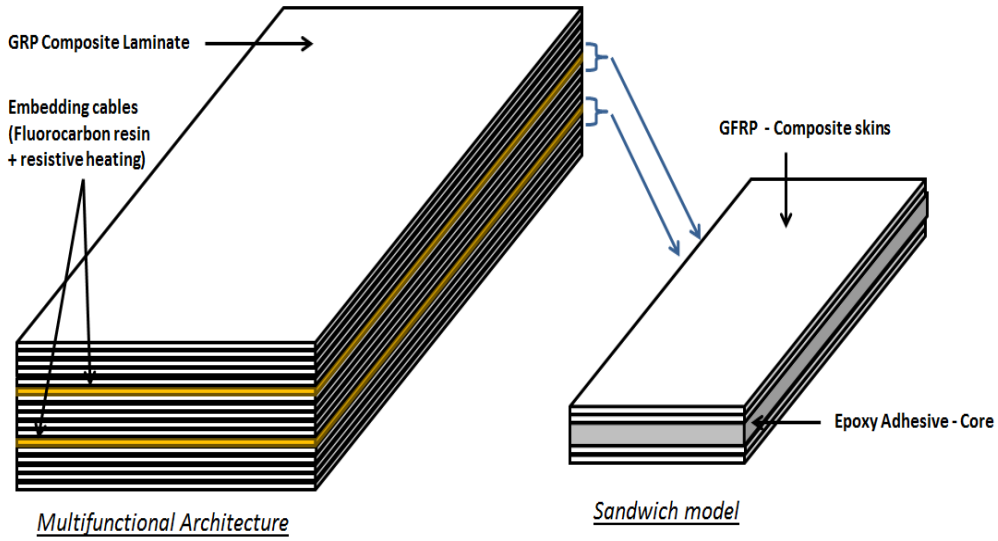

Figure 5. 12 The temperature-dependent bending behaviour of the multifunctional sandwich architecture is investigated based on a sandwich model

3.1. Materials and test method

A sandwich was manufactured and tested according to the table shown below. The composite skins were made of the same 4HS (harness satin) equilibrated glass-fibre woven fabric, referenced as Hexply1458/50%/120, and used to manufacture the multifunctional structure.

Two plies were cured in an autoclave for 3 hours at 160°C, 7bar pressure and under -0.8 bar vacuum. This resulted in a skin thickness e_p of 0,26 +/-0,02mm. Assuming no resin loss, the resin content and fibre volume were determined based on the cured ply thickness according to the manufacturer's datasheet: a resin content of 52% is estimated and associated with a fibre volume content of 31%. It is reminded that the reinforcement is an epoxy resin referenced as Hexply1458 with a glass transition temperature comprised between 145°C and 155°C according to manufacturer's datasheet.
Once cured, the GFRP composite skins were pasted with a bi-component structural epoxy adhesive referenced as AXSON H9952 composing the core of the sandwich. This assembly was first cured at 80°C for 2hours, and post-cured at 120°C for 1hour. The cured sandwich was approximately 1,6mm thick, with an epoxy adhesive core e_c = 1,05+/-0,05mm thick. Two kind of sandwich beams were manufactured: either with the skins oriented at 0°, or with the skins oriented at 45°.
In this study, the stiffness of the skins are denoted E_p and G_p while the stiffness of the core are denoted E_c and G_c.

<table>
<tr><th>Composite Skins (0° or 45°)</th><th>Epoxy Adhesive Core</th></tr>
<tr><td>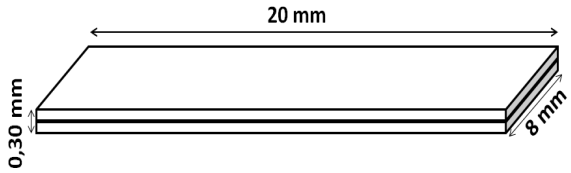
</td><td>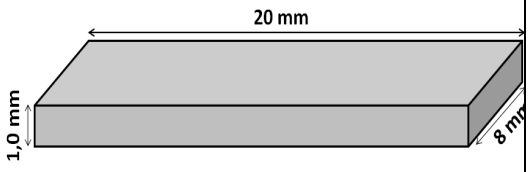
</td></tr>
<tr><td>DMA mode: tension</td><td>DMA mode: tension</td></tr>
<tr><td>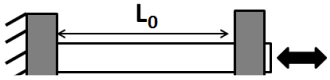
</td><td>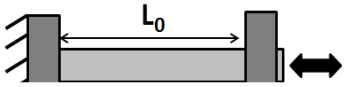
</td></tr>
<tr><td>Output : E_p (T), G_p(T)</td><td>Output : E_c (T), G_c (T)</td></tr>
<tr><td colspan="2">Sandwich Beam</td></tr>
<tr><td rowspan="2"></td><td>DMA mode: dual cantilever</td></tr>
<tr><td></td></tr>
<tr><td colspan="2">Output : Bending stiffness K_s(T)</td></tr>
</table>

The temperature-dependent storage modulus of the GFRP skins and epoxy adhesive core were first determined with a TA Instruments DMA Q800 machine, under the tensile mode between 25°C and 150°C with a heating rate of 5°C/min at a frequency of 1Hz. The temperature-dependent bending stiffness of the sandwich beam was then determined under the same conditions, with the dual cantilever mode.

3.2. Results

Figure 5. 13 shows the evolution of the storage moduli of the constituents plotted against temperature. Within the temperature range considered (300K-420K) the core undergoes a complete glass transition: the epoxy adhesive is in the glassy state at temperature below 310K with a stable storage modulus of about 3000MPa, and in the rubber state at temperatures above 360K with a storage modulus of about 30MPa. The glass transition temperature equals approximately 340K.

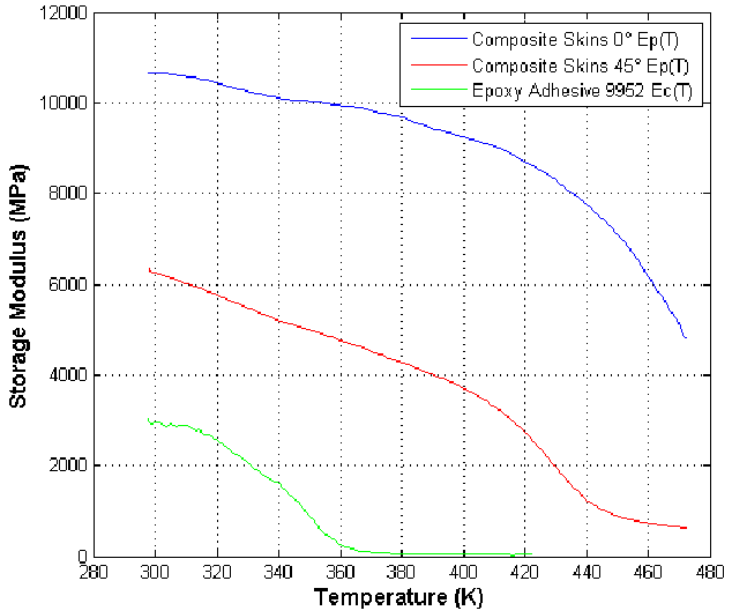

Figure 5. 13 Storage modulus of the composite skins and epoxy structural adhesive under tensile mode

The evolution of the storage moduli of the composite skins were determined up to 200°C and exhibited a different behaviour. No stable region was observed over a wide range of temperature from room temperature (298K) to approximately 420K. When temperature was further increased the storage moduli dropped more significantly, which most likely corresponds to the glass transition of the epoxy resin Hexply1458 (420K according to manufacturer's datasheet).

3.3. Modelling of the temperature-dependent stiffness

Efforts in modelling temperature-dependent mechanical properties of Fibre Reinforced Polymer (FRP) go back to the 1980s: a complete review of such models has been done by Keller, et al. [13], [14]. Among the existing models, many consist in stepped functions connecting experimentally gathered key points such as the glass transition temperature, and E-modulus values.

Mahieux, et. Al [15], [16] defined a theoretical model for temperature-dependent E-modulus where they assumed a Weibull distribution to represent the process of bond failure according to (Eq.5.10).

$$E = (E_1 - E_2).\exp\left(-\left(\frac{T}{T_1}\right)^{W_1}\right) + (E_2 - E_3).\exp\left(-\left(\frac{T}{T_2}\right)^{W_2}\right) + E_3.\exp\left(-\left(\frac{T}{T_3}\right)^{W_3}\right) \text{(Eq.5.10)}$$

where T is the temperature and E_i(i=1, 2, 3) represents the instantaneous stiffness of the material at the beginning of each plateau or state, as shown in Figure 5. 14. The Weibull coefficients w_i corresponds to the statistics of bond failure. This model successfully correlated experimental data conducted on six different polymers [16].

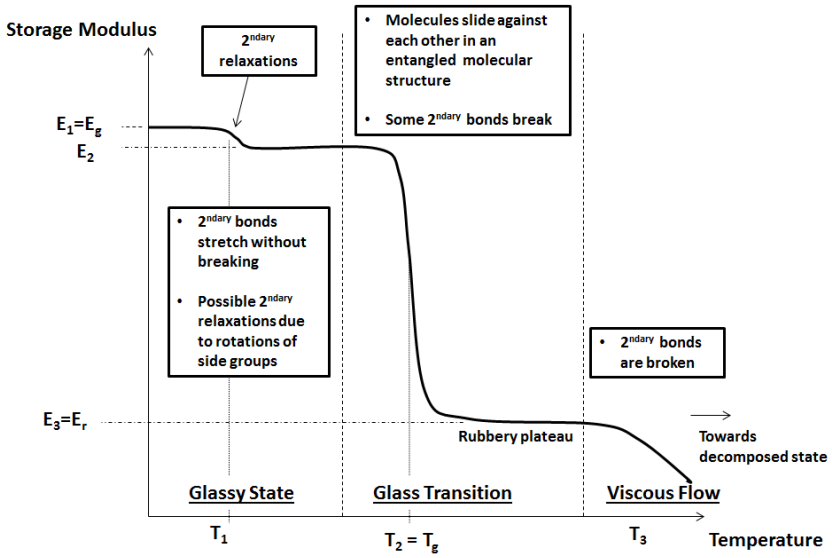

Figure 5. 14 Typical temperature-dependent storage modulus of a polymer

Other models were developed, for instance by Bai, et al. [17] who modelled the temperature-dependent modulus using an Arrhenius-type equation. Gibson, et al. [18] who developed a semi-empirical model derived from phenomenological observations, allowing to describe the temperature-dependent modulus from the glass to the rubber state. And more recently, Feng and Guo [19]–[21] who added a physical meaning to Gibson's model by using the intrinsic growth rate of the number of rubber-state molecule per unit temperature [20], based on a population growth model (logistic model).

Here, the model of Mahieux [15], [16] is used to model the temperature-dependent storage moduli of the constituents, cf. (Eq.2). It seems necessary to note that when applied to the composite skins, the model parameters have no physical significance and only serve as fitting parameters.
A first estimate of the storage moduli values and temperatures was used according to the various areas of the modulus versus temperature curve depicted in Figure 5. 14. The final parameters were then determined with a non-linear least square fitting method. Decomposed states were only taken into account to fit the model described by Mahieux, but do not have any significant meaning here since our study is limited to an upper temperature of 420K.

	E1	E2	E3	T1	T2	T3	w1	w2	w3
Comp45	8,717	3,000	502	345	430	450	4	35	20
Comp0	11,055	9,423	0	357	483.5	-	6.7	17.3	-
AXSON	3,092	85	0	345	400	-	21.7	8.2	-

Table 5. 3 Parameters used to fit the experimental data according to the model presented by Mahieux [17]

The evolution of the stiffness of the epoxy adhesive was modelled by taking a glass transition near 345K into account, and an arbitrary decomposed state near 400K.
As the composite skins exhibited a long and slowly decreasing storage modulus with increasing temperature, a first transition was modelled near 350K with a rather low Weibull coefficient (w_1 ≈5), and a second one (glass transition) near 430K for the 45° composite skins, and near 480K for the 0° composite skins. An arbitrary decomposed state was taken into account for the 45° skins with T_3 = 450K.

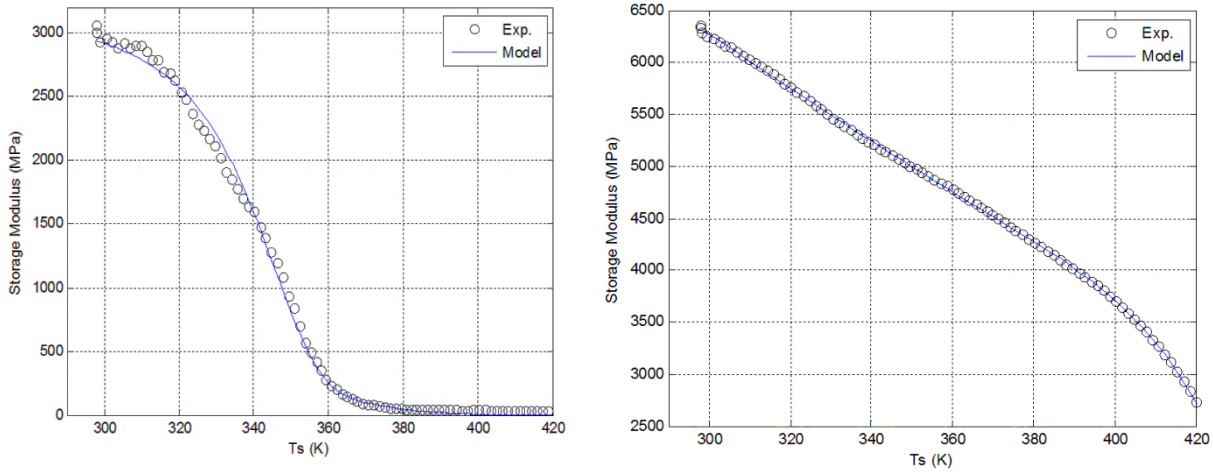

(a) (b)

Figure 5. 15 Numerical fitting of the storage moduli of (a) the epoxy adhesive core and (b) the 45° composite skins under tensile modes

These temperature-dependencies were then implemented in an analytical model based on the Timoshenko beam theory to predict the temperature-bending stiffness of the sandwich.

4. Sandwich composite beam theory

According to the Timoshenko beam theory, the total maximum deflection Δ of a beam can be calculated as the sum of the deflections due to flexural and shear deformations (Δ_f and Δ_s respectively). For a dual cantilever beam, the equation can be written as follows [22]:

$$\Delta = \Delta_f + \Delta_s = \frac{FL^3}{24\langle EI\rangle} + \frac{FL}{2}\frac{k}{\langle GS\rangle} \qquad \text{(Eq.5.11)}$$

where F is the vertical load at midspan, L is half the distance between the supports, E and G are the elastic and shear moduli, I the centroidal moment of inertia, S the cross-sectional area and k is a shear coefficient known as the shear area factor accounting for the fact that

the shear stress distribution is not uniform through the thickness. The configuration is shown by Figure 5. 16.

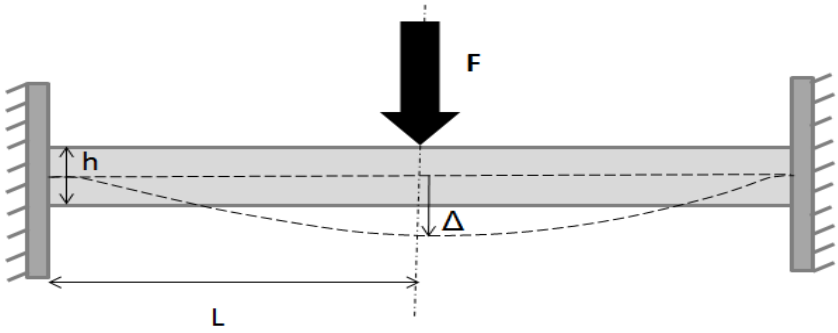

Figure 5. 16 Dual cantilever configuration

In addition, it can be shown [22] that for a sandwich composite beam of width b, composed of two skins of thickness e_p with an elastic modulus E_p and shear modulus G_p, and a core of thickness e_c with an elastic modulus E_c and a shear modulus G_c:

$$\langle EI \rangle = E_p e_p b \frac{(e_c+e_p)^2}{2} + E_c \frac{e_c^3 b}{12} \quad \text{(Eq.5.12)}$$

and

$$\langle GS \rangle = G_p e_p b + G_c e_c b \quad \text{(Eq.5.13)}$$

For an isotropic material such as a structural epoxy adhesive, it can be further assumed that:

$$G_c = \frac{E_c}{2(1+\vartheta_c)} \quad \text{(Eq.5.14)}$$

with ϑ_c is the Poisson's ratio of the core material.

Besides, for an homogeneous rectangular cross section, the shear area factor k is usually chosen equal to 6/5. Yet, Gay [22] gives a more detailed expression when dealing with sandwich beam composites:

$$\begin{cases} k = \dfrac{a_k}{8\left[E_c H_c^3 + E_p(H_p^3 - H_c^3)\right]} expr_1 + expr_2 \\ expr_1 = \dfrac{E_c}{G_c} H_c^3 \left[E_p H_p^2 + (\dfrac{4}{5}E_c - E_p)H_c^2\right] + \dfrac{E_p^2}{G_p}(\dfrac{4}{5}H_p^5 + \dfrac{H_c^5}{5} - H_p^2 H_c^3) \\ expr_2 = \dfrac{3b_k E_p (H_p^2 - H_c^2)}{E_c H_c^3 + E_p(H_p^3 - H_c^3)} \\ b_k = \dfrac{a_k}{16} H_c \dfrac{E_p}{G_p}\left\{\dfrac{H_c^2}{3} + H_p^2\left(\dfrac{G_p}{G_c} - 1\right) - H_c^2 \dfrac{G_p}{G_c}(1 - \dfrac{2}{3}\dfrac{E_c}{E_p})\right\} \end{cases}$$

(Eq.5.15)

These equations allow computing the temperature-dependent bending stiffness of a sandwich composite beam (K_s=F/Δ) based on the stiffness temperature-dependency of the constituents (E_p, E_c, G_p, G_c) determined through DMA.

In order to estimate the accuracy of the prediction, the experimental temperature-dependent bending stiffness of the sandwich is first determined.

4.1. Experimental temperature-dependent bending stiffness under dual cantilever mode

Under the dual cantilever mode, the storage modulus of a test sample is determined according to the equation below [23]:

$$E' = \frac{K_S}{F_c}\frac{L^3}{24I}\left[1 + 2.\frac{6}{5}(1+\nu)\left(\frac{h}{L}\right)^2\right] \qquad \text{(Eq.5.16)}$$

With ν the Poisson's ratio, L the sample length, h the sample thickness, I the sample moment of inertia, E the elastic modulus, K_s the measured stiffness and F_c a clamping correction factor. This expression assumes an isotropic homogeneous beam, hence it is likely that it is incorrect for the case considered here (sandwich composite beam). In particular, the second term of the expression is determined assuming a constant shear area factor (k=6/5) [24], whereas it has been seen previously that this factor depends on the skins and core stiffness according to (Eq.5.15) that vary with the temperature. Hence, plotting the storage modulus of such assemblies determined through DMA makes no sense, and it is preferable to work on the bending stiffness K_s of the sandwich beam cf. Figure 5. 17. Experimentally, it is determined as the ratio of the dynamic force by the dynamic displacement.

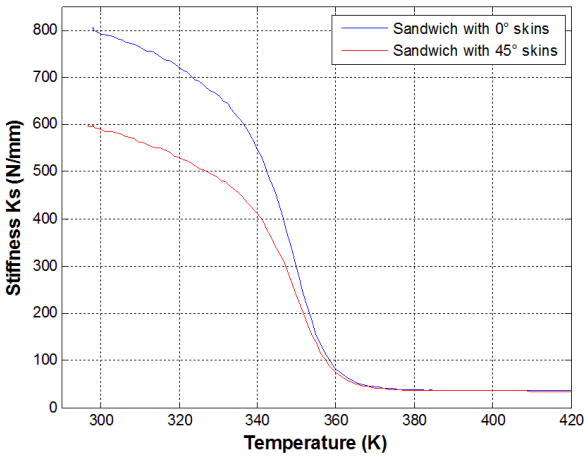

Figure 5. 17 Storage modulus evolution of the sandwich samples under the dual cantilever mode

The temperature-dependency of the bending stiffness exhibit a behaviour very similar to the storage modulus of the epoxy adhesive, with a glass transition observed near 350K. At room temperature, the bending stiffness of the sandwich with 0° skins is higher than the bending stiffness of the sandwich with 45° skins, hence indicating a higher contribution of the skins to the bending stiffness of the sandwich at lower temperatures.

4.2. Analytical calculation of the sandwich beam's bending stiffness

The experimental stiffness is plotted in Figure 5. 18 and compared with the analytical prediction determined by (Eq.5.11) with $K_s = F/\Delta$. A temperature-dependent shear area factor according to (Eq.5.15) is considered. A good correlation is observed between the temperature-dependencies even though there are discrepancies in terms of absolute values.

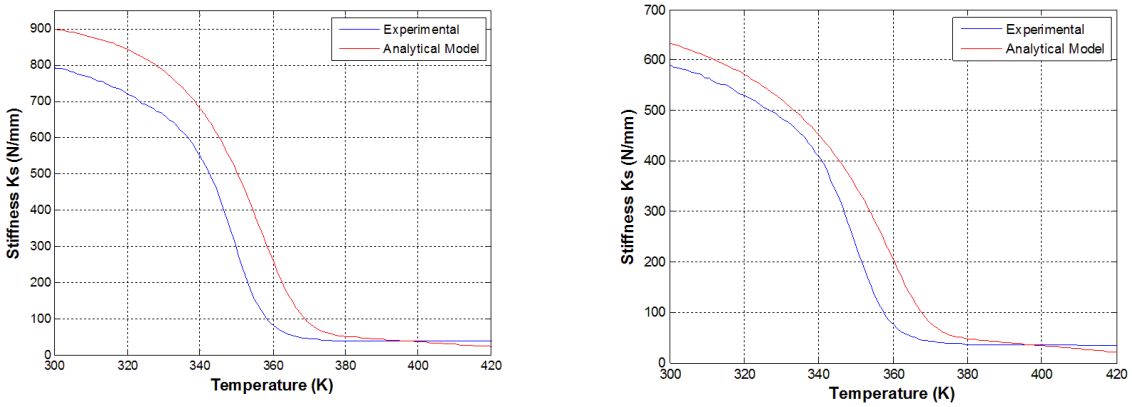

Figure 5. 18 Analytical prediction of the bending stiffness of the sandwich composite beam with (a) 0° Composite skins and (b) 45° Composite skins

As was noted by previous studies [6], [7], it is likely that a proportionality factor needs to be applied to the storage moduli of the composite skins and epoxy adhesive core to better represent the actual values of their elastic moduli. This might explain why we observe a good correlation in terms of temperature dependencies but not in terms of absolute values. Hence, we choose to solve a nonlinear least-square curve-fitting problem so as to determine the proportionality factors α_p (with $E_p = \alpha_p E'_p$) and α_c (with $E_c = \alpha_c E'_c$) needed to fit the analytical and experimental bending stiffness from Figure 5. 18. The optimisation yields $\alpha_p = 0.87$ and $\alpha_c = 0.93$, which corresponds to a shift factor of approximately 15K and is consistent with the observations made by Ropers et al. [2] and Deng et al. [6].

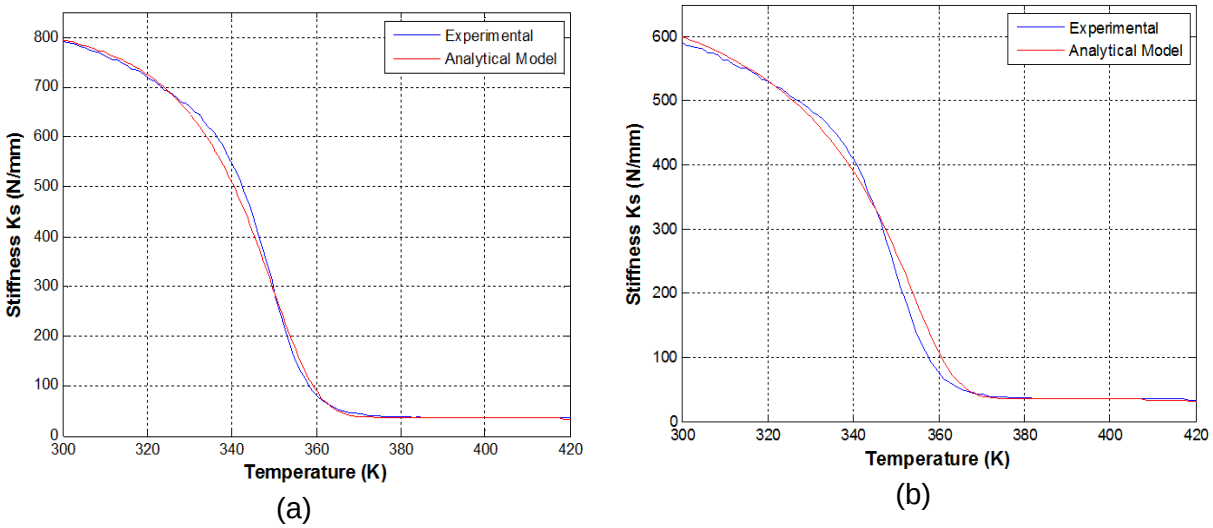

Figure 5. 19 Optimised analytical prediction of the bending stiffness of the sandwich composite beam with shifted DMA data with (a) 0° Composite skins and (b) 45° Composite skins

With these small adjustments, the method allows computing the temperature-dependent bending stiffness of the sandwich assembly and offers a good correlation between experimental DMA data and analytical prediction. It also justifies the use of the temperature dependency of the elastic moduli derived from the DMA to compute the bending stiffness of the sandwich beam.

4.3. Discussion on the shear correction factor

It is interesting to notice that the temperature dependency of the shear area factor has a significant influence. Indeed, as shown by Figure 5. 20, a constant shear area factor with a value of 6/5 (value commonly used for an homogeneous isotropic beam, and assumed by the DMA Q800 machine to compute the storage modulus of a beam under the dual cantilever mode) poorly estimates the evolution of the bending stiffness. When the temperature-dependency of k is taken into account according to (Eq.5.15), a room temperature shear area factor of k≈1,5 is obtained while at T = 100°C k≈25,2.

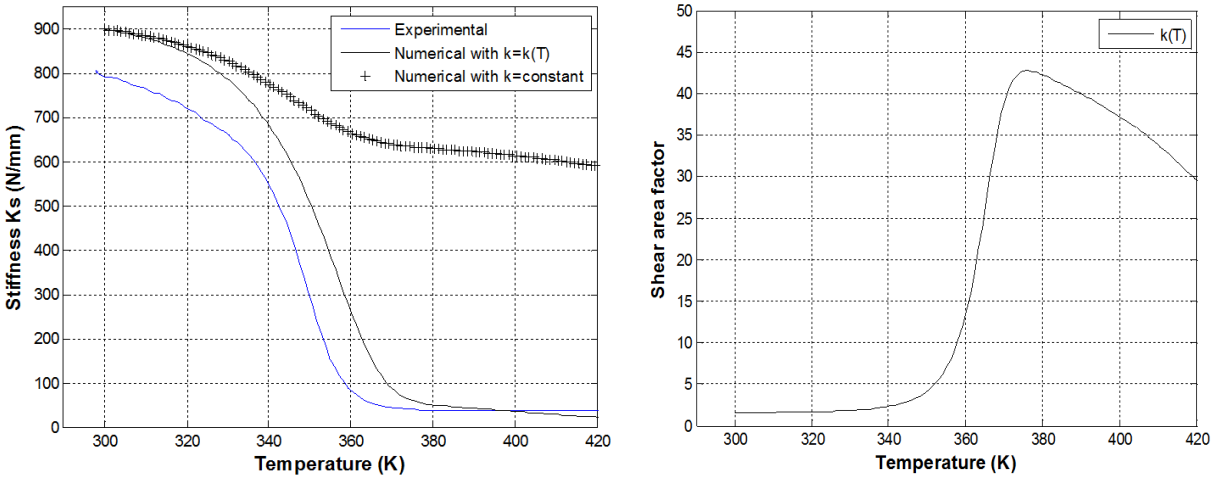

(a) (b)

Figure 5. 20 (a) Prediction of the bending stiffness of the sandwich composite beam with a temperature dependent shear area factor and (b) Evolution of the shear area factor with regards to temperature

It underlines that the higher the temperature, the higher the contribution of the shear deformations to the total deflection of the sandwich beam. In addition, Figure 5. 21 plots the contribution of the flexural and shear deformations to the total deflection of the sandwich beam versus temperature. It further highlights the increasing contribution of the shear deformations to the total deflection of the beam at increasing temperature.

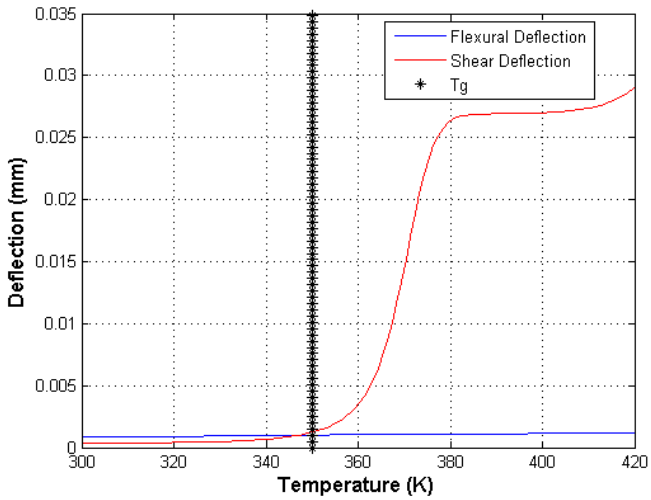

Figure 5. 21 Flexural Δf and shear Δs deformations versus temperature

4.4. Parameters sensitivity

In order to study the influence of the various parameters and mechanical properties on the bending stiffness of the sandwich beam, a sensitivity study was performed.

The system of equations (Eq.5.11) to (Eq.5.15) leading to the computation of the bending stiffness of the composite sandwich beam as a function of the dimensions of the test sample (ec, ep, b, L) and of the stiffness parameters (E_c, E_p, G_p) has been modelled with Artificial Neural Networks (ANN). Artificial neural networks consist in modelling complex nonlinear systems that are not easily modelled with a closed-form equation. Here, we want to quickly estimate the influence of each parameter on the bending stiffness of the sandwich as a function of the temperature. The neural network is created with the Matlab's neural network toolbox.

Once the neural network has been created, it requires 7 inputs (e_c, e_p, b, L, E_c, E_p, G_p) and returns the bending stiffness of the sandwich composite beam as a function of temperature. The sensitivity of each parameter is then easily investigated. Figure 5. 22 considers a variation of +/- 10% of the stiffness and thickness of the skins and core taken separately and plots the absolute variation of the resulting bending stiffness.

For instance, to investigate on the influence of E_p, a bending stiffness "$K_s_E_p$" is computed thanks to the neural network with two values of E_p taken equal to $0{,}90.E_p$ and $1{,}10.E_p$. The absolute variation of the bending stiffness is then computed according to (Eq.5.17) below.

$$Stiffness\ variation = \frac{K_s_E_p - K_s}{K_s} * 100 \qquad \text{(Eq.5.17)}$$

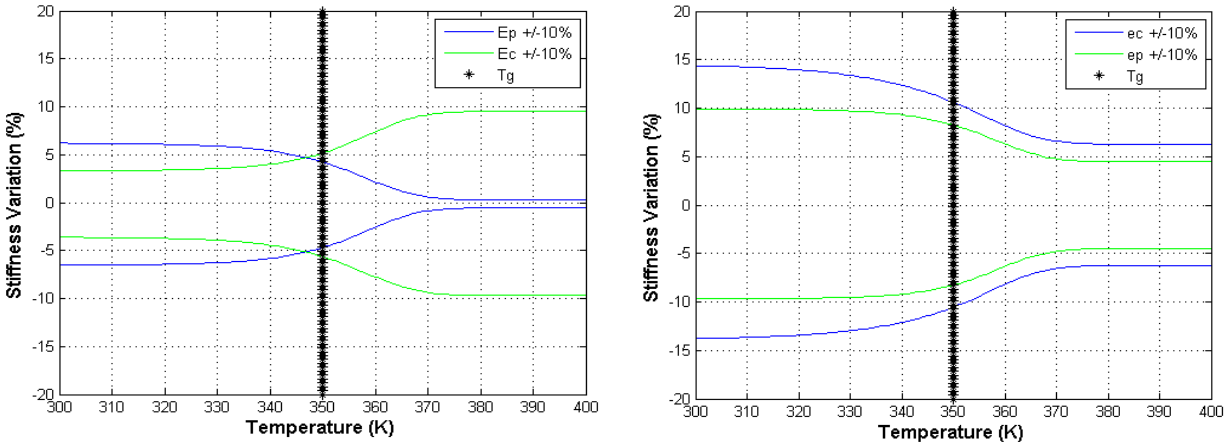

(a) (b)

Figure 5. 22 Variation of the bending stiffness of the sandwich beam resulting from a +/-10% variation of (a) the stiffness and (b) the thickness of the skins and core

Figure 5. 22 (a) underlines that at temperatures lower than the glass transition of the core material, the stiffness of the skins has a slightly higher influence on the bending stiffness of the sandwich than the stiffness of the core. On the contrary, at temperatures higher than the glass transition of the core material, the stiffness of the core has a significant influence on the bending stiffness of the sandwich as compared to the stiffness of the skins which have barely any influence at all.

As regards to the thicknesses, Figure 5. 22 (b) shows that the thickness of the core has a slightly higher influence than the thickness of the skins on the bending stiffness of the sandwich, regardless of the temperature.

5. Finite Element Modelling

In this part, the temperature-dependencies of the mechanical properties of the composite skins and epoxy adhesive core are implemented in a finite element model to assess the 3D stress field within the sandwich beam.

5.1. Material Parameters

A 3D FE model was developed to represent the DMA testing under the dual cantilever mode. Based on the results of the DMA tests under tensile mode on the composite skins and epoxy adhesive, each material properties was scaled according to Figure 5. 23. The in-plane elastic moduli E11 and E22 of a composite ply are scaled according to the evolution of the storage modulus of the 0° composite skins under tensile mode. The shear moduli G_{12}, G_{13} and G_{23} are scaled according to the evolution of the storage modulus of the 45° composite skins under tensile mode. The out-of-plane elastic modulus E_{33} is approximated with the assumed thermo-mechanical behaviour of the resin matrix Hexply1458 considering a glass transition temperature comprised between 145°C and 155°C according to manufacturer's datasheet. All Poisson's ratios (v_{12}, v_{13}, v_{23}) remain constant during the analysis (chich is not verified, as our test campaign was limited to the prediction of main temperature effects at the first order).

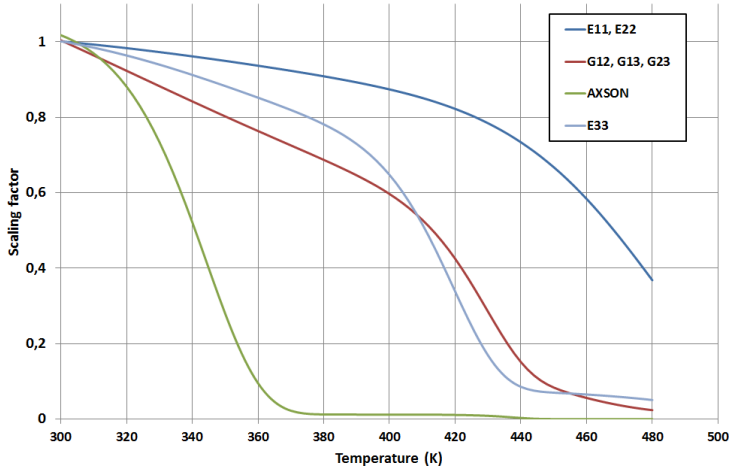

Figure 5. 23 Scaling factors applied to the mechanical properties as a function of temperature

The room temperature in-plane mechanical properties E_{11}^0 and E_{22}^0 are derived from the DMA data by assuming that $E_{11}^0 = E_{22}^0 = E'_p$ (T=30°C). The other room-temperature mechanical properties were previously determined based on the microstructure of the woven fabric using the method developed by the Polymer Research Group at the University of Nottingham and the TexGen geometric modelling software package [25], [26], cf. Chapter 2.

E_{11}^0 (GPa)	E_{22}^0 (GPa)	E_{33}^0 (GPa)	G_{12}^0 (GPa)	G_{13}^0 (GPa)	G_{23}^0 (GPa)
10.63	10.63	5.60	2.37	1.54	1.54

Table 5. 4 Mechanical properties of a composite ply at room temperature (T=30°C)

5.2. Model description

The FE model is built under ABAQUS CAE. The static and drive shafts are fully modelled as rigid bodies and the displacement of the mobile shaft is set to 4µm (which was the displacement imposed during the experimental tests). Tie constraints are applied between the upper and lower composite plies and the machine supports.

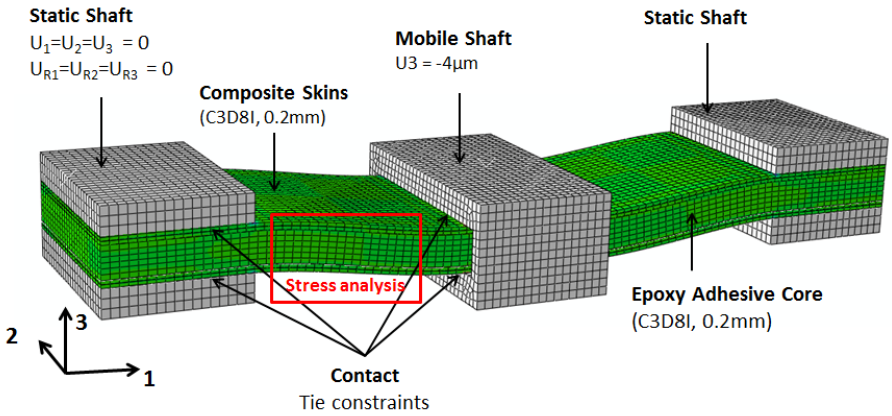

Figure 5. 24 Finite element model of the dual cantilever setup and area chosen for the stress analysis

As detailed in Chapter 4, the choice of the best solid elements to model the bending behaviour of a structure is a trade-off between accuracy and computational efficiency.

Several elements were compared with various mesh size to assess the mesh convergence as regards to the reaction force measured on the mobile shaft, cf. Figure 5. 25. C3D8I (incompatible mode eight-node brick elements) were chosen with a mesh size of 0.2mm with 6 elements through the thickness of the core and one element through the thickness of each composite ply. Quadratic elements with reduced integration (C3D20R) are expected to be more accurate but are much more costly than the linear elements with incompatible modes.

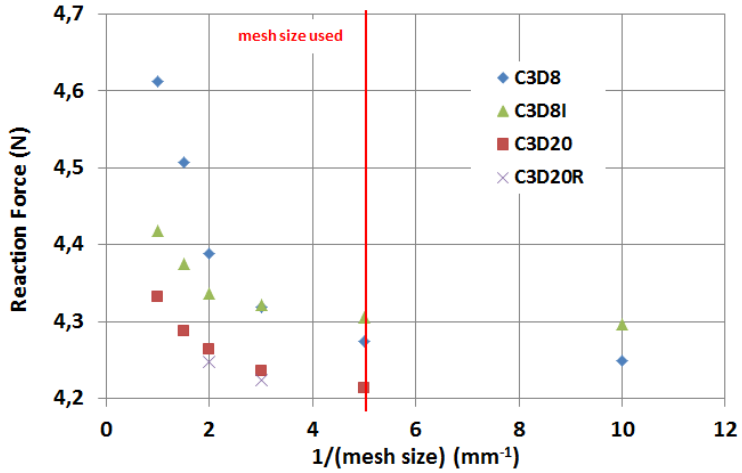

Figure 5. 25 Mesh convergence as a function of the element types

5.3. Results

The first analysis consists in computing the bending stiffness of the test specimen at several temperatures. The results slightly over-predict the experimental bending stiffness, cf. Figure 5. 26. One of the explanations is the mesh size used: our model tends to slightly over-predict the reaction force, hence the bending stiffness, as shown in Figure 5. 25.

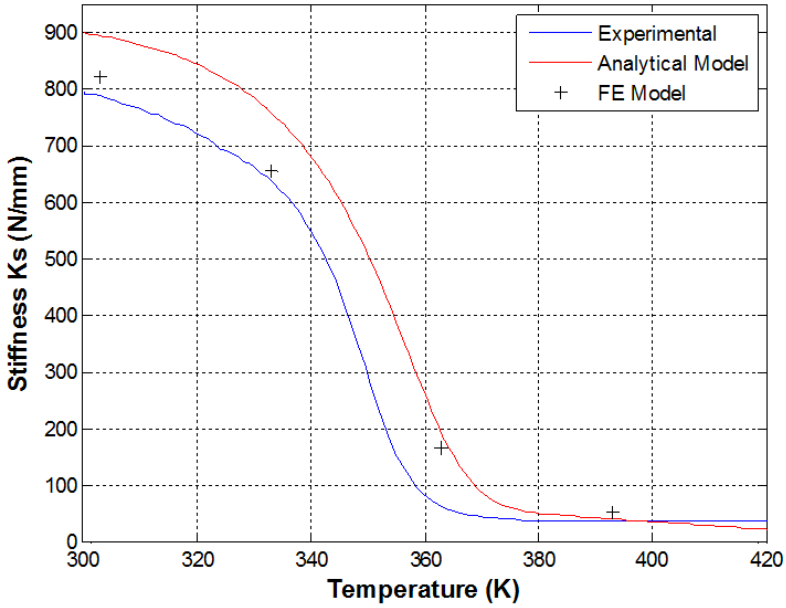

Figure 5. 26 Comparison between Experimental DMA Data, Analytical Model and FE Model

The second analysis consists in extracting the inter-laminar stress distribution in the middle of the sandwich beam (area shown in Figure 5. 24). Hence, Figure 5. 27 below plots the inter-laminar stresses S_{13} at mid-distance from each support as a function of the thickness of the laminate.

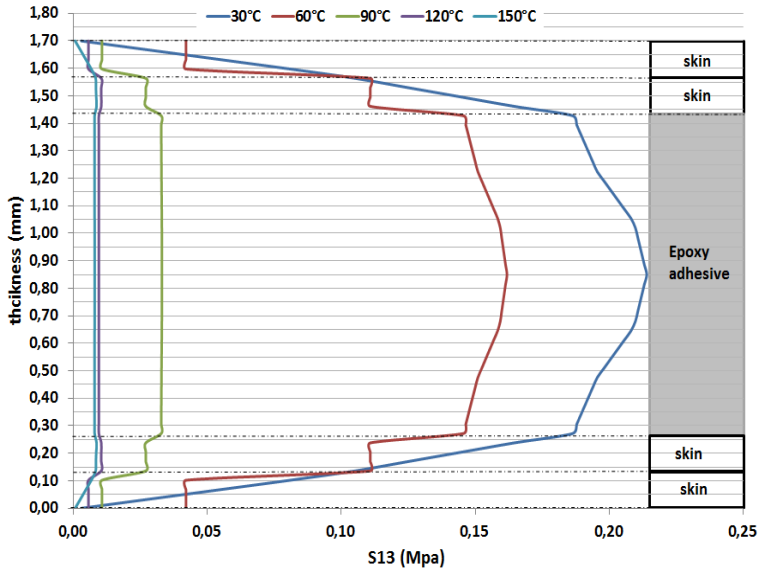

Figure 5. 27 Profile of the inter-laminar stresses within the sandwich structure with 0° skins as a function of the temperature

It is clearly observed that the inter-laminar stress distribution evolves with increasing temperature. Hence it appears that the temperature-dependencies of the constituents need to be taken into account to properly study the behaviour of such structures at increasing temperature.
DMA should no longer be considered as a simple material testing method for such layered structures.

It is worth noticing that the temperature-dependency of the inter-laminar stresses is based on the assumption that the temperature-dependencies of the out-of-plane shear moduli G_{13} and G_{23} are similar to the temperature-dependency of the storage modulus of the +/-45° plies loaded under tension, i.e. similar to G_{12}. Very few studies have been conducted to estimate the temperature-dependency of the out-of-plane shear modulus of composite laminates. However, the work of Nagatsuka et al. [4], [5] indicate that a good correlation can be found between the stiffness temperature-dependency of the resin matrix and the resulting temperature-dependency of the out-of-plane shear modulus. Yet, using rules of mixture-based models, the in-plane and out-of-plane shear moduli of a composite laminate are similarly related to the shear modulus of the resin matrix [26]. Hence the assumption made in this work seems appropriate in a first analysis.

Further work is also needed on the characterisation of the temperature-dependent Poisson's ratios (assumed constant in this work). For an epoxy resin, it is typically expected that the Poisson's ratio increases from 0.35 in the glassy state to 0.5 in the rubbery state [28].

Similarly, the relation between the storage moduli of the constituents and the actual elastic moduli needs to be further investigated.

6. Concluding remarks

A methodology of characterisation of the thermo-mechanical behaviour of a GFRP skin/epoxy adhesive core/GFRP skin sandwich structure has been presented. DMA is used to estimate the temperature-dependency of the mechanical properties of the constituents. These data are then used in an analytical model based on the Timoshenko's beam theory taking into account a temperature-dependent shear area factor to describe the contribution of the shear effect on the bending stiffness of the sandwich beam. A finite element model is also developed to take the temperature-dependent mechanical properties of the constituents into account and to assess the stresses distribution within the sandwich up to 150°C. A good correlation is found between the experimental, analytical, and finite-element bending stiffness of the sandwich structure.

Further work is required to more accurately correlate the experimental and analytical bending stiffness of the sandwich. Nevertheless, the method allows comparing several sandwich designs and materials very quickly with a minimum number of tests. This could be particularly relevant to estimate the potential use of polymer resins in sandwich-structured polymer composites for multifunctional applications such as the one investigated in this work, or for energy storage applications [29], [30].

The next step involves using this method to correlate experimental and numerical data on a sandwich structure under quasi static bending at various temperatures.

References

[1] A. Manalo, G. Maranan, S. Sharma, W. Karunasena, and Y. Bai, 'Temperature-sensitive mechanical properties of GFRP composites in longitudinal and transverse directions: A comparative study', *Compos. Struct.*, vol. 173, pp. 255–267, Aug. 2017.

[2] S. Ropers, M. Kardos, and T. A. Osswald, 'A thermo-viscoelastic approach for the characterization and modeling of the bending behavior of thermoplastic composites', *Compos. Part Appl. Sci. Manuf.*, vol. 90, pp. 22–32, Nov. 2016.

[3] A. Margossian, S. Bel, and R. Hinterhoelzl, 'Bending characterisation of a molten unidirectional carbon fibre reinforced thermoplastic composite using a Dynamic Mechanical Analysis system', *Compos. Part Appl. Sci. Manuf.*, vol. 77, pp. 154–163, Oct. 2015.

[4] W. Nagatsuka, T. Matsuo, F. Yano, K. Furukawa, and J. Takahashi, 'Formulation about time- and temperature-dependent flexural modulus of discontinuous carbon fiber mat reinforced thermoplastics', *20th International Conference on Composite Materials*, Copenhagen, 19-Jul-2015.

[5] W. Nagatsuka, T. Matsuo, T. Murakami, M. Kan, and J. Takahashi, 'Evaluation and verification of temperature dependent out-of-plane shear modulus of discontinuous carbon fiber reinforced thermoplastic composite by modified double notched compression method', *ECCM17 - 17th European Conference on Composite Materials*, Munich, Germany, 26-Jun-2016.

[6] S. Deng, M. Hou, and L. Ye, 'Temperature-dependent elastic moduli of epoxies measured by DMA and their correlations to mechanical testing data', *Polym. Test.*, vol. 26, no. 6, pp. 803–813, Sep. 2007.

[7] T. Hobbiebrunken, B. Fiedler, M. Hojo, S. Ochiai, and K. Schulte, 'Microscopic yielding of CF/epoxy composites and the effect on the formation of thermal residual stresses', *Compos. Sci. Technol.*, vol. 65, no. 10, pp. 1626–1635, Aug. 2005.

[8] ESA, 'ESCC Detail Specification No. 3901/001, Polyimide insulated wires and cables, Low frequency, 600V, -100 to +200°C'. Issue 3, Jan-1996.

[9] T. Seong Jang, D. Soo Oh, J. Kyu Kim, K. In Kang, W. Ho Cha, and S. Woo Rhee, 'Development of multi-functional composite structures with embedded electronics for space application', *Acta Astronaut.*, vol. 68, no. 1–2, pp. 240–252, Jan. 2011.

[10] J. P. Holman, *Heat Transfer*, 10th ed. .

[11] 'UNI EN ISO 6946 Building components and building elements - thermal resistance and thermal transmittance - Calculation method'. .

[12] J. Beigbeder, 'Etudes des propriétés physiques de nanocomposites à matrice polysiloxane: application au développement d'un revêtement de contrôle thermique froid et antistatique', Université de Toulouse, Université Toulouse III-Paul Sabatier, 2009.

[13] T. Keller, C. Tracy, and A. Zhou, 'Structural response of liquid-cooled GFRP slabs subjected to fire – Part I: Material and post-fire modeling', *Compos. Part Appl. Sci. Manuf.*, vol. 37, no. 9, pp. 1286–1295, Sep. 2006.

[14] T. Keller, C. Tracy, and A. Zhou, 'Structural response of liquid-cooled GFRP slabs subjected to fire – Part II: Thermo-chemical and thermo-mechanical modeling', *Compos. Part Appl. Sci. Manuf.*, vol. 37, no. 9, pp. 1296–1308, Sep. 2006.

[15] C. A. Mahieux and K. L. Reifsnider, 'Property modeling across transition temperatures in polymers: a robust stiffness–temperature model', *Polymer*, vol. 42, no. 7, pp. 3281–3291, 2001.

[16] C. A. Mahieux, 'A systematic stiffness-temperature model for polymers and applications to the prediction of composite behavior', Ph.D. Dissertation, Virginia Polytechnic Institute and State University, 1999.

[17] Y. Bai, T. Keller, and T. Vallée, 'Modeling of stiffness of FRP composites under elevated and high temperatures', *Composites Science and Technology*, pp. 3099–3106, 2008.

[18] A. Gibson, T. Brownes, S. Feih, and A. Mouritz, 'Modeling composite high temperature behavior and fire response under load', *Journal of Composite Materials*, pp. 2005–2022, 2012.

[19] J. Feng and Z. Guo, 'Temperature-frequency-dependent mechanical properties of epoxy resin and its composites', *Compos. Part B Eng.*, vol. 85, pp. 161–169, 2016.

[20] J. Feng, W. Hui, Z. Guo, H. Hu, and J. Zhang, 'Model for Temperature-dependence modulus of Glass/Epoxy Composite', presented at the Third International Conference on Smart Materials and Nanotechnology in Engineering, Shenzen, China, 2012, vol. 8409.

[21] Z. Guo, J. Feng, H. Wang, H. Hu, and J. Zhang, 'A new temperature-dependent modulus model of glass/epoxy composite at elevated temperature', *J. Compos. Mater.*, vol. 47, no. 26, pp. 3303–3310, 2013.
[22] D. Gay, *Matériaux Composites*, 5th ed. Paris: Lavoisier, 2005.
[23] *Technical Manual for DMA 2980 - Operator's Manual*. 2002.
[24] H. Osnes and T. Thorvaldsen, 'Dynamic mechanical analysis–theoretical considerations on mechanical properties', *Nor. Def. Res. Establ. FFI-Rapp.*, vol. 1656, 2011.
[25] M. Sherburn, A. C. Long, I. A. Jones, and C. D. Rudd, 'TexGen: geometric modelling schema for textile composites', presented at the Proc. 8th Int. Conference on Textile Composites (TEXCOMP 8), Nottingham, UK, 2006, vol. Paper T19.
[26] J. J. Crookston, W. Ruijter, A. C. Long, N. A. Warrior, and I. A. Jones, 'A comparison of mechanical property prediction techniques using conformal tetrahedra and voxel-based finite element meshes for textile composite unit cells', *Proc. Finite Elem. Model. Text. Text. Compos.*, pp. 26–28, 2007.
[27] M. A. Mbacke, 'Caractérisation et modélisation du comportement mécanique des composites tressés 3D: Application à la conception de réservoirs GNV', Ecole Nationale Supérieure des Mines de Paris, 2013.
[28] D. J. O'Brien, N. R. Sottos, and S. R. White, 'Cure-dependent Viscoelastic Poisson's Ratio of Epoxy', *Exp. Mech.*, vol. 47, no. 2, pp. 237–249, Feb. 2007.
[29] T. Carlson, D. Ordéus, and M. Wysocki, *Load carrying composites for electrical energy storage*. Chalmers tekniska högskola, 2007.
[30] Y. Wang, Y. Hou, and Y. Deng, 'Effects of interfaces between adjacent layers on breakdown strength and energy density in sandwich-structured polymer composites', *Compos. Sci. Technol.*, vol. 145, pp. 71–77, Jun. 2017.

General Conclusion

General Conclusion

The use of sandwich-structured polymer composites is gaining increasing interest in the aeronautical and aerospace industry for multifunctional applications such as energy storage materials and composite structures embedding electronic devices. In this framework, this PhD aimed at investigating the mechanical behaviour of a composite structure embedding electrical wires for aerospace applications.

Aerospace specifications combined to the expected weakness of such structures under out-of-plane deformations drove the need for investigations on the mechanical behavior of such assemblies under low energy impacts (hails, drop tools, maintenance operations, etc.). In particular, the influence of such embodiments on the damage modes of the structure as well as the post-impact electrical performances of the embedded cables were characterized. In order to develop a good understanding of the damage sequence, samples of the multifunctional structure were first tested under quasi-static short 3 point bend tests and dynamic bending tests for which a specific test bench was developed. Finally, impact tests were performed with a drop weight tower on fully clamped test specimens which were then submitted to dielectric strength tests. This lead to the identification of specific damage modes within the structure, associated with an electrical degradation criteria.
Indeed, the structure appeared to be particularly weakened when loaded in bending due to the low shear stiffness of the embedded cables which induced higher internal shear strains. Ultimately, these additional shear strains led to induced both internal fiber failure of the composite plies at the interface with the embedded cables, and de-cohesions within the cables. In addition, they were shown to alter the electrical performances of the embedded cables as they result in insulation degradation between two adjacent wires, which was revealed by the post-impact dielectric strength tests. These observations are particularly helpful to determine electrical degradation criteria and to choose an appropriate non-destructive testing technique for such multifunctional sandwich structures embedding flat electrical cables.

These experimental investigations were finally complemented by numerical simulations using a finite element model which included a progressive damage model and cohesive interactions. Despite a few strong assumptions, in particular about the elastic behavior and homogenization of the embedded cables, the cohesive interactions coupled to the progressive damage model were able to reproduce reasonably well the specific damage modes observed experimentally. It further underlined the damage sequence which consisted first in inter-laminar failure (slipping and de-cohesion) among the embedded cables, and then in internal tension-shear fiber failure of the composite plies at the interface with the embedded cables. Hence, it was noted that the insulator resin within the cables plays a major role in transmitting the out-of-plane stresses through-the-thickness of the multifunctional sandwich structure. In particular, the low shear stiffness of the resin was held responsible for resulting in a highly heterogeneous distribution of the transverse shear strains through the thickness of the multifunctional sandwich structure.

As this assembly aim at being used in the thermal environment of a space launcher, the second part of this thesis consisted in evaluating the influence of the temperature on the

mechanical behavior of such sandwich-structured polymer composites under out-of-plane loadings.
A first section consisted in evaluating the temperature increase within the structure due to the resistive heating of the embedded wires. It was shown both experimentally and numerically that the embodiment of the cables is likely to degrade the electrical performances of the embedded wires due to additional internal heating as compared to conventional wiring solutions. The numerical model developed in this section could be particularly helpful for parameters sensitivity analysis and the elaboration of a design that favours heat dissipation.
A methodology of characterization was then developed to take the temperature-dependent stiffness of the various materials characterized through dynamic mechanical analyses into account. These temperature-dependencies were successfully implemented in the Timoshenko beam theory, and in a non-linear finite element model. This allows linking the temperature-dependent stiffness of the skins and core to structural properties such as the temperature-dependent bending stiffness of the sandwich, and the temperature-dependent transverse shear stresses. This provides an efficient tool to optimize the choice of the best polymer insulating resin based on a minimum number of tests.

Therefore, this PhD has helped unveiling both design and electrical degradation criteria for the development of multifunctional sandwich structure embedding electrical cables. It especially provided insights into the mechanical behaviour and damage modes of such assemblies under out-of-plane and bending deformations. Several tools were proven efficient in analysing the behaviour of the multifunctional structure under such loadings: dynamic bending tests, progressive damage model and cohesive zone method, post-impact dielectric strength tests, and thermo-mechanical characterisations through dynamic mechanical analyses.

Prospects

In an industrial application, issues about the electrical continuity, especially with regards to electric connections, and complex part geometry would arise. While the industrial use case aimed at designing such structures for space launcher applications, the work carried out in the frame of this PhD has also unveiled some critical issues that might arise if such architectures should be implemented in other aeronautical or aerospace vehicles (aircrafts and satellites). For instance, the internal heat generation was shown to be much higher than the temperature increase of single cables, which is likely to hinder the electrical performances of the embedded wires as regards to aerospace specifications, or potentially limit their applications to low currents data transmission.
For aircrafts applications, electrical cycling (and thus, thermal cycling) should be investigated to ensure that it does not lead to delamination or de-cohesion within the cables due to the difference of thermal expansions between the various materials. In addition, mechanical cycling should not be neglected, including in-plane loads since the mismatch of fatigue life between the composite and copper could led to premature electrical failure.

Appendix 1. Equations of the rule of mixtures

In this appendix, the most known formulas of the classical rule of mixtures are presented [12]. The longitudinal direction is assumed to be aligned with the fibres and denoted as 11, the transverse directions are noted 22 and 33. The signification of the letters and indices are listed at the end of the appendix.

$$E_{11} = V_f E_{fl} + V_m E_m \tag{Eq. A1.1}$$

$$E_{22} = \left(\frac{V_f}{E_{ft}} + \frac{V_m}{E_m}\right)^{-1} \tag{Eq.A1.2}$$

$$v_{12} = V_f v_f + V_m v_m \tag{Eq.A1.3}$$

$$G_{12} = \left(\frac{V_f}{G_f} + \frac{V_m}{G_m}\right)^{-1} \tag{Eq.A1.4}$$

$$G_{13} = G_m\left(1 + \frac{V_f}{\frac{G_m}{G_f - G_m} + \frac{k_m + \frac{7}{3}G_m}{2k_m + \frac{8}{3}G_m}(1 - V_f)}\right) \tag{Eq.A1.5}$$

$$k_m = \frac{E_m}{3(1 - 2v_m)} \tag{Eq.A1.6}$$

It has been observed in the literature that formulas (Eq.A1) and (Eq.A3) correlate reasonably well with experimental data. On the contrary, equations (Eq.A1.2) and (Eq.A1.4) used to compute the transverse properties E_{22} and G_{12} assume that the fibres are isotropic (E_{fl}=E_{ft} with l denoting the longitudinal direction and t the transverse direction) and generally don't correlate well with experimental data since fibers usually do not exhibit an isotropic behaviour [14]. Several alternative models have been proposed in the literature to account for these discrepancies. Among them, a commonly alternative model used is the Halpin-Tsai model for the determination of the transverse and shear moduli (Eq.A1.7) and (Eq.A1.8) [15].

$$E_{22} = E_m \frac{1 + \eta_E V_f}{1 - \eta_E V_f} \quad with \quad \eta_E = \frac{E_f - E_m}{E_f + E_m} \tag{Eq.A1.7}$$

$$G_{12} = G_m \frac{1 + \eta_G V_f}{1 - \eta_G V_f} \quad with \quad \eta_G = \frac{G_f - G_m}{G_f + G_m}$$

(Eq.A1.8)

With:

V_f	Volume ratio of fibre
V_m	Volume ratio of matrix
v	Poisson’s ratio
E	Young’s modulus
G	Shear modulus
k	Bulk modulus

And the following subscripts:

f	fibre
m	matrix
l	longitudinal direction
t	transverse direction
11	longitudinal direction
22	transverse direction